UNIVERSITAT DE BARCELONA

From molecular force generation to large scale cellular movements

Otger Campàs i Rigau

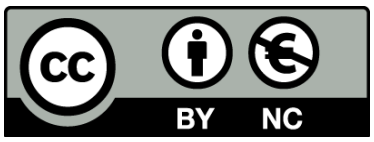

Aquesta tesi doctoral està subjecta a la llicència ***Reconeixement- NoComercial 4.0. Espanya de Creative Commons***.

Esta tesis doctoral está sujeta a la licencia ***Reconocimiento - NoComercial 4.0. España de Creative* Commons**.

This doctoral thesis is licensed under the ***Creative Commons Attribution-NonCommercial 4.0. Spain License***.

From molecular force generation to large scale cellular movements

– Ph.D. thesis –

July 2006

Programa de doctorat de Física Avançada
Bienni 2003-2005
Departament d'Estructura i Constituents de la Matèria
Universitat de Barcelona

Otger Campàs i Rigau

Ph.D. advisors:

Jaume Casademunt Viader
Jean-François Joanny
Jacques Prost

From molecular force generation to large scale cellular movements

Ph.D. thesis, Otger Campàs

Ph.D. advisors:

Jaume Casademunt Viader (Universitat de Barcelona).

Jean-François Joanny (Institut Curie and Université Paris VI)

Jacques Prost (Institut Curie and École Supérieure de Physique et de Chimie Industrielles)

Programa de doctorat de Física Avançada
Departament d'Estructura i Constituents de la Matèria
Universitat de Barcelona

Barcelona, July 2006

About the cover

Modified image from the original artwork in the Kapoor Lab webpage, showing the microtubules and chromosomes during the division of an eukaryotic cell.

That was the beginning, and the idea seemed so obvious to me and so elegant that I fell deeply in love with it. And, like falling in love with a woman, it is only possible if you do not know much about her, so you cannot see her faults. The faults will become apparent later, but after the love is strong enough to hold you to her. So, I was held to this theory, in spite of all difficulties, by my youthful enthusiasm.

Richard P. Feynman, Nobel lecture 1965

Acknowledgments, remerciements i agraïments

Writing these lines is perhaps the most difficult and beautiful part of my thesis. I am extremely grateful to all the people who helped me, who participated directly or indirectly in this work and supported me in the difficult times. It is not possible to express the gratitude I feel in the simple words I write, but still, I hope you all feel that some part of this work is yours.

M'agradaria primer de tot agrair a en Jaume tot el que ha fet per mi. Hem passat molt temps treballant junts i m'has ensanyat un munt de coses, tant a nivell científic com personal. Gràcies per haver-me donat la llibertat de treballar com a mi m'agrada i per haver-me aguantat! Gràcies per haver-me ajudat sempre que ho he necessitat, per tot el teu suport, per haver confiat en mi des del principi i, sobretot, per la teva amistat.

J'ai fait une grande partie de ma thèse à Paris, au laboratoire "Physico-Chimie Curie" de l'Institut Curie. Je remercie Jean-François et Jacques de m'avoir accueilli dans leur laboratoire. Depuis mon arrivée à Paris, vous m'avez donné toute votre confiance et vous m'avez toujours aidé. Vos qualités scientifiques et humaines sont impressionantes et un exemple à suivre pour tout le monde. Je me suis beaucoup amusé, et ça a été un honneur pour moi de faire de la physique avec vous. Un grand merci à tous les deux pour votre disponibilité, pour toutes les choses que vous m'avez apprises, pour votre bonne humeur lors de nos discussions et aussi pour votre amitié. Vous serez toujours une référence pour moi.

J'aimerais remercier chaleureusement tous les gens avec qui j'ai travaillé directement (autres que mes directeurs de thèse, bien entendu), qui m'ont appris énormement de choses et qui ont dû me supporter (je sais que ce n'est pas facile!).

Un grand merci à Cécile. Merci de m'avoir montré comment marche une manip', merci pour ton écoute dans les moments difficiles, merci pour tous les bons moments qu'on a passés ensemble et, surtout, merci pour ton amitié. Tu m'as montré un côté different de la vie qui m'a beaucoup aidé. J'espère qu'on va se retrouver et qu'on pourra encore faire du bon travail ensemble.

Un grand merci aussi à Pierre Sens qui m'a bien encadré scientifiquement grâce à l'aide d'une agrafeuse! Tes nombreuses qualités ont été une réference pour moi.

Merci pour ton amitié, pour ton écoute et pour ta façon d'être, qui permet en même temps de travailler et de prendre un verre dans un bar - c'est génial!

Je remercie aussi Hakim, avec qui je me suis bien amusé à travailler sur la motilité des gouttes et qui n'arrêtait pas de bouger le microscope pour éviter que les theoriciens n'aient raison! Merci aussi à Léa pour toutes les discussions scientifiques, mais surtout pour ton amitié. Le temps passé au labo n'aurait pas été le même sans t'entendre rigoler tout le temps!

I warmly thank Yariv and Konstantin for the nice time we had working together, for your advises and for all the things you have both taught me. I hope we will have the opportunity to keep working together in the future.

L'Ignacio ha estat el meu tutor durant la tesi (per sort no va tenir massa feina en aquest sentit) i també he tingut el plaer de treballar amb ell. Gràcies per la teva ajuda, pel teu suport i per la teva amistat.

Je veux aussi remercier les chefs de groupe avec qui j'ai eu l'opportunité de pouvoir travailler. Merci à Patricia, Cécile, Julie et Giovanni pour votre disponibilité, votre aide et pour ne pas avoir perdu votre bonne humeur même lors de nos discussions scientifiques. Je pense qu'on a bien travaillé ensemble et j'espère pouvoir continuer à le faire dans le futur.

Je tiens à remercier chaleureusement aussi les gens avec qui j'ai passé le plus de temps à Paris, car on partagait le même bureau. Tout d'abord, un grand merci à Philippe, qui m'a énormement aidé dès mon arrivé à Paris et aussi après. C'est lui qui a donné le plus de vie à notre bureau, et je ne parle pas que de l'aquarium. J'espère qu'on va fêter cette thèse avec une soirée sur une péniche! Merci aussi à Boris, avec qui on a partagé des moments très intéressants, et qui m'a fait toujours rigolé avec sa bonne humeur. Bon courage pour la suite! Je salue aussi le remplaçant de Philippe dans notre bureau, Martin. Je te souhaite bon courage pour ta thèse.

Les premiers mois à Paris n'ont pas été faciles. Merci Jérôme pour ton amitié et pour m'avoir fait apprécier les vins français. Merci Aurélien pour ton amitié et pour m'avoir appris plein des choses en biologie et sur la cuisine française. Merci de m'avoir aidé au début et d'avoir supporté mon anglais quand je ne savais pas encore enchaîné deux mots en français.

J'ai passé des très bons moments à Paris avec les "jeunes" du labo. Merci à Philippe G. (je sais que tu aimes beaucoup mon accent catalan!), à Damien (les "DJ sessions" chez toi étaient géniales!) et à Aurélie (la maîtresse du tennis français). Merci aussi à Ewa, Sébastien, Guillaume, Jean-Yves, Pierre-Yves, Faris, Martial, Nicolas B., Nicolas D., Pia, Léa-Laetitia, Raphaële, Ludwig, Mathieu, Paul, Jasper, Marco, Kirill, Simon, Raphaël, Judith,... pour tous les moments de détente et de rire qu'on a passés ensemble (surtout à la caffette). Je remercie aussi Wouter (avec qui j'ai aussi eu le plaisir de travailler) et Gerbrand, les holandais qui ont contribué à faire augmenter la hauteur de Curie dans tous les sens du terme, pour nos discussions au moment du café et aussi pour votre bonne humeur.

Enfin, je tiens à remercier l'ensemble des gens qui font de Curie une grande famille, un endroit formidable. Merci à tous les chefs d'équipe, Pascal, Pierre, Hervé, Françoise,..., aux postdocs et étudiants qui viennent d'arriver et ceux qui sont partis pendant le cours de ma thèse, à l'équipe d'informatique, qui nous aide avec les

problèmes de communication avec le monde exterieur, à Brigitte, qui m'a acueilli tous les matins avec un sourire et m'a aidé avec les questions plus pratiques, à Patrick, avec qui on a partagé des weekends au labo et des moments uniques à l'hôpital, et à tous ceux qui ont contribué à créer l'ambience exceptionnelle du labo. Je vous remercie toutes et tous pour tous les moments qu'on a partagés à la caffete, pour votre bonne humeur et pour avoir fait de mon passage à Curie un temps que je ne vais jamais oublier.

Malgrat he passat molt temps a Paris, Barcelona ha estat sempre present. És amb vosaltres, Jan, Pau i Guille amb qui he passat moments que sempre estaran amb mi, i no només durant la tesi, sinó durant tota la carrera. Us agraeixo de tot cor que m'hagueu ajudat sempre, que m'hagueu fet tocar de peus a terra quan ha estat necessari (heu tingut feina aquí, eh!) i, sobretot, que m'hagueu donat la vostra amistat incondicional. Gràcies també a en Membranelo (altrament conegut com Fèlix, o com "la Feli"), a l'inspector Ratchet (amb el sobrenom d'Àlex) i en Kinesino (algú comenta que abans es deia Aleix...), per tots els bons moments passats al nostre despatx i pel vostre bon humor. Em permeto el luxe d'agrair a l'Aleix, en nom de tots els companys de despatx, la seva contribució a la ciència pel descobriment d'un dels fenòmens més impressionants de la natura, el ben conegut fenòmen Wenk. Vull agrair també a en Toni i en Marc els bons moments que hem compartit tot dinant (juntament amb el grupet citat anteriorment), amb aquells comentaris que haurien d'haver estat recollits i publicats perquè les futures generacions no perdin el nord.

Durant les meves estades a Barcelona he tingut la sort de poder conviure amb l'Uri. Gràcies per tota la teva ajuda en els moments que ho he necessitat i, sobretot, gràcies per la teva amistat. També vull agrair a l'Òscar i a la resta de membres de la secretaria del departament la seva ajuda en les questions potser més pràctiques, però no menys importants.

Potser sense ser-ne conscient, és l'Albert qui em va dur pel camí de la Física. Gràcies de tot cor per estar sempre al meu costat, per la teva ajuda en els moments més baixos, per les interessants converses filosòfiques i pels teus preuats consells que em fan veure la vida des d'un altre punt de vista.

Des d'abans que comencés el trajecte que ara acaba, he compartit moments meravellosos amb la Roser. T'agraeixo de tot cor que m'hagis acompanyat fins al final malgrat els problemes i obstacles que han aparegut. Gràcies pel teu suport incondicional, per estar al meu costat en tot moment malgrat la distància i, sobretot, per haver-me ensenyat a disfrutar d'aquells petits moments que donen sentit a la vida.

Vull agrair a la meva familia tot el que ha fet per mi durant aquests anys en els que no he estat massa per casa. Especialment al meu germà, l'Arnau, i a la meva germana, la Meri, que sempre em fan passar bons moments amb el seu bon humor. Malhauradament, el meu avi Ramón no ha pogut compartir amb nosaltres el final de la meva tesi, encara que sé com li hagués agradat. Mai oblidaré el seu suport en tot el que he fet i la seva actitud positiva davant la vida, que ha estat i serà sempre un exemple a seguir per mi. Finalment, vull agrair de manera molt especial al meu pare el seu suport incondicional, la seva ajuda inestimable, i la seva confiança en mi ja des de ben petit. Gràcies per haver-me transmès la teva curiositat per la natura, sense la qual res del que faig seria possible i que fa de la vida un lloc ple de sorpreses.

Al meu pare

Contents

1

General introduction

The propulsion mechanisms that drive the movements of living cells constitute perhaps the most impressive engineering works of nature. Still, it is simply the interaction between molecules which is responsible for these complex and robust motility mechanisms. A question that arises naturally is thus how the underlying molecules self-organize to perform such highly coordinated tasks. Although a global understanding of cell behavior is still out of reach, the study of particular aspects of biological systems may help building up a more clear picture.

Biologists have made lots of efforts to characterize the proteins involved in cellular movements, to identify their interactions and to understand their regulation. This information is very important and has explained several aspects of the motility of living cells. The discovery of proteins able to generate forces at molecular scales, known as motor proteins, provided essential information to understand the observed cellular movements. However, the force developed at the molecular level by a single protein is too weak to drive cellular movement on its own. Probably the clearest example is the functioning of muscles. The forces developed are about 12 orders of magnitude larger than the forces generated at molecular scales. This is possible because the contraction of muscles involves the collective action of many motor proteins (Alberts et al., 2004; Bray, 1992). Although each one of these proteins generates a small force (in the picoNewton range), the sum of their individual contributions leads to large forces. At the cellular scales something similar occurs. The necessary forces for the motion of a cell and even for intracellular movements, are larger than molecular forces. The collective action of molecular force generators is thus essential to understand most cellular movements.

Here we study theoretically some examples of cellular movements and compare quantitatively, when possible, our results to the experimental observations. The work is divided in three parts: we first study the motion of oil drops propelled by an actin comet tail, which closely mimics the motility mechanism of several bacterial pathogens, as the bacteria *Listeria*. The second part is devoted to particular aspects of intracellular transport. We study the physical mechanism of membrane tube extraction by motor proteins, the traffic of motor proteins at large scales and the collective force generation of molecular motors pulling on fluid membranes. In the last part we

address both the motion of chromosomes in eukaryotic cell division and the stability of spindle-like structures, as the mitotic spindle.

Our aim is to understand how these movements arise from the cooperative action of molecular force generators. The forces developed by ensembles of force generators are not static, but depend on the dynamic state of the system. This is so because the kinetics of the individual force generators is strongly affected by the forces created by themselves. As we discuss below, this force-dependent kinetics imposes a highly non-linear dynamics for the system and, as a consequence, several dynamic instabilities occur. Our work shows that the collective behavior of molecular force generators is essential to understand some features of cellular movements.

1.1 Examples of cellular movements

Living cells display an amazing variety of movements, both at intracellular level and at level of the cell as a whole (Alberts et al., 2004; Bray, 1992). Although already very complex, the propulsion mechanisms of bacteria are typically simpler than those of eukaryotic cells. Some eukaryotic cells use cilia (e.g. *Paramecium*; Fig. 1.1b) or flagella (e.g. animal sperm cells; Fig. 1.1a) to induce the motion of the surrounding fluid. The induced fluid flow brings nutrients near the cell and allows it to move. Some multicellular organisms, like *Volvox*, also use eukaryotic flagella for the same goals (Solari et al., 2006). The bacteria *Escherichia Coli* are also propelled by flagella, but of a different class, with different structure and beating mechanism. Besides ciliary and flagellar beating, there exist bacteria (e.g. *Listeria*; Fig. 1.1d) that use actin polymerization to move through the cytoplasm of infected cells (see chapters 2 and 3). The force generation by polymerization of actin filaments is not exclusive of bacteria. The crawling motion of eukaryotic cells also involves the constant growth of entangled actin filaments (Fig. 1.1c; see chapter 2). All these motility mechanisms drive the motion of the cell as a whole. Nevertheless, at intracellular level there are also many processes that involve force and motion generation. The process of intracellular transport (see chapters 4 and 5), cell division (Fig. 1.1f; see chapters 7, 8 and 9), phagocytosis (Fig. 1.1e), cell adhesion and the reorganization of the cytoskeleton, are examples of processes that require force generation at cellular scales.

Eukaryotic cells have a toolbox of molecular force-generating elements that can be combined in many different ways, leading to distinct motility mechanisms (Bray, 1992; Murase, 1992). For instance, eukaryotic flagella and cilia are extremely ordered structures where ensembles of dynein motors collectively generate the sliding of microtubules, inducing the observed beating patterns. On the other hand, the extension of the leading edge of a crawling cell is due to the simultaneous polymerization of many actin filaments that are crosslinked in a network structure. In all cases, however, it is the combined action of many molecular force generators which produces the necessary forces for both intracellular movements and the motion of the cell as a whole. This cooperativity between the elementary force generators is essential to understand the dynamics of several cellular processes, and even the force production at larger scales, like in muscle contraction.

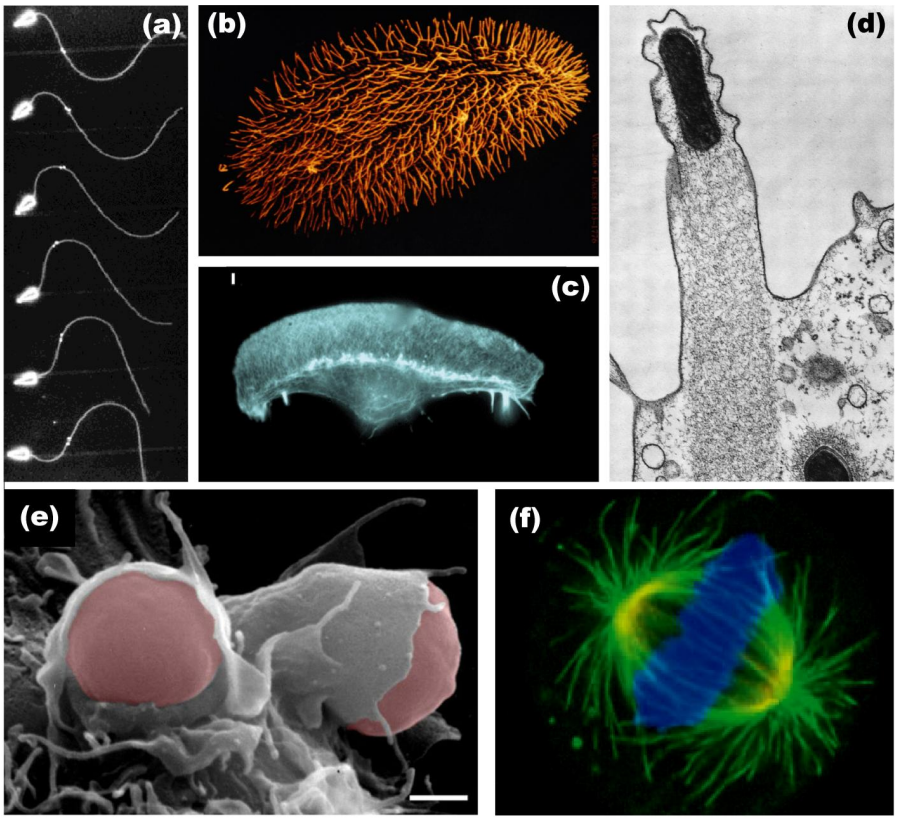

Fig. 1.1. Examples of cellular movements. (a) Flagellar beating of a sperm cell. Time sequence of the beating pattern: time increases from top to bottom. A wave propagates along the flagellum from the head to the tail, inducing the motion of the surrounding fluid and propelling the sperm cell. (Image by C. Brokaw). (b) Field of cilia (orange) on the surface of a *Paramecium*. The coordinated motion of the cilia generates the fluid flow that propels the cell. (Image by A. Fleury). (c) Fluorescence image showing the actin distribution in a crawling keratocyte. (d) Image of the bacteria *Listeria* moving in an infected cell. The actin comet tail that extends at the back of the bacterium generates the necessary force to propel it in the cytoplasm of the host cell and deform its membrane. (Adapted from Ref. (Mahadevan and Matsudaira, 2000)). (e) Image showing a macrophage engulfing two objects by phagocytosis. (Figure taken from the P. Chavrier Lab website (Institut Curie)). (f) Fluorescence image of the mitotic spindle during the division of an eukaryotic cell. The microtubules (green) are organized in a bipolar structure and the chromosomes (blue) are positioned at the mitotic midplane before segregation. (Adapted from Ref. (Gruss et al., 2002)).

1.2 Molecular basis of force and motion generation

The forces driving cellular movements have their origin at molecular scales (Alberts et al., 2004; Bray, 1992; Howard, 2001). There exist several processes able to generate forces at the molecular level, and most of them require nucleotide hydrolysis as energy supply. The hydrolysis of a Nucleotide-TriPhosphate (NTP) into Nucleotide-DiPhosphate (NDP) and an inorganic phosphate provides an energy of about $10K_BT$, where K_BT is the thermal energy. While Adenosine TriPhosphate (ATP) is the most common molecule involved in processes of force generation, Guanosine TriPhosphate (GTP) provides, for instance, the necessary energy for microtubule polymerization/depolymerization. As we discuss below, this energy drives motions of a few nanometers. Hence, the order of magnitude of the forces generated by elementary molecular force generators are of order $10\,K_BT/\text{nm}$ and, thus, in the picoNewton range.

The chemical energy from the nucleotide hydrolysis is converted into mechanical work by specialized proteins. Most cellular and intracellular movements involve the assembly of protein filaments (actin filaments and microtubules [1]) and/or the action of motor proteins. There exist, however, other molecular force-generating mechanisms that we do not address here, like rotatory motors that drive the rotational motion of bacterial flagella. We briefly describe below the mechanisms by which protein filaments (actin filaments and microtubules) and motor proteins generate forces and motion at molecular scales.

1.2.1 Actin filaments and microtubules

Actin filaments and microtubules are biopolymers with distinct biochemical and physical properties that allow them to perform different functions in living cells. These two types of filaments are directly or indirectly responsible for most, if not all, large scale movements in eukaryotic cells. In some situations, the growth of actin filaments generates the necessary forces for motion, like in the extension of the lamellipodium of a crawling cell or the motion of several bacterial pathogens (see chapter 2), whereas in other cases, molecular motors (myosin) associated to actin filaments drive the movement, as in muscle contraction. The growth and shrinkage of individual microtubules generates forces that are important for the process of intracellular transport, organelle positioning and cell division. However, most cases of microtubule-based movements involve motor proteins (kinesins and dyneins) that move along microtubules and generate the necessary forces for motion, as in intracellular transport (see chapters 4 and 5) and cell division (see chapters 8 and 9). Moreover, microtubules and motor proteins form also specialized structures (cilia, flagella,...) which are responsible for the motion of some cells and organisms (Volvox (Solari et al., 2006)).

[1] Besides microtubules and actin filaments, the cytoskeleton of eukaryotic cells contains also intermediate filaments, which confer further mechanical consistency to the cell.

The necessary forces to generate large scale movements can be thus developed directly by the growth of ensembles of filaments (actin filaments or microtubules) or through motor proteins associated to these filaments.

Biochemical structure and growth properties

Both actin filaments and microtubules are repetitive assemblies of small protein subunits, actin for actin filaments and tubulin for microtubules. The protein subunits forming these polymers have a structural polarity, which guides the assembly process in such a way that only linear structures are formed. The filaments are composed of a given number of linear arrays of subunits, called protofilaments. We now describe the protein subunits forming these filaments and discuss their structure and growth properties.

Actin filaments

Actin is a very conserved protein throughout evolution and it typically constitutes approximately the 10% of the protein content of an eukaryotic cell. Both the polymerized form of actin (filamentous actin or F-actin; Fig. 1.2) and its monomeric form (globular actin or G-actin; Fig. 1.2) are found in different proportions in cells. The continuous conversion of F-actin to G-actin and vice-versa allows the cell to rapidly reorganize its cytoskeleton and adapt to different conditions.

Actin filaments are composed of two linear arrays of actin monomers (protofilaments), arranged as a right-handed double helix that twists around itself every 37 nm (Fig. 1.2). This helical structure confers more stability to the filament as each actin monomer not only contacts the monomers along a single protofilament but also contacts laterally monomers from the other protofilament.

Actin monomers have an structural polarity. As a result, two actin monomers can only assemble in a particular spatial arrangement, which leads to a “head-to-tail” assembly of the monomers in a protofilament. Moreover, the two protofilaments are arranged with parallel polarities. This organization leads to an overall structural polarity of the actin filaments, with the two ends being structurally different. The dynamics of the two filament ends can be thus regulated differently by the association of distinct regulatory proteins. There exist many actin associated proteins that regulate the dynamics of the filament ends and organize actin filaments. Indeed, actin filaments appear typically organized in networks, bundles or other structures, depending on the accessory proteins connecting the actin filaments (Fig. 1.2). In chapter 2 we briefly describe the roles of the most important proteins that regulate actin assembly and large scale organization of actin filaments.

The polymerization process leading to the growth of an actin filament is ATP dependent. Actin monomers exist in two different conformational states, depending on whether they are bound to ATP or ADP molecules. Monomers in a given conformation tend to assemble with those having the same conformation. ATP-bound monomers assemble faster than ADP-bound monomers and the resulting structure is more stable (Fig. 1.3a). As a consequence of this different stability, actin filaments

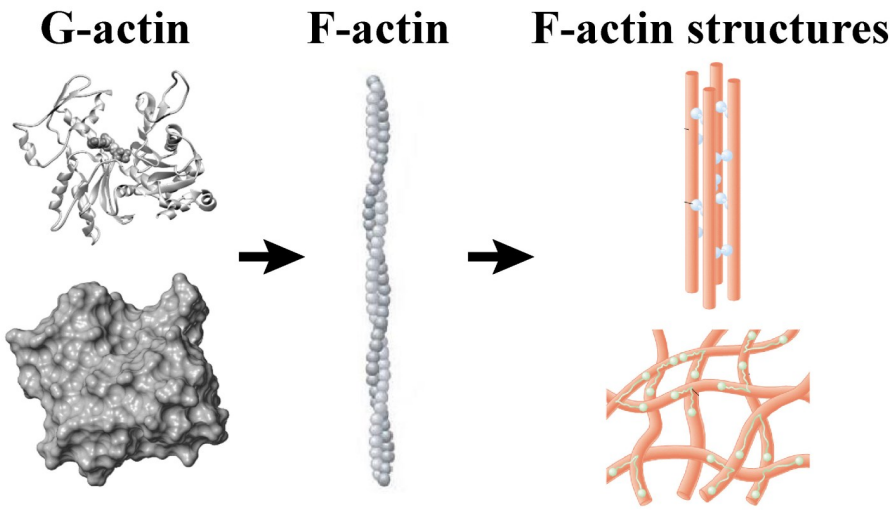

Fig. 1.2. Actin monomers, filaments and large scale actin structures. (a) Structure of an actin monomer (G-actin). The actin monomer in ribbon representation together with an ATP molecule in its binding site (above), and the solvent-accessible surface of actin (below). (Image taken from the website http://www.mih.unibas.ch/Booklet/Chapter1/Chapter1.html). (b) Sketch of the structure of an actin filament (F-actin), showing the two protofilaments arranged in a double helix structure. (Adapted from Ref. (Fujiwara et al., 2002)). (c) Typical large scale organizations of actin filaments (pink) mediated by accessory proteins (light blue). Depending on the type of proteins that crosslink the filaments, the resulting structure can be a F-actin bundle or a network. (Modified from Ref. (Lodish et al., 2000)).

with ADP-bound monomers depolymerize faster. The existence of these two states for monomer assembly characterizes the growth dynamics of actin filaments.

The polymerization of an actin filament starts with a slow nucleation phase, where some ATP-bound monomers assemble and create a seed for further polymerization. Once these nucleation centers are assembled, the growth of the filament is faster. The ATP molecules associated with the actin monomers are hydrolyzed some time after the addition of the monomer to the filament (Fig. 1.3a). As a consequence, the actin filament is typically composed of two regions, one with ATP-bound monomers and another with ADP-bound monomers. The two ends of the filament have thus different growth properties, because the assembly and dissociation rates are different for ATP and ADP-bound monomers. In particular, the ATP-containing end grows faster than the ADP-containing end, and are referred to as plus end (or barbed end) and minus end (or pointed end), respectively. The distinct growth properties and stability of the two ends give rise to different dynamical regimes of growth (Fig. 1.3b), namely treadmilling and growth catastrophes (dynamic instability). Treadmilling is an steady state in which, on average, the barbed end grows and the pointed end shrinks, leading to a constant length of the filament in spite of the existence of a net flux of actin monomers through the filament. Catastrophes take place

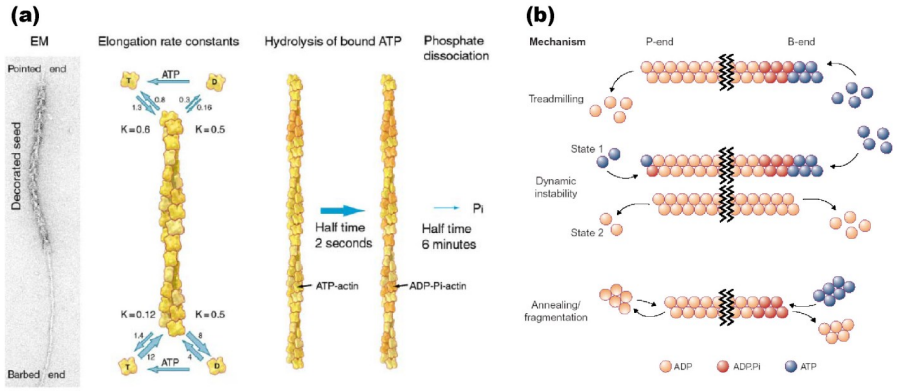

Fig. 1.3. Dynamics of actin filaments. (a) Electron microscopy (EM) image of an actin filament with a portion of its length decorated with myosin heads, showing the helical structure of the filament (left). Sketch of actin filament elongation, ATP hydrolysis and phosphate dissociation. The association and dissociation rates are in units of $\mu M^{-1} s^{-1}$ and s^{-1} respectively. The ratio of the dissociation and association constants, K, is in units of μM. (Adapted from Ref. (Pollard and Borisy, 2003)). (b) Dynamical regimes of an actin filament: Treadmilling, dynamic instability and annealing/fragmentation. (Adapted from Ref. (Littlefield and Fowler, 2002)).

when the ATP-containing region stochastically disappears, leading to a rapid disassembly of actin monomers at the barbed end. While treadmilling has been directly observed, only indirect proves exist for growth catastrophes of actin filaments (Littlefield and Fowler, 2002).

Microtubules

Like actin, tubulin is also one of the most conserved proteins throughout evolution. The microtubules, which result from the self-assembly of tubulin dimers, are necessary for many essential processes in eukaryotic cells, and play a crucial role in their internal organization and transport (see chapter 4).

Tubulin is a dimeric molecule composed of two slightly different subunits, namely α and β-tubulin (Fig. 1.4a). The tubulin dimers are thus characterized by a structural polarity, and assemble into linear arrays (protofilaments) with alternated α and β-tubulin subunits (Fig. 1.4a). The microtubule has a cylindrical hollow structure, formed typically by 13 protofilaments with parallel polarities, which confer an overall polarity to the microtubule, with α-tubulin exposed at one end and β-tubulin at the other (Fig. 1.4b-c). The distinct microtubule ends are recognized by microtubule associated proteins which can regulate the dynamics of each end differently.

Each subunit forming the tubulin dimer has a binding site for GTP, but only that exposed to water in the β-tubulin subunit can be hydrolyzed into GDP. In a similar way as for actin, there is an initial nucleation phase of microtubules, in which GTP-bound tubulin dimers assemble and create a seed. The growth of the filament once the seed is created is much faster. The GTP molecules are hydrolyzed quickly after

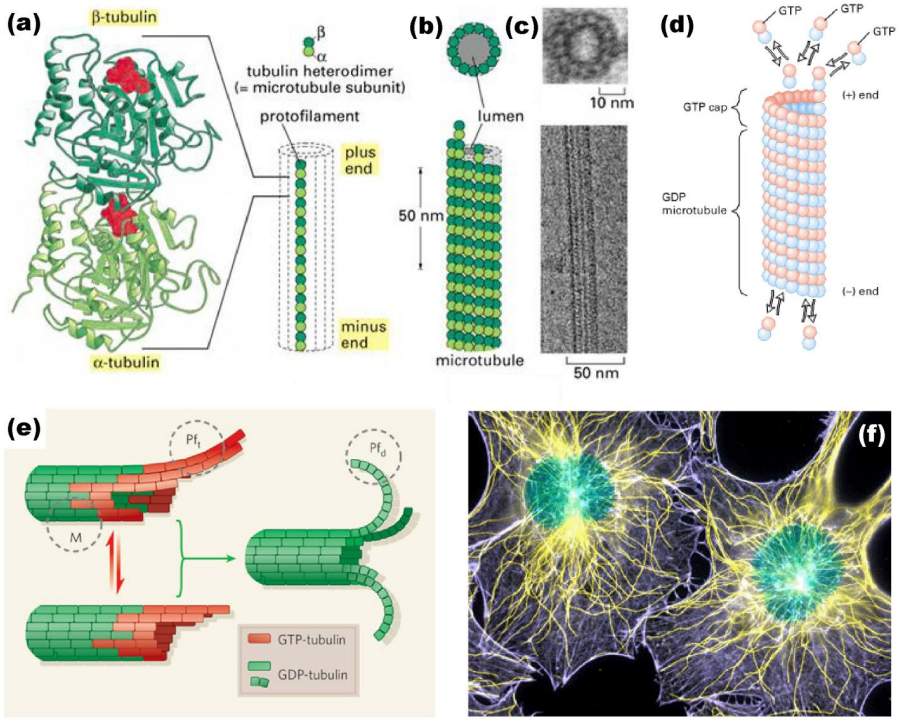

Fig. 1.4. Microtubule structure and dynamics. (a) Structure of an $\alpha - \beta$ tubulin dimer composing the microtubule. (b) Sketch of a microtubule showing its hollow tubular structure composed of 13 protofilaments: cross-section (above) and side-view (below). (c) Electron microscopy image of a microtubule: cross-section (above) and side-view (below). (Adapted from Ref. (Alberts et al., 2004)). (d) Growth dynamics of a microtubule. GTP-bound tubulin dimers are added at the plus end, whereas at the minus end the GDP-bound dimers dissociate from the microtubule. A GTP cap forms at the plus end and maintains the stability of the microtubule. (Adapted from Ref. (Lodish et al., 2000)). (e) Dynamics and structure of growing and shrinking microtubule ends. Growing ends (left) fluctuate between gently curved and straight protofilament sheets; shrinking ends (right) are dominated by highly curved, peeling protofilaments. The transition between a slowly growing and a rapidly shrinking microtubule end is known as dynamic instability. (Adapted from Ref. (Mahadevan and Mitchison, 2005)). (f) Fluorescence image showing the microtubules (yellow) and actin filaments (violet) during the interphase of eukaryotic cells (mouse fibroblast). (Figure by T. Wittmann).

the initial assembly. As a consequence, the microtubule is characterized by a GTP-cap at the β-tubulin end, and the rest of the microtubule, and in particular the α-tubulin end, contains GDP (Fig. 1.4d). Tubulin dimers are added more rapidly to the β-tubulin end (plus end) than to the α-tubulin end (minus end) of the microtubule. The GTP hydrolysis has important consequences for the dynamics of the filament. If the GTP-cap at the plus end disappears, the microtubules quickly disassemble until a new GTP-cap is formed, allowing the microtubule to grow again (Fig. 1.4e). This slow growth and rapid shrink of microtubules is called dynamic instability. A microtubules can also undergo treadmilling, in which case it grows at the plus end and shrinks at the minus end, with a net flux of tubulin going through the filament. These two dynamical regimes are of crucial importance during cell division (see chapter 7).

The organization of microtubules in an eukaryotic cell depends on the stage of the cell cycle. During cell division, microtubules form a highly ordered structure called mitotic spindle (see chapters 7 and 9). In the rest of the cell cycle (interphase) microtubules display an approximately radial distribution from the cell center (Fig. 1.4f).

Elastic properties

At scales much larger than the individual monomers constituting the polymer (microtubules or actin filaments), the elastic properties of these biopolymers can be understood in the same framework (de Gennes, 1979; Doi and Edwards, 1986). The bending rigidity B quantifies the energy cost of bending deformations of the polymer [2]; the stiffer the polymer, the larger the value of its bending rigidity. The comparison between the energy cost of bending the polymer and the thermal energy, K_BT, defines the persistence length, $\ell_p = B/K_BT$, which sets the length scale at which thermal fluctuations are able to significantly contort the filament.

If the polymer length L is such that $L \ll \ell_p$ the polymer appears straight (Fig. 1.5b), whereas for $L \gg \ell_p$ the polymer appears as a random tangled mess (Fig. 1.5a). Microtubules have a persistence length $\ell_p \simeq 1-5$ mm, much larger that the typical size of a cell (~ 10 μm) and behave thus as rigid rods inside the cell. This is not to say that microtubules are straight in a living cell. Indeed, the buckling force [3] of a microtubule of 5 μm in length is about 1 pN, meaning that the typical forces developed by motor proteins and the polymerization process itself, which are of several picoNewtons (see below), can deform microtubules significantly (Fig. 1.4f). Actin filaments are more flexible at cellular scales as their persistence length is about 15 μm. Therefore, under no applied load, actin filaments of several microns long are already contorted as a consequence of thermal fluctuations. As we explain below, the elastic properties of the filaments are crucial to understand how do filaments organize to generate forces.

[2] There is also an energy cost associated to twist that we do not address here.

[3] The buckling force, $F_B \sim B/L^2$, is the necessary force to bend a straight rod of length L and bending rigidity B (Landau and Lifshitz, 1986).

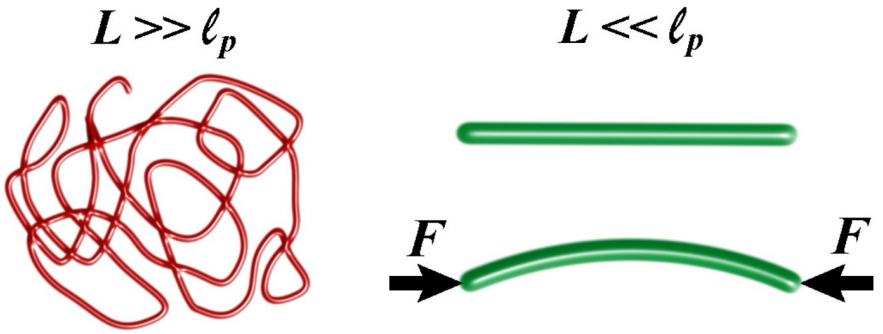

Fig. 1.5. Sketch of a filament with a length L much larger (a) and smaller (b) than the persistence length ℓ_p. For filament lengths smaller than the persistence length the filament appears straight (b; above). The filament bends under the action of a compressive force, F, larger than its buckling force (b; below).

Force generation by polymerization

The polymerization process of actin filaments and microtubules is able to generate force. *In vitro* experiments using individual microtubules have shown that a microtubule polymerizing against an obstacle generates large enough forces to induce its own bending (Dogterom et al., 2005; Janson and Dogterom, 2004; Dogterom and Yurke, 1997) (Fig. 1.6b). The forces developed by the polymerization process can be measured from the shape of the bent microtubule and are of the order of several picoNewtons. Moreover, these experiments allow to measure the growth velocity of the microtubule as a function of the applied load (Fig. 1.6a). The polymerization velocity decreases exponentially with the magnitude of the opposing force. Although the necessary force to stall the growth of a microtubule (stall force) has not yet been measured, forces up to 4 pN are developed by the growth of individual microtubules. The applied force not only affects the polymerization kinetics, but also the dynamical state of the growing microtubule. In particular, the rate at which catastrophes occur increases exponentially with the opposing load (Janson et al., 2003).

Although the precise mechanism of force generation by polymerization remains unclear, a simple model that includes the force-dependent polymerization kinetics accounts for the observed behavior (Dogterom and Yurke, 1997). The filament growth requires the addition of new subunits at its growing end (plus end). When the filament is growing against an obstacle, it is not possible to add new subunits to the growing end unless a large enough gap between the filament plus-end and the obstacle transiently forms, allowing new subunits to be incorporated to the filament (Fig. 1.6c). The model proposes that the energy barrier separating the polymerized and non-polymerized tubulin forms is increased by a load opposing the filament growth. According to Kramers rate theory (van Kampen, 2004; Kramers, 1940) the polymerization and depolymerization rates are exponentially affected by the force. The experimental observations show that rate at which tubulin dimers are added to

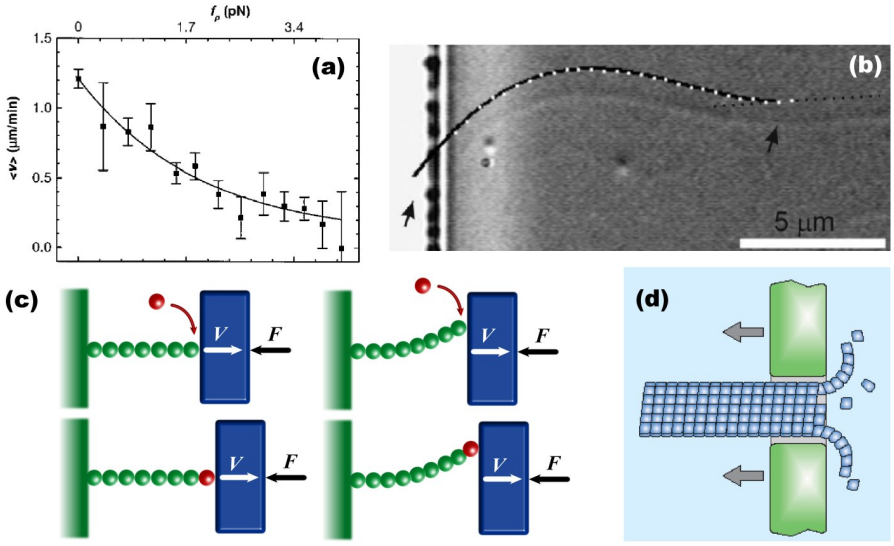

Fig. 1.6. Force generation by polymerization and depolymerization. (a) Average growth velocity of a microtubule as a function of the compressive force, f_p. The solid line corresponds to an exponential fit of the experimental data. (Adapted from Ref. (Dogterom and Yurke, 1997)). (b) Experiments in which microtubules grow from nucleation sites attached to the surface. Upon growth, a microtubule may reach a wall (left arrow). The microtubule appears buckled as a consequence of its growth against the wall. The force that the microtubule is applying can be deduced from its buckled shape (continuous line). (Adapted from Ref. (Janson and Dogterom, 2004)). (c) Sketch of the force-generating process of a growing filament. When a filament hold at a given point (green wall) polymerizes against an obstacle (blue), the addition of new monomers to the filament induces the motion of the obstacle even in the presence of compressive loads. The filament may be straight (left) or buckled (right) when sustaining the applied load. (d) Sketch of the process of force generation by depolymerization of a microtubule. A depolymerizing microtubule can induce the motion of an object attached to it thanks to the curled configuration of the protofilaments at the depolymerizing end. The arrows indicate the direction of the force applied by the depolymerizing microtubule. (Adapted from Ref. (Mogilner and Oster, 2003b)).

the microtubule decreases exponentially with the opposing force, f, whereas the depolymerization rate is nearly not affected by the load. The growth velocity of the filament can thus be written as (Dogterom and Yurke, 1997)

$$v_p(f) = \delta \left[\alpha \exp\left(-\frac{f\delta}{K_B T} \right) - \beta \right] , \tag{1.1}$$

where δ is the increase in filament length per added dimer, α is the polymerization rate at vanishing load (which depends on the bulk concentration of non-polymerized dimers) and β is the depolymerization rate. In most conditions, the polymerization rate is much larger than the depolymerization rate at the plus-end and β can be neglected. The "Brownian ratchet" model (Mogilner and Oster, 2003b; Mogilner and

Oster, 1996), which describes the mechanism by which new subunits are added to a filament under applied load, leads to similar results. This model states that bending fluctuations of the filament and/or thermally induced fluctuations of the cargo, can transiently open up a large enough gap between the filament and the obstacle, allowing the addition of new subunits to the filament.

In contrast to microtubules, the relation between the growth velocity and the opposing force for an actin filament has not yet been measured. However, it is known that actin filaments can develop forces of several picoNewtons upon polymerization (Miyata et al., 1999; Marcy et al., 2004; Mogilner and Oster, 2003a). The maximal force (stall force) developed by the polymerization of a single actin filament has been estimated to be of a few picoNewtons (Peskin et al., 1993). As the bending rigidity of actin filaments is much smaller than that of microtubules, actin filaments longer than several tenths of nanometers are easily bent by the forces developed upon their own growth. In order to efficiently generate directed forces, only portions of actin filaments shorter than about 200 nm should be involved in force generation by polymerization. Indeed, actin filaments assemble into dense crosslinked networks, so that only short portions of individual filaments push against opposing loads (see chapter 2). Besides the active pushing force developed by the growth of actin filaments, these actin networks also resist stresses and confer consistency to the cell. Although microtubules are much stiffer than actin filaments, in some situations the compressive forces they must resist are larger than their buckling force. In these cases, microtubules appear in bundles, which are characterized by a larger bending rigidity and can sustain larger compressive forces without buckling significantly (see chapter 9).

In addition to the force generation by polymerization, microtubule depolymerization can also generate forces (Fig. 1.6d). This type of force generation has attracted much attention because it is thought to provide a major contribution to the force responsible for chromosome motion during cell division (see chapters 7 and 8).

1.2.2 Motor proteins

Motor proteins are specialized enzymes able to convert the energy from ATP hydrolysis into mechanical work (Alberts et al., 2004; Howard, 2001; Bray, 1992). These molecular machines move along cytoskeletal filaments, and are involved in many different tasks that involve force generation and motion, like intracellular transport (see chapters 4 and 5), cell division (see chapters 7, 8 and 9), cell locomotion, muscle contraction, flagellar and ciliary beating,... There exist very many different kinds of motor proteins (Howard, 2001; Hirokawa, 1998), which differ in the type of filament they bind to, the direction in which they move along the filament and the cargo they carry. While myosin motors move along actin filaments, kinesin and dynein motors move along microtubules. Although these are the most studied type of molecular motors, there exist other molecular machines, like the DNA polymerase (that moves along DNA) or rotatory motors (responsible for the rotation of bacterial flagella).

Here we focus on conventional kinesin (Kinesin-I), as it is the most studied molecular motor and there is a lot of biochemical and biophysical data available. Al-

though other motor proteins may differ in the precise internal structure and the details of their motion and force generation, the general picture concerning the motion of the motor and the way forces are developed is similar. Conventional kinesin is mainly involved in intracellular transport, where it carries small vesicles and pulls membrane tubes that allow the communication between different organelles in eukaryotic cells. Other kinesin motors are involved in cell division (e.g., chromokinesins or the bipolar kinesin Eg5). Some others have microtubule depolymerizing activity (e.g., MCAK or KinI) and are able to control the dynamics of the microtubule ends.

Biochemical structure

The structure of kinesin-I is sketched in Fig. 1.7a. It is composed of two heavy chains and two light chains. Each one of the two heavy chains contains a motor domain or head, which binds to microtubules and has a binding site for ATP. Each head is connected to a "neck linker", a mechanical element that undergoes a conformational change that depends on the state of the ATP hydrolysis cycle and enables motor motion. The neck linker is, in turn, connected to a long coiled-coil stalk that allows the dimerization of the heavy chains. Finally, there is a globular tail domain that participates in cargo binding and the regulation of the motor activity. When the motor is not attached to any cargo, it folds on itself and the motor tail interacts with the motor domains, preventing motor motion. The light chains are situated at the level of the tail and mediate specific attachment to different cargos, allowing selective transport.

The kinesin motor domain is the only domain conserved among the different kinesin sub-families. It is essential as it is the place where the conformational change of the protein takes place upon ATP hydrolysis, leading eventually to the motion of the protein. The small conformational change in the motor domain is amplified by the neck linker, that enables the nanometer scale conformational change observed during motor stepping. In addition, it has been shown that the neck linker determines the directionality of the motor protein.

Motor motion in the absence of applied load

Although the mechano-chemical coupling at molecular scales responsible for the movement of the motor is still under debate, there are several characteristics of the motor motion that are established.

Kinesin-I moves toward the plus-end of microtubules by a sequence of 8 nm steps (Howard, 2001; Svoboda et al., 1993; Carter and Cross, 2005; Nishiyama et al., 2002), which coincide with the size of the tubulin dimers that constitute the microtubule (Fig. 1.7b,c). The motor moves along a single protofilament (Ray et al., 1993), and the step size does not depend on the load applied to the motor (Carter and Cross, 2005) [4]. The motor stepping is done in an asymmetric "hand-over-hand"

[4] Unlike conventional kinesin, dynein motors change the step size depending on load they sustain (Mallik et al., 2004).

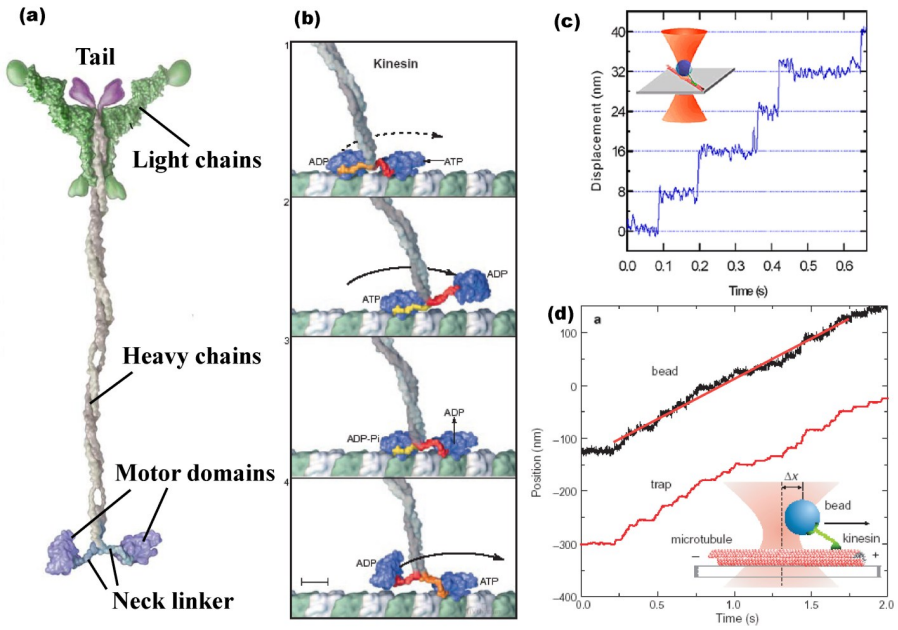

Fig. 1.7. Conventional kinesin structure and motion. (a) Structure of a single conventional kinesin motor. (Modified from Ref. (Vale, 2003)). (b) Mechano-chemical cycle. Four steps of the cycle are shown, ordered in time from top to bottom. Frame 1: Each motor domain (blue) is bound to a tubulin dimer (green, β subunit; white, α subunit) of a protofilament. Frame 2: ATP binding on the leading head induces its docking on the microtubule and promotes a conformational change that results in the motion of the trailing head by approximately 16 nm toward the next tubulin binding site. Frame 3: After a random diffusional search, the new leading head docks tightly onto the binding site. In this process, the kinesin center of mass and, thus, the cargo attached to its tail (not shown) moves forward by approximately 8 nm. The binding process also accelerates ADP release and, during this time, the trailing head hydrolyzes ATP to ADP·P_i. Frame 4: After ADP release in the leading head, ATP binds to the empty catalytic site of the leading motor domain. The trailing head, which has released its inorganic phosphate (P_i) and detached from the microtubule, is moved forward by a conformational change to the next tubulin binding site. (Adapted from Ref. (Vale and Milligan, 2000)). (c) Step-like motion of conventional kinesin motors. A single kinesin motor is attached to a bead, which is hold by an optical trap. The motion of the bead is tracked over time and results from the motion of the kinesin motor, which is composed of alternated pauses and rapid transitions to the next tubulin binding site. The time between steps (dwell time) is an stochastic variable and the motor advances 8 nm in each step. The inset shows an sketch of the experimental set-up. (Image taken from the website http://www.azonano.com/details.asp?ArticleID=1248). (d) Motion of a conventional kinesin motor over time and length scales larger than those of individual motor stepping. A single kinesin motor is attached to a bead, which is hold by a force clamp. The motion of the bead, resulting from the motor stepping, is followed over time. The continuous read line over the bead trajectory indicates the convective motion of the motor. The inset shows an sketch of the experimental set-up. (Modified from Ref. (Visscher et al., 1999)).

fashion (Yildiz et al., 2004; Hua et al., 2002); in each step the rear head moves forward by 16.6 nm and the front head does not move, leading to an overall motion of the kinesin center of mass of 8.3 nm. The asymmetric character was established by the observation that the kinesin stalk does not rotate upon motor stepping (Hua et al., 2002).

The energy required for motor stepping comes from the hydrolysis of ATP. One ATP molecule is consumed (hydrolyzed) per step (Schnitzer and Block, 1997). The process of motor stepping couples the hydrolysis of ATP at the motor domains with a conformational change of the protein and its motion along the microtubule (Howard, 2001; Vale and Milligan, 2000; Carter and Cross, 2005). There are several internal states of the motor, associated to the stage of the ATP hydrolysis cycle and the conformational state of the motor. The details of the hydrolysis cycle and the associated conformational changes of the motor are described in Fig. 1.7b.

Independently of the internal functioning of the motor, the observed stepping is as follows. The motor performs alternated steps and pauses (Carter and Cross, 2005; Nishiyama et al., 2002) (Fig. 1.7c). The time between two motor steps is called the dwell time, which is of order of several milliseconds in the absence of applied load. The mechanical stepping is done much faster. New experiments with high time resolution report that the motor takes less than 30 μs to perform the step (Busoni et al., 2006). This difference of time scales in the mechanical steps and the pauses explains the stair-like trajectory of a moving motor (Fig. 1.7c). Moreover, no substep related to the internal functioning of the motor has been detected with a time resolution of $30\mu s$ and nanometer spatial resolution (Busoni et al., 2006). However, the existence of sub-steps is still under debate.

At length scales much larger than the step size of the motor and time scales much larger than the dwell time, the motor motion can be thought as the combination of a convective motion, which accounts for the motor bias, and a diffusive term arising from the fluctuations in the motor stepping kinetics (Fig. 1.7d; see chapter 6). In this description the motor moves with an average velocity V and the fluctuations of the trajectory are characterized by a diffusion constant D (Fig. 1.7d). The average velocity V of single conventional kinesin motors depends on the ATP concentration and can be well described by the Michaelis-Mentel kinetics (Hackney, 1994; Visscher et al., 1999; Block et al., 2003). At saturating ATP concentrations, i.e. when the time for an ATP molecule to bind the motor domain does not limit the stepping kinetics, the average velocity of conventional kinesin is about 0.6 μm/s.

Motor proteins do not remain attached indefinitely to the filament they walk along. The capacity of motor proteins to perform several steps along the filament without detaching from it is called processivity (Howard, 2001). Processive motors, like conventional kinesin, perform many steps before detaching from the filament, whereas non-processive motors perform only a single step before detaching. In the absence of force, conventional kinesin performs, on average, 125 steps before detaching from the microtubule, leading to a processivity length, i.e. the length traveled by the motor along the filament before detaching, of about 1 μm. On the contrary, myosin-II motors, responsible for muscle contraction, are non-processive (Veigel et al., 2003).

Many theoretical descriptions have been proposed to explain the mechanochemical coupling that leads to the motor motion (Julicher et al., 1997; Astumian, 1997; Leibler and Huse, 1993; Fisher and Kolomeisky, 1999; Duke and Leibler, 1996; Lipowsky, 2000). Although the characteristics of motor stepping depend on many details, the basic physical requirements to generate the directed motion of a motor with several internal states on an asymmetric substrate are established (Julicher et al., 1997). Specifically, it is necessary to break the spatial symmetry (parity) and the temporal symmetry (detailed balance). The first symmetry is directly broken due to the local structural polarity of tubulin dimers and detailed balance is broken by ATP hydrolysis, which drives the system out of equilibrium. The simplest model that explains the motor motion is the two-state ratchet model (Julicher et al., 1997), which sets the basic physical requirements for motor motion.

Force generation and force-dependent motor kinetics

The force generation at molecular level has been studied in detail for myosin-II (Veigel et al., 2003) and myosin-V (Veigel et al., 2005) motors, for which it has been possible to characterize the load dependence of internal motor transitions. Although for conventional kinesin the load dependence of its internal transitions is not that well characterized, the force dependence of the motor transitions that result in movement or detachment from the microtubule have been studied. Here we describe how the motor kinetics depends on the load applied to the motor.

The first single molecule experiments proving the load dependence of kinesin motion showed that the average velocity of kinesins decreases with the applied load, f, and vanishes at a force about $6-7$ pN (Fig. 1.8a) (Visscher et al., 1999; Schnitzer et al., 2000; Block et al., 2003; Nishiyama et al., 2002; Carter and Cross, 2005). The force, f_s, needed to stop the directed motion of the motor is called stall force. Although the force-velocity relation of single conventional kinesin motors is nonlinear (Fig. 1.8a), for forces opposing the motion of the motor it can be approximated by a linear dependence, so that

$$V(f) = V_0 \left(1 - \frac{f}{f_s}\right) , \tag{1.2}$$

where V_0 is the average kinesin velocity in the absence of load. Both V_0 and f_s depend on the ATP concentration and reach maximal values at saturating ATP concentrations (Visscher et al., 1999; Block et al., 2003). In chapter 6 we discuss the force-velocity relation in more details. The stall force indicates that conventional kinesin can carry loads that do not exceed a few picoNewtons. However, even if the force necessary to carry a cargo is below the stall force, the detachment of the motor from the microtubule establishes important limitations to large scale transport.

A further insight in the load dependence of motor stepping was achieved by the detailed measurement of the force dependence of the dwell time for forward and backward kinesin stepping (Carter and Cross, 2005; Nishiyama et al., 2002). The

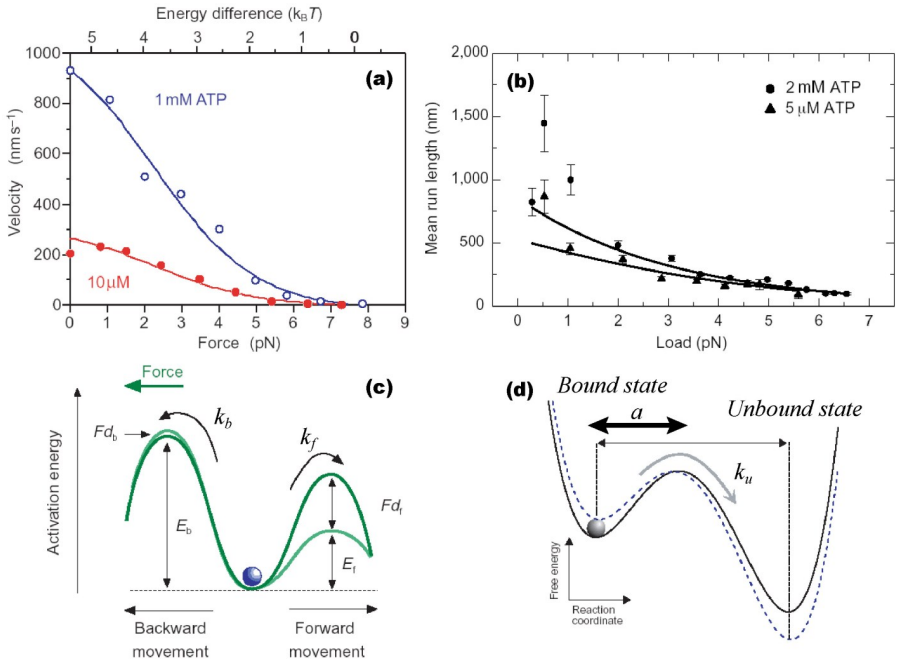

Fig. 1.8. Force-dependent motor kinetics. (a) Force-velocity relation of single conventional kinesin motors at 1 mM (blue) and 10 μM (red) ATP concentrations. The velocity decreases for increasing loads opposing the motor motion. The energy difference between the energy barriers for backward and forward motor stepping (sketched in (c)) is shown on the top axis. (b) Processivity length of conventional kinesin motors as a function of the load opposing motor motion for two fixed ATP concentrations: 2 mM (circles) and 5 μM (triangles). The solid lines correspond to exponential fits to the data. (c) Sketch of the possible energy landscape characterizing the forward and backward motor stepping in absence (light green) and presence (dark green) of a force opposing the motor motion. A force applied in the direction opposite to motion increases the energy barrier for forward stepping (E_f) and lowers that of backward motor stepping (E_b). The rates of forward and backward stepping, k_f and k_b respectively, change exponentially with the applied force (Nishiyama et al., 2002). (d) Motor unbinding from the microtubule. Sketch of the possible energy landscape characterizing the bound and unbound states of a kinesin motor and a microtubule, in absence (solid line) and presence (dashed line) of a force applied to the motor. The effect of the force is to lower the energy barrier between bound and unbound states, increasing exponentially the motor detachment rate k_u. The distance from the bound state equilibrium position (along the reaction coordinate) to the maximum of the energy barrier is a. ((a) and (c) adapted from Ref. (Nishiyama et al., 2002); (b) and (d) adapted from Ref. (Schnitzer et al., 2000)).

rates for forward and backward steeping were shown to depend exponentially with a force opposing kinesin motion. These observations can be explained by modeling the motor forward and backward transitions as activated processes that necessitate the passage of an energy barrier (Fig. 1.8c). This analysis is done in the discussion of chapter 6.

The processivity of kinesin motors is also affected by the load. It has been reported that the processivity length of conventional kinesin decreases exponentially with a force opposing kinesin motion (Vale et al., 1996) (Fig. 1.8b). Indeed, the average time, τ_b, that kinesin spends bound to the microtubule decreases exponentially with the applied force, f (Thorn et al., 2000). This exponential dependence can be explained by an energy barrier separating the bound and unbound states of the motor. When a force is applied to the motor, the energy barrier is lowered and, according to Kramers rate theory (van Kampen, 2004; Kramers, 1940), the average time necessary to stochastically overcome the energy barrier decreases exponentially (Fig. 1.8d). Therefore, the detachment rate, $k_u \equiv 1/\tau_b$, at which the motor detaches from the filament reads

$$k_u(f) = k_u^0 \exp\left(\frac{fa}{K_B T}\right) , \tag{1.3}$$

where a is the length characterizing the position of the energy barrier between bound and unbound states, and k_u^0 is the detachment rate at vanishing load. For conventional kinesin motors $k_u^0 \simeq 0.5\,\mathrm{s}^{-1}$ (Vale et al., 1996) and $a = 1.3 - 1.4$ nm (Schnitzer et al., 2000). This exponential sensitivity of the detachment rate to the applied load has also been reported for myosin motors (Veigel et al., 2003).

In summary, the transitions that a molecular motor can undergo, i.e. forward stepping, backward stepping and detachment from the filament, are characterized by rates that depend exponentially on the forces applied to the motor. Note that when a motor is attached to a cargo and pulls on it, the motor feels the force applied by the cargo, which influences in turn its own kinetics. In particular, when the motor applies a force on a cargo, it detaches exponentially faster from the filament. This force-feedback in the motor kinetics is essential to understand the collective behavior of molecular motors, as we discuss in several chapters below.

Part I

Actin-based motility

2

Introduction

Living cells have evolved different propulsion mechanisms that allow them to move (Alberts et al., 2004; Bray, 1992). In chapter 1 we have discussed some examples of intracellular movements and cell motility. While some cells use cilia or flagella to induce the motion of the surrounding fluid and generate the necessary forces to move, many others use the combination of actin polymerization and myosin motors, or even actin polymerization alone, to develop such forces. One of the most studied examples of motility is the crawling of eukaryotic cells on surfaces (Bray, 1992; Pollard and Borisy, 2003; Pantaloni et al., 2001; Cameron et al., 2000; Mitchison and Cramer, 1996; Stossel, 1993) (Fig. 2.1a). This motility process constitutes probably the most complex case of force and motion generation and involves the combined action of polymerization of actin filaments at the plasma membrane, myosin motors and the adhesion of the cell to a substrate. A crawling cell advances by the extension of its leading edge due to the polymerization of a network of actin filaments at the plasma membrane, which subsequently depolymerizes away from the leading edge. Besides this forward growth, the cell must detach its backmost region from the surface in order to move. Myosin motors, localized at the rear of the cell, are thought to induce this detachment by contracting the actin cytoskeleton in this region. Importantly, it has been shown that cell fragments lacking the nucleus and most of the organelles still move by the same motility mechanism (Verkhovsky et al., 1999) (Fig. 2.1b).

Most of the motility mechanisms discussed above involve the action of motor proteins. There exists, however, a particularly simple mechanism that does not involve molecular motors at all. Several bacterial pathogens (*Listeria monocytogenes*, *Shigella flexneri*, *Rickettsia conorii*) are propelled solely by the growth of an actin network at their surface (Bray, 1992; Goldberg, 2001; Cameron et al., 2000). The network is formed of crosslinked actin filaments and extends away from the back of the bacterium in a characteristic comet-like shape (Fig. 2.1c). The growth of the actin comet tail by the constant addition of actin filaments at the bacterium surface generates the forces that propel the bacterium inside the infected cell. This motility mechanism has attracted much attention because it constitutes the simplest example of actin-based motility, and its understanding may shed some light on the complex

crawling of eukaryotic cells. Moreover, the movement of some endocytic vesicles is also driven by the same mechanism (Taunton et al., 2000) (Fig. 2.1d).

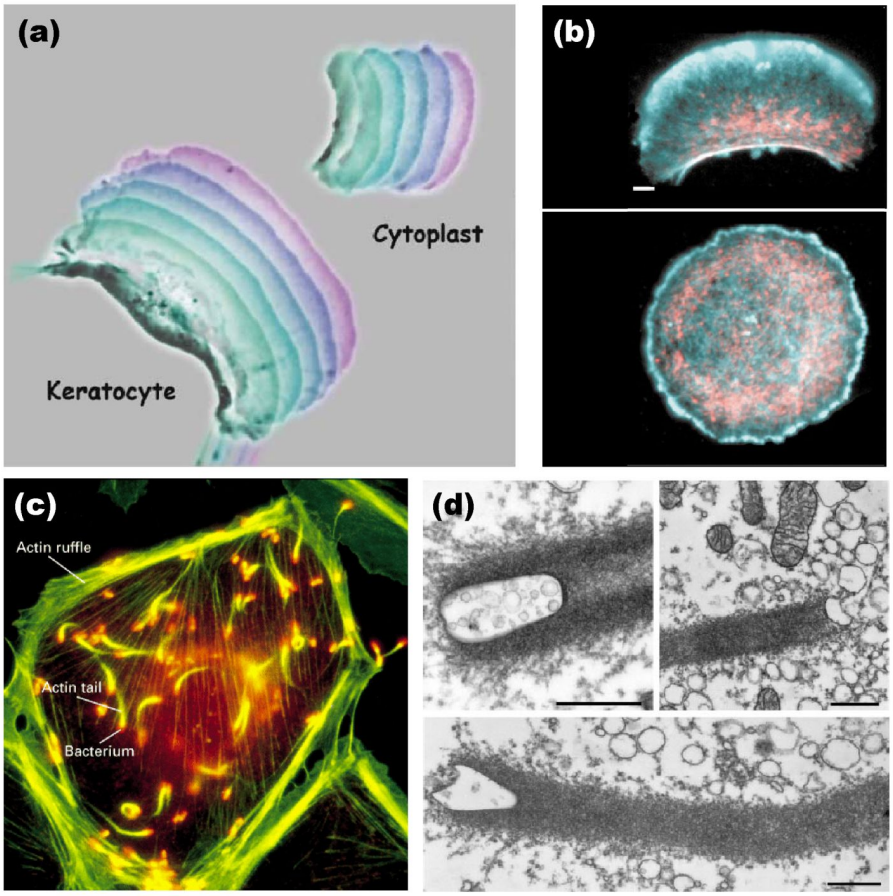

Fig. 2.1. Examples of actin-based motility. (a) Motion of a crawling cell (keratocyte) and a cell fragment lacking the nucleus (keratocyte cytoplast). Overlays of two series of phase contrast micrographs taken at intervals of 15 seconds. The false colors indicate different times: time increases from turquoise to violet. (Adapted from Ref. (Pollard and Borisy, 2003)). (b) Fluorescence image of the cytoskeletal organization of a moving (top) and stationary (bottom) keratocyte fragment. Myosin-II is labeled in red and actin in cyan. Bar, 2 μm. (Modified from Ref. (Verkhovsky et al., 1999)). (c) Fluorescence image showing the bacteria *Listeria* moving inside an infected eukaryotic cell. Actin is labeled in green and the bacteria in red. The actin-comet tails are visible at the back of the bacteria. (Figure taken from the Theriot Lab website: http://cmgm.stanford.edu/theriot). (d) Electron microscopy images of endosomes and lysosomes associated with actin comets tails in living *Xenopus eggs*. Bars, 500 nm. (Modified from Ref. (Taunton et al., 2000)).

Force generation by polymerization of actin filaments plays thus an important role in biology. At molecular scales, it is thought that the bending of single filaments driven by thermal fluctuations allows for polymerization against applied forces (see chapter 1). Indeed, it has been reported that the growth of an actin network generates forces on the surface from which it grows (Miyata et al., 1999). Each single actin filament is thought to individually generate forces of several picoNewtons (Mogilner and Oster, 2003a). However, the typical forces in actin-based motility ($\sim$nN (Marcy et al., 2004)) are much larger and require the cooperative action of ensembles of actin filaments. This cooperativity is achieved by the growth of a network of crosslinked actin filaments.

Eukaryotic cells contain a large number of actin associated proteins that regulate actin assembly and control the interaction between actin filaments (Alberts et al., 2004; Pollard and Borisy, 2003; Small et al., 2002; Pantaloni et al., 2001; Pollard et al., 2000; Borisy and Svitkina, 2000). The assembly of a filamentous actin network requires a particular set of proteins that trigger the polymerization of actin filaments and organize them in a particular way. In Fig. 2.2a we sketch the main proteins involved in the nucleation and organization of a growing actin network at the leading edge of a crawling cell. We briefly describe the roles of the most important proteins in the process:

- *Arp2/3 complex*. Actin nucleation is a slow process (Pollard and Borisy, 2003). It is therefore necessary to somehow trigger the nucleation of actin filaments. The Arp2/3 complex is a cellular factor that stimulates actin nucleation. It increases the nucleation rate of actin and promotes the growth of actin filaments at their barbed ends (Mullins et al., 1998; Welch et al., 1998). In addition to this nucleating activity, the Arp2/3 complex can also attach to pre-existing actin filaments and initiate the nucleation of another actin filament at that position, with a prefered angle of 70° (Mullins et al., 1998). This branching activity leads to dense networks of actin filaments with an arborescent structure (Svitkina and Borisy, 1999) (Fig. 2.2). Arp2/3 has been shown to localize to regions of highly dynamic actin assembly, like the leading edge of crawling cells, which display the characteristic branched network structure (Welch et al., 1997).
- *WASP/Scar*. Although the Arp2/3 complex is essential for the generation of branched actin networks, it must be activated by other factors. The Wiscott-Aldrich syndrome protein (WASP (Yarar et al., 1999)) and related proteins (N-WASP, Scar) activate the Arp2/3 complex in eukaryotic cells (Weaver et al., 2003). When WASP is activated by a specific stimuli, it stimulates in turn the Arp2/3 complex and results in a rapid actin assembly. We shall describe below other proteins that mimic WASP function and activate the Arp2/3 complex in bacterial motility.
- *Capping proteins*. Actin filaments grow from the nucleation sites provided by the activated Arp2/3 complex. In order to suppress the elongation of old filaments, there exist proteins with barbed-end capping activity (Pantaloni et al., 2001). Such capping proteins stop the growth of actin filaments at their barbed ends,

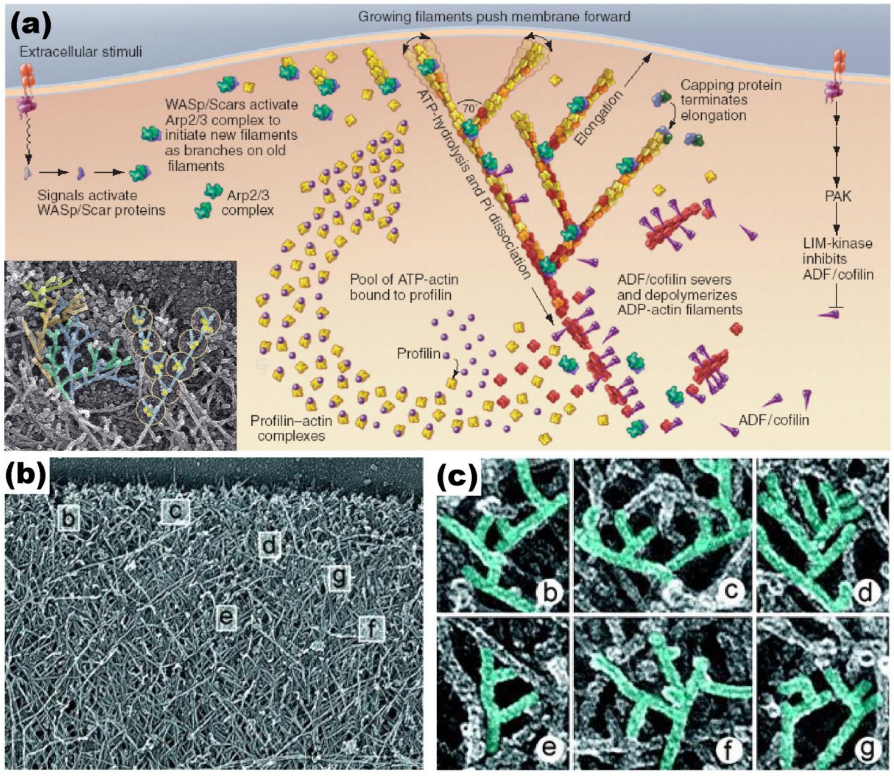

Fig. 2.2. (a) Sketch of the nucleation and growth of an actin network at the leading edge of a crawling cell. The proteins WASP/Scar activate the Arp2/3 complex at the leading edge. The Arp2/3 complex nucleates and branches actin filaments, which push the membrane forward and they elongate. The barbed ends of old actin filaments are capped by capping proteins and the ADP-containing regions of the filaments are severed by ADF/Cofilin. The recycled ATP-actin monomers associated with profilin polymerize new actin filaments at the leading edge. (Modified from Ref. (Kiehart and Franke, 2002)). The inset shows the typical arborescent structure of the actin network, with the Arp2/3 complex at the branching between filaments. False color is used to highlight branched filaments and the circles identify the Arp2/3 complex. (Figure taken from the Borisy Lab website: http://www.borisylab.northwestern.edu). (b-c) Multiple branching of actin filaments in the lamellipodia of crawling cells. Electron microscopy images of the actin network in the lamellipodia of *Xenopus* keratocytes. Overview of the leading edge (b) and close-ups showing different examples of branched actin filaments (c). (Modified from Ref. (Svitkina and Borisy, 1999)).

allowing the formation of new actin filaments at the surface from which the actin network is growing (e.g. the leading edge of a crawling cell).

- *ADF/Cofilin*. In order to allow the continuous growth of the actin network from the surface where the nucleation takes place, it is essential to recycle the previously polymerized actin filaments. The protein ADF (Actin Depolymerization Factor) or Cofilin, which associates to the sides of the ADP-containing region of actin filaments, increases their twist and destabilizes the filaments (McGough et al., 1997), leading to a enhancement of the filament breakage rate (Bamburg et al., 1999). This process, which takes place far from the surface at which actin filaments are nucleated, generates new uncapped barbed ends of actin filaments that can be used again to extend the actin network.
- *Profilin*. Although not essential for the growth of the actin network, the protein profilin is thought to bind to ADP-actin monomers and promote the nucleotide exchange to ATP-actin monomers, enhancing in this way the actin turnover in the growth process of the network (Schluter et al., 1997).
- *Crosslinking proteins*. The actin meshwork is constituted of interdigitated arborescent F-actin structures. In order to confer consistency to the actin network, there exist other proteins that crosslink the actin filaments. While α-actinin crosslinks actin filaments in parallel bundles, the protein filamin crosslinks the filaments at approximately right angles. These proteins change considerably the network structure and are used for different functions in the cell (Alberts et al., 2004).

There exist very many situations where the growth of an actin network is essential to generate forces and motion. Phagocytosis (Aderem and Underhill, 1999; Champion and Mitragotri, 2006) and the movement of several bacteria involve the growth of an actin network, similarly to the process of lamellipodia extension in crawling cells. In all this situations, the mechanism of force generation by actin network assembly is very similar, and it is referred to as “actin-based motility”.

2.1 *Listeria* motility

Listeria are gram-positive bacteria that infect mammalian eukaryotic cells and may cause, among other diseases, meningitis. This bacterium constitutes the simplest example of actin-based propulsion (Cameron et al., 2000). Actin filaments are constantly polymerized and branched at the surface of the bacterium. Upon growth, the actin network polarizes into a comet-like tail that extends from the back of the bacterium (Fig. 2.3). The extension of the actin tail provides the necessary force to propel the bacterium inside the host cell and to spread to adjacent cells. Other bacteria (e.g. *Shigella flexneri* and *Rickettsia conorii*) and the vaccinia virus use the same propulsion mechanism. Moreover, the pathogenic cycle of these organisms is the same (Fig. 2.3a). They are first internalized in the host cell and, once in the cytoplasm, they use the protein machinery and energy from the host cell to move. The forces developed are large enough to deform the membrane of the host cell and create protrusions that allow them to spread to other cells (Tilney and Portnoy, 1989; Goldberg,

2001). Although the mechanisms triggering actin assembly on the bacterium surface are distinct for different pathogens (*Listeria*, *Shigella* and *Rickettsia*), the motility mechanism they use is the same, suggesting that actin-based motility is a robust and efficient way to propel. This idea is also supported by the fact that some endocytic vesicles use the same motility mechanism and several other processes (cell crawling, filipodia extension, phagocytosis,...) also involve polymerization of actin networks at surfaces (Pantaloni et al., 2001).

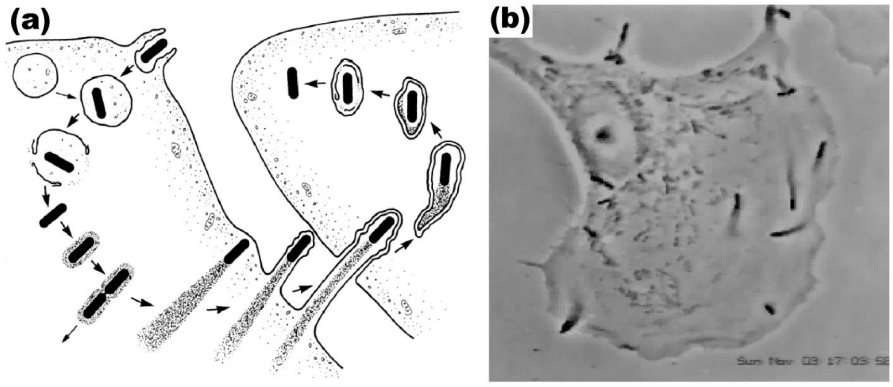

Fig. 2.3. (a) Pathogenic cycle of *Listeria*. The bacterium is first internalized by phagocytosis in the host cell. After degrading the membrane of the phagocytic vacuole, it recruits actin on its surface, assembles an actin tail and moves. The forces developed by the actin tail allow the bacterium to deform the plasma membrane and spread to adjacent cells. (Adapted from Ref. (Tilney and Portnoy, 1989)). (b) PtK2 cells infected by the bacteria *Listeria*, which appear as small black spots with a fuzzy tail extending at their back. (Figure obtained from a film by J. Theriot and D. Portnoy: http://cmgm.stanford.edu/theriot).

It has been shown that only the presence of the protein ActA at the *Listeria* surface is necessary to induce the polymerization of actin filaments (Kocks et al., 1992; Smith et al., 1995). ActA is a transmembrane protein that activates the Arp2/3 complex by mimicking the function of WASP. *Listeria* uses ActA to activate the actin assembly machinery of the host cell; this is to say that the bacterium uses both the necessary proteins and the energy (ATP) from the host cell to move and eventually kill it. ActA is distributed all over the surface of the bacterium, except at its front part (Kocks et al., 1993). This asymmetric distribution establishes the direction of motion of the bacterium, because the actin network only assembles around and at the back of the bacterium. Actin assembly and branching at the surface creates a network of actin filaments that polarizes into a comet-like structure (Fig. 2.4a,b). The proteins involved in the assembly of the actin comet tail are detailed in Fig. 2.4c,d.

At mesoscopic scales, much larger than the scales at which actin nucleation and branching take place, the actin comet tail has been shown to behave as a soft elastic gel (Gerbal et al., 2000b). Moreover, the actin tail is strongly attached to the

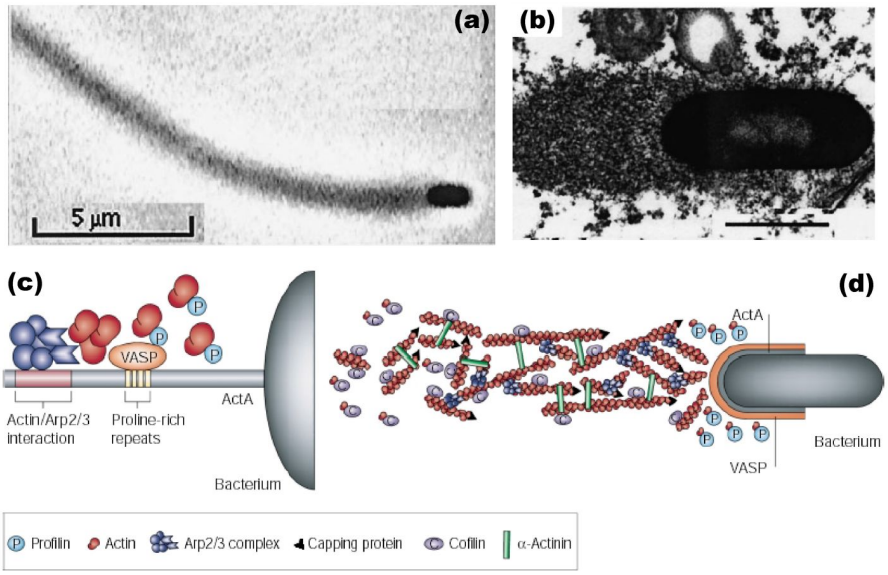

Fig. 2.4. (a) Phase contrast image of the bacterium *Listeria* moving in platelet extract. The cylindrical-shaped bacterium appears black and the fuzzy actin network conforming the comet tail extends away from the bacterium. For slow enough depolymerization of actin filaments, the actin comet tail can be even $\sim 100\ \mu$m. (b) Electron microscopy photograph of *Listeria monocytogenes* in an infected cell, showing a dense network of actin filaments being polymerized from the surface of the bacterium, except at its front part. Bar, 1 μm. (a-b, modified from Ref. (Gerbal et al., 2000a)). (c-d) Sketch of the molecular components necessary for *Listeria* motility. (c) Interactions between the host cell proteins and the actin polymerization promoter ActA at the surface of the bacterium. The amino-terminal domain of the protein ActA triggers actin filament nucleation via activation of the Arp2/3 complex. The proline-rich domain of ActA interacts with VASP (Vasodilator-stimulated phosphoprotein), which interacts, in turn, with profilin, enhancing filament growth. (d) In addition to the ActA mediated interaction at the bacterium surface, other actin associated proteins modify the structure of the actin network. Capping proteins attach to the barbed ends of growing filaments, preventing the elongation of old filaments. α-actinin crosslinks actin filaments and ADF/cofilin disassembles old filaments. (c-d, modified from Ref. (Cameron et al., 2000)).

bacterium. Indeed, the application of forces in the picoNewton range with optical tweezers, did not succeed in detaching the bacterium from its tail (Gerbal et al., 2000b). These observations are at the basis of the mesoscopic theory for actin-based propulsion (Gerbal et al., 2000a; Gerbal et al., 1999; Prost, 2001). The addition of actin filaments on the bacterium surface generates elastic stresses in the gel, which relax at the rear of the bacterium as this moves, providing the propulsive force (see below).

Recent experiments have shown that the forces involved in actin-based motility are in the order of several nanoNewtons (Marcy et al., 2004). Both the propulsive force and the necessary forces to detach the comet tail from the object being pro-

pelled are of this magnitude. These forces are much larger than the hydrodynamic drag of the bacterium moving in the cytoplasm of the host cell. Therefore, *Listeria* moves in the cell cytoplasm as in free space. In absence of a substantial external force ($\sim$nN), the forces must be balanced internally in the system, i.e. the propulsive force must be balanced by the friction forces arising from the attachment of the comet tail and the bacterium.

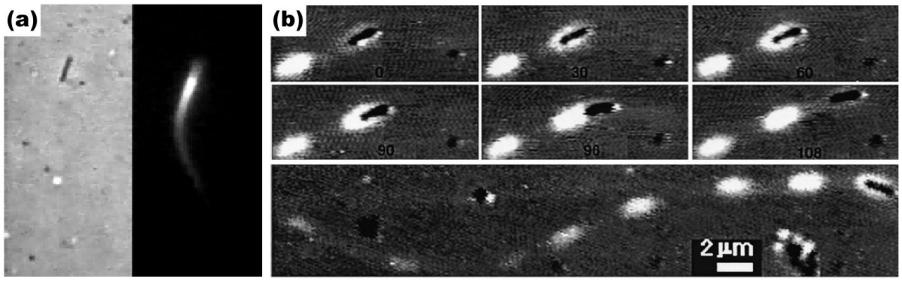

Fig. 2.5. Observed dynamical regimes of *Listeria* motion. (a) Continuous motion of *Listeria* in *Xenopus* extract observed by optical (left) and fluorescence (right) microscopy. Actin is labeled fluorescently and appears bright when observed by fluorescence microscopy (left). (Figure obtained from film by D. Fung: http://cmgm.stanford.edu/theriot). (b) Saltatory motion of the *Listeria* mutant $\mathrm{ActA}_{\Delta 21-97}$. (Top) Snapshots of the mutant movement observed by both phase-contrast and fluorescence microscopy. Actin is labeled fluorescently and appears bright. The time of each snapshot is indicated in seconds. (Bottom) Photograph of the mutant motion, showing the dashed appearance of the actin comet tail that results from the saltatory motion on the bacterium. Regions of high actin density are associated with the low velocity phases of the bacterium. (Adapted from Ref. (Gerbal et al., 2000a)).

The motion of *Listeria* is typically continuous, with a velocity about $0.1\ \mu\mathrm{m/s}$ (Fig. 2.5a). However, some *Listeria* mutants show a characteristic saltatory motion, with periods in which the bacterium hardly moves separated by velocity bursts, in which the bacterium is expelled from the actin sheath surrounding it (Fig. 2.5b). This nonlinear oscillatory behavior has been reproduced and explained by the elastic theory that we explain below.

2.2 Biomimetic systems

Actin-based motility appears thus to be a robust force production mechanism used by different organisms. In principle, it should then be possible to induce the motion of a synthetic object solely from the growth of an actin gel on its surface. This situation has been indeed successfully carried out and has shown that a large variety of objects with different shapes and characteristics can be propelled by actin tail formation (Upadhyaya and van Oudenaarden, 2003).

2.2.1 Hard beads

The growth of an actin gel on spherical particles covered with ActA provided evidence that elastic stresses are generated in the actin gel upon polymerization (Noireaux et al., 2000). Moreover, the experimental data showed that the elastic stress affects, in turn, the kinetics of actin polymerization. These experimental observations are in quantitative agreement with a theoretical description that accounts for both the gel elasticity and the dependence of the actin polymerization velocity on the elastic stresses (Noireaux et al., 2000).

A further step in understanding the propulsion mechanism is provided by the study of biomimetic experimental systems where *Listeria* are replaced by solid spherical beads on which actin polymerization promoters are attached (Cameron et al., 1999; Bernheim-Groswasser et al., 2002; Noireaux et al., 2000; Yarar et al., 1999). These beads mimic closely the natural propulsion mechanism of *Listeria* with comet tail formation (Fig. 2.6a,b). The actin gel initially grows isotropically around the spherical bead and, after a spontaneous symmetry breaking (van Oudenaarden and Theriot, 1999; Bernheim-Groswasser et al., 2002), the actin network reorganizes into a comet-like structure that propels the bead. Both the continuous and saltatory motion of *Listeria* have been also observed for synthetic beads (Bernheim-Groswasser et al., 2002) (Fig. 2.6a,b). Other synthetic objects with different shapes have also been shown to move by the action of an actin comet tail (Schwartz et al., 2004).

Similar biomimetic experiments have focused on the symmetry breaking process, by which a solid bead, surrounded initially by an isotropic gel, develops an actin comet tail and moves (Sekimoto et al., 2004; van Oudenaarden and Theriot, 1999; van der Gucht et al., 2005). It has been recently shown that the symmetry breaking results from the rupture of the gel as a consequence of the elastic stresses generated by actin polymerization at the bead surface (van der Gucht et al., 2005).

2.2.2 Soft objects

The comparison between the elastic theory and the experimental data for a growing actin gel on a spherical bead showed the existence of elastic stresses in the actin gel (Noireaux et al., 2000). However, the stress distribution applied by the actin gel on the surface of an object propelled by an actin comet tail is difficult to measure. The clear deformation of endosomes and lysosomes propelled by an actin tail *in vivo* (Taunton et al., 2000) is a signature of the stresses applied by the growing actin gel.

In order to qualitatively obtain the stress distribution, lipid vesicles partially covered with actin polymerization promoters were used as a cargo for actin-based motility (Upadhyaya et al., 2003; Giardini et al., 2003). When placed in cell extracts, an actin gel grows isotropically around the initially spherical vesicle and, after a spontaneous symmetry breaking, the vesicle develops an actin comet tail and moves. Due to the elastic stresses exerted by the actin tail, the vesicle appears deformed (Fig. 2.6c,d). The distribution of elastic stresses can be deduced from the vesicle

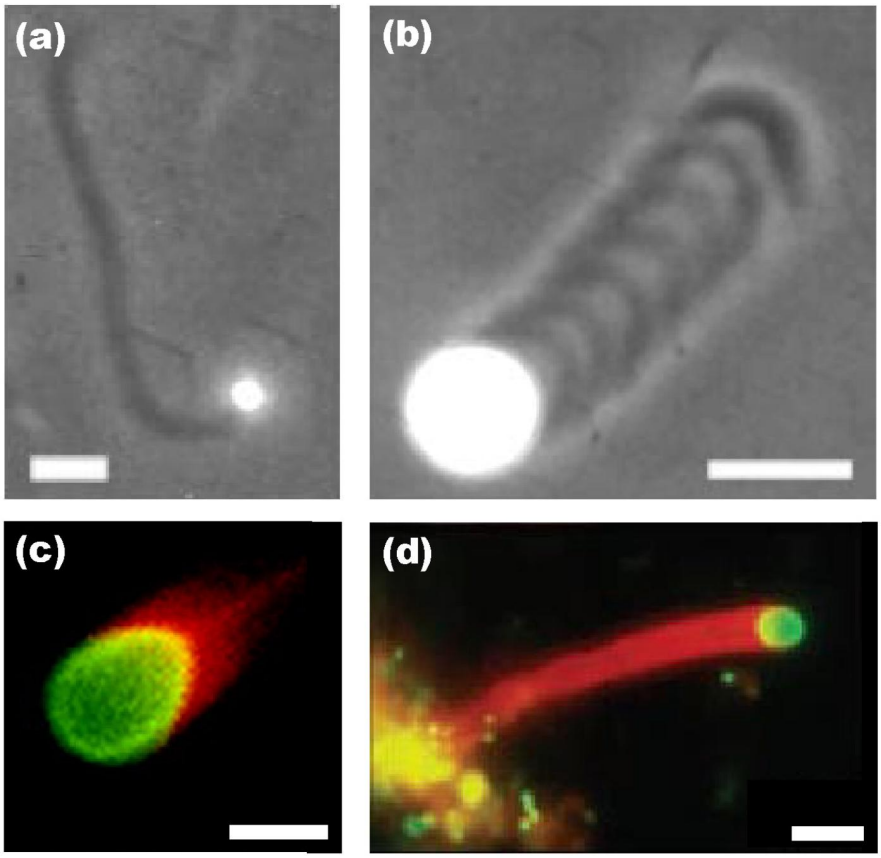

Fig. 2.6. (a-b) Motion of spherical beads covered with actin polymerization promoters (VCA), propelled by an actin comet tail. While small beads show a continuous motion with an homogeneous actin tail (a), large beads move by a sequence of jumps (b). Bars: (a) 5 μm and (b) 10 μm. (Modified from Ref. (Bernheim-Groswasser et al., 2002)). (c-d) Actin-driven motility of lipid vesicles covered with ActA. Fluorescence images of lipid vesicles associated with actin comet tails: actin is labeled in red and some of the lipids in green. The lipid vesicles display different deformations: Pear-like shape (c; bar, 2 μm; modified from Ref. (Giardini et al., 2003)) and nearly round shape (d; bar, 4 μm; modified from Ref. (Upadhyaya et al., 2003)).

shape. It was observed that the actin gel squeezes the vesicle on the sides and pulls it at the back, in the direction opposite to motion. Unfortunately, the use of lipid vesicles as cargo have several drawbacks. The vesicle tension and volume are difficult to measure and may considerably change in the time of an experiment. Although the qualitative stress distribution applied by the actin gel could be accessed in these experiments, it is not possible to quantitatively measure the stresses. In chapter 3 we study theoretically the deformation of an oil drop propelled by and actin comet

tail and compare the results to the experimental observations by Hakim Boukellal (Institut Curie). We measure the stress distribution quantitatively and show that the propulsive force cannot be obtained solely from the drop deformation, as assumed in Ref. (Giardini et al., 2003).

2.3 Theoretical approaches

Several theoretical approaches have been proposed to explain the physical mechanism of force production driving *Listeria* motion. They mainly differ by the scale at which they describe the system.

Molecular models (Mogilner and Oster, 2003a; Mogilner and Oster, 1996) consider the Brownian flexibility of actin filaments growing against the surface of the bacterium. These models focus on the dynamics of individual actin filaments in the vicinity of the surface where polymerization takes place, and take into account the effects of many proteins controlling actin dynamics. An important drawback of this approach is the large number of parameters needed to describe the system. This detailed analysis provides a reasonable description of the system at molecular scales, but does not properly account for the global balance of forces. The predictions of these models are in contrast with several experimental observations concerning the large scale motion of *Listeria*. The estimated total propulsive force ($\sim$ 100pN) is in disagreement with the typical forces in actin-based motility ($1-10$nN) (Marcy et al., 2004), and the force-velocity relation does not agree neither with the experimental data (Marcy et al., 2004).

The growth of branched actin networks on flat surfaces has been studied both experimentally (Schwartz et al., 2004) and numerically (Carlsson, 2001; Carlsson, 2003). The numerical works, which also take into account many molecular details, constitute a coarse-grained description at intermediate length scales, in between the molecular and mesoscopic scales. They provide theoretical predictions for the local growth velocity of an actin network as a function of the local forces acting on the network at the surface. Note that the growth velocity of a single actin filament is, in general, different from the average local velocity of a coarse-grained portion of the actin network. Although these works do not directly address the bacterial motion, they study the force generation by growth of actin networks and are thus important for a general understanding of actin-based motility.

Listeria motility has been studied at mesoscopic scales ($\sim 1-10\mu m$), much larger than the typical scales ($\sim$ 10nm) at which polymerization and branching of the actin network take place. At these scales the actin network behaves as an elastic gel (Gerbal et al., 2000b). This approach analyses the elastic stresses exerted by the deformed comet tail on the bacterium, which result in the propulsive force (Gerbal et al., 2000a; Gerbal et al., 1999; Prost, 2001). Mesoscopic theories are robust as they describe the dynamics from general conservation laws, and very few phenomenological parameters are needed to characterize the system. The theoretical predictions from this approach concerning the total propulsive force are in agreement with the experimentally measured values for actin-based motility (Marcy et al., 2004). We

describe in more details the mechanism of *Listeria* motility proposed by this mesoscopic approach below.

Both molecular models and those at intermediate length scales provide theoretical relations for the velocity of the growing actin network as a function of the local forces. Such relations constitute an important input for mesoscopic theories. It is thus the combination of the descriptions at different scales that leads to a global understanding of the motility process.

Elastic theory for actin-based propulsion

As described above, *Listeria* contains a transmembrane protein called ActA that covers the lateral and back surface of the bacterium. This protein stimulates Arp2/3 activity and promotes the growth of an actin meshwork from the bacterium surface. At a mesoscopic scale, this filamentous actin network behaves as a soft elastic gel, with an elastic modulus about $10^3 - 10^4$Pa (Gerbal et al., 2000b). Based on this observation, the motion of *Listeria* has been described using a continuum approach, which accounts for the gel elasticity and the dependence of actin polymerization on the elastic stresses in the gel. Such a description provides a general framework to understand actin-based motility, as it relies on general conservation laws (Gerbal et al., 2000a; Gerbal et al., 1999; Prost, 2001).

In this mesoscopic approach, the growth of a new gel layer at the bacterial surface upon actin polymerization stretches the previously polymerized gel layer, generating elastic stresses in the gel (Fig. 2.7b). The energy from actin polymerization is transiently stored as elastic energy in the gel. When the bacterium moves forward, the gel relaxes progressively at its back, releasing the elastic energy and propelling the bacterium. In the absence of external forces, the propulsive force is balanced by the friction force due to the attachment of the actin filaments to the surface of the bacterium. In Fig. 2.7a we sketch and explain in more details how actin polymerization at a surface leads to a stress build-up in the gel.

Several important predictions derive from the elastic theory. In particular, it is expected that the actin gel at the back of the bacterium may, in some regimes, pull the bacterium in the direction opposite to motion (Gerbal et al., 2000a). This prediction is confirmed by our results in chapter 3. Moreover, both the continuous and saltatory motion of the bacterium are reproduced and explained. While the continuous motion is characterized by a steady growth of the actin tail, in the saltatory regime, the bacterium moves by a sequence of jumps. At slow velocities, the attachment/detachment events of actin filaments to the bacterial surface lead to an effective fluid-like friction, whereas at large velocities the filaments are ripped off the surface and the bacterium is expelled from the actin sheath surrounding it (Fig. 2.5). Interestingly, this saltatory motion corresponds to a stick-slip behavior that arises from the non-linear nature of friction forces (Urbakh et al., 2004).

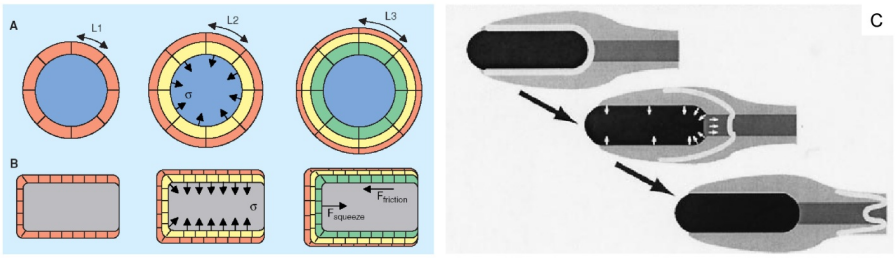

Fig. 2.7. Elastic model for actin-based propulsion (Gerbal et al., 2000a; Gerbal et al., 1999; Prost, 2001). (A-B) Sketch of the increase of elastic stresses upon growth of an actin gel on curved surfaces. (A) A bead (blue) coated with actin polymerization promoters initiates the growth of an actin gel layer (red). As polymerization progresses, a new gel layer is polymerized between the bead surface and the previously polymerized gel layer, stretching the initial gel ($L_2 > L_1$). This stretching of the gel generates elastic stresses in the gel and, in particular, normal elastic stresses σ at the bead surface (arrows). As the polymerization velocity of the actin gel at the bead surface decreases with the normal stress, when the stresses become large enough, the polymerization rate at the bead surface equals the depolymerization rate at the outer gel surface. The system reaches a steady state with a gel of constant thickness undergoing permanent treadmilling (Noireaux et al., 2000). (B) In the case of the cylindrical geometry of *Listeria*, actin polymerization around the bacterium generates elastic stresses, in the same way than for a bead (A). The elastic energy in the gel is relaxed at the back as the bacterium moves, leading to a propulsive force ($F_{squeeze}$). This force is balanced by the friction forces ($F_{friction}$) between the actin comet and the bacterium (A-B, adapted from Ref. (Upadhyaya and van Oudenaarden, 2003)). (C) Elastic model for the *Listeria* propulsion. Polymerization of actin at the bacterium surface (light gray layer) expands the older gel layers (gray), inducing a stress in the actin gel and a normal stress at the bacterium surface (white arrows). The forward motion of the bacterium leads to the strain relaxation in the tail and generates the propulsive force. This description predicts that the gel may pull on the bacterium at the back. (Modified from Ref. (Gerbal et al., 2000a)).

3

Actin-based propulsion of liquid droplets

As discussed in the previous chapter, the bacteria *Listeria* are propelled by an actin comet tail, composed of a cross-linked network of actin filaments, which grows at the bacterium surface (Tilney and Portnoy, 1989; Cameron et al., 2000; Goldberg, 2001). The same motility mechanism has been reproduced *in-vitro* using rigid beads coated with actin polymerization promoters (Cameron et al., 1999; Yarar et al., 1999; Bernheim-Groswasser et al., 2002; Wiesner et al., 2003). At mesoscopic scales, the filamentous actin network that forms the actin comet tail behaves as a soft elastic gel (Gerbal et al., 2000b; Gerbal et al., 1999). The growth of an actin gel on a curved surface generates elastic stresses in the gel that affect, in turn, the actin polymerization kinetics at the surface (see chapters 1 and 2). As actin-based motility relies on the polymerization of actin filaments, it is essential to understand the forces affecting the polymerization process. The knowledge of the elastic stresses developed by an actin comet tail on the object being propelled could thus provide an important insight in the force production mechanism driving actin-based motility. A direct measurement of such stresses for *Listeria* or hard beads is however challenging. For soft enough objects, the elastic stresses in the gel deform the object being propelled. The deformation allows a direct measurement of the local stresses applied by the gel on the surface of the moving object. Moreover, the study of the actin-based motility of deformable objects has an intrinsic biological relevance. Some endocytic vesicles, which mediate the transport from the plasma membrane to internal regions of the cell, have been shown to move by the action of an actin comet tail and appear clearly deformed (Taunton et al., 2000) (see chapter 2).

Hakim Boukellal, in the group of Cécile Sykes (Institut Curie), has developed an experimental system consisting of oil drops with actin polymerization promoters adsorbed on their surface. Once placed in cell extracts, the oil drops move by actin polymerization and deform under the action of the elastic stresses exerted by the gel. The same squeezing effect is observed on endosomes (Taunton et al., 2000) driven by actin comets and on synthetic vesicles covered with the bacterial protein ActA (Upadhyaya et al., 2003; Giardini et al., 2003). However, for liquid drops, the knowledge of their surface tension and their constant volume allow for a quantita-

tive analysis of the observed shape and thus the determination of the elastic stress distribution on the drop surface.

The aim of our work is to understand both the origin of the propulsive force and the distribution of stresses created by the actin gel on deformable objects such as droplets. We describe theoretically a liquid drop deformed and propelled by an actin comet tail. We solve this free boundary problem and calculate the drop shape and local stresses taking into account the elasticity of the actin gel and the variation of the polymerization velocity with normal stress. In the steady state, the droplet acquires a pear-like shape which is determined by the balance between elastic stresses and the restoring force due to surface tension. The stress distribution shows that the gel pushes forward and squeezes the droplet along the sides, while pulling it backward at the rear. Moreover, the drop deformation is such that the propulsive force strictly vanishes if surface tension gradients and internal pressure variations are not taken into account. For soft objects with a liquid surface, the total propulsive force cannot thus be estimated solely from the drop shape. The quantitative comparison between the theoretical results and the experimental data allows the determination of molecular parameters related to actin growth on surfaces.

3.1 Biomimetic experiments

The experimental system mentioned above, consisting of oil drops propelled by an actin comet tail, allows for a quantitative analysis of the stresses generated by the polymerization of the actin network on the surface of the object being propelled. The experiments we discuss in this section have been carried out by Hakim Boukellal, and their detailed description can be found in his Ph.D. thesis (Boukellal, 2004).

An emulsion of oil drops (Fig. 3.1a), with radii ranging from 1.5 to 5.5 μm is incubated with the actin polymerization promoter VCA, derived from the Wiskott-Aldrich syndrome protein (WASP) [1]. In this incubation period, VCA adsorbs onto the oil drops, covering partially their surface (Fig. 3.1b). The emulsion containing the VCA-coated drops is then added to HeLa cell extracts (Fig. 3.1c-d), which provide the proteins (actin, Arp2/3,...) and molecules (e.g., ATP) necessary for the formation of the actin gel. Finally, fluorescently-labeled actin is added to the mixture so that the actin comet can be visualized. In some experiments, VCA is labeled fluorescently in order to observe its distribution on the drop surface.

The sample is observed by bright field or fluorescence microscopy depending on needs. As for *Listeria*, actin polymerizes only at the interface between the drop and the comet and depolymerizes at the back of the comet. When placed in cell extracts, actin is first polymerized on the drops with a spherical symmetry (Fig. 3.1c). After roughly one hour, symmetry is broken for approximately 70% of the drops. They develop an actin comet, deform into a pear-like shape and move (Fig. 3.1d). An example of a moving drop is shown in Fig. 3.2a.

[1] VCA is the domain of the protein WASP that is responsible for Arp2/3 nucleation (Welch et al., 1998).

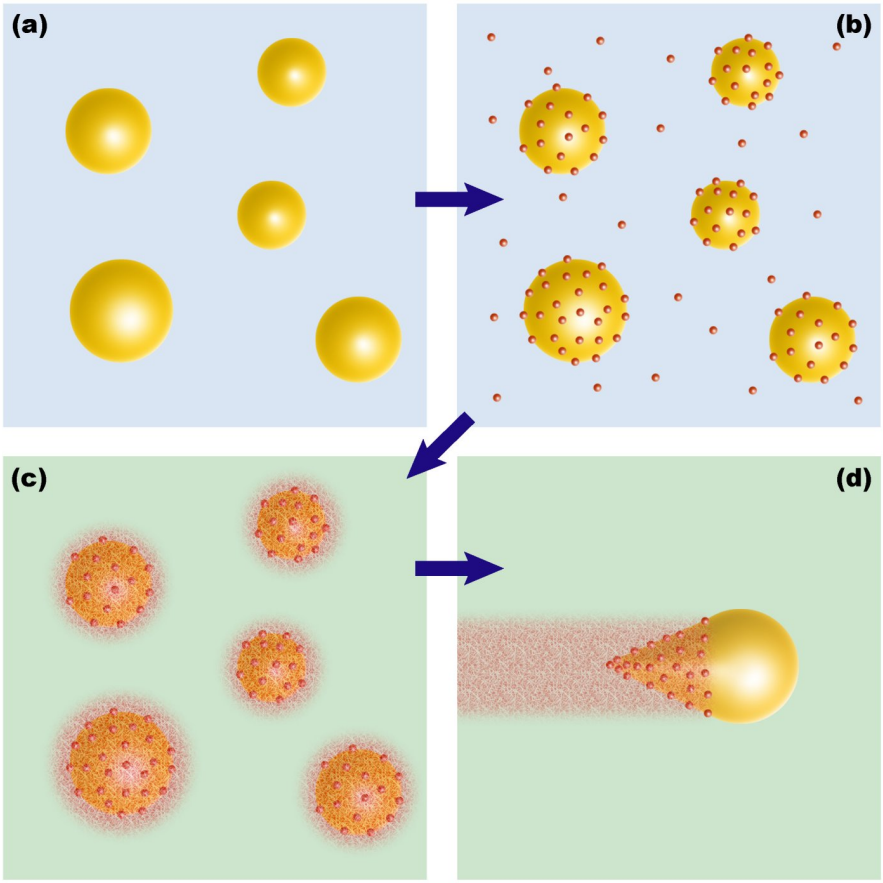

Fig. 3.1. Sketch of the experimental procedure to obtain droplets propelled by an actin comet tail. (a) Emulsion of oil drops (yellow) in solution (light blue). (b) The drops are incubated with VCA molecules (red dots), which partially adsorb onto the surface of the drops. (c) The VCA-coated drops are added to cell extracts (light green) and an isotropic actin network (red mesh) grows around the spherical drops. (d) After approximately one hour, some droplets develop an actin comet tail and move. Moving drops are deformed into a pear-like shape due to the stresses developed by the actin tail.

Initially, the actin polymerization factor VCA is uniformly distributed around the spherical drop. After deformation of the drop and formation of the comet, fluorescence intensity measurements using fluorescently-labeled VCA show that 90% of the VCA is found on the region of the drop associated with the actin tail (Fig. 3.2b). This means either that VCA has been displaced from the interface to the bulk of the extract except where the gel is present, or that all VCA has been collected by the gel during the symmetry breaking process. In any event this also means that the VCA surface density is comparable to the density of filament extremities at the surface. The aver-

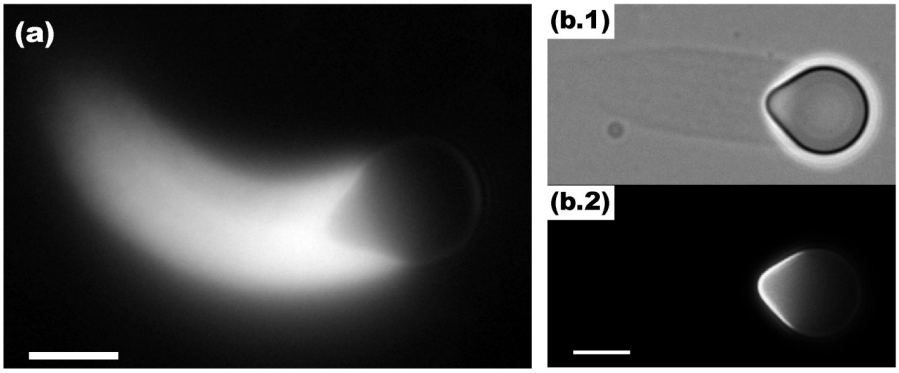

Fig. 3.2. (a) Oil drop covered with VCA placed in HeLa cell extracts supplemented with fluorescently labeled actin and observed by fluorescence microscopy. The actin comet appears bright. Bar, 4μm. (b) Oil drop covered with fluorescently-labeled VCA and placed in cell extracts, observed by bright field microscopy (b.1) and by fluorescence microscopy (b.2). VCA appears bright in (b.2) and reveals the association of VCA with the actin tail. Bar, 3μm. (Modified from Ref. (Boukellal et al., 2004)).

age distance d between filament extremities is larger than the close-packing distance. Indeed, the mesh size [2] of the actin gel provides a lower bound of $d = 10$nm. The surface tension change due to the presence of VCA at the interface is then of order $K_B T/d^2 < 4\,10^{-2}$mN/m, more than 100 times smaller than the oil-extract surface tension, γ_0, which was measured by the pendant drop method to be $\gamma_0 = 4 \pm 0.6$ mN/m.

This experimental set-up allows a quantitative study of the drop motion. The drop is followed using videomicroscopy and its shape is obtained by digitalization of the drop contour. The stresses developed the actin comet tail on the drop can be obtained from the drop deformation, and the drop velocity is measured from its trajectory.

3.2 Theoretical description

Unlike bacteria, the liquid surface of the droplet is characterized by a surface tension γ and can thus be deformed under the action of elastic stresses. In a steady state, the shape of the droplet is specified by the balance between normal elastic stresses applied by the actin gel and the restoring force due to surface tension. The front part of the drop is a spherical cap of radius R not covered by actin (Fig. 3.2b). The radius R is different from the radius R_0 of the undeformed spherical drop, which fixes the volume $4\pi R_0^3/3$. The back part of the drop, surrounded by the comet, has a blunted cone-like shape (rotationally symmetric around the direction of motion). In Fig. 3.3 we sketch the typical shape of a moving drop and define the coordinate system and variables used to theoretically describe it.

[2] The mesh size is the average length at which the filaments forming the gel cross.

We parameterize the drop by the liquid thickness, h, and the local angle, θ, between the local tangent to the shape and the direction of motion (Fig. 3.3b). The spherical cap and the cone match at the triple line between the drop, the comet and the surrounding solvent; we call the tangent angle at the contact point θ_m, where the corresponding oil thickness is $h_m = R\cos\theta_m$. The pressure inside the drop, P_{in}, varies from point to point since the drop motion induces an internal flow. At the interface with the extract, in the spherical part, it is given by Laplace's law and reads

$$P_{in} = 2\frac{\gamma_0}{R} + P_0 \,, \tag{3.1}$$

where P_0 is the pressure in the liquid surrounding the drop, and γ_0 is the surface tension in the front part of the drop, where no VCA is present. At any point inside the drop, the pressure, P, differs from P_{in} and is given by $P = P_{in} + \delta P$. At a point of thickness h, the balance of local stresses along the normal of the drop is given by the local Laplace's law, and reads

$$\frac{2\gamma_0}{R} + \delta P(h) = \gamma\left(\kappa_\phi + \kappa_s\right) - \sigma_{nn}(h) \,, \tag{3.2}$$

where κ_s and κ_ϕ are the local curvatures along the principal directions at each point of the surface, and σ_{nn} is the normal stress exerted by the drop at the surface of the comet [3] (σ_{nn} is positive, dilative stress, if the comet pulls on the drop and negative, compressive stress, if the comet pushes the drop). Although we argued that the surface tension gradients are small, we consider here that the surface tension $\gamma = \gamma_0 + \delta\gamma(h)$ varies along the interface; it is constant in the spherical part with a value γ_0 and it is continuous at the contact line, so that $\delta\gamma(h_m) = 0$.

The curvatures κ_s and κ_ϕ along the principal directions at each point of the surface can be calculated using basic differential geometry (Morse and Feshbach, 1953; DoCarmo, 1995). In Fig. 3.3a we sketch the typical shape of the drop and define the local coordinate system on the drop surface. It is specified by the unit vectors $\mathbf{e_s}$ and $\mathbf{e}_\phi$, with ϕ being the azimuthal angle around the axis of symmetry (z axis) and s being the arclength along the drop contour at a fixed value of ϕ; the origin, $s = 0$, is located at the back of the drop. The normal vector, $\mathbf{n}$, is given by the cross product of the unit vectors on the surface, so that $\mathbf{n} = \mathbf{e}_\phi \times \mathbf{e_s}$. The curvature κ_s corresponds to the variation of the normal vector along s, projected in the $\mathbf{e_s}$ direction, and reads

$$\kappa_s = \mathbf{e_s} \cdot \frac{d\mathbf{n}}{ds} = -\frac{d\theta(s)}{ds} = \frac{d\left(\cos\theta(h)\right)}{dh} \,, \tag{3.3}$$

where we have used the relation $dh/ds = \sin\theta$ in the last equality. The curvature κ_ϕ is given by the variation of the normal vector along ϕ (with the corresponding scaling factor) projected in the $\mathbf{e}_\phi$ direction, so that

$$\kappa_\phi = \mathbf{e}_\phi \cdot \left(\frac{1}{h}\frac{d\mathbf{n}}{d\phi}\right) = \frac{\cos\theta(h)}{h} \,. \tag{3.4}$$

[3] We use here the definition of the stresses in Elasticity Theory. The stresses applied by the comet on the drop are $-\sigma_{nn}$.

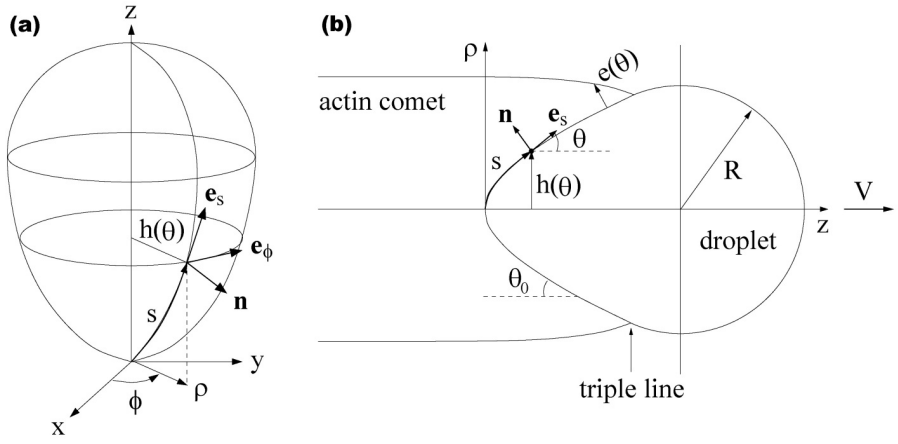

Fig. 3.3. (a) Definition of the local coordinate system on the surface of the drop. The coordinates describing the points on the drop surface are the arclength s (with $s = 0$ located at the origin of the cartesian coordinate system), and the azimuthal angle ϕ. Their associated unit vectors are $\mathbf{e_s}$ and $\mathbf{e}_\phi$ respectively, and the normal vector, $\mathbf{n}$, at each point is given by $\mathbf{n} = \mathbf{e}_\phi \times \mathbf{e_s}$. The drop shape is rotationally symmetric around the direction of motion (z axis) and given by the function $h(\theta)$. (b) Sketch of the moving oil drop. Two-dimensional projection of the three-dimensional drop shape in (a) at constant ϕ. The drop shape is parameterized by the local thickness h and the local angle θ between the local tangent to the shape ($\mathbf{e_s}$) and the direction of motion.

Using the expressions for the curvatures along the local principal directions, the local balance of stresses at each point of the surface reads

$$\frac{2\gamma_0}{R} + \delta P(h) = \gamma\left(\frac{\cos\theta(h)}{h} + \frac{d\left(\cos\theta(h)\right)}{dh}\right) - \sigma_{nn}(h)\,. \tag{3.5}$$

Local mechanical equilibrium on the surface of the drop (Eq. 3.5) does not fully specify the shape of the drop, which we derive below. However, a general expression for the total propulsive force developed by the actin tail can be obtained without the need of any particular model for the gel elasticity or the actin growth at the surface of the drop.

3.2.1 The propulsive force

The total elastic force, F_e, exerted by the comet on the drop is obtained by integrating the projection of the normal elastic stress on the direction of motion, and reads

$$\begin{aligned} F_e &= \int_{\Sigma_g} dS\,(-\sigma_{nn})\sin\theta \\ &= 2\pi\int_0^{h_m} dh\,h\left(\cos\theta\frac{d\gamma}{dh} + \delta P\right)\,, \end{aligned} \tag{3.6}$$

where Σ_g is the surface of the drop in contact with the actin comet. In order to obtain the last equality in Eq. 3.6 we have used the relation between the normal stress and the drop shape in Eq. 3.5. If both the pressure gradient inside the drop and the surface tension gradient are ignored, the propulsive force vanishes exactly. This result holds for any axisymmetric drop shape whatever the elastic stress distribution along the surface, independent of any model for the comet elasticity and the actin polymerization velocity. A direct consequence of this result is that the total propulsive force cannot be estimated solely from the drop shape. This hypothesis, used in Ref. (Giardini et al., 2003), is unable to produce an estimate of the propulsive force. An experimental measurement of the force propelling the drop must thus take into account the surface tension gradient and fluid flow inside the drop.

The reason why the total elastic force vanishes for $\delta P = 0$ and $\delta\gamma = 0$ is that a drop with homogeneous surface tension and internal pressure deforms in such a way that the global contribution of the local normal stresses cancels out exactly. Only the local inhomogeneities of surface tension and internal pressure can thus contribute to the global propulsive force.

We argued above that surface tension variations are small compared to the actual value of the surface tension. This argument holds for local considerations at each point of the surface, meaning that surface tension gradients can be neglected for local equations. However, the cumulative contribution of the surface tension gradient all over the surface is not only important but essential to understand the propulsive force. We discuss below the origin of this surface tension gradient.

3.2.2 Droplet shape and stresses

We now proceed with the determination of the drop shape and stress distribution. Given that the surface tension variation is small along the drop contour and neglecting hydrodynamic effects, we consider, for local equations, that the surface tension and the internal pressure are constant, so that $\gamma = \gamma_0$ and $\delta P = 0$. In these conditions, the local normal force balance on the surface of the drop reads

$$\sigma_{nn}(h) = \gamma_0 \left[\frac{\cos\theta(h)}{h} + \frac{d\left(\cos\theta(h)\right)}{dh} - \frac{2}{R} \right] . \tag{3.7}$$

In regions where the mean curvature $(\kappa_s + \kappa_\phi)/2$ is larger than the mean curvature $1/R$ of the spherical cap at the front, the normal stress is positive and the gel pulls on the drop ($\sigma_{nn} > 0$). On the contrary, in regions with mean curvature $(\kappa_s + \kappa_\phi)/2 < 1/R$ the gel pushes and squeezes the drop ($\sigma_{nn} < 0$).

The actin polymerization at the surface of the drop generates stresses in the actin network. These elastic stresses in the gel influence, in turn, the polymerization kinetics. Polymerization is normal to the surface of the drop and it is accelerated by a dilative stress ($\sigma_{nn} > 0$) and slowed down by a compressive stress ($\sigma_{nn} < 0$). The polymerization velocity v_p corresponds, in our mesoscopic description, to the local polymerization velocity of the actin network on the drop surface. Although the relation between the polymerization velocity of an actin network and the normal stresses

may be, in general, different than that of a single filament under applied load, we assume for simplicity the same relation. Indeed, the functional relations for $v_p(\sigma_{nn})$ suggested by numerical simulations (Carlsson, 2001) leave our results unchanged. Classical rate theories (van Kampen, 2004; Kramers, 1940) predict a polymerization velocity, v_p, varying as a Boltzmann law

$$v_p(h) = v_p^0 \exp\left[\frac{\sigma_{nn}(h)}{\sigma_0}\right] , \qquad \sigma_0 \equiv K_B T / a^2 \delta , \tag{3.8}$$

where a is the distance between actin polymerization promoters on the drop surface, δ is of the order of the size of an actin monomer and v_p^0 is the polymerization velocity in the absence of stress.

The last equation determining the shape of the drop is the conservation of the gel volume upon polymerization. In a first approximation, we assume both that the gel density is constant and that the comet is a perfect cylinder. Indeed, the Poisson ratio, σ, of an actin network is thought to be $\sigma \simeq 0.4$ (Gerbal et al., 2000a), meaning that the gel in nearly incompressible. In a steady state, the drop advances at a constant velocity V. The local gel thickness, e, shown on Fig. 3.3b is then such that $de/ds = -\tan\theta$. With these simplifying approximations, the local polymerization velocity is related to the advancing velocity by

$$v_p(h) = V \sin\theta(h) . \tag{3.9}$$

Combining Eqs. 3.7, 3.8 and 3.9, we obtain the equation

$$\ln\left(\frac{V}{v_p^0}\sin\theta(h)\right) = \frac{\gamma_0}{\sigma_0}\left[\frac{\cos\theta(h)}{h} + \frac{d\left(\cos\theta(h)\right)}{dh} - \frac{2}{R}\right] , \tag{3.10}$$

which specifies the angle, $\theta(h)$, between the tangent to the drop shape and the direction of motion, at each point of the surface. The shape of the drop, $h(z)$, can be then calculated by direct integration of

$$\frac{dh}{dz} = \tan\theta(h) . \tag{3.11}$$

Note that the present description does not specify the drop velocity V. Indeed, neglecting both the surface tension gradient and internal pressure variations, it is not possible to determine the drop velocity V since the propulsive force vanishes. We thus find a family of solutions for the drop shape parameterized by the advancing velocity V.

Analytical results

The shape of the comet-drop interface departs from a pure cone when the Boltzmann factor in Eq. 3.8 is significantly larger than 1. This defines the size of the blunted region at the rear of the drop as $\ell \equiv \gamma_0 a^2 \delta / K_B T$, which leads to $\sigma_0 = \gamma_0/\ell$. The ratio,

$\varepsilon \equiv \ell/R$, of this characteristic length ℓ and the radius R of the spherical cap at the front of the drop is a dimensionless parameter that quantifies the amount of deformation of the drop. Values of $\varepsilon \sim 1$ indicate that the back of the drop is characterized by a radius of curvature similar to that at the front. A value $\varepsilon \ll 1$ corresponds to highly deformed droplets, characterized by an accentuated pear-like shape. Although the value of ε can be estimated using the experimentally measured values for R and γ_0 and typical values for δ and a, we consider it an unknown parameter and analyze the drop shape for different values of ε.

The typical pear-like shape of the droplets observed experimentally suggests $\varepsilon \ll 1$. We thus consider it a small number in order to obtain analytical solutions of the drop shape. Mathematically, ε is a singular perturbation parameter and the size ℓ defines a boundary layer at the back of the drop. We now calculate the shape at length scales of order $\sim R$ and $\sim \ell$ separately, and match asymptotically the solutions.

For h of order R, the elastic stress $\sigma_{nn}(h)$ is small ($\mathscr{O}(\varepsilon)$) and can be neglected. Then Eq. 3.9 describes a perfect cone with angle $\theta = \theta_0$, defined by the ratio, $\sin\theta_0 \equiv v_p^0/V$, of the polymerization velocity at vanishing stress, v_p^0, and the drop velocity, V (Fig. 3.4a). This result is independent of the polymerization law giving v_p as a function of $\sigma_{nn}(h)$. The measure of θ_0 and V gives thus access to the polymerization velocity in the absence of elastic stress. For small but finite ε, the corrections to the perfect cone shape at length scales $\sim R$ are given by

$$\frac{dh}{dz} \simeq \tan\theta_0 + \varepsilon \frac{1}{\cos^2\theta_0}\left[\frac{\sin\theta_0}{\tan\theta_0}\frac{R}{z} - 2\tan\theta_0\right] , \tag{3.12}$$

where the first term, $\tan\theta_0$, describes the perfect cone shape in the limit $\varepsilon \to 0$.

In the blunted region at the back of the drop, h is of order ℓ and the stresses applied by the gel are large ($\sim \gamma_0/\ell$) compared to the Laplace pressure term $2\gamma_0/R$ (of $\mathscr{O}(\varepsilon)$ in this region), which can be neglected in Eq. 3.10. In the vicinity of the rear point, the drop profile is given by

$$\frac{h(z)}{\ell} = 2\sqrt{\frac{1}{\ln\left(1/\sin\theta_0\right)}\frac{z}{\ell}} . \tag{3.13}$$

This solution corresponds to the drop profile in the boundary layer of size ℓ at the back of the drop.

The normal stress in the region of size ℓ at the rear of the drop is positive and of order γ_0/ℓ. At the backmost point, the stress is

$$\sigma_{nn}(h=0) = \frac{\gamma_0}{\ell}\ln\left(\frac{1}{\sin\theta_0}\right) . \tag{3.14}$$

In the conical region, the stress, at lowest order in ε, reads

$$\sigma_{nn}(h) = \frac{\gamma_0}{R}\left[\cos\theta_0\frac{R}{h} - 2\right] \tag{3.15}$$

It is positive at the back of the drop (pulling the drop backward) and negative in the front part of the cone (pushing the drop forward) as qualitatively observed in

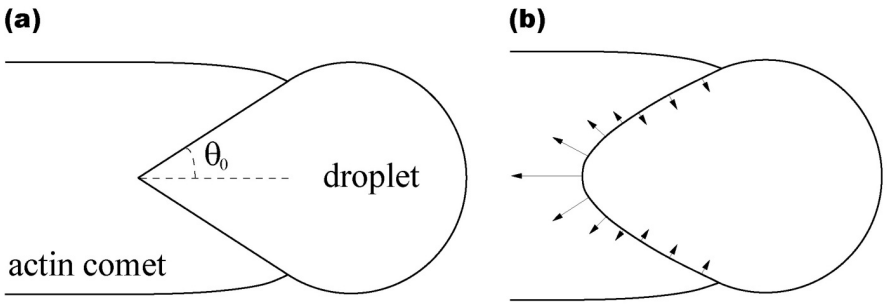

Fig. 3.4. (a) Sketch of the shape of the drop in the limit $\varepsilon \to 0$. The interface between the drop and the comet tail is perfect cone with angle θ_0. (b) Sketch of the local forces (normal stress) applied by the actin gel on the drop. The gel pulls the droplet backward at the rear, while pushing it forward and squeezing it at the sides.

Refs. (Upadhyaya et al., 2003; Giardini et al., 2003). It vanishes for a thickness $h = (R\cos\theta_0)/2 = h_m/2$. In Fig. 3.4b we sketch the normal local forces applied by the actin gel on the drop. This result is in accordance with the prediction made in Ref. (Gerbal et al., 2000a) that the actin gel could pull at the rear of *Listeria* and explains the pear-like deformation of the drop.

The asymptotic limit ($h \gg \ell$) of the solutions in the boundary layer should match the asymptotic solutions ($h \ll R$) outside the boundary layer. The asymptotic expression for the stress in the boundary layer at the rear of the drop, in the limit $h \gg \ell$ and $\theta \to \theta_0$, reads

$$\sigma_{nn}(h) = \frac{\gamma_0}{h}\cos\theta_0 \,, \tag{3.16}$$

which exactly matches the asymptotic solution for the stress outside the boundary layer (Eq. 3.15) in the limit $h \ll R$.

Numerical results and comparison to the experimental data

A more detailed description of the drop profile is obtained by solving numerically equation 3.10. Scaling the fluid thickness h with the radius R ($\tilde{h} \equiv h/R$), the normal force balance on the drop surface (Eq. 3.10) reads

$$\ln\left(\frac{\sin\theta}{\sin\theta_0}\right) = \varepsilon\left[\frac{\cos\theta(\tilde{h})}{\tilde{h}} + \frac{d\left(\cos\theta(\tilde{h})\right)}{d\tilde{h}} - 2\right] \,, \tag{3.17}$$

and only depends on the two dimensionless parameters, $\varepsilon = \ell/R$ and $\sin\theta_0 = v_p^0/V$.

The movement of the droplet is a free boundary problem and obtaining the drop shape is not straightforward. The integration of Eq. 3.17 determines the angle θ as a function of the fluid thickness h and once $\theta(h)$ is known, the integration of equation

$dh/dz = \tan\theta(h)$ provides the drop shape $h(z)$. This is so if the boundary conditions and the position of the boundaries are known. At the origin, $z = 0$, the boundary condition for Eq. 3.17 is $\theta(h = 0) = \pi/2$. On the other hand, the position of the boundary where the drop-comet interface contacts the spherical cap is unknown *a priori*. Imposing continuity of both the droplet shape and its tangent at $h = h_m = R\cos\theta_0$, specifies the position of the triple line and the solution $h(z)$. Note that three boundary conditions have been imposed in spite of having only two first order differential equations. The extra boundary condition is necessary to specify the position of the boundary with the spherical cap. Numerically, we first determine the position of the boundary with the spherical cap using a shooting method (Press et al., 2002), and calculate the drop shape once the position of this boundary in known.

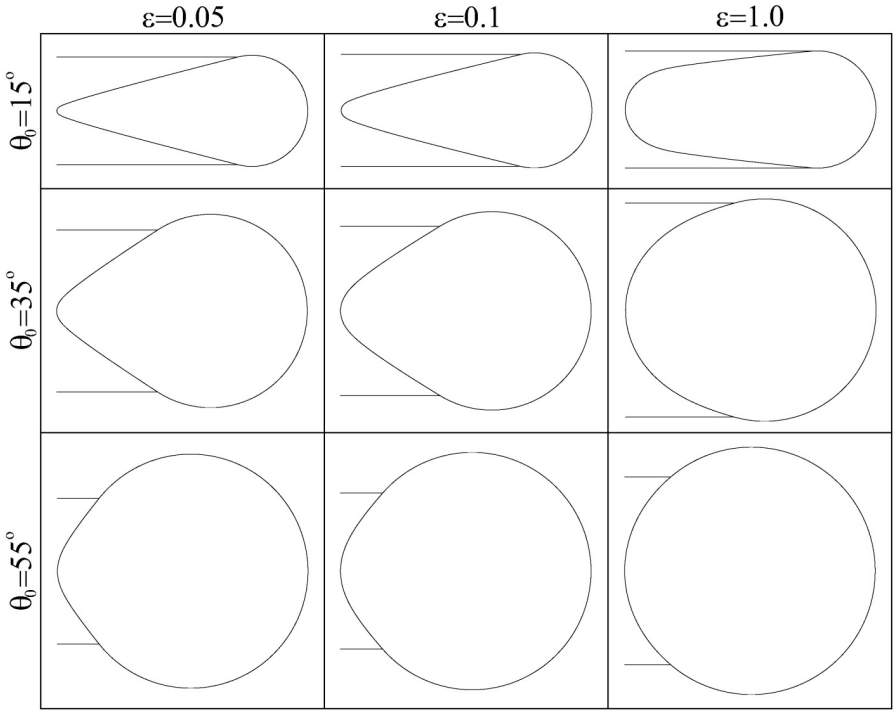

Fig. 3.5. Numerically integrated drop shape for various values of the parameters ε and θ_0. The largest drop deformations correspond to small values of both ε and θ_0, whereas for $\varepsilon \sim 1$ and large enough values of θ_0, the drop is hardly deformed. For a given drop velocity V (fixed value of θ_0), larger droplets, corresponding to smaller values of ε, are more deformed.

In Fig. 3.5 we show the numerically obtained drop shape for different values of the parameters ε and θ_0. For a given value of the drop velocity (fixed value of θ_0), larger values of ε correspond to less deformed drops. Experimentally, the length ℓ is

constant [4], and smaller drops, corresponding to larger values of ε, are less deformed, in agreement with the theoretical predictions. The parameter $\sin\theta_0$ controls the elongation of the drop. For drop velocities $V \gg v_p^0$, corresponding to small values of the angle θ_0, the drop displays elongated shapes, with a pear-like shape for $\varepsilon \ll 1$ and a cylindrical shape for values of $\varepsilon \sim 1$. Therefore, more elongated drop shapes are expected for drops moving at larger velocities. This prediction has been corroborated experimentally, as elongated drops move faster than less deformed drops.

We now compare at quantitative level the theoretical results to the experimental data. In Fig. 3.6a we show a comparison of the calculated and experimental drop profiles. The experimental profile for the drop in Fig. 3.6c is digitized and adjusted by a continuous curve. We then perform a two-parameter fit of the experimental drop profile with the numerically integrated drop shapes. The best fitting parameters are $\varepsilon = 0.049$ and $\sin\theta_0 = 0.58$ ($\theta_0 = 35.6^\circ$). The numerically obtained drop shape for this values of the parameters is shown in Fig. 3.6a, together with the experimental drop profile; its three dimensional reconstruction is shown in Fig. 3.6d. The measured values for the radius R of the spherical cap and the drop velocity V are, for this particular drop, $R \simeq 2.55\ \mu$m and $V \simeq 0.15\ \mu$m/min. With the values obtained from the fit for ε and $\sin\theta_0$, and the measured values of R, V and the surface tension γ_0, we determine

$$\ell \simeq 0.125\ \mu\text{m}\,, \qquad \sigma_0 = 32\ \text{nN}/\mu\text{m}^2 \qquad \text{and} \qquad v_p^0 = 1.4\ \text{nm/s}\,. \tag{3.18}$$

The error in these estimations for a single drop is small ($\simeq 5\%$). Series of measurements for several drops in a given preparation of cell extract show a dispersion both in ℓ and v_p^0 of order $\pm 20\%$. A much larger spread of several hundred percent is found between different preparations, with different total protein concentrations.

The normal stress distribution can be directly obtained from the experimental drop profile. We calculate the curvatures κ_s and κ_ϕ from the drop shape and determine the normal stress distribution using Eq. 3.7. The experimentally obtained normal stress distribution is shown in Fig.3.6b, where it is compared to the numerically obtained normal stress distribution for the drop profile in Fig.3.6a ($\varepsilon = 0.049$ and $\sin\theta_0 = 0.58$). In accordance to the analytical results above, the gel pulls the drop backward at the rear ($\sigma_{nn} > 0$), while pushing and squeezing it in the conical region ($\sigma_{nn} < 0$). The magnitude of the dilative stresses at the rear, of order γ_0/ℓ, is much larger than the compressive stresses on the sides, of order γ_0/R. Their ratio is of order ε, in agreement with the analytical results above. Note that the normal stress distribution obtained theoretically is not a fit of the experimental one. Once the values of ε and θ_0 are known from the fit of the drop shape, the stress distribution is determined with no fitting parameters.

Stress distribution in the vicinity of the triple line

In the description proposed so far, the curvature of the interface between the comet and the drop has a discontinuity at the triple line. In the spherical region, the mean

[4] Although the length ℓ may change in different experiments with different preparations, in a particular experiment it is constant.

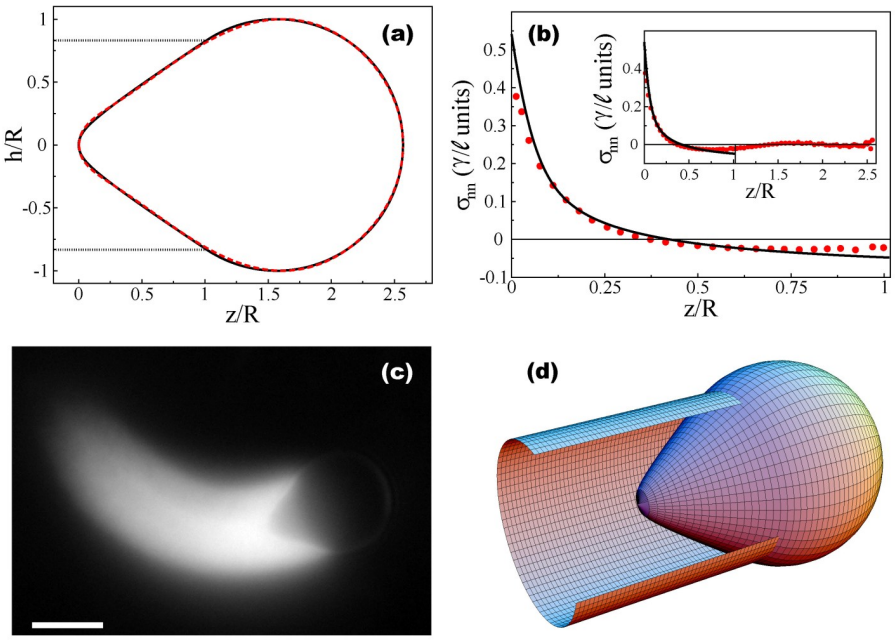

Fig. 3.6. Comparison of the theoretical results and experimental data. (a) Numerical integration of the drop profile for the best fitting parameters, $\varepsilon = 0.049$ and $\sin\theta_0 = 0.58$ (continuous line), compared to the experimental drop profile (dashed line). (b) Numerically obtained normal stress distribution (continuous line) for the numerical drop profile in (a) compared to the experimental stress distribution (circles). The inset shows the normal stress distribution all along the drop contour. The normal stresses vanish in the front part of the drop, where no VCA is present. (c) Fluorescence image of the drop used for this particular comparison to theory. Actin is labeled fluorescently and the actin comet appears bright. Bar, 4 μm. (d) Three-dimensional reconstruction of the drop shape. The actin comet is represented by a perfect cylinder, which we show only partially to allow the visualization of the drop shape.

curvature of the interface is $1/R$, whereas in the conical region, the interface is curved only in the ϕ direction ($\kappa_\phi(h = h_m) = 1/R$ and $\kappa_s(h = h_m) = 0$) and the mean curvature is $1/2R$. The local forces normal to the interface are still balanced and the elastic normal stress in the comet at the triple line is $\sigma_{nn}(h_m) = -\gamma_0/R$ (Fig. 3.6b). At the triple line, the gel thickness e vanishes and cannot create a finite stress. This explains why in Fig. 3.6b, the theoretical and experimental normal stresses are in disagreement in the close vicinity of the triple line. We now assume that the gel density remains constant but that the comet shape is not a perfect cylinder in the region close to the triple line. Volume conservation then imposes a polymerization velocity

$$v_p = -V\cos\theta\,\frac{de}{ds}\,. \tag{3.19}$$

When a gel element is created in a time δt, it is stretched by an amount δu, given by

$$\delta u = \delta t(-V\sin\theta + v_p)\ , \tag{3.20}$$

and the tensile stresses σ_{ii} in the azimuthal direction ($i=\phi$) and in the tangential direction along the interface ($i=s$) are increased. At the level of scaling laws, we write this increase as

$$\frac{d\sigma_{ii}}{ds} = \frac{E\kappa_i}{V\cos\theta}\left(V\sin\theta - v_p\right)\ , \tag{3.21}$$

where κ_i is the curvature of the interface in the direction i and E is an elastic modulus of the comet. In the vicinity of the triple line, where the gel thickness is small compared to R, we use the thin shell approximation (Landau and Lifshitz, 1986) and relate the tensile and normal stresses in the gel, so that

$$\sigma_{nn} = -e\left(\sigma_{ss}\kappa_s + \sigma_{\phi\phi}\kappa_\phi\right)\ . \tag{3.22}$$

In the region of length ℓ close to the triple line (boundary layer), the two tensile stresses can be considered as constant at lowest order. The matching to the pear-like shape imposes that the azimuthal tensile stress $\sigma_{\phi\phi}$ vanishes. Defining the dimensionless tensile stress as $\tilde{\sigma}_s = \ell\sigma_{ss}/\gamma_0$, the normal stress in the boundary layer close to the triple line reads

$$\sigma_{nn} = -\frac{\gamma}{R}\frac{e\tilde{\sigma}_s}{\ell + e\tilde{\sigma}_s}\ . \tag{3.23}$$

As the thickness of the gel vanishes ($e\to 0$), the normal stress vanishes as expected. The boundary layer, where the comet is deformed, has a thickness $\ell/\tilde{\sigma}_t$ of order ℓ and is thus small in the limit where ε is small. When e is large ($e\gg\ell$), further away from the triple line, the comet reaches a cylindrical shape and the normal stress is $-\gamma/R$. Therefore, for distances larger than ℓ from the triple line one can consider the comet to be a perfect cylinder, as done above.

3.2.3 Origin of the propulsive force

We have shown above that the drop shape and stress distribution applied by the actin gel can be determined without taking into account the differences in internal pressure, δP, and the surface tension gradient, $\delta\gamma$. This is so because only local equations are needed to specify the shape of the drop. However, in section 3.2.1 we calculated the total elastic force propelling the drop and showed that the contribution of these terms is essential. We now discuss both terms separately and provide an estimation of the total propulsive force.

Internal pressure variations

The motion of the drop generates an internal fluid flow that induces a difference in the pressure at each point of the drop. Although the fluid flow inside the drop is difficult to calculate for an arbitrary axisymmetric shape, the order of magnitude of the maximal pressure differences inside the drop can be estimated. To this end, we use the known results for a spherical drop falling inside another fluid under the

action of gravity (Batchelor, 2000). Similarly to the oil drop we consider, a falling drop moves with constant velocity in the steady state. The fluid inside the falling drop is sheared at its surface and a closed internal fluid circulation sets up inside the drop. In the steady state, the pressure difference, ΔP, between the back and the front of the drop is of order (Batchelor, 2000)

$$\Delta P \sim \frac{10V}{R}\frac{\eta\bar{\eta}}{\eta+\bar{\eta}}\,, \tag{3.24}$$

where η and $\bar{\eta}$ are the buffer and oil viscosities respectively. Using typical experimental values in our problem for the velocity $V \simeq 0.15\ \mu$m/min and the radius $R \sim 2.5\ \mu$m of the drops, together with the viscosity of the buffer and the oil viscosity, we estimate the variation in internal pressure to be

$$\Delta P \sim 10^{-2}\ \mathrm{mN/m^2}\,, \tag{3.25}$$

This value constitutes an upper bound because the maximal difference of internal pressure is that existing between the back and the front of the drop. The pressure differences induces by the fluid flow must be compared to the magnitude of the surface tension gradient, which we analyze below.

Surface tension gradient

In the beginning of this chapter we assumed the existence of a surface tension gradient $\delta\gamma$ without any further explanation. The surface tension of the drop depends on the concentration, ρ, of adsorbed molecules on its surface (Safran, 2003). In case there is an inhomogeneous distribution of the molecules on the surface, a surface tension gradient, that follows the distribution of adsorbed molecules, sets up. Fig. 3.2b shows that VCA molecules on the drop surface are colocalized with the actin comet. A closer look at the VCA concentration on the drop surface shows that their distribution is inhomogeneous. In particular, the VCA concentration decreases monotonically from the back of the drop and has negligible values at the front (spherical cap). The relation between the surface tension, γ, and the surface concentration of adsorbed molecules, ρ, reads (Safran, 2003)

$$\gamma = \gamma_0 + \frac{K_B T}{a_0^2}\ln\left(1 - a_0^2\rho\right)\,, \tag{3.26}$$

where a_0 is the size of the adsorbed molecule. The surface tension is thus smaller in regions with larger concentration of adsorbed molecules. Independently of any particular model for the mechanism that establishes the VCA gradient, we can estimate the magnitude of the propulsive force from the experimentally measured VCA distribution. Using the expression for the total elastic force (Eq. 3.6) and Eq. 3.26, we obtain

$$F_e \sim 2\pi\frac{K_B T}{\lambda}\rho R^2\,, \tag{3.27}$$

where λ is the typical decay length of the VCA concentration along the drop contour. The value of ρ can be estimated from the measured values for ℓ and γ_0 (Eq. 3.18). Indeed, the value of a, which provides an estimate VCA concentration ($\rho \simeq 1/a^2$), is $a = 7$nm. The value of λ can be estimated from the decay of the VCA concentration along the drop contour to be $\lambda \sim 2\,\mu$m. Using these values and $R \simeq 5\,\mu$m, we obtain an estimation of the propulsive force

$$F_e \sim 2\pi \frac{K_B T}{\lambda} \rho R^2 \sim 10^3 \text{ pN} , \tag{3.28}$$

which is in the range of the typical forces measured experimentally for actin-based propulsion (Marcy et al., 2004).

Although the underlying mechanism propelling the drop is the same than for hard beads or *Listeria*, i.e. actin polymerization, the force generation mechanism is distinct for soft, fluid drops and hard objects. In particular, the analysis presented here does not depend at all on the elastic modulus of the gel. This is so because the scale of the stresses is fixed by the typical drop size and its surface tension, whereas for a hard bead there is no other stress scale than the elastic modulus of the gel. As the equations determining the drop shape and the propulsive force do not depend on the elastic modulus of the gel, the shape of the drop and its velocity should not be altered by changes in the gel structure. Indeed, changing considerably the elastic modulus via the addition of biotin-streptavidin crosslinks between the actin filaments, does not modify the drop shape and its velocity (J. Plastino, personal communication).

Distribution of polymerization nucleators on the drop surface

When describing theoretically the drop shape we neglected the surface tension gradient, and the concentration of VCA molecules on the drop surface was considered to be constant underneath the actin comet accordingly. In particular, the surface concentration of VCA molecules was given by $\rho = 1/a^2$ in the region where actin is present. We now describe the dynamics of actin polymerization promoters on the surface of the drop and show that the inhomogeneous distribution of VCA molecules results from the coupled dynamics of the droplet and the nucleators on the surface.

The VCA molecules on the drop surface can be either connected to one of the actin filaments forming the comet (bound state) or freely moving on the surface, with no connection to the actin gel (unbound state). The connection between a VCA molecule and an actin filament has a finite lifetime due to thermal fluctuations. At vanishing stress, actin filaments detach from VCA molecules at an average rate k_d. Actin filaments also bind to (or start polymerizing at) free VCA molecules at a rate k_a. As the drop interface is fluid, the VCA molecules that are not attached to an actin filament freely diffuse on the drop surface and tend to homogenize the VCA surface concentration. On the other hand, a VCA molecule attached to an actin filament is dragged by the actin comet tail toward the back of the drop. Indeed, in the reference frame of the drop, the actin comet tail moves backward with velocity $-V$ in the z direction. On the drop surface, the tangential component of the gel velocity generates a convective flow of the VCA molecules attached to actin filaments toward the back of the drop.

The convection of bound VCA molecules toward the back of the drop leads to a larger VCA concentration at the rear. It is the competition between the dynamic events defined above that sets the distribution of VCA. We are currently studying the dynamics of VCA on the curved surface of the drop. However, we develop here a simplified description in which curvature effects are neglected and we assume no stress dependence of the rate k_d at which actin filaments detach from VCA molecules.

With these simplifying approximations, the dynamics for the density of bound and unbound VCA molecules, ρ_b and ρ_u respectively, read

$$\begin{aligned} \frac{\partial \rho_b}{\partial t} + \frac{\partial J_b}{\partial s} &= -k_d \rho_b + k_a \rho_u \ , \\ \frac{\partial \rho_u}{\partial t} + \frac{\partial J_u}{\partial s} &= k_d \rho_b - k_a \rho_u \ , \end{aligned} \tag{3.29}$$

where s is the spatial coordinate ($s = 0$ at the drop back and $s \in [0, \pi R]$), $J_b = -V\rho_b$ is the convective flux of bound VCA molecules toward the back and $J_u = -D\partial_s \rho_u$ the diffusive flux of unbound VCA molecules (D being the diffusion constant of VCA molecules on the surface). Assuming the VCA distribution to decay at length scales smaller than πR, as observed experimentally, the steady state solutions of Eq. 3.29 with zero total flux ($J_b + J_u = 0$) read

$$\rho_b(s) = \rho_b^0 \exp\left(-\frac{s}{\lambda}\right) \ , \qquad \rho_u(s) = \rho_b^0 \frac{v\lambda}{D} \exp\left(-\frac{s}{\lambda}\right) \ , \tag{3.30}$$

where ρ_b^0 is a constant of integration fixed by the total amount of VCA molecules on the surface, and

$$\lambda = \frac{\lambda_2^2}{2\lambda_1} \left[1 + \sqrt{1 + \left(\frac{2\lambda_1}{\lambda_2}\right)^2} \right] \ , \tag{3.31}$$

is the characteristic decay length of the VCA distribution, which results from the combination of two characteristic length scales in the system: the average length $\lambda_1 \equiv V/k_d$ that VCA molecules attached to actin filaments travel before detaching, and the average length $\lambda_2 \equiv \sqrt{D/k_a}$ that free (unbound) VCA molecules travel by diffusion until attaching to the actin gel.

Although qualitative and too simplified, the analysis above is in qualitative agreement with the experimental observations. Experiments performed by Léa Trichet in the group of Cécile Sykes (Institut Curie), show that the ratio between the VCA density at the back and front parts of the drop depends exponentially on the drop radius. From the analysis above, the ratio of VCA density at the back, $\rho_b(s=0) + \rho_u(s=0)$, and at the front, $\rho_b(s=\pi R) + \rho_u(s=\pi R)$, reads

$$\frac{\rho_b(s=0) + \rho_u(s=0)}{\rho_b(s=\pi R) + \rho_u(s=\pi R)} = \exp\left(\frac{\pi R}{\lambda}\right) \ , \tag{3.32}$$

in qualitative accordance with the experimental observations. A more quantitative comparison of the theoretical results and the experimental data concerning the VCA distribution will be published soon (Trichet et al., 2006).

3.3 Conclusions

The experimental observations presented in this chapter on the shape of liquid drops propelled by actin polymerization are well described by the theoretical description based on a local normal force balance and on a Boltzmann variation of the polymerization velocity with normal stress. The results are robust if we use, for the polymerization velocity, the mathematical forms suggested by simulations on flat surfaces (Carlsson, 2001). We demonstrate that the elastic propulsive force cannot be calculated from a stress distribution that ignores both pressure variations inside the drop and surface tension gradients. Therefore, the total propulsive force cannot be estimated only from the drop shape. The advancing velocity of the drop results from a balance between the total propulsive force and the total friction force between the comet and the drop but a precise study of the velocity selection requires a more refined analysis. We are currently studying in detail the propulsive and friction forces.

Our description reproduces and explains several aspects of the drop motion and agrees at quantitative level with the experimental observations by Hakim Boukellal (Institut Curie). In particular, our calculations indicate that the growth of the actin network generates stresses that push and squeeze the drop along the sides and pull the drop backward at the rear. It has been suggested that a similar stress distribution propels the bacterium *Listeria* (Gerbal et al., 2000a). Although in a different system, our results confirm that the actin comet tail not only pushes on the object being propelled but also pulls on it. In the experiments above (section 3.1), as well as in reference (Upadhyaya et al., 2003), the motion stops when the drop (or the liposome) becomes spherical. The large stress at the back of the drop could lead to “cavitation” or rupture of the links between the drop and the comet. The elastic stresses exerted on the drop then relax and provoke the experimentally observed arrest. Our results could be also helpful to understand the process of phagocytosis, as the pulling stresses may promote the internalization of the object being engulfed. Finally, the peculiar stress distribution found sets important constraints to the microscopic modeling of actin-based motility. The microscopic models proposed to date should be reviewed in the view of our results. It would also be interesting to connect the mesoscopic and microscopic approaches with a theoretical description at intermediate length scales.

The drop shapes obtained in our analysis agree with those observed experimentally for oil drops. By comparing the theoretically calculated drop shape with the experimental observations, we estimate of the polymerization velocity of an actin gel in the absence of stress and its variation with stress. Moreover, endosomes and lysosomes which are propelled by an actin comet tail also show deformations which are in qualitative agreement with our results. However, we believe that our description should be extended to account for other observed behaviors. For instance, there exist different dynamical regimes for the drop motion. Similarly to *Listeria* or synthetic beads, lipid vesicles and drops propelled by an actin comet also display a saltatory motion. It is possible that the collective behavior of the actin filaments generating forces at the surface leads to similar instabilities than those observed in the collective behavior of motor proteins.

The fluidity of the drop interface constitutes an important feature of the system dynamics, as it allows the movement of the actin polymerization promoters. Our analysis highlights the importance of the attachment/detachment kinetics of the actin filaments at the surface of the cargo, and the motion of the nucleators on the fluid interface. Previous studies on *Listeria* motion showed that the dynamic attachment of the actin comet to the bacterium can be responsible for the observed saltatory behavior. The plasma membrane at the leading edge of a crawling cell is fluid and the motion of the actin nucleators on its surface can be important for the motility process. In this case, the growth of the actin network would not be equally promoted all along the leading edge. Instead, the coupled dynamics of the actin polymerization promoters and the growth of the actin network would determine the distribution of nucleators and the structure of the actin network.

We have shown that the mesoscopic approach adopted here is in quantitative agreement with several experimental observations. In this approach the coupling between the growth dynamics of the filaments at the surface is effectively taken into account in the gel elasticity. Indeed, the stresses developed at a given point deform the gel and the drop, affecting thus the growth of actin filaments at other points of the drop surface. Yet, it would be interesting to study how the dynamics of distant actin filaments polymerizing at a surface are coupled by the network structure and what is the dynamics of the growing network under applied loads. While it is known that the growth of individual actin filaments can develop forces, the precise mechanism of force generation is still unclear and it would be interesting to study it in more details. Although solving these questions is important to understand actin-based motility, the mesoscopic properties of actin networks allow coarse-grained descriptions based on general conservation laws that are very helpful to understand the motion at large scales.

Part II

Intracellular traffic

4

Introduction

Many different processes take place simultaneously in eukaryotic cells. These processes are carried out by biochemical reactions and each one of them requires a specific set of proteins (Alberts et al., 2004). Some of the biochemical reactions, like protein synthesis and degradation, are necessarily incompatible with each other and must be physically separated. In order to overcome this problem, eukaryotic cells have a set of membrane-bounded compartments (organelles), each one containing specific proteins that perform a particular set of functions. Although all proteins are synthesized in the cytosol (outside the organelles), they associate to particular organelles in a process called protein sorting. The different compartments maintain a certain level of autonomy, but they must also interact with other cellular regions in order to ensure the global functioning of the cell. There exist different mechanisms by which membrane-bounded compartments interact with the cytosol and with other compartments. The membrane that bounds a compartment have many different membrane proteins that control the direct exchange of specific material with the cytosol. This interaction takes place in the closed neighborhood of the compartment. However, cells also need to transport material, such as the newly synthesized proteins or lipids, to different and distant regions in the cell (Fig. 4.1). For instance, the endoplasmic reticulum delivers the newly synthesized proteins to the Golgi apparatus, which distributes them afterwards to other cellular regions. Moreover, the internalized material at the plasma membrane, or the material to be secreted to the extracellular medium, must be transported over large distances, of the order of several microns. Different mechanisms are involved in this long range transport and require a sophisticated machinery that we briefly describe below.

4.1 Intracellular transport

Ions and small molecules (like ATP) are needed everywhere in a cell, and are homogeneously distributed in the cytosol. Each membrane-bounded compartment has selective transmembrane proteins (e.g. ion channels) that specifically control the permeation of these small molecules to their interior, depending on the needs. Diffusion

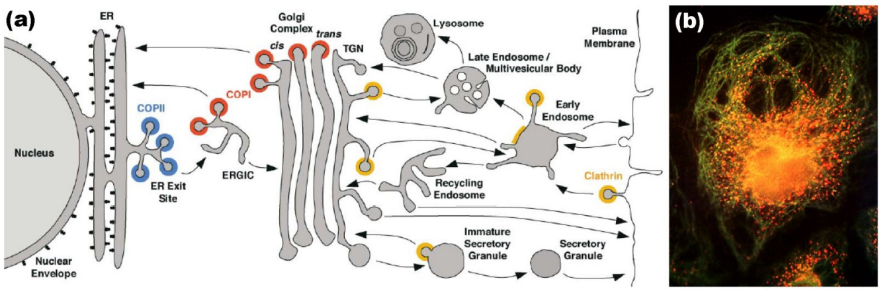

Fig. 4.1. (a) Sketch of intracellular transport, showing the compartments (Endoplasmic Reticulum (ER), Golgi apparatus, lysosomes,...) involved in the biosynthetic-secretory, lysosomal/vacuolar, and endocytic pathways. Arrows indicate the transport steps. The location of COP-I (red), COP-II (blue) and clathrin (orange) is indicated by different colors. (adapted from Ref. (Bonifacino and Glick, 2004)). (b) Distribution of conventional kinesin (red) and microtubules (green) in a PtK1 cell. The red dots are kinesin motors associated with transport vesicles from the Endoplasmic reticulum and Golgi, moving along microtubules. (Figure taken from the Kinesin homepage: http://www.proweb.org/kinesin/index.html).

tends to homogenize the concentrations of ions and small molecules in the cytosol, and is a relatively fast mechanism to transport them all over the cell. Unlike this non-specific diffusional transport of small molecules, the long distance specific transport mentioned above requires energy consumption. The physical mechanism for transport relies on the interaction of transport intermediates (small vesicles and membrane tubes) with the cell cytoskeleton through motor proteins, which move along the cytoskeletal filaments and transport the cargo (Alberts et al., 2004; Bray, 1992; Howard, 2001).

4.1.1 Vesicular transport

The process of vesicular traffic requires first the budding of small vesicles, which enclose the material to be transported, from a membrane-bounded compartment (Fig. 4.2a,b). A protein coat assembles on the surface of the membrane and induces the formation of a membrane bud. Different proteins (Clathrin, COP-I, COP-II) have been shown to induce budding by coating locally the membrane (Bonifacino and Glick, 2004; Farsad and Camilli, 2003). Once the bud is formed, it pinches off the original membrane, in a process that requires the action of other proteins (e.g. dynamin (McNiven, 1998)). The small vesicles resulting from this fission are then moved along the cytoskeletal filaments by motor proteins toward the target compartment (Howard, 2001; Hirokawa, 1998; Hirokawa, 1996; Vale, 2003) (Fig. 4.1b and Fig. 4.2c,d). Once the vesicles reach their destination, they fuse with the membrane of the target compartment and release the transported material. The process of vesicle docking and fusion is highly specific. This specificity is controlled by markers on the transport vesicles that recognize complementary receptors on the surface of the target organelle (Bonifacino and Glick, 2004). The SNARE family of proteins is

thought to mediate the recognition process (Pfeffer, 1999), although other proteins could also be involved.

Cells can internalize macromolecules in a process called endocytosis, and transport them to the lysosomes using transport vesicles (Alberts et al., 2004; Bonifacino and Glick, 2004). This inward transport is called endocytic pathway (Fig. 4.1a), and allows the cell to take material from the exterior of the cell and digest it afterwards. There is also an outward transport of vesicles, initially created in the endoplasmic reticulum, that move toward the Golgi apparatus and are transfered later to the plasma membrane. The material in these transport vesicles is released to the exterior of the cell (exocytosis). This outward transport constitutes the biosynthetic-secretory pathway and allows the cell to interact with the external world by secreting specific molecules (Fig. 4.1a).

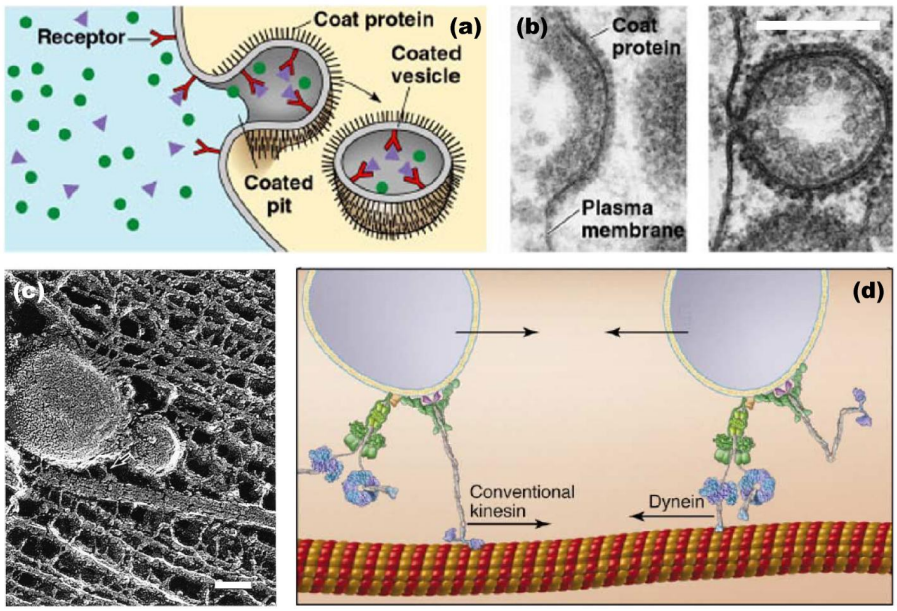

Fig. 4.2. (a) Sketch of the process of membrane budding by clathrin coating. (b) Electron microscopy image of the initial (left) and final (right) states of budding induced by clathrin coating. Bar, 0.25 μm. (c) Electron microscopy image of a transport vesicle attached to the microtubule by a short cross-bridge (arrow) which could be a motor protein. Bar, 50 nm. (Adapted from Ref. (Hirokawa, 1998)). (d) Sketch of small vesicles with motors of different directionalities (kinesins and dyneins) bound to their surface. Kinesin motors carry the transport vesicles toward the plus-end of the microtubule, while dynein motors carry them toward the minus-end. The regulation of the directionality in transport vesicles with both minus-ended and plus-ended motors remains unknown. (Modified from Ref. (Vale, 2003)).

The motion of the transport vesicles is due to molecular motors attached to the surface of the vesicles (Alberts et al., 2004; Howard, 2001; Vale, 2003) (Fig. 4.2b,c).

Depending on the destination of the vesicle, different motors drive the movement. While the forward motion from the center of the cell (where the minus-ends of microtubules are located) toward its periphery is due to plus-ended motors (kinesins), the inward motion is mediated by minus-ended motors (cytoplasmic dyneins). It is thought that vesicles have both plus-ended and minus-ended motors attached to them, and their respective activities are regulated to generate motion in a prefered direction, depending on the final destination. Indeed, the characteristic saltatory motion of vesicles suggests the competition of motor activities with different directionality (Welte, 2004).

The main inward and outward transport pathways in the cell are driven by microtubule-based motors (kinesins and dyneins). This is so because the microtubules in the cell are distributed radially from the center, connecting it directly to the cell periphery, and acting as rigid rails for long distance transport. On the other hand, the local transport over shorter distances (transversal motion more or less perpendicular to the radial direction in the cell) is thought to involve actin-based processive motors (like myosin-V) that move in the meshwork of actin filaments (Snider et al., 2004). In a similar way as in a city, the microtubules act as highways allowing long distance and fast transport directed radially from the center, whereas actin filaments provide a network of local roads for transport on smaller scales.

4.1.2 Transport mediated by membrane tubes

Membrane tubes are tubular extensions of membrane-bounded compartments which can extend from an organelle to distant regions in the cell, connect different parts of the same organelle and even connect different organelles. The endoplasmic reticulum constitutes the most spectacular example; it is composed of a tubular network that extends all over the cell (Vedrenne and Hauri, 2006; Waterman-Storer and Salmon, 1998; Terasaki et al., 1986; Lane and Allan, 1999) (Fig. 4.3A and Fig. 4.4). In Fig. 4.3 we show the distribution of the endoplasmic reticulum in an eukaryotic cell. The network of membrane tubules is highly ramified and extends over a large portion of the cytoplasm. Membrane tubes are also involved in the internal transport of the Golgi apparatus, where they connect different regions of this compartment (Rambourg et al., 1979). The transport between different organelles is not only mediated by transport vesicles but also by membrane tubes. In particular, the transport from Golgi to the endoplasmic reticulum has been shown to involve a network of membrane tubes *in vivo* (Lippincott-Schwartz et al., 1990). Although the precise mechanism for transport mediated by membrane tubes is unknown, it has been argued that tubes connecting Golgi and the endoplasmic reticulum could generate a fluid flow inside the tube, resulting from the difference in surface tension of these organelles, that would drive the transport of material from one organelle to the other (Upadhyaya and Sheetz, 2004; Dommersnes et al., 2005; Sciaky et al., 1997).

The formation and maintenance of several organelles, like the endoplasmic reticulum and the Golgi apparatus, have been shown to require the presence of microtubules and the action of motor proteins (Alberts et al., 2004). In case microtubules are depolymerized, the membrane tube network forming the endoplasmic reticulum

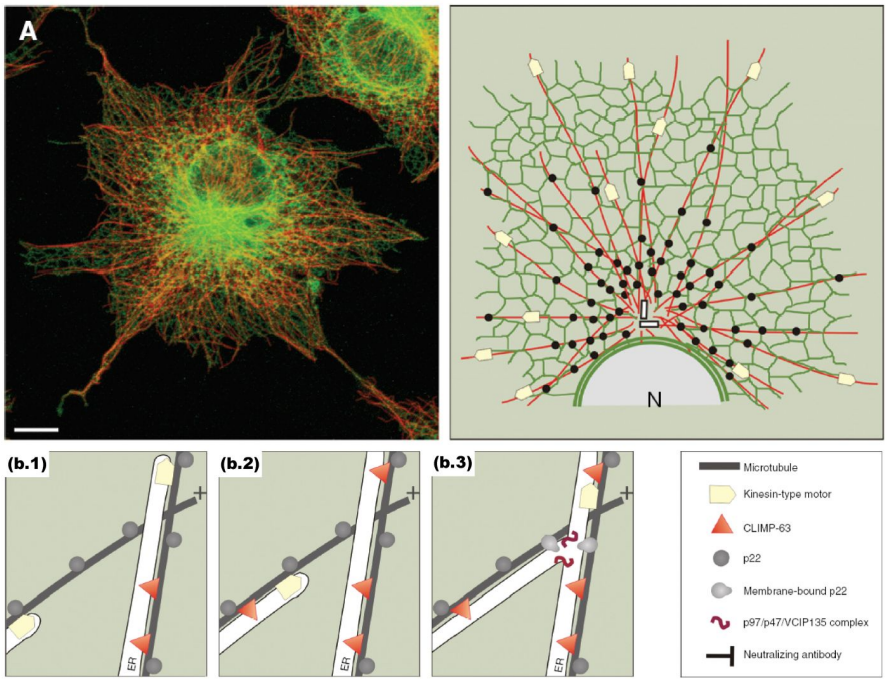

Fig. 4.3. (A) Structure of the Endoplasmic Reticulum (ER) in COS cells. (Left) Fluorescence image showing the distribution of microtubules (red) and CLIMP-63, a protein associated to the ER (green). The schematic representation is shown on the right. The protein CLIMP-63 (black dots) is thought to stabilize the attachment of the ER membrane to microtubules. The network of membrane tubules constituting the ER is superimposed with the network of microtubules, which extends radially from the centrosome (rectangles) close to the nucleus (N). Motors proteins (yellow arrows) extend the ER tubule network all over the cell. (b) Sketch of the growth process of ER membrane tubes (white). (b.1), (b.2) and (b.3) represent different stages of the growth, with time increasing from left to right. ER tubules are actively pulled along microtubules by plus-ended kinesin motors. The anchoring of the tubes to the microtubules is thought to be mediated by CLIMP-63. The interaction between different membrane tubules is mediated by other proteins (p22,SNAREs,...), which can reorganize the already extended ER tube network. (Modified from Ref. (Vedrenne and Hauri, 2006)).

collapses onto the center of the cell and the Golgi apparatus fragments into separated vesicles. The dynamics of the membrane tubes that form the endoplasmic reticulum has been studied in detail (Waterman-Storer and Salmon, 1998; Lane and Allan, 1999) (Fig. 4.4). The tubes can either grow by the growth of a microtubule or can grow along preexisting microtubules (Fig. 4.4c). If microtubules are stabilized, tubes only grow toward the plus-end of preexisting microtubules and their typical velocities are similar to those of kinesin motors (Waterman-Storer and Salmon, 1998). These observations strongly suggested that membrane tubes are extracted from the endoplasmic reticulum by kinesin motors. Moreover, kinesin motors have been shown

to be necessary for membrane tube formation from Golgi (Lippincott-Schwartz et al., 1995). Molecular motors attached to the membrane of an organelle interact with microtubules, walk along them and pull on the membrane until they extract a tube (Vedrenne and Hauri, 2006; Waterman-Storer and Salmon, 1998) (Fig. 4.3b and Fig. 4.4c). This tube extends further along the microtubule due to the action of the motors and can eventually fuse with another compartment or a different region of the same compartment. Motor proteins are thus not only involved in the maintenance of the shape and proper positioning of important organelles in the cell but also in the transport between organelles, either carrying small vesicles or pulling membrane tubes.

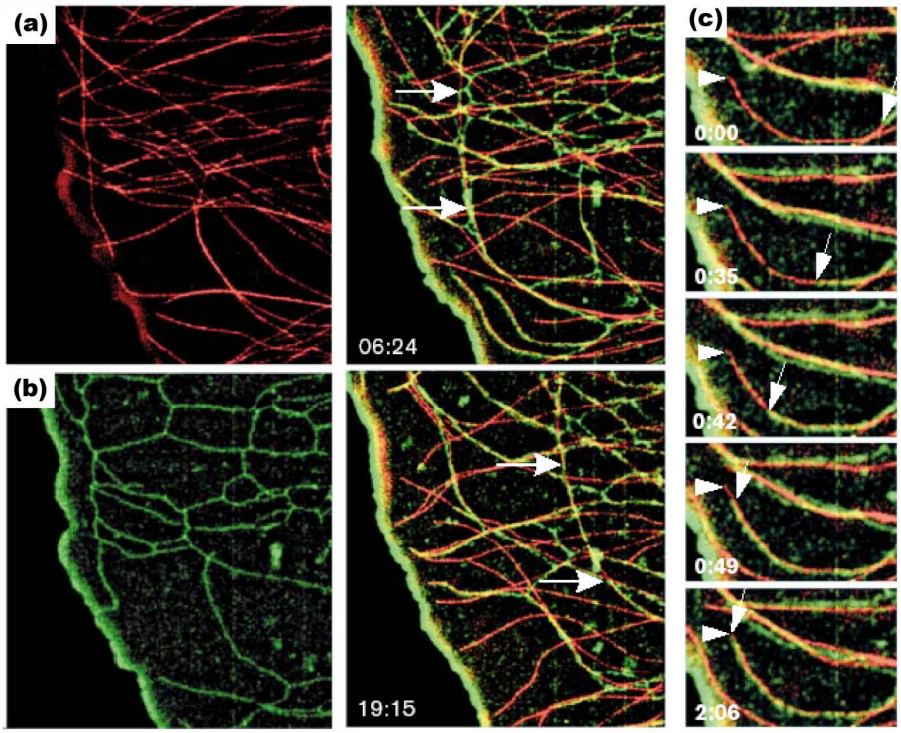

Fig. 4.4. Structure and dynamics of Endoplasmic Reticulum (ER) tubes in the lamellipodium of a Newt lung cell. (a-b) Fluorescence images showing the colocalization of ER (green) tubules and microtubules (red). Distribution of the microtubule network (a; right) and simultaneous labeling of microtubules and ER (a; left). (b) Structure of the ER network (left) and simultaneous labeling of microtubules and ER (right). The time in (a) and (b) is different and indicated in min:sec. Bar, 5 μm. (c) Growth of a ER tubule (arrow) along a preexisting microtubule (microtubule tip indicated by an arrowhead). The different figures are snapshots at different times, increasing from top to bottom, and indicated in min:sec. (Modified from Ref. (Waterman-Storer and Salmon, 1998)).

The work we present in this part focuses mainly in the physical formation of membrane tubes by the action of molecular motors. In chapter 5 we study theoretically the process of membrane tube extraction by motor proteins, and quantitatively compare our results to *in vitro* experiments that mimic the *in vivo* tube formation. In chapter 6 we analyze the mechanism by which molecular motors are able to collectively generate large forces when pulling on fluid membranes.

4.2 Membranes

Membranes are self-assembled structures, composed of many lipids arranged in a bilayer configuration (Lipowsky and Sackmann, 1995). Individual lipids are amphiphilic molecules, with a polar hydrophilic head and a hydrophobic tail (hydrocarbon chains) (Fig. 4.5a). In contrast to the hydrophilic head of the lipid, which has a certain affinity for water molecules, the hydrocarbon chains tend to avoid the contact with water. When many individual lipids are in water solution, these spontaneously form closed aggregates, with the hydrophilic heads forming the surface exposed to water and the hydrocarbon chains contacting each other in order to minimize the exposure to water molecules (Israelachvili, 1992; Lipowsky and Sackmann, 1995). This is known as the hydrophobic effect and is responsible for the self-assembly of lipids in solution (Widom et al., 2003). Depending on the geometric properties of individual lipids, the structure of the assembly is different (Israelachvili, 1992) (Fig. 4.5b). Cone-like lipids lead to spherical micelles, whereas cylindrical lipids assemble into planar bilayer, composed of two leaflets (Fig. 4.5c). If the geometry of the lipids is in between these two cases (truncated cone), the resulting structures may be cylindrical micelles or bilayers with a prefered curvature (called spontaneous curvature). Lipid bilayers may form closed structures, called vesicles. The most studied vesicles are those with spherical topology. Typically, most *in vitro* studies use large vesicles, called Giant Unilamellar Vesicles (GUV), with radius ranging from 1 μm to 100 μm (Girard, 2004).

Lipid bilayers exist in different phases depending on the lipid structure and several physical quantities, as pressure and temperature (Lipowsky and Sackmann, 1995). In typical physiological conditions, the bilayer is in a liquid disordered phase and behaves as a two dimensional fluid. An important property of fluid lipid bilayers is that the individual lipids forming a leaflet constantly interchange their positions, leading to a diffusional motion of the lipids in each leaflet (Lipowsky and Sackmann, 1995). The diffusion constant of the lipids is about 1 $\mu\mathrm{m}^2\,\mathrm{s}^{-1}$ for a membrane in a liquid disordered phase (Chapman, 1975; Lipowsky and Sackmann, 1995; Bretscher, 1973). This in-plane fluidity of the membrane have interesting consequences on its behavior at large scales.

The mesoscopic properties of a vesicle depend on the interaction between the constituting lipids. However, when the length scales of interest are larger than the individual size of a lipid and the thickness of the bilayer, the elastic properties of the membrane are well described by coarse-grained theories (Canham, 1970; Helfrich, 1973; Lipowsky and Sackmann, 1995; Safran, 2003; Nelson et al., 2004; Kamien,

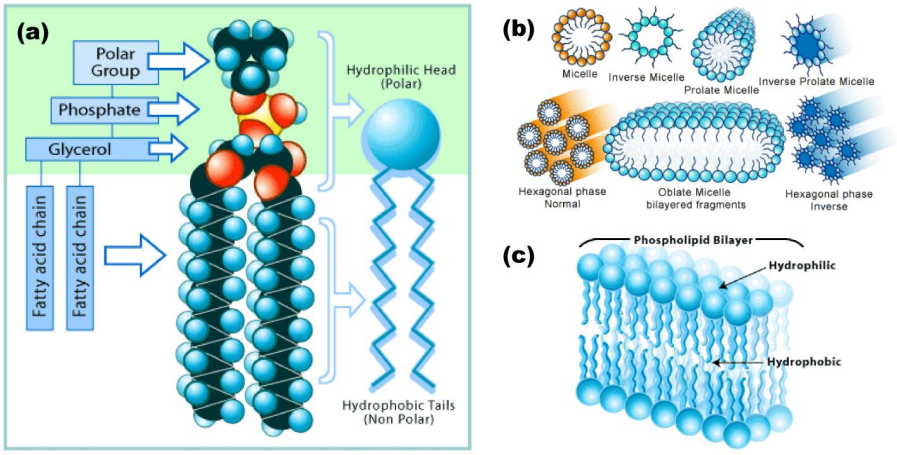

Fig. 4.5. Sketch of a phospholipid (a), some of the possible self-assembled structures of different lipids (b) and a portion of a phospholipid bilayer (c). (Figures taken from the website http://www.bioteach.ubc.ca/Bio-industry/Inex).

2002). At large scales, the membrane can be thought as a two-dimensional surface. Unlike a mathematical surface, which can be freely distorted, there is an energy cost associated to each elementary deformation of the membrane, namely bending, stretching and shear (Lipowsky and Sackmann, 1995; Safran, 2003; Safran, 1999; Sackmann, 1990). Any deformation of a membrane can be expressed as a combination of these three elemental deformations. Specifically, the microscopic origin and the phenomenological description of the elemental deformations are the following:

- *Stretching*. The stretching mode accounts for the energy cost of changing the area of an element of surface. At molecular level, this situation corresponds to increasing the average distance between lipids from their equilibrium separation. The energy per unit area, e_{st}, associated with a relative change in area $\Delta A/A$ is

$$e_{st} = \frac{K_a}{2}\left(\frac{\Delta A}{A}\right)^2 , \tag{4.1}$$

  where K_a is the compressibility modulus of the membrane and has been measured to be $K_a \simeq 0.2$ N/m for typical lipid vesicles (Girard, 2004; Evans and Rawicz, 1990; Olbrich et al., 2000). The extension that a membrane can support is, however, small. Above a relative extension in area of about 8%, there appear pores in the membrane and a fraction of its volume is ejected (Sandre et al., 1999), reducing significantly the membrane tension [1]. The typical membrane tension at which pores are observed is about $\sim 10^{-3}$ N/m (Sandre et al., 1999).
- *Shear*. The shear mode accounts for the energy cost of deforming an element of surface at constant area. This situation corresponds to lipid rearrangements

[1] The concept of membrane tension is defined below.

in the plane of the membrane. Shear deformations are only relevant when the membrane is in phases where the mobility of the lipids is largely reduced (e.g. liquid ordered phase or gel phase (Lipowsky and Sackmann, 1995; Bretscher, 1973)). For vesicles in a liquid disordered phase, the lipids can diffuse in the plane of the membrane with no substantial energy cost compared to stretching or bending. As a consequence, in most cases, the shear energy cost can be neglected for these vesicles.

- *Bending*. The bending mode accounts for the energy cost of deforming the membrane out of the plane. Out-of-plane deformations induce a local rearrangement of the lipids, with the lipids in the inner leaflet closer to each other and those in the outer leaflet further way from each other, with respect to their equilibrium distances. Assuming the membrane to be a two dimensional surface with principal curvatures c_1 and c_2, the energy per unit area, e_b, associated to a bending deformation is (Canham, 1970; Helfrich, 1973)

$$e_b = \frac{\kappa}{2}\left(c_1 + c_2 - c_0\right)^2 + \kappa_G c_1 c_2 \,, \tag{4.2}$$

where κ and κ_G are, respectively, the bending modulus and the Gaussian bending modulus. The curvature c_0 corresponds to the spontaneous curvature of the membrane. Typical values for the bending rigidity of a vesicle are $\kappa \simeq 10 K_B T$ (Evans and Rawicz, 1990; Rawicz et al., 2000; Girard, 2004). Note that this value is of order $K_B T$ and, as a consequence, thermal fluctuations play an important role.

The energy costs described above for the different elementary deformations are related to local deformations. The total energy of the vesicle is the sum of these energy contributions all over the surface. The derivative of the energy with respect to the area defines the membrane tension, σ. With the energy contributions defined above, $\sigma = K_a \Delta A/A$. It is only associated to stretching deformations because these are the only deformations that lead to a change in area. The energy cost to stretch the membrane is much larger than that of bending deformations. As a result, the membrane can be considered as an object of fixed area and no surface tension. Note however than in this description only enthalpic contributions have been considered. A vesicle in solution is strongly affected by thermal fluctuations, which induce fluctuations of the membrane itself (Brochard and Lennon, 1975; Kwok and Evans, 1981; Evans and Rawicz, 1990). Such membrane fluctuations generate an entropic contribution to the membrane tension, which we describe below.

The total energy of a membrane with fixed total area is expressed by its Hamiltonian, $\mathscr{H}$, which reads (Helfrich, 1985)

$$\mathscr{H} = \int dS \left[\frac{\kappa}{2}(2H)^2 + \kappa_G K + \sigma\right] \,, \tag{4.3}$$

where $H \equiv (c_1 + c_2)/2$ and $K \equiv c_1 c_2$ are the mean and Gaussian curvatures respectively, and the surface tension σ is the Lagrange multiplier associated to the constraint of fixed total area. The mean and Gaussian curvatures are given by the trace and determinant of the curvature tensor respectively, and are thus invariant under coordinate transformations (Kamien, 2002; DoCarmo, 1995; Safran, 2003). Typically,

the deformations of a vesicle do not lead to changes in topology. The Gauss-Bonnet Theorem states that the integral of the Gaussian curvature over a closed surface is a topological invariant (DoCarmo, 1995; Kamien, 2002). Therefore, as long as the deformation does not involve a topological change, the term in the Hamiltonian associated to the Gaussian curvature can be omitted as it contributes only with a constant to the total energy.

The presence of thermal fluctuations induces undulations of the membrane, as the thermal energy is comparable to typical values of the bending modulus κ. All deformation modes are excited by the thermal fluctuations and, in equilibrium, each mode carries the same average energy by the Equipartition Theorem. As a consequence of these fluctuations, the membrane becomes rough. The only fluctuations that can be observed by optical microscopy are those with wavelength larger than $\sim$ mum (Fig. 4.6a). Although the total area A of the vesicle is fixed, a fraction of the area is stored in membrane fluctuations. The average position of the fluctuating membrane defines its projected area, A_p (Fig. 4.6c). The total area, A, of the membrane and the projected area are, in general, different. Therefore, there is a fluctuation-induced change in area, $\Delta A = A - A_p$, known as the excess area. Associated to this change in area, there is tension that builds up in the membrane (Evans and Rawicz, 1990; Fournier et al., 2001). In general, the tension, σ_0, of a vesicle with no external force applied on it, does not strictly vanish but is small ($\sigma_0 \sim 10^{-7}\mathrm{N\,m^{-1}}$ (Girard, 2004)). For a vesicle with tension σ_0, the excess area is $\Delta A^0 = A - A_p^0$. When a force is applied to the vesicle, both the enthalpic and entropic contributions to the relative change in area can be important. In this case, the difference between the initial relative excess area $\alpha_0 \equiv \Delta A^0/A_p^0$ (at tension σ_0) and the relative excess area $\alpha = \Delta A/A_p$ of the vesicle at tension σ is given by (Fournier et al., 2001; Evans and Rawicz, 1990; Girard, 2004)

$$\alpha_0 - \alpha \simeq \frac{K_B T}{8\pi\kappa} \ln\left(\frac{1+\frac{A_p^0}{(2\pi)^2}\frac{\sigma}{\kappa}}{1+\frac{A_p^0}{(2\pi)^2}\frac{\sigma_0}{\kappa}}\right) + \frac{\sigma-\sigma_0}{K_a}\,. \tag{4.4}$$

There exist two limiting regimes as the tension of the vesicle is varied (Evans and Rawicz, 1990; Rawicz et al., 2000; Fournier et al., 2001; Girard, 2004). When an increasing force is applied on a vesicle with initial tension σ_0, the progressive unfolding of membrane fluctuations controls the tension increase. For vesicle tensions below $\sigma \simeq 10^{-5}$ N/m, this entropic contribution dominates (entropic regime). Above this value of the tension, almost all the fluctuations have been unfolded and the stretching of the membrane becomes dominant (elastic regime).

Biological membranes

The description of membranes presented above accounts for membranes assembled out of mixtures of lipids only. Biological membranes are however more complex (Alberts et al., 2004). Many different proteins are embedded in the membrane and play an important role in membrane transport. Indeed, transmembrane proteins mediate

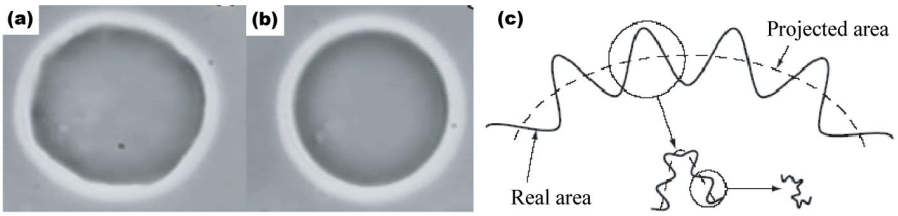

Fig. 4.6. (a-b) Giant Unilamellar vesicle (GUV) observed by phase contrast. (a) The vesicle tension is low (entropic regime) and the membrane undulations caused by thermal fluctuations are visible at micron scale. (b) Vesicle characterized by a large tension. In this case the membrane undulations are not observable at micron scale and the vesicle appears spherical. (c) Schematic representation of a fluctuating membrane at different length scales. The membrane has a real area A (continuous line), and a projected area A_p (dashed line). (Modified from Ref. (Girard, 2004)).

the exchange of small molecules between the organelle and the cytosol and maintain a specific environment inside the organelle. The content of proteins in a biological membrane can be as large as 75%, highlighting the importance of such interaction.

The lipids forming a biological membrane are of many types and heterogeneously distributed (Alberts et al., 2004). Moreover, the two leaflets of the bilayer have different lipid compositions (Devaux and Morris, 2004). In spite of all these important details, a biological membrane can be characterized at larger scales using the effective coarse-grained description above, with probably slightly different values for the bending rigidity and stretching modulus.

The tension of the organelles *in vivo* is regulated by an unknown mechanism. Different mechanisms allowing the control of tension in membrane-bounded organelles have been proposed. The existence of small membrane invaginations, called caveolae, could provide a suitable way of tension control (Sens and Turner, 2006). Upon tension increase, some of the caveolae would be unfolded, increasing the membrane surface and lowering the tension. The dynamic equilibrium between folded and unfolded caveolae would thus fix the organelle tension. Other works focus on the tension control of the plasma membrane and argue that it is achieved by the unfolding of membrane fluctuations that appear in between the connection points of the membrane with the underlying cytoskeleton (Fournier et al., 2004).

5

Membrane tube extraction by molecular motors

As discussed in the last chapter, membrane nanotubes play an important role in intracellular traffic, in particular for lipid and protein exchange between various compartments in eukaryotic cells. Several works have shown the existence of dynamic membrane tube networks in living cells (Cole and Lippincott-Schwartz, 1995; White et al., 1999; Polishchuk et al., 2003). *In vitro* assays using purified organelles and cellular extracts have led to the formation of similar membrane networks and showed that microtubules and molecular motors are necessary for tube formation (Dabora and Sheetz, 1988; Allan and Vale, 1994; Waterman-Storer and Salmon, 1998; Upadhyaya and Sheetz, 2004). As membrane and cytosol compositions are complex, it was not possible to identify the minimal components required to pull tethers until recently. In Ref. (Roux et al., 2002), it was shown that these membrane networks could be formed simply by fixing kinesins on giant liposomes in contact with immobilized microtubules. This minimal system provided a clear evidence that molecular motors were able to pull tubes, in the absence of any other protein. For typical values of membrane bending rigidity and membrane tension, the force necessary to pull a tube is more than 15 pN (Derenyi et al., 2002). However, the maximum force that a kinesin motor can exert (stall force) is about 6 pN (Block et al., 2003), implying that more than a single motor is required to pull tubes. This suggests that the force is distributed over a few motors. In Ref. (Roux et al., 2002), motors were permanently attached to small beads and, typically, between 15 and 30 motors were estimated to be in contact with microtubules and able to pull on the membrane simultaneously. More recently, using a similar minimal system, Koster *et al.* (Koster et al., 2003) succeeded to form tethers when motors were individually attached to membrane lipids. They proposed that clusters of motors could be formed dynamically at the tip of a growing tube. However, these motor clusters had not been observed yet. The experiments that we describe in section 5.1 (see also Ref. (Leduc et al., 2004)), performed by Cécile Leduc in the group of Patricia Bassereau (Institut Curie), showed that motors dynamically accumulate at the tip of growing tubes. From the comparison between the theory in this chapter and these experiments, we determine the binding rate of kinesins onto microtubules in a geometry close to the *in vivo* situation, we

estimate the number of motors needed to pull a membrane tube and we show the existence of a threshold in tube extraction.

The theoretical work in this chapter is divided in three parts. First, we perform a theoretical analysis of the process of tube extraction by molecular motors, where we describe the dynamics of motors on both vesicle and tube surfaces. We analytically determine the conditions leading to tube extraction and show the existence of an initial minimal surface density of motors on the vesicle below which no tubes can be pulled. Moreover, we determine the motor density profile along the tube and discuss the existence of a steady state for tube growth. These theoretical results are then compared at quantitative level to the experimental data. The main results of this part can be found in Ref. (Leduc et al., 2004). In the second part, we study theoretically the extraction of long tubes, for which the variation of vesicle tension upon tube growth is important. We show the existence of highly nonlinear oscillations in the tube length and analytically determine the possible dynamical regimes of the system. These theoretical findings are then compared at qualitative level with the experimental observations. Finally, using numerical simulations, we study the motor cooperation and organization at the tip of growing tubes, and analyze the traffic of motors along the tube.

5.1 *In vitro* biomimetic experiments

In order to understand at quantitative level the process of tube extraction by molecular motors, the group of Patricia Bassereau in Institut Curie designed an *in vitro* system to mimic the tube extraction observed *in vivo*. All the experiments we present in this section have been carried out by Cécile Leduc. Although we describe briefly how the experiments are done, a detailed version of these experiments can be found in the Ph.D. work of C. Leduc (Leduc, 2005).

These experiments are called minimal because only require a vesicle, microtubules, kinesin motors and ATP. Removing any of these components prevents tube formation. It has been previously shown (Koster et al., 2003), and corroborated in these experiments, that the components just mentioned are indeed necessary and sufficient for membrane tube formation. The aim of these experiments is to visualize the kinesin motors during tube extraction in controlled conditions. To do so, kinesin motors must be attached to the lipids in the membrane, their location must be somehow labeled and the relevant physical parameters must be controlled. Moreover, the parameters which cannot be externally tuned, like the intrinsic properties of the motors, must be measured.

The process of attaching and visualizing the motors in the membrane was done as follows. A special lipid, rhodamin-biotin Di-hexadecanoyl-phosphatidylethanolamine (DHPE-Biot-Rhod), with both a biotin function and a fluorophore (Rhodamine) on the head group was synthesized by P. Jolimaitre and L. Bourel-Bonnet (Institut Pasteur, Lille; Ref. (Jolimaitre et al., 2005)). Such lipids were mixed with another type of lipids, mainly Egg phosphatidylcholine (EPC), and vesicles were formed from this lipid mixture. As a result, the vesicles had a certain fraction of DHPE-Biot-Rhod

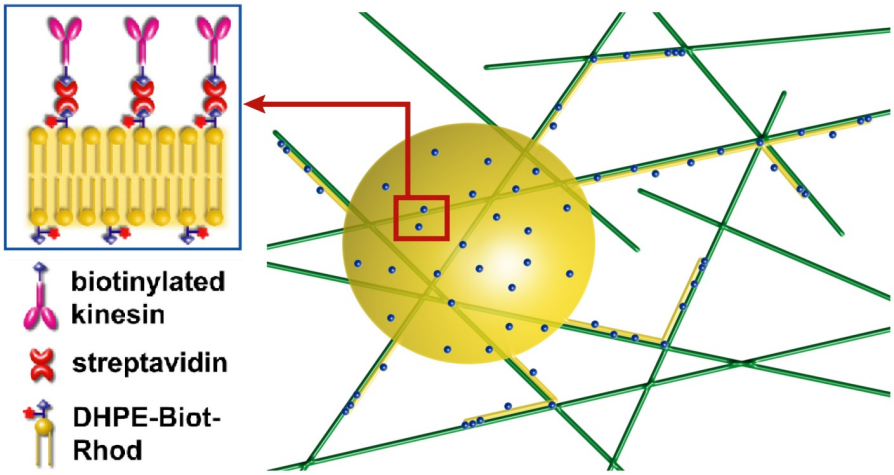

Fig. 5.1. Sketch of the experimental set-up. A giant unilamellar vesicle (yellow), partially covered with motors (blue dots), is placed over a network of microtubules (green) in presence of ATP. The motors bound to microtubules apply forces on the membrane and, under certain conditions, pull membrane tubes (yellow). The box shows the detail of a small portion of the membrane and sketches the binding of a biotinylated kinesin to a rhodamin-labeled biotinylated lipid (DHPE-Biot-Rhod) through a streptavidin molecule (Modified from Ref. (Leduc et al., 2004)). When observed through fluorescence microscopy, the location of the motors is revealed by the fluorophore (rhodamine) attached to the DHPE-Biot-Rhod head.

lipids on the surface that could be observed through fluorescence microscopy. The molecular motors used in the experiments were conventional kinesin motors with a biotin molecule attached to their tail (biotinylated kinesins; Fig. 5.1). Streptavidin was used to attach biotinylated kinesins to DHPE-Biot-Rhod lipids. Biotin molecules attach specifically to the binding sites of streptavidin. Although there exist four binding sites for biotin in a single streptavidin molecule, only two of them are functional, meaning that only two biotin molecules can attach to one streptavidin molecule at the same time. First, streptavidin molecules were attached to the biotin molecules in the kinesins tail. Then, these streptavidin-kinesin complexes were put in contact with vesicles containing a fraction of DHPE-Biot-Rhod lipids, and the streptavindin-kinesin complexes attached to the biotin molecules in a DHPE-Biot-Rhod lipids (box in Fig. 5.1). With this protocol, it is possible to obtain vesicles partially covered with kinesin motors and their location can be observed through fluorescence microscopy. We now explain how the experiments are done and how the density of motors in the vesicle can be controlled.

The minimal system consisted of a partly biotinylated Giant Unilamellar Vesicle (GUV), coated with biotinylated kinesins through streptavidin molecules (Fig. 5.1). The vesicle played the role of a membrane reservoir. This vesicle sedimented onto

a taxol-stabilized [1] microtubule network in presence of 1 mM ATP (Fig. 5.2). The ATP concentration was chosen in such a way that the motor velocity was close to maximum, while motors stayed sufficiently attached to microtubules (Block et al., 2003). In this assay, the number of kinesins was directly controlled by fixing the biotinylated lipid (DHPE-Biot-Rhod) concentration in the membrane. The protocol was set up so that one kinesin molecule binds to one biotinylated lipid. First, kinesin and streptavidin concentrations were adjusted such as at most one kinesin binds to one streptavidin, due to the large excess of streptavidin compared to kinesin (step 1 in Fig. 5.2). Then, by immobilizing streptavidin-kinesin complexes on the microtubules before vesicle injection (step 2 in Fig. 5.2), it was possible to thoroughly rinse the chamber and get rid of free streptavidins and non-active motors in solution (step 3 in Fig. 5.2). As the total number of biotinylated lipids in the vesicle was much lower than the number of available streptavidin-kinesin complexes (by at least one order of magnitude), every binding site for motors was occupied due to the high affinity of streptavidin for biotin (step 4 in Fig. 5.2), and the streptavidin-kinesin complexes not attached to DHPE-Biot-Rhod lipids remained in solution. The site saturation was achieved faster than the time required to pull the first tube ($\sim$ 1 minute). The number of motors attached to the membrane is therefore equal to the number of biotinylated lipids. Moreover, for concentrations above 0.01 mol% DHPE-Biot-Rhod, it was also checked that the number of streptavidin molecules per biotinylated lipids remains constant when varying the DHPE-Biot-Rhod concentration (Leduc et al., 2004). Besides, it was also verified that the quantity of streptavidin-kinesin complexes attached to the lipids through non-specific interactions can be neglected for concentrations of DHPE-Biot-Rhod above 0.001 mol%.

The measurement of fluorescence intensity of DHPE-Biot-Rhod along the tube gives the motor distribution as the experimental protocol was adjusted to have one motor per DHPE-Biot-Rhod. With this protocol, it is then possible to simultaneously visualize the motor distribution and control the concentration of motors on the vesicle.

Various parameters can be tuned in this assay. The initial concentration of motors on the vesicle surface, called ρ_∞ in the theoretical description below (section 5.3), can be modified by changing the concentration of biotinylated lipids (DHPE-Biot-Rhod) in the vesicle. Variations in the vesicle tension, σ, lead to changes in the necessary force to pull a tube (see section 5.2). It is thus an important parameter which should also be controlled. Indeed, the vesicle tension can be adjusted by changing the osmolarity of the solution inside the vesicle. Optimizing these parameters, it was possible to obtain either very dense networks of membrane tubes with many bifurcations and bundles as in Ref. (Koster et al., 2003) (Fig.5.3a), or sparse ones with only one or two tubes per vesicle (Fig.5.3b). The last case corresponds to high vesicle tensions and low motor concentrations, and is more suitable for a proper comparison to the theory.

[1] Taxol is a molecule that stabilizes microtubules by preventing its depolymerization (Schiff and Horwitz, 1980).

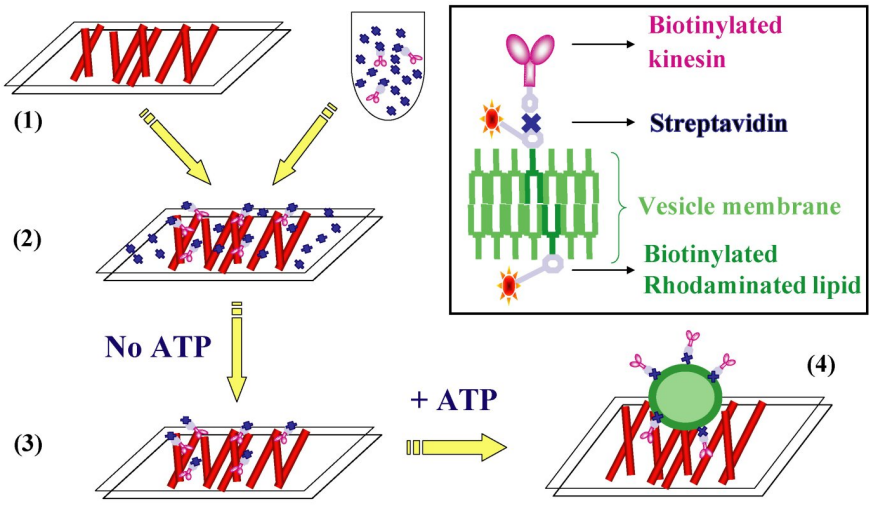

Fig. 5.2. Experimental protocol to prepare the vesicles partially covered by motors that allow the formation of membrane tubes. (Step 1) Taxol-stabilized microtubules (red) are placed on the lower surface of the observation chamber, and biotinylated kinesins (kinesin and biotin are shown in purple and gray respectively) are incubated with a large excess of streptavidin (dark blue). (Step 2) The streptavidin-kinesin complexes are fluxed into the observation chamber. Kinesin motors attach to microtubules and stay attached due to the absence of ATP in the chamber. (Step 3) The chamber is rinsed to get rid of free streptavidin and unattached motors in solution. (Step 4) The chamber is rinsed with ATP and the vesicles (green) are fluxed into the chamber. In presence of ATP, the motors detach from the microtubules, diffuse in the solution and attach to the DHPE-Biot-Rhod lipids (dark green) in the vesicle through the streptavidin molecule. The box show a detail of the streptavidin-mediated motor-DHPE-Biot-Rhod attachment. (Figure by C. Leduc).

5.2 Physics of membrane tube extraction

Before addressing the problem of membrane tube extraction by molecular motors, we briefly describe the physics of tube extraction itself.

5.2.1 Tube extraction from an infinite membrane reservoir

When a force is applied on a vesicle, it responds by changing its shape. Under certain conditions it is energetically more favorable to pull a membrane tube, rather than inducing an overall deformation of the membrane. Several works have studied experimentally and theoretically the physics of membrane tubes. Tubes can be extracted from vesicles by a shear flow (Rossier et al., 2003; Borghi et al., 2003), or applying localized forces on the membrane, for instance, with optical tweezers (Koster et al., 2003; Koster et al., 2005; Cuvelier et al., 2005b; Cuvelier et al., 2005a). At the theoretical level, several groups have studied their properties (Derenyi et al., 2002; Powers et al., 2002; Rossier et al., 2003). We briefly describe here part of the work

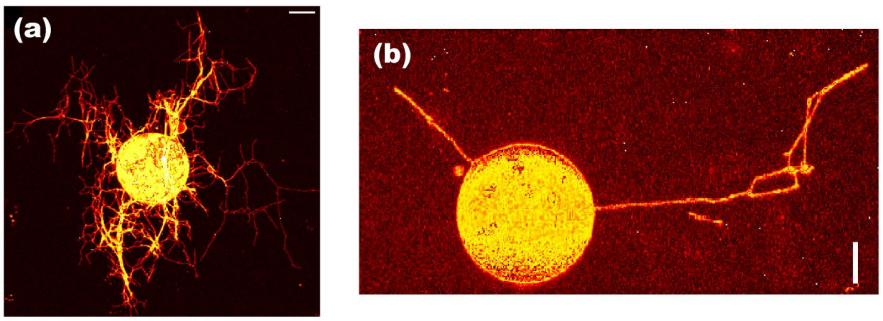

Fig. 5.3. Confocal images of membrane tubes pulled by kinesin motors from GUV in different conditions. The images are two-dimensional projections of the three-dimensional confocal reconstruction. The membrane was uniformly labeled with fluorescent lipids (DHPE-TRITC), and the biotinylated lipids to which motors are attached were not specifically labeled. The images are shown in false color to enhance the contrast. (a) Dense tube network pulled from a vesicle with an initially low membrane tension ($\sigma \sim 10^{-6}$ N/m). Bar, 10 μm. (b) Membrane tubes pulled from an initially tensed vesicle ($\sigma \sim 2\,10^{-4}$ N/m). Bar, 5 μm. (Modified from Ref. (Leduc, 2005)).

in Ref. (Derenyi et al., 2002) which studies the formation of membrane tubes by a localized forced.

We are interested in the case where both the pressure, p, and tension, σ, of the vesicle are fixed. In such conditions, the free energy, $\mathscr{F}$, of a membrane with a point-like force F applied on it reads

$$\mathscr{F} = \int dS \frac{\kappa}{2} (2H)^2 + \sigma A - pV - FL \,, \tag{5.1}$$

where κ is the bending rigidity, H the mean curvature, A the total area and V the vesicle volume. If the membrane is placed in the $\{x,y\}$ plane and the force is applied in the z direction, the distance between the plane and the point of application of the force is L (Fig. 5.4a). For a membrane tube of radius r and length L the free energy at vanishing pressure reads

$$\mathscr{F}_{tube} = \left(\frac{\kappa}{2r^2} + \sigma \right) 2\pi r L - FL \,. \tag{5.2}$$

The bending rigidity opposes the reduction of the tube radius, whereas the surface tension promotes such a reduction. This competition between the bending and surface tension terms, sets the equilibrium tube radius, r_0 and the force F_0 of the tube. Minimizing the free energy of the tube with respect to its radius and length, one obtains

$$r_0 = \sqrt{\kappa/2\sigma}, \qquad F_0 = 2\pi\sqrt{2\kappa\sigma} \,. \tag{5.3}$$

For the typical values of the membrane rigidity ($\kappa \simeq 10 K_B T$) and surface tension ($\sigma \simeq 5\,10^{-5}$ N/m), the radius of the tube is about $r_0 \simeq 20$ nm and the tube force $F_0 \simeq 12.6$ pN.

For forces below the tube force ($F < F_0$), the membrane deforms and adopts a catenoid shape (Fig. 5.4a), which results from the minimization of the membrane free energy (Eq. 5.1). In this regime, the force F increases linearly with the magnitude of the deformation L (Fig. 5.4b). As the force is increased further, the system eventually reaches a critical point at which a membrane tube is extracted (Fig. 5.4a). The value of the force at which the tube appears is above the force F_0 and, as the tube is pulled further, the tube force converges to F_0. The force-length relation is thus non-monotonic, with a force overshoot of $0.13F_0$ at the point where the tube is extracted (Fig. 5.4b). This relation has been indeed observed experimentally (Koster et al., 2003). Moreover, the magnitude of the overshoot has been shown to depend strongly on the size of the patch used to apply the force on the membrane (Koster et al., 2005). Once the tube is formed, the necessary force to keep pulling it is F_0, no matter how long the tube is pulled. This behavior, in which the force does not increase with the length of the tube, holds only for infinite membrane reservoirs because the tension remains constant upon tube extraction. We derive in the next section the relation between the tube force F_0 and its length for a finite vesicle.

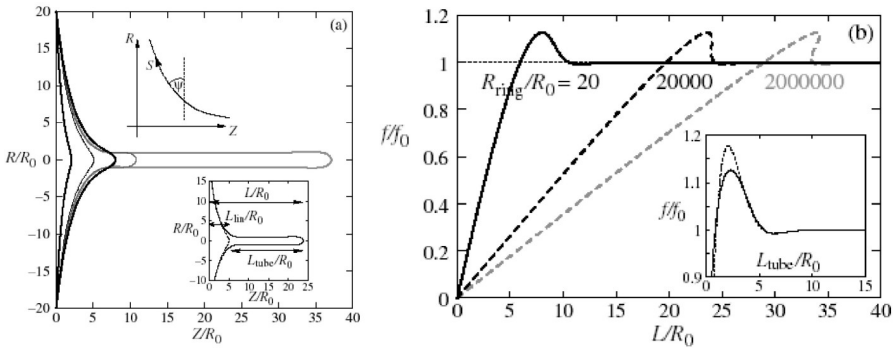

Fig. 5.4. (a) Membrane deformation and formation of a membrane tube induced by the application of a point-like force on the membrane. Notation is different than in the main text ($R_0 = r_0$ and $f_0 = F_0$). The inset depicts the definition of the tube length L. (b) Tube force as a function of the tube length, showing the existence of a force overshoot associated to tube formation. Once the tube is extracted, the tube force is constant and given by F_0. (Modified from Ref. (Derenyi et al., 2002)).

5.2.2 Tube extraction from a vesicle

It is clear that a membrane tube cannot be pulled as long as desired from a vesicle because the amount of membrane is finite. We derive here the relation between the force needed to pull the tube, F, and the length, L, of the tube at equilibrium. Our aim is not to describe the formation of the tube, but only to understand the variation of the tube force with its length once it has been formed.

When a tube is pulled out of a vesicle, the amount of membrane needed to form the tube is taken from the excess area of the vesicle. As the tube is extracted, the initial excess area stored in the vesicle progressively diminishes and the tension increases accordingly. Such an increase in membrane tension leads to an increase of the tube force for increasing tube length. The relative excess area, $\Delta A/A_i$, taken from a vesicle of initial radius R_i (and initial projected area A_i) to create a tube of length L and radius r is

$$\frac{\Delta A}{A_i} = \frac{rL}{2R_i^2} \,. \tag{5.4}$$

For low vesicle tensions, the additional area comes from the unfolding of membrane fluctuations (entropic regime) and the vesicle tension, σ, depends exponentially on the relative excess area. For tensed vesicles the microscopic stretching of the membrane dominates (elastic regime) and the vesicle tension scales linearly with the excess area (Fournier et al., 2001; Girard, 2004). As discussed above, at equilibrium, for a given membrane tension σ and bending rigidity κ, the force needed to pull a tube is $F = 2\pi\sqrt{2\kappa\sigma}$, and its radius $r = \sqrt{\kappa/2\sigma}$. In the case of a vesicle in the entropic regime, this argument leads to the following relation between the tube force $F(L)$ and the length L of the tube

$$\frac{L}{L_c^{ent}} = 2\frac{F}{F_0}\ln\left(\frac{F}{F_0}\right) \,, \tag{5.5}$$

where $F_0 = 2\pi\sqrt{2\kappa\sigma_0}$ is the initial tube force (with σ_0 being the initial vesicle tension). The characteristic length scale at which the increase of force becomes noticeable, L_c^{ent}, reads

$$L_c^{ent} = \frac{K_B T}{4\pi\kappa}\frac{R_i^2}{r_0} \,, \tag{5.6}$$

where $r_0 = \sqrt{\kappa/2\sigma_0}$ is the tube radius for the initial vesicle tension σ_0. For typical vesicles ($R_i \sim 10\,\mu$m and $F_0 \sim 10$ pN) the force increase is appreciable for tube lengths greater than about 30 μm. In case several tubes are pulled from the same vesicle (tube network, Fig. 5.3a), the relevant length is the sum of all tube lengths and the increase of tension may become important very quickly.

If the vesicle is already initially tensed ($\sigma_0 \simeq 10^{-4}$ N/m), the stretching of the membrane dominates the tension increase. In this case, the dependence of the tube force F on the tube length is given implicitly by

$$\frac{L}{L_c^{el}} = \frac{F}{F_0}\left[\left(\frac{F}{F_0}\right)^2 - 1\right] \,, \tag{5.7}$$

In this case, the characteristic length of force increase, L_c^{el}, for a vesicle in an elastic regime is given by

$$L_c^{el} = R_i\frac{R_i F_0^3}{8\pi^3\kappa^2 K_a} \,, \tag{5.8}$$

where K_a is the compressibility modulus of the membrane, which has been measured to be $K_a \simeq 0.2$ N/m for a typical membrane (Evans and Rawicz, 1990; Olbrich et al.,

2000). For a typical vesicle in the elastic regime ($R_i \sim 10\,\mu$m and $\sigma_0 \simeq 10^{-4}$ N/m) the length L_c^{el} at which the force increase becomes noticeable is about 20 μm. Both entropic and elastic behaviors have been observed experimentally by pulling long tubes from an adhered vesicle using optical tweezers (Cuvelier et al., 2005a).

When a long membrane tube ($L > L_c^{ent}$ or $L > L_c^{el}$) is pulled from a vesicle, the membrane taken from the vesicle to form the tube leads to an increase of the necessary force to pull the tube. Therefore, for long enough tubes, the tube can be seen as a nonlinear spring acting on the motors that pull collectively at the tip.

5.3 Theoretical description

In this section, we theoretically describe the mechanism by which molecular motors cooperatively pull membrane tubes from vesicles. The analysis is done in two parts. First, we consider short tubes ($L < L_c$), for which the force increase during tube extraction is negligible, and study both the conditions leading to tube extraction and the tube growth. The results of this part are quantitatively compared to the experimental data in the discussion. Separately, we study the growth dynamics of long tubes ($L > L_c$), for which the increase in the tube force is important.

5.3.1 Short tubes

We only consider in this section tubes of length below $L_c \simeq 20\,\mu$m. The increase in tube force upon tube growth is thus negligible and the tube force is constant and given by $F_0 = 2\pi\sqrt{2\kappa\sigma}$.

In order to describe theoretically the tube extraction by molecular motors, we divide the system in the three regions sketched in Fig. 5.5b, namely, the vesicle, the tube and the tip of the tube. This division appears to be the most natural one, as suggested by the experimental observations (Fig. 5.5a). The motors located at the tip of the tube are the only motors able to exert significant forces on the membrane, as it is only at the tip that the motors can exert normal forces to the membrane. A motor moving on the microtubule in the tube region is subject to the drag force that arises from the motion of the lipid to which it is attached in the fluid membrane. This force is of hydrodynamic origin and of order $\sim (K_B T/D)V_0$ during tube growth, where D is the diffusion coefficient of the motor-lipid complex in the membrane and V_0 the velocity of the motor at vanishing force. Using the values measured in the experiments (see discussion below), this drag force is below 10^{-3} pN and thus negligible as far as motor movement is concerned. Therefore, for short tubes, the forces transmitted to the tube by the motors moving along the tube do not exceed a few percent of the force needed to extract a tube. A finite force is thus applied to each motor in the tip region. As the motor velocity decreases with applied load (see chapter 1), these motors move more slowly than the motors moving along the tube, resulting in an accumulation of motors at the tip (Fig. 5.5c). Moreover, those motors working to pull the tube detach from the microtubule faster than the motors along the tube. The loss of working motors is compensated, under certain conditions, by the

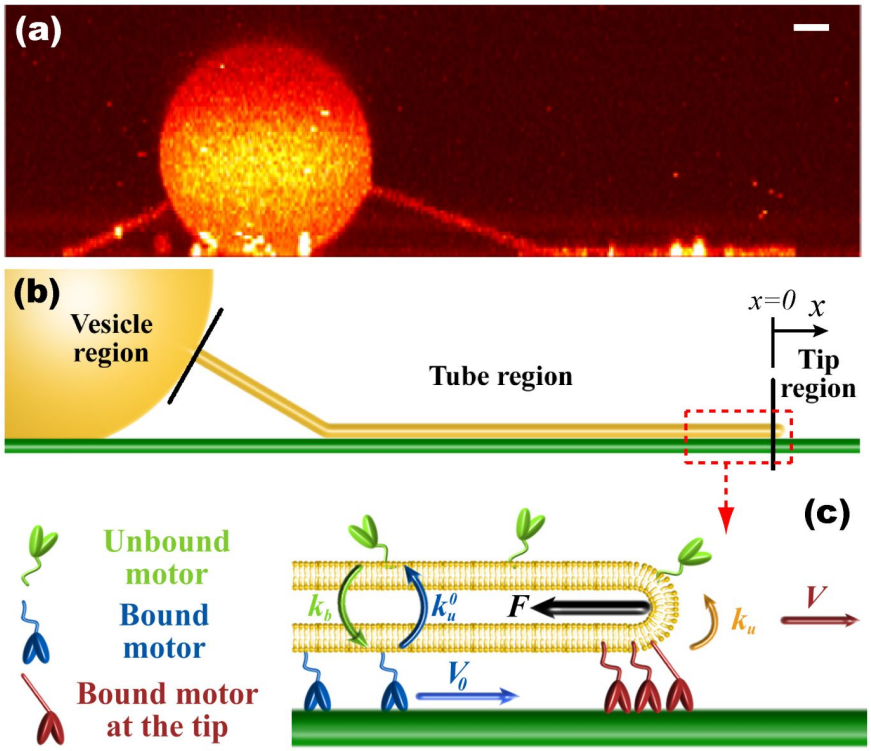

Fig. 5.5. (a) Confocal side-view image of a membrane tube representing the typical geometry of the system and suggesting the natural regions dividing it. The membrane is uniformly labeled. Bar, $2\,\mu m$. (Image by C. Leduc). (b) Schematic representation of the different regions considered in the theoretical description: vesicle, tube, tip. The membrane is shown in yellow and the microtubule in dark green. (c) Sketch of the tube-tip boundary and tip region representing the accumulation process at the tip. The bound motors at the tip (red) move against the tube force F with velocity V and detach from the microtubule (dark green) at a rate k_u. The tube grows with average velocity V due to the motion of the motors at the tip. The bound motors along the tube (blue) do not support any substantial force, move with velocity V_0 (motor velocity under vanishing load) and detach from the microtubule at a rate k_u^0. The motors not bound to the microtubule (unbound motors; light green) attach to the microtubule at a rate k_b. These unbound motors diffuse along the tube and are dragged by the tube itself as it grows.

incoming flux of motors from the tube. At the same time, the tube is constantly fed by motors coming from the vesicle. In what follows, we mathematically describe the coupled dynamics of the different regions and determine self-consistently the tube motion.

Tip region

We define the tip as the front part of the tube where motors apply forces. Bound motors are those attached to the tube and to the microtubule, whereas unbound motors

are only attached to the tube (Fig. 5.5c). The dynamics of motors at the tip is given by the conservation equations for the numbers of bound and unbound motors, n_b and n_u respectively, and read

$$\begin{aligned} \frac{dn_b}{dt} &= \hat{J}_b(x=0,t) - k_u(n_b)n_b \ , \\ \frac{dn_u}{dt} &= \hat{J}_u(x=0,t) + k_u(n_b)n_b \ , \end{aligned} \tag{5.9}$$

where $\hat{J}_b$ and $\hat{J}_u$ are, respectively, the flux of bound and unbound motors reaching the tip from the tube region (expressed in the tube reference frame), and $k_u(n_b)$ is the unbinding rate of bound motors. The tube is along the x-axis (oriented along the direction of the tube motion); the origin $x = 0$ is at the position of the tip. Note that we have neglected the motor binding events at the tip. This is because the time required for a motor to leave the tip region by diffusion is much smaller than the binding time. With the values measured experimentally, the ratio of these two times is smaller than 10^{-3}. The total force, F_0, that the motors exert is the critical force necessary to pull a tube from a membrane, $F_0 = 2\pi\sqrt{2\sigma\kappa}$ (see section 5.2), where σ is the membrane tension and κ the membrane bending rigidity. The unbinding rate of the bound motors from the microtubule, k_u, depends on the force applied to each bound motor, f_m, which is assumed, for the sake of simplicity, to be equally distributed between all motors in the tip, so that $f_m = F_0/n_b$. Kramers rate theory (van Kampen, 2004; Kramers, 1940) leads to

$$k_u(n_b) = k_u^0 \exp\left(\frac{F_0 a}{K_B T}\frac{1}{n_b}\right) \ , \tag{5.10}$$

where k_u^0 is the unbinding rate at vanishing force and a is a length in the nanometer range characterizing the potential barrier between bound and unbound states. As a first approximation, we assume that the velocity, V, of a bound motor is a linearly decreasing function of the applied force and write $V = V_0(1 - f_m/f_s)$, where f_s is the stall force of the motor and V_0 is the motor velocity at vanishing load. As the membrane tube is pulled by bound motors, in a mean field description its growth velocity is the velocity V of the motors pulling the tube at the tip.

Tube region

We describe the dynamics along the tube by two populations of motors, namely bound and unbound motors, which are characterized by their linear densities ρ_b and ρ_u. As argued above, the bound motors along the tube do not feel any substantial force. Consequently, bound motors move in this region at constant velocity V_0 and detach stochastically from the microtubule at a rate k_u^0 (Fig. 5.5c). The motion of unbound motors is restricted to the tube surface and has both diffusive and convective components in the laboratory reference frame. The convective feature stems from the membrane flow resulting from the tube growth. It corresponds almost to pure convection at the velocity V, since the buffer viscosity is two orders of magnitude

smaller than that of the membrane. The diffusive motion is due to the diffusion of the lipid to which the motor is attached in the membrane, and it is characterized by a diffusion coefficient D. Moreover, unbound motors also bind stochastically to the microtubule at a rate k_b. The mean-field dynamic equations for bound and unbound motors can be written as

$$\begin{aligned}\frac{\partial \rho_b(x,t)}{\partial t}+\frac{\partial J_b(x,t)}{\partial x} &= -k_u^0\rho_b(x,t)+k_b\rho_u(x,t)\ ,\\ \frac{\partial \rho_u(x,t)}{\partial t}+\frac{\partial J_u(x,t)}{\partial x} &= -k_b\rho_u(x,t)+k_u^0\rho_b(x,t)\ .\end{aligned} \tag{5.11}$$

In the laboratory reference frame, the fluxes of bound and unbound motors , $J_b(x,t)$ and $J_u(x,t)$ respectively, read

$$\begin{aligned}J_b(x,t) &= V_0\rho_b(x,t)\ ,\\ J_u(x,t) &= V\rho_u(x,t)-D\partial_x\rho_u(x,t)\ .\end{aligned} \tag{5.12}$$

We ignore here the variations of the motor velocity with the density of motors. At very high density of bound motors this approximation breaks down and, for instance, the motion of one motor could be hindered by the preceding motors, leading to the formation of traffic jams (Parmeggiani et al., 2003; Lipowsky et al., 2001). As we shall explain below, the experimental data support this low density assumption.

Vesicle region

Before the tube is extracted, the motors on the vesicle are characterized by an initial surface density ρ_∞, which evolves to a space-time dependent value ρ_m as the tube is progressively pulled. If a tube of radius r and length L is pulled from a vesicle with initial radius R_i, the radius, R, of the vesicle is given, from volume conservation arguments, by

$$\frac{R}{R_i}=\left(1-\frac{3}{4}\frac{r^2L}{R_i^3}\right)^{1/3}\ . \tag{5.13}$$

Using typical experimental values for $r\sim 20$ nm, $R_i\sim 10\ \mu$m and $L\sim 10\mu$m, the variation of the vesicle radius is negligible. We thus consider the radius of the vesicle to be constant in what follows.

We are interested in the time evolution of the motor density field, ρ_m, on the surface of the vesicle, because it controls the flux of motors entering the tube. As the radius of the vesicle is about 10^3 times larger than the typical radius of the tube, we consider the vesicle to be a sphere of constant radius R with a point-like sink of motors at the pole specified by $\theta=0$ (in spherical coordinates; Fig. 5.6). The motors on the surface of the vesicle diffuse with a diffusion coefficient D. In addition, when a tube is pulled from a vesicle, there is also a convective flux of lipids being extracted from the vesicle, which leads to a convective motion of the motors on the vesicle surface. We now show that this convective flux is negligible compared to diffusion for all practical purposes.

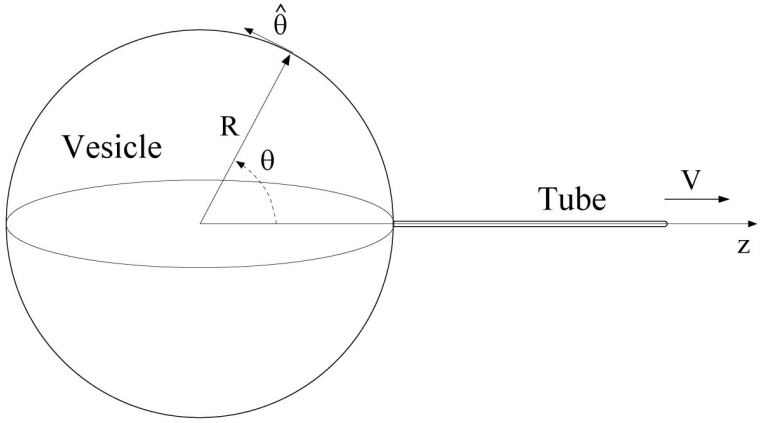

Fig. 5.6. Geometry of a vesicle with a membrane tube being extracted at $\theta = 0$ in the z direction with velocity V. The symmetry of the problem ensures that the membrane velocity field is in the $\tilde{\theta}$ direction and that both the membrane velocity and the surface motor density depend only on the spatial coordinate θ.

To this end, we calculate the membrane surface velocity field, $\mathbf{v} = v_\theta \hat{\theta}$ [2], when a point-like sink of membrane is situated at the pole specified by $\theta = 0$ (Fig. 5.6). Assuming the density of lipids in the membrane to be homogeneous, the membrane velocity field $\mathbf{v}$ is given by

$$v_\theta(\theta) = -\frac{V}{2}\frac{r}{R}\frac{1+\cos\theta}{\sin\theta}\ , \tag{5.14}$$

where V is the velocity at which the tube is extracted. Note that there is a cut-off angle associated to the finite radius of the tube which prevents the divergence of the velocity field. The velocity of the lipids is of order Vr/R everywhere on the vesicle surface, except in a very close neighborhood of the tube, where is of order V due to flux continuity conditions.

The dynamics of the surface motor density field is given, at mean-field level, by

$$\frac{\partial \rho_m}{\partial t} + \mathbf{v}\cdot\nabla\rho_m - D\nabla^2\rho_m = 0\ . \tag{5.15}$$

There is a single dimensionless parameter, namely Vr/D, that quantifies the importance of the convective flux compared to the diffusive one. For the typical values measured experimentally, $Vr/D \sim 10^{-2}$ ($V \sim 0.1\ \mu\mathrm{m\,s^{-1}}$, $D \simeq 1\ \mu\mathrm{m^2\,s^{-1}}$ and $r \simeq 20$ nm; see discussion below). The convective flux can thus be neglected everywhere on the surface except in the close neighborhood of the tube. The motor density field can be thus calculated considering only a diffusive flux on the surface, and accounting for the convective flux with a sink of motors at the position where the tube is located ($\theta = 0$; Fig. 5.6). In these conditions, the motor density field is given by

[2] Due to the symmetry of the problem, the velocity only has a component in the direction $\hat{\theta}$.

$$\left(\partial_t - D\nabla^2\right)\rho_m = -J(t)\delta(\mathbf{x})\,, \tag{5.16}$$

where $J(t)$ is the flux of motors entering the tube.

The time scale to propagate all over the vesicle the effect of motor depletion induced by the tube growth is $R^2/D \sim 10^2$ s. The growth of a tube of about 10 μm in length at a typical velocity $V \simeq 0.1$ μm/s, takes about 10^2 s. Therefore, during the initial stages of tube extraction ($L \lesssim 10\,\mu$m), the depletion of motors has not reached the other side of the vesicle ($\theta = \pi$) and Eq. 5.16 can be solved in the flat space within a good approximation.

With these assumptions, the motor density field can be solved in the two-dimensional space using polar coordinates, with s being the radial distance from the center, where the motor depletion takes place. The motor flux, $J(t)$, at the origin is fixed by the flux of motors taken by the growing tube and the solution for the motor density field reads

$$\rho_m(s,t) = \rho_\infty - \int_0^t dt'\, J(t')\frac{\exp\left(-\frac{s^2}{4D(t-t')}\right)}{4\pi D(t-t')}\,. \tag{5.17}$$

In case the motor flux J is constant, the latter expression reduces to

$$\rho_m(s,t) = \rho_\infty + \frac{J}{4\pi D}\mathrm{Ei}\left(-\frac{r^2}{4Dt}\right)\,, \tag{5.18}$$

where $\mathrm{Ei}(z)$ is the exponential integral function (Gradshteyn and Ryzhik, 2000).

In spite of this detailed description of the depletion of motors on the vesicle surface, we shall show below that in the conditions of the experiments described in section 5.1 the motor depletion is negligible.

Quasi-steady state approximation

The equations given above for the dynamics of the motors in the tip region, along the tube and on the vesicle surface are coupled. In order to fully specify the solutions of Eq. 5.9 for the dynamics of the motors at the tip, it is necessary to know the flux of motors reaching the tip region. The flux is given by the solutions of Eq. 5.11 which depend on the surface motor density field on the vesicle, as it specifies the flux of motors entering the tube. The system of equations must be then solved self-consistently. This is done by assuming that there exists a quasi-steady state, with a constant tube velocity V (or very slowly varying on time), and solving the equations in this limit. Note that, in general, there is no steady-state for the system because there is always a net flux of motors entering the tube. However, we show below that a quasi-steady state indeed exists.

As the tube velocity is considered to be constant in the quasi-steady state approximation, Eq. 5.11 can be expressed in the tube reference frame. The fluxes of bound and unbound motors in this reference frame are $\hat{J}_b = (V_0 - V)\rho_b(x,t)$ and $\hat{J}_u = -D\partial_x\rho_u(x,t)$ respectively, where x is the position along the tube (oriented along

the direction of the tube motion) and the origin $x = 0$ is at the position of the tip. We apply the Laplace transform on time to Eq. 5.11 and write the solutions for the density fields, $\bar{\rho}_b(x,s)$ and $\bar{\rho}_u(x,s)$, in the Laplace space as

$$\begin{aligned}\bar{\rho}_b(x,s) &= \frac{\rho_b^\infty}{s} + B(s)\exp(qx) \ , \\ \bar{\rho}_u(x,s) &= \frac{\rho_u^\infty}{s} + U(s)\exp(qx) \ ,\end{aligned} \tag{5.19}$$

where ρ_b^∞ and ρ_u^∞ represent solutions of constant density of bound and unbound motors respectively, and s is the conjugate variable for the time in the Laplace space. All eigenfunctions must obey Eq. 5.11 independently. The substitution of the exponential eigenfunctions (exponential terms in Eq. 5.19) into Eq. 5.11 give rise to an algebraic equation for $B(s)$ and $U(s)$. Imposing non-zero solutions leads to the characteristic equation, which reads

$$-\lambda_1\lambda_2^2 q^3 - \left(1+\frac{s}{k_u^0}\right)\lambda_2^2 q^2 + \left(1+\frac{s}{k_b}\right)\lambda_1 q + \frac{s}{k_b}\frac{s+k_b+k_u^0}{k_u^0} = 0 \ , \tag{5.20}$$

where $\lambda_1 \equiv (V_0 - V)/k_u^0$ is the average length that a bound motor travels along the microtubule before detaching and, $\lambda_2 \equiv \sqrt{D/k_b}$ is the average distance that an unbound motor travels along the tube before re-attaching back to the microtubule. The characteristic equation sets two limiting time regimes. For times t smaller than $\left(k_u^0 + k_b\right)^{-1}$ ($s \gg k_u^0 + k_b$) the solution of the characteristic equation is $q = \sqrt{s/D}$ [3]. On the other hand, for $t \gg \max[(k_u^0)^{-1}, k_b^{-1}]$, the solution of the characteristic equation is [4]

$$q = \frac{1}{2\lambda_1}\left[\sqrt{1+\left(2\frac{\lambda_1}{\lambda_2}\right)^2} - 1\right] \ . \tag{5.21}$$

Note that there exist two different regimes, depending on whether $\lambda_1/\lambda_2 \gg 1$ or $\lambda_1/\lambda_2 \ll 1$. We will discuss the characteristics of these two regimes below, when describing the density field along the tube.

As the solutions must obey Eq. 5.11, the functions $B(s)$ and $U(s)$ and the constants ρ_b^∞ and ρ_u^∞ are not independent from each other. The relations between them are

$$\begin{aligned}&k_u^0 \rho_b^\infty = k_b \rho_u^\infty \ , \\ &B(s)\left(s + q\left(V_0 - V\right)\right) = \left(Dq^2 - s\right)U(s) \ .\end{aligned} \tag{5.22}$$

The relation between ρ_b^∞ and ρ_u^∞ corresponds to the equilibrium condition between the constant values of the density field (detailed balance). Note that the relation between $B(s)$ and $U(s)$ depends on time. The limiting expressions for this relation at

[3] There are actually two solutions, $\pm\sqrt{s/D}$, but the physically relevant solution is $\sqrt{s/D}$.

[4] Again, the are two solutions, but we only write the solution that corresponds to non-diverging density profiles away from the tip.

short time scales ($t < \left(k_u^0 + k_b\right)^{-1}$) and long time scales ($t > \max[(k_u^0)^{-1}, k_b^{-1}]$) can also be found using the limiting solutions for q.

The quasi-stationary solutions of Eq.5.11 for the motor density profiles $\{\rho_b, \rho_u\}$ along the tube are thus exponentially decaying functions of the distance from the tip with a characteristic length scale $\lambda \equiv q^{-1}$. The decay length λ is much larger than the typical size of the tip region which is in the nanometer range and cannot be resolved in the experiments. The value of λ is independent of the particular definition of the tip and is fixed by the dynamics of motors along the tube.

Although all the analysis must be done in the Laplace space, in what follows we express the solutions using the time variable for simplicity.

Conditions for tube extraction

During the initial stages of tube extraction ($t < \left(k_u^0 + k_b\right)^{-1} \sim 10^{-1}s$), the tube length Vt is always smaller than the characteristic length λ, which is given in this regime by the diffusion length $\lambda = \sqrt{Dt}$, and the density profiles can be considered as linear. In the quasi-steady state approximation, both the average number of bound and unbound motors, n_b and n_u respectively, are approximately constant in time, so that $dn_b/dt \simeq 0$ and $dn_u/dt \simeq 0$. Consequently, the average tube velocity V is constant. Note that these conditions specify the boundary conditions for the density fields at the boundary between the tube and the tip regions. Specifically, using Eq. 5.9 and the conditions just mentioned the following relations are obtained

$$\begin{aligned} &\hat{J}_b(x=0) + \hat{J}_u(x=0) = 0 \,, \\ &\hat{J}_b(x=0) = k_u(n_b) n_b \,. \end{aligned} \tag{5.23}$$

The first equation indicates that the flux of bound motors entering the tip must equal the flux of unbound motors leaving it, so that the total flux in the tube-tip boundary vanishes (Fig. 5.7). The second equation states that the flux of motors entering the tip must balance the detachment flux of motors at the tip. In case the detachment motor flux at the tip were larger than the rate at which motors are fed into the tip region, there would be an eventual loss of all motors sustaining the tube and the tube would retract back to the vesicle.

On the other hand, the boundary conditions at the vesicle-tube boundary are the continuity of both motor density and flux, which are given respectively by

$$\begin{aligned} &2\pi r_0 \rho_m(r_0,t) = \rho_b(x=-Vt,t) + \rho_u(x=-Vt,t) \,, \\ &2\pi r_0 \left(V\rho_m(r_0,t) + D\partial_s \rho_m(r_0,t)\right) = \\ &\qquad V\rho_u(x=-Vt,t) + V_0 \rho_b(x=-Vt,t) - D\partial_x \rho_u(x=-Vt,t) \,. \end{aligned} \tag{5.24}$$

With these conditions, the bound and unbound motor density fields, ρ_b and ρ_u respectively, read

$$\begin{aligned} \rho_b &= 2\pi r_0 \rho_\infty \frac{k_b}{k_u^0 + k_b} \,, \\ \rho_u(x,t) &= 2\pi r_0 \rho_\infty \frac{k_b}{k_u^0 + k_b} \left[\frac{k_u^0}{k_b} + \frac{(V_0 - V)}{D}(x + Vt)\right] \,. \end{aligned} \tag{5.25}$$

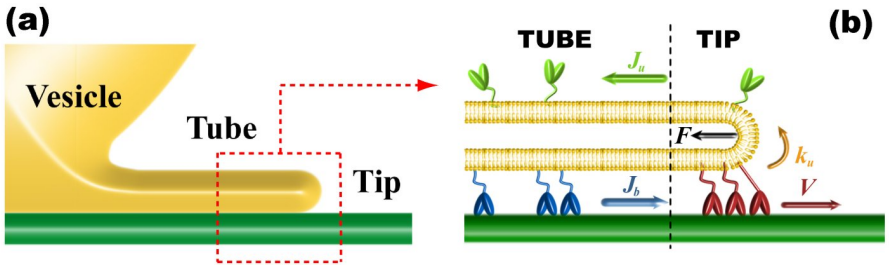

Fig. 5.7. (a) Sketch of the tube during the initial stages of growth. Unlike later stages of tube growth (Fig. 5.5a,b), during the initial formation of the tube, this is connected to the microtubule all along its length through bound motors. (b) Tube-tip boundary showing the flux of bound motors, J_b, reaching the tip region by convective motion and the flux of unbound motors, J_u, leaving the tip by diffusion. The color code is the same than in Fig. 5.5.

Note that the fluxes of bound and unbound motors balance each other at each position x along the tube. In this case, there is no depletion of motors on the vesicle as the total net flux of motors entering the tube vanishes. Indeed, we are assuming that, initially, there is no accumulation of motors, so that the motors already bound to the microtubule, characterized by their equilibrium density ρ_b^∞, are able to extract the tube by themselves.

Although we have found a closed form for the solutions, we have to determine whether these solutions indeed exist and, in case they exist, we have to determine their stability. In other words, we have assumed that a solution for a tube existed and now we have to check that this is indeed the case. In order to extract tubes from the vesicle, there are two conditions to be fulfilled. The incoming flux of bound motors must balance the motor loss at the tip (Fig. 5.7), i.e.

$$\hat{J}_b(x=0,t) = k_u(n_b)n_b \,, \tag{5.26}$$

and the average velocity of the tube must be positive ($V > 0$). Note that the first condition on the fluxes is not new, but is one of the boundary conditions imposed, namely $dn_b/dt = 0$ (Eq. 5.23). However, it is only when all the boundary conditions mentioned above have been imposed that a closed solution of Eq. 5.26 can be found. Using the solutions for the density fields (Eq. 5.25), the explicit form of Eq. 5.26 reads

$$\Gamma^2 \equiv 4\pi^2\rho_\infty \frac{k_b}{k_b+k_u^0}\frac{V_0}{k_u^0}\frac{\kappa}{f_s} = \exp\left(\frac{F_0 a}{K_B T}\frac{1}{n_b}\right) n_b^2 \,. \tag{5.27}$$

The parameter Γ sets the scale for the number of bound motors n_b at the tip. Scaling the number of motors with Γ ($\tilde{n}_b \equiv n_b/\Gamma$) and defining the parameter, ν, as

$$\nu \equiv \frac{F_0 a}{K_B T}\frac{1}{\Gamma} \,, \tag{5.28}$$

the condition of flux balance at the tip (Eq. 5.27) can be rewritten as

$$1 = \exp\left(\frac{\nu}{\tilde{n}_b}\right)\tilde{n}_b^2 \,. \tag{5.29}$$

The right-hand side of Eq. 5.29 (or Eq. 5.27 equivalently), has a minimum at a number of motors $\tilde{n}_b = \nu/2$ and, depending on the value of ν, the minimum is above or below 1. Therefore, there is not always a solution for the system and, as a consequence, tubes cannot always be pulled from the vesicle. In cases where solutions exist, they can be stable or unstable. In Fig. 5.8a we plot the variation of the number of bound motors ($d\tilde{n}_b/dt$) as a function of $\tilde{n}_b$ for different values of the parameter ν, and show that above a critical value ν_c no solutions of Eq. 5.29 exist. Moreover, above ν_c the variation of the number of bound motors is always negative, indicating that the detachment flux of motors at the tip is larger than the flux of bound motors reaching the tip, preventing tube formation. Below the critical value ν_c, two solutions exist for $d\tilde{n}_b/dt = 0$ (Eq. 5.29; Fig. 5.8a). The solution with fewer number of bound motors is unstable as the detachment of one motor induces the loss of the remaining bound motors. On the contrary, the solution with larger number of bound motors is stable, because the detachment of one motor can be compensated by the flux of bound motors reaching the tip (Fig. 5.8a).

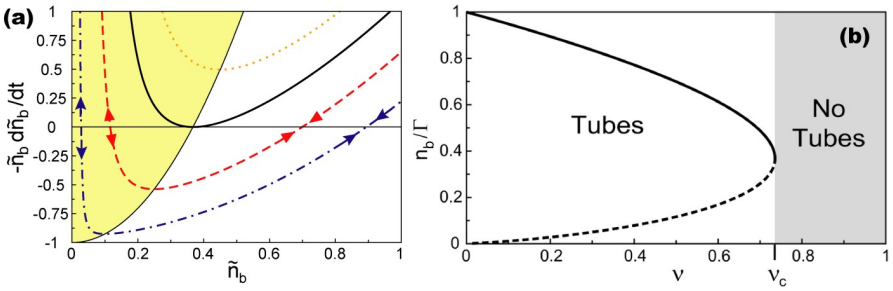

Fig. 5.8. (a) Variation of the number of motors at the tip as a function of n_b for different values of the bifurcation parameter ν: $\nu = 0.9$ (dotted line), $\nu = \nu_c = 2e^{-1} \simeq 0.74$ (continuous line), $\nu = 0.5$ (dashed line) and $\nu = 0.2$ (dashed-dotted line). Below ν_c there exist solutions for $d\tilde{n}_b/dt = 0$ (Eq. 5.29). The arrows close to the solutions indicate the tendency of the bound motor number variation upon fluctuations in n_b. The arrows point toward a stable solution and away from unstable solutions. (b) Bifurcation diagram showing the stable (continuous line) and unstable (dashed line) solutions of the system in the flux limited regime. For $\nu < \nu_c$, motors are able to extract tubes. For $\nu > \nu_c$ (gray region), there are no solutions, meaning that motors are not able to extract tubes. (Adapted from Ref. (Leduc et al., 2004)).

If the flux balance condition (Eq. 5.26) is prevalent (flux limited regime), there is a single relevant dimensionless parameter, ν, that specifies all possible solutions of the system. Although there are many parameters $(\rho_\infty, \sigma, k_u^0, k_b, \cdots)$ that influence the dynamics, the different dynamical behaviors are all determined by a combination of them, ν. These dimensionless numbers (ν and Γ) appear naturally by equating the flux of incoming bound motors to the rate of motor loss at the tip: $\hat{J}_b(x = 0, t) =$

$k_u(n_b)n_b$. In Fig. 5.8b, we represent the analytical solutions of Eq. 5.29 which fixes the number of bound motors at the tip as a function of ν. The parameter ν is a bifurcation parameter and the system undergoes a saddle-node bifurcation at $\nu_c = 2e^{-1} \simeq 0.74$. As already mentioned, ν_c is a critical value below which there are stable solutions for the system, meaning that motors are able to pull tubes from the membrane. For $\nu > \nu_c$ no solutions exist and, therefore, no tubes can be extracted from the vesicle. Using the definition of the parameter ν (Eq. 5.28), the critical point ν_c can be expressed as a function of the original physical magnitudes in the system. The critical point ν_c implies that there is a threshold value, $\rho_{\infty,1}^{min}$, for the surface density of motors on the vesicle above which tubes can be extracted:

$$\rho_{\infty,1}^{min} \equiv \frac{e^2}{2}\,\sigma\, f_s \left(\frac{a}{K_B T}\right)^2 \frac{k_b + k_u^0}{k_b}\,\frac{k_u^0}{V_0}\,. \tag{5.30}$$

At threshold, i.e. $\rho_\infty = \rho_{\infty,1}^{min}$, the number of bound motors at the tip, $n_{b,1}^t$, and the velocity, V_t, are given respectively by

$$n_{b,1}^t = \frac{F_0 a}{2K_B T}\,, \qquad V_t = V_0\left(1 - \frac{F_0}{f_s n_{b,1}^t}\right) = V_0\left(1 - \frac{2K_B T}{a\, f_s}\right)\,. \tag{5.31}$$

In this flux limited regime, the velocity at threshold is thus finite and independent of membrane tension and curvature.

The description of the threshold above (flux limited regime) holds when the tube velocity is finite at threshold. If there exist stable solutions of Eq. 5.29 leading to a negative tube velocity at threshold, the most restrictive condition is $V > 0$ (stall regime), and the threshold is specified by $V = 0$. In this case, the number of bound motors at threshold is given by $n_{b,2}^t = F_0/f_s$ which, together with flux conservation (Eq. 5.26), leads to a minimal density:

$$\rho_{\infty,2}^{min} \equiv 2\,\sigma \frac{k_b + k_u^0}{k_b}\,\frac{k_u^0}{V_0 f_s}\exp\left(\frac{f_s a}{K_B T}\right)\,. \tag{5.32}$$

If $n_{b,1}^t > n_{b,2}^t$, the expression for the threshold density is given by Eq. 5.30, and, conversely, if $n_{b,1}^t < n_{b,2}^t$ it is given by Eq. 5.32. Interestingly, the crossover between the two regimes depends on motor properties only: the flux limited regime is expected if the stall force f_s is larger than $2K_B T/a$ and the stall regime if f_s is smaller than $2K_B T/a$.

Therefore, above $\rho_{\infty,1}^{min}$ or $\rho_{\infty,2}^{min}$ depending on the regime, tubes can be extracted from the vesicle and the number of bound motors at the tip n_b ranges between $\max\{F_0 a/2K_B T, F_0/f_s\} \leq n_b \leq \Gamma$. On the contrary, below the threshold concentration, no tube can be extracted. Similarly, tube extraction can be monitored by changing the tension σ at constant motor density ρ_∞. It is important to understand the dynamical nature of both thresholds: a minimum flux of bound motors towards the tip is required to balance the detachment flux of bound motors which, in turn, depends strongly on the force applied per motor. Note that the bifurcation is not related

to the existence of an overshoot in the static force/length relation for tube extraction (Derenyi et al., 2002). A threshold has also been predicted in Ref. (Koster et al., 2003) using a simplified approach which does not take into account the transport of motors along the tube. We give here a complete description of the transport which characterizes quantitatively both the threshold and the motor distribution.

Density of motors along the tube

If the parameters are such that membrane tubes can be extracted from the vesicle, both the density profile of motors along the tube and the tube growth characteristics can be studied. In order to understand the experimental density profiles, we study the long time scale behavior ($t > \max[(k_u^0)^{-1}, k_b^{-1}] \sim 1s$). Assuming that the tube velocity V varies only weakly during tube extraction, the density profiles of bound and unbound motors are exponentially decaying functions away from the tip, with a decay length λ given by

$$\lambda = \frac{2\lambda_1}{\sqrt{1+\left(2\frac{\lambda_1}{\lambda_2}\right)^2}-1} , \tag{5.33}$$

where λ_1 and λ_2 are the two characteristic lengths defined above (Eq. 5.21). The ratio λ_1/λ_2 distinguishes two limiting dynamical regimes at long time scales. If $\lambda_1 \ll \lambda_2$, the decay length of the density profiles is given by

$$\lambda \simeq \lambda_2 \frac{\lambda_2}{\lambda_1} = \frac{D}{k_b}\frac{k_u^0}{V_0 - V} . \tag{5.34}$$

In this regime, the decay length λ depends on the velocity of the tube V. On the other hand, if $\lambda_1 \gg \lambda_2$, the decay length is

$$\lambda \simeq \lambda_2 = \sqrt{\frac{D}{k_b}} , \tag{5.35}$$

and does not depend on the velocity V. In this case the decay length λ is fixed by the average length, $\sqrt{D/k_b}$, that the unbound motors travel along the tube by diffusion until they re-attach to the microtubule.

The existence of a portion of the tube in contact with the microtubule (Fig. 5.5), together with continuity conditions, imply that no stationary state can be reached. The growth of the tube observed experimentally suggests, however, a quasi-steady state as the average velocity is nearly constant. Quasi-steady state solutions can be obtained by solving Eq. 5.9 and 5.11 assuming that both the number of bound and unbound motors at the tip, n_b and n_u respectively, vary slowly on time, so that $dn_b/dt \simeq 0$ and $dn_u/dt \simeq 0$. Note that these conditions are necessary in order to obtain an average tube velocity V that varies only weakly on time, as $V = V_0\left(1 - F_0/f_s n_b\right)$.

In the limiting regimes where $\lambda_1/\lambda_2 \ll 1$ and $\lambda_1/\lambda_2 \gg 1$, the analytical quasi-steady state solutions for the number of bound motors at the tip and the density

profiles can be found. For $\lambda_1 \ll \lambda_2$ the number of bound motors at the tip, $n_b(t)$, is given by

$$n_b(t) = \frac{1}{\Gamma(5/4)}\sqrt{\frac{k_b}{k_u^0}}\left[\left(\frac{F_0}{f_s}\right)^3 \frac{V_0^3 \rho_b^\infty}{D(k_b+k_u^0)}\, t\right]^{1/4} , \tag{5.36}$$

where $\Gamma(z)$ is the Gamma function (Gradshteyn and Ryzhik, 2000). In this regime, the density profiles of bound ($i=b$) and unbound ($i=u$) motors $\rho_i(x,t)$ read

$$\frac{\rho_i(x,t)}{\rho_i^\infty} = 1 + 2\frac{k_b}{k_u^0}\sqrt{\frac{F_0}{f_s}\frac{k_u^0}{(k_b+k_u^0)}\frac{k_u^0 V_0}{D\rho_b^\infty}}\sqrt{\frac{t}{\pi}}\exp\left(\frac{x}{\lambda}\right) , \tag{5.37}$$

where ρ_b^∞ is the constant equilibrium density of bound motors far from the tip, and $\rho_u^\infty = \rho_b^\infty(k_u^0/k_b)$. The solutions are not fully determined because the value of the equilibrium density ρ_b^∞ is not yet fixed. However, the scaling form of the solutions already shows a weak dependence on time. This slow increase of the number of motors pulling the tube with time, $n_b(t) \sim t^{1/4}$, is consistent with our quasi-steady state approximation.

When $\lambda_1 \gg \lambda_2$ the solution for the number of bound motors pulling the tube is

$$n_b(t) \simeq \frac{1}{\Gamma(4/3)}\left(\sqrt{\frac{k_b}{D}}\frac{\rho_b^\infty V_0^2}{k_u^0}\left(\frac{F_0}{f_s}\right)^2 t\right)^{1/3} , \tag{5.38}$$

and the density profiles away from the tip for bound and unbound motors, $\rho_b(x,t)$ and $\rho_u(x,t)$ respectively, are given by

$$\begin{aligned}
\frac{\rho_b(x,t)}{\rho_b^\infty} &= 1 + \frac{1}{\Gamma(5/3)}\sqrt{\frac{k_b}{D}}\left(\frac{F_0 V_0}{f_s}\sqrt{\frac{D}{k_b}}\frac{k_b^0}{\rho_b^\infty}\right)^{1/3} t^{2/3}\exp\left(\frac{x}{\lambda}\right) , \\
\frac{\rho_u(x,t)}{\rho_u^\infty} &= 1 + \frac{1}{\Gamma(4/3)D}\frac{k_b}{k_u^0}\left(\frac{F_0 V_0}{f_s}\sqrt{\frac{D}{k_b}}\frac{k_u^0}{\rho_b^\infty}\right)^{2/3} t^{1/3}\exp\left(\frac{x}{\lambda}\right) .
\end{aligned} \tag{5.39}$$

Similarly to the previous limiting case ($\lambda_1 \ll \lambda_2$) the slow time evolution of the number of bound motors at the tip, $n_b(t) \sim t^{1/3}$, is consistent with the quasi-steady state approximation, because in the long time limit being considered, $dn_b/dt \sim t^{-2/3} \to 0$.

In Fig. 5.9 we sketch the mechanism by which the tube is pulled, and plot the solution of the total motor density field using experimentally measured values for all parameters [5]. The bound motors moving along the tube dynamically accumulate at the tip, because of the slower growth velocity of the tube. At the same time, the bound motors at the tip detach faster than those along the tube, resulting in a larger density of unbound motors close to the tip. These unbound motors diffuse away from the tip, following the direction of decreasing unbound motor density, and re-attach to the microtubule at an average distance $\sqrt{D/k_b}$ from the tip. All these events constitute

[5] The experimental values of the parameters are discussed below.

a treadmilling mechanism, in which the motors repeat the same sequence of events. This turnover of motors sets a closed circuit of motor flux in the vicinity of the tip (Fig. 5.9a). In addition to these motor fluxes there is a net flux of bound motors moving from the vesicle toward the tip. In case this latter flux of motors coming from the vesicle is not present, the system would reach a steady state. Indeed, if the tube is initially fed by a fixed amount of motors and no more motors enter the tube from the vesicle, the tube can also grow by the mentioned treadmilling mechanism, constantly replacing the motors working to pull the tube and recycling them back afterwards (Fig. 5.9a).

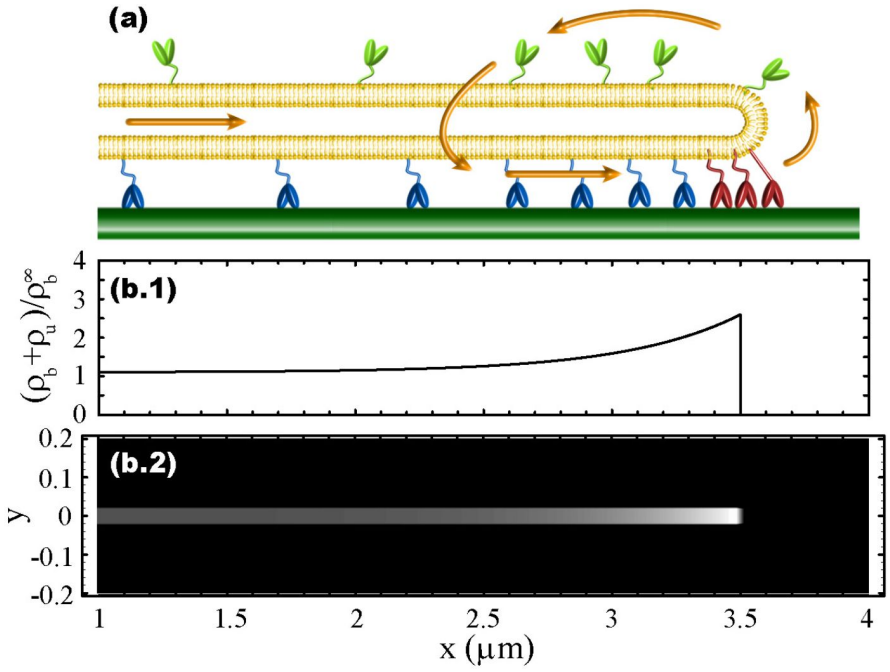

Fig. 5.9. (a) Sketch of motor fluxes in the vicinity of the tip (tube reference frame). The motors circulate in a closed loop, in which they spend a portion of their time pulling the tube. Moreover, there is a net flux of bound motors constantly feeding the vicinity of the tip with new motors and responsible for the lack of steady state in the system. (b-c) Total motor density profile, $\rho_b(x,t)+\rho_u(x,t)$, in the vicinity of the tip (obtained from Eq. 5.39), showing the exponential decrease of the motor density away from the tip ($t = 35$ s). The values for the parameters are very similar to those measured experimentally (see discussion below): $D = 1\ \mu\text{m}^2\text{s}^{-1}$, $k_b = 5\ \text{s}^{-1}$, $k_u^0 = 0.5\ \text{s}^{-1}$, $F_0 = 20$ pN, $f_s = 6$ pN, $V_0 = 0.6\ \mu\text{ms}^{-1}$, $V = 0.1\ \mu\text{ms}^{-1}$ and $\kappa = 10K_BT$. The value of ρ_b^∞ is given by Eq. 5.44 with $\rho_\infty = 5000\ \mu\text{m}^{-2}$. (c) Density plot showing the total motor density along the tube. The tube is in the $x-y$ plane and the motor density is color-coded: regions with no motors are represented in black and increasing motor densities by lighter gray. White color corresponds to 3.0 in the density scale of (b.1).

The lack of steady-state in the system can be understood from the expression of the total motor flux far way from the tip. The densities of bound and unbound motors away from the tip are the equilibrium densities ρ_b^∞ and ρ_u^∞ and the total net flux, expressed in the tube reference frame, is $\hat{J}_b = (V_0 - V)\rho_b^\infty$. Hence, for non-vanishing motor densities away from the tip, there is always a net bound motor flux constantly feeding the tip region. As a result, there is no steady-state and the density profiles are time-dependent. We shall show below that the central region of the tube, characterized by constant motor densities, acts as a pump, taking motors from the vesicle and transferring them to the tip region.

As mentioned above, the solutions for the number of bound motors and the density profiles are fixed up to a constant, ρ_b^∞. The reason why the equilibrium density of bound motors, ρ_b^∞, is not yet fixed is that it depends on the physics close to the vesicle. In order to obtain the actual value of ρ_b^∞, continuity conditions for both motor density and fluxes must be imposed at the tube-vesicle boundary. In spite of the details of the contact between the tube and the vesicle, the equilibrium bound motor density must be $\rho_b^\infty \sim 2\pi r_0 \rho_\infty$ at leading order. We now give a detailed analysis of the dynamics close to the tube-vesicle boundary.

Unlike the initial stages of tube extraction, where the tube is in contact to the microtubule all along its length, for tubes of several microns there is a region where the tube loses its contact with the microtubule (Fig. 5.5a,b). The geometry of the tube-vesicle boundary is thus slightly different than that at short time scales. In Fig. 5.10 we sketch the vesicle and the tube, with a connection region of length L_d where the tube is not in contact with the microtubule. We now solve the dynamics of the motors in the different regions and match the solutions at the boundaries imposing continuity of motor density and flux.

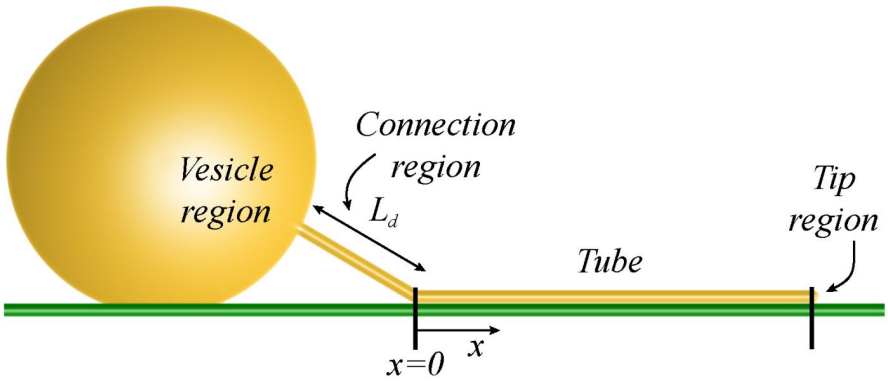

Fig. 5.10. Sketch of the different regions of the system at long-time scales, showing the connection region in which the tube is not in contact with the microtubule. The x axis is along the tube and the origin $x = 0$ is at the position where the tube contacts the microtubule. Note that the coordinate x follows the tube up to the contact with the vesicle.

In the connection region, the motors can only be unbound as there is no microtubule to which they can attach (Fig. 5.10). The dynamics of the motors in this region, expressed in the laboratory reference frame, is given at mean field-level by

$$\frac{\partial \rho_u(x,t)}{\partial t} + V\frac{\partial \rho_u(x,t)}{\partial x} - D\frac{\partial^2 \rho_u(x,t)}{\partial x^2} = 0\,. \tag{5.40}$$

In this reference frame, x is the position along the tube (oriented along the direction of the tube motion) and the origin $x = 0$ is at the position where the tube contacts the microtubule (Fig. 5.10). Therefore, values $x < 0$ and $x > 0$ describe, respectively, the connection region and the region where the tube is in contact with the microtubule. The quasi-steady state solution of Eq. 5.40 is

$$\rho_u(x) = \frac{J_d(x=0)}{V}\left(1 - \exp\left(\frac{V}{D}x\right)\right) + \frac{J_c(x=0)}{V}\,, \tag{5.41}$$

where $J_c(x=0)$ and $J_d(x=0)$ are, respectively, the convective and diffusive motor fluxes at the origin, i.e. where the tube contacts the microtubule. In order to determine these fluxes it is necessary to find the solution for the bound and unbound motor density fields along the region of the tube in contact with the microtubule. The dynamics of the motors in this region is given by Eq. 5.11. The boundary condition for the bound motor density field is $J_b(x=0) = 0$ (or $\rho_b(x=0) = 0$ equivalently) as there are no bound motors in the connection region. Moreover, the solutions must match the equilibrium densities and total flux along the tube, far from the contact point at $x = 0$. With this conditions, the quasi-steady state solution for the density fields of bound and unbound motors, $\rho_b(x)$ and $\rho_u(x)$ respectively, read

$$\begin{aligned}
\rho_b(x) &= \rho_b^{\infty}\left[1 - \exp\left(-\frac{x}{\lambda_c}\right)\right]\,, \\
\rho_u(x) &= \rho_u^{\infty}\left[1 - \left(1 - \frac{V_0}{\lambda_c k_u^0}\right)\exp\left(-\frac{x}{\lambda_c}\right)\right]\,,
\end{aligned} \tag{5.42}$$

where λ_c is the characteristic length of the density profile (obtained from the characteristic equation), and is given by

$$\lambda_c = \frac{2DV_0}{Dk_u^0 - V_0 V}\left[1 + \sqrt{1 + 4DV_0\frac{(V_0 k_b + V k_u^0)}{(k_u^0 D - V_0 V)^2}}\right]^{-1}\,. \tag{5.43}$$

Continuity conditions for both the density field and flux of unbound motors at $x = 0$ [6], lead to a closed expression for the diffusion and convection fluxes, $J_d(x=0)$ and $J_c(x=0)$ respectively, which read

$$\begin{aligned}
J_c(x=0) &= \rho_u^{\infty} V\frac{V_0}{\lambda_c k_u^0}\,, \\
J_d(x=0) &= J_T - J_c(x=0)\,,
\end{aligned}$$

[6] Note that the density field of bound motors and its flux are already continuous.

where J_T stands for the total motor flux along the tube and is given by $J_T = \rho_b^\infty V_0 + \rho_u^\infty V$. These two fluxes specify the solution of the unbound motor density in the connection region (Eq. 5.41) up to a constant, namely ρ_b^∞. Finally, continuity of the motor density field and flux at the contact with the vesicle, determines the value of ρ_b^∞, which reads

$$\rho_b^\infty = \frac{2\pi r_0 \rho_\infty \frac{k_b}{k_u^0}}{\frac{V_0}{\lambda_c k_u^0}\exp\left(-\frac{V}{D}L_d\right) + \left(1+\frac{V_0 k_b}{V k_u^0}\right)\left[1+\frac{r_0 V}{2D}\mathrm{Ei}\left(\frac{-r_0^2}{4Dt}\right) - \exp\left(-\frac{V}{D}L_d\right)\right]}\,, \quad (5.44)$$

where ρ_∞ is the initial surface density of motors on the vesicle. It is important to note that ρ_b^∞ depends only weakly on time. In accordance with our quasi-steady state approximation, the time dependence of ρ_b^∞ is essentially logarithmic. Moreover, using the experimentally measured values ($V \sim 0.1\,\mu\mathrm{m\,s^{-1}}$, $D \simeq 1\,\mu\mathrm{m^2\,s^{-1}}$ and $r \simeq 20$ nm; see discussion below), the coefficient in front of the time-dependent term, $r_0 V/2D$, is of order 10^{-2}, and for the typical time of an experiment, the time-dependent term is almost negligible, meaning that the depletion of the motors on the vesicle can be neglected. Indeed, the ratio of the number of motors in the tube ($\sim (\rho_b^\infty + \rho_u^\infty)L$) and the initial number of motors on the vesicle ($\sim 4\pi R^2 \rho_\infty$) is given approximately by $r_0 L/2R^2$. In typical experimental conditions ($R \sim 5\,\mu$m and $L \simeq 10\,\mu$m), this ratio is $r_0 L/2R^2 \sim 0.01$, meaning that during tube extraction less than about the 1% of the available motors on the vesicle have been depleted. However, when a large membrane tube network is formed, the depletion of motors on the vesicle can become important.

In case the length of connection region L_d is much longer than the characteristic length scale D/V ($L_d \gg D/V \simeq 10\mu$m), the expression for the equilibrium density of bound motors along the tube (Eq. 5.44) reduces to

$$\rho_b^\infty = 2\pi r_0 \rho_\infty \frac{V}{V_0}\,, \quad (5.45)$$

where we have totally neglected depletion effects for the reasons discussed above and we have used the fact that $V_0 k_b / V k_u^0 \gg 1$ in typical experimental conditions. On the other hand, if $L_d \ll D/V \simeq 10\mu$m and neglecting depletion effects, Eq. 5.44 reduces to

$$\rho_b^\infty = 2\pi r_0 \rho_\infty \frac{\lambda_c k_b}{V_0}\,. \quad (5.46)$$

Note that in the first limiting case ($L_d \gg D/V$), the value of the equilibrium bound motor density depends on the tube velocity V, whereas for $L_d \ll D/V$ it does not (at leading order). The typical length of the connection region measured experimentally is of a few microns and, thus, similar to D/V, meaning that the system is in between the two limiting cases discussed.

The continuity conditions at the contact with the vesicle also fix the depletion flux, J, of motors on the vesicle (see Eq. 5.18a). This flux is nothing else than the total flux of motors in the central region of the tube in contact with the microtubule, so that

$$J = J_T = \rho_b^\infty V_0 + \rho_u^\infty V \ . \tag{5.47}$$

The last expression highlights the mechanism driving the motors from the vesicle to the vicinity of the tip (Fig. 5.11a). Once a long enough region of the tube is contacting the microtubule, the flux of motors set by the equilibrium densities $(\rho_b^\infty, \rho_u^\infty)$, induces the depletion of motors on the vesicle, and establishes a net flux of motors toward the tip. The central region of the tube acts thus as a pump to transfer the motors from the vesicle to the vicinity of the tip.

In Fig. 5.11b,c we plot the density fields of motors on the vesicle (Fig. 5.11b) and along the portion of the tube in contact with the microtubule (Fig. 5.11c), for typical experimental values of the parameters. There is a long portion of the tube characterized by the equilibrium densities ρ_b^∞ and ρ_u^∞ of bound and unbound motors. The density of unbound motors decreases in the vicinity of $x = 0$ because the motors attach to the microtubule, and reaches the equilibrium density ρ_u^∞ in the central region of the tube. Accordingly, the density of bound motors increases from $x = 0$ and reaches its equilibrium value in the central region. In the vicinity of the tip, we observe the accumulation of motors previously described.

The dynamical regimes described here provide a good description of the tube motion as long as the density of motors just behind the tip remains small. This is true under typical experimental conditions. At very long times, the steric interactions between motors become important and lead to the formation of a traffic jam of bound motors behind the tip (Parmeggiani et al., 2003; Lipowsky et al., 2001). Fig. 5.13D supports the low density approximation as it shows an exponential decay of the motor density away from the tip. The flux of motors toward the tip is compensated to some extent by the growth of the tube itself which keeps the densities low enough. If the tube growth is stopped, self-dilution of the motors disappears and a micron-sized traffic jam develops at the tip. We address these phenomena using numerical simulations in section 5.4.

Discussion

Here we describe the conditions in which the experiments were done and compare quantitatively the theoretical predictions to the experimental data.

Applying an osmotic pressure in the bulk 10% lower than in the vesicle, it was possible to impose a high tension, σ, on the membrane which can be estimated using Laplace's Law to be $\sigma = \Delta\Pi R/2$. Taking an average vesicle radius R of 10 μm and an osmotic pressure difference $\Delta\Pi$ of 20 mOsm gives $\sigma \simeq (2.5 \pm 1.3)\, 10^{-4}$ N/m. This tension value was further checked by directly measuring the force needed to pull a tube, $F_0 = 2\pi\sqrt{2\sigma\kappa}$, using optical tweezers. The obtained value $F_0 \simeq 27.5 \pm 2.5$ pN for a 7 μm radius vesicle is compatible with the known value of the bending modulus $\kappa \simeq 10 K_B T$ (Olbrich et al., 2000) and our estimated tension. It was also checked that the force and thus the tension remains constant during the tube growth. This requires that sufficiently few tubes are pulled from the same vesicle and that the tubes are not longer than ~ 20 μm. All the experiments used in the comparison with the theoretical results were done in these conditions.

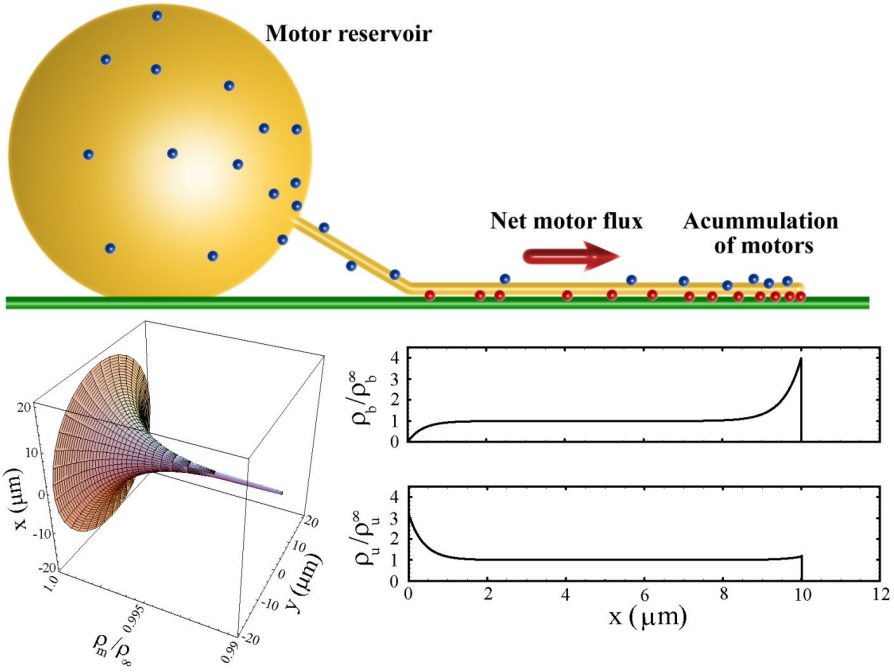

Fig. 5.11. (a) Sketch of the mechanism driving the transfer of motors from the vesicle to the vicinity of the tip. The bound motors along the tube impose a net motor flux from the vesicle to the tube tip. (b) Motor density profiles on the vesicle (b.1) and along the portion of the tube in contact with the microtubule (b.2,b.3), at $t = 100s$. Note that the motor depletion on the vesicle is nearly insignificant (b.1). The density of bound (b.2) and unbound (b.3) motors are shown. The parameters are the same than in Fig. 5.9.

Threshold in tube extraction

For DHPE-Biot-Rhod concentrations higher than 0.01 mol%, tubes could be formed consistently in less than a few minutes. In contrast, for concentrations lower than 0.01 mol%, no tube could be extracted over a period of more than three hours (Fig. 5.12). This suggests the existence of a threshold for the concentration of biotinylated lipids in the membrane, corresponding to a threshold for the motor density on the vesicle. Equivalently, at fixed motor density, there is a maximal tension above which no tubes can be extracted. These results are in accordance to those in Ref. (Koster et al., 2003). Using the value of the surface of a lipid in the membrane (0.4 nm^2) and the measured value for the lowest concentration at which tubes are observed (0.01 mol% of biotinylated lipids), we obtain the experimental value of the threshold density

$$\rho_{\infty}^{min} \simeq 200 \pm 100\,\mu m^{-2}\,. \tag{5.48}$$

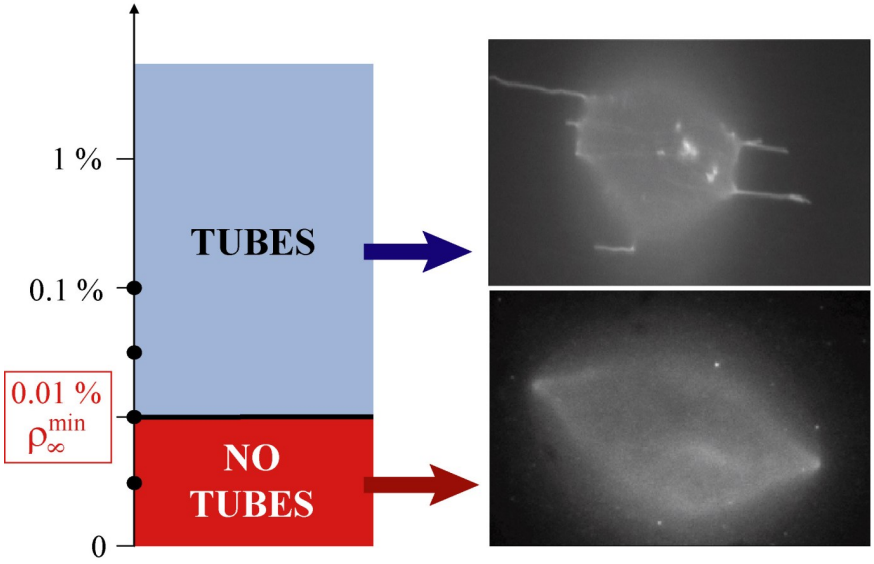

Fig. 5.12. Experimental determination of the threshold in tube extraction. (Left) Diagram showing the existence of a threshold at a finite motor concentration on the surface of the vesicle ($\sigma \simeq 2\,10^{-4} N/m$ and $\kappa \simeq 10 K_B T$). The dots represent the values of DHPE-Biot-Rhod concentrations tested experimentally. Below a DHPE-Biot-Rhod concentration of 0.01 mol%, corresponding to a initial motor concentration on the vesicle of 200 motors per squared micron ($\rho_\infty^{min} = 200 \mu m^{-2}$), no tubes are observed. (Right) Examples of vesicles above (top) and below (bottom) the threshold. Above the threshold tubes are pulled from the vesicle, whereas below the threshold the vesicle is deformed due to the action of the motors, but no tubes are formed. The lipids in the membrane are uniformly labeled and the binding sites of motors are not labeled. (Images by C. Leduc).

As discussed in the theoretical section above, the threshold regime is determined by motor properties only. The wild type kinesin has been extensively studied (Howard et al., 1989; Yildiz et al., 2004; Block et al., 2003) in conditions close to the ones being considered here. In particular, both f_s and a have been measured: $f_s \simeq 6\,\text{pN}$ and $a \simeq 1.3\,\text{nm}$ (Visscher et al., 1999; Schnitzer et al., 2000). These values lead to $2K_BT/a \simeq 6\,\text{pN}$ which shows that the system is almost at the transition between the two threshold regimes. In order to calculate the threshold value predicted theoretically, it is necessary to know the values of several parameters, namely σ, f_s, a, V_0, k_u^0 and k_b. The tension σ is fixed to $\sigma \simeq 2\,10^{-4}$ N/m, $f_s \simeq 6$ pN and $a \simeq 1.3$ nm. The value of the detachment rate at vanishing force, k_u^0, is also known for conventional kinesin motors, $k_u^0 \simeq 0.42\ \text{s}^{-1}$ (Vale et al., 1996). The value of the kinesin velocity at vanishing load V_0 was measured using bead assays to be $V_0 \simeq 0.6\ \mu\text{ms}^{-1}$ (see below). The only unknown parameter is the attachment rate of kinesins onto microtubules, k_b. We show below that the comparison between the theoretical results concerning the motor density profile along the tube to the experimental data, allows

the determination of k_b, which we estimate to be $k_b \simeq 4.7 \pm 2.4\,\mathrm{s}^{-1}$. With all these values, we can calculate both $\rho_{\infty,1}^{min}$ and $\rho_{\infty,2}^{min}$ (Eqs. 5.30 and 5.32 respectively). We find

$$\rho_{\infty,1}^{min} \simeq \rho_{\infty,2}^{min} \simeq 400 \pm 200\ \mu\mathrm{m}^{-2}\,, \tag{5.49}$$

which compares favorably well with the experimental value (Eq. 5.48). As all the parameters are known, we can also estimate the number of motors necessary to pull a tube at threshold. In both threshold regimes the number of pulling motors at threshold is

$$n_{b,1}^{t} \simeq n_{b,2}^{t} \simeq 4\,. \tag{5.50}$$

Recent experiments on conventional kinesin (Nishiyama et al., 2002; Carter and Cross, 2005) report that the stall force for kinesin is likely to be slightly larger than 6 pN. In particular, a value of $f_s \simeq 7$ pN was found. This value suggests that the actual threshold regime is the flux limited regime, as $f_s > 2K_BT/a \simeq 6$ pN. In this case, the tube velocity at threshold is finite (Eq. 5.31). Using $f_s = 7$ pN and the measured value of $V_0 \simeq 0.6\ \mu\mathrm{ms}^{-1}$ leads to

$$V_t = 0.07\ \mu\mathrm{ms}^{-1}\,. \tag{5.51}$$

We compare below this value to the velocity of tubes in far from threshold conditions.

Motor density profile

The growth of single tubes was followed by fluorescence videomicroscopy (Fig. 5.13A). The fluorescence intensity and therefore the distribution of motors along the tube is inhomogeneous, especially at the tip, where an excess of fluorescence can be seen (Fig. 5.13B).

The fluorescence distribution along the tube for each frame (Fig. 5.13B) was determined. An example of the resulting space-time plot is given in Fig. 5.13C; it is a three-dimensional diagram, showing fluorescence intensity (z-axis, color coded) as a function of the position along the tube path (y-axis) and time (x-axis). We observed that on every frame the tip was more fluorescent than the rest of the tube. The rest of the image, where no tube could be seen, was not fluorescent. The position of the tip of the tube was determined by detecting the position of the transition between the maximum intensity and the background. The instantaneous velocity of tube growth between two consecutive images was calculated by derivation of the position of the tip as a function of time.

The distribution of motors is found experimentally from the fluorescence intensity along the tube. Fig. 5.13D shows an example of an instantaneous fluorescence profile. The motor density decreases exponentially from the tip of the tube as expected theoretically. When the membrane was labeled using a fluorescent lipid with no biotin function (BODIPY PC) and motors were not specifically labeled (control experiment), fluorescence was uniform along the extracted tube and no accumulation at the tip was observed (Fig. 5.13D). The decay length λ was measured for various tubes with different velocities V at a concentration of 0.1 mol% biotinylated lipids in the membrane, corresponding to 10 times the threshold concentration. It ranges

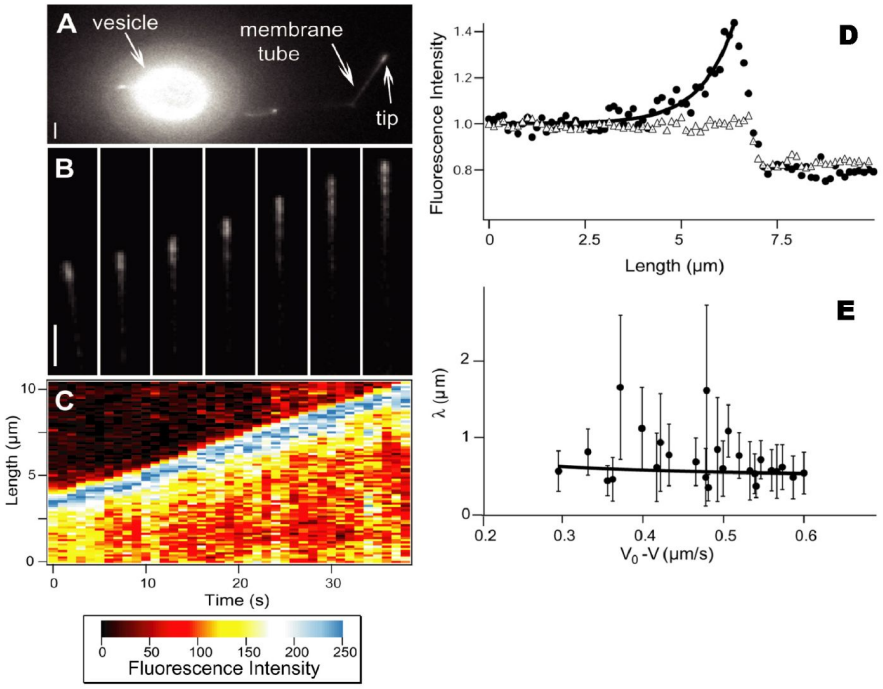

Fig. 5.13. (A) Fluorescence image showing a vesicle, a tube and the accumulation of motors at its tip. The vesicle contains 0.1 mol% DHPE-Biot-Rhod lipids. Bar, $2\,\mu$m. (B) Time sequence of a the growing tube in (A) (1 image/5s). The tube grows along a microtubule with an average velocity of about $0.16\,\mu\mathrm{m/s}$. Bar, $2\,\mu$m. (C) Fluorescence intensity plot as a function of position along the tube path and time, for the same tube as in (B). (D) Fluorescence intensities along the tube path normalized by the average intensity far from the tip. Filled circles: the binding sites of motors are labeled using DHPE-Biot-Rhod; Triangles: the membrane is uniformly labeled with BODIPY PC, and the binding sites of motors are not specifically labeled (control experiment); Solid line: Exponential fit of the intensity profile represented by the circles. The best fitting value for the characteristic decay length is $\lambda \simeq 1.0\,\mu$m. (E) Characteristic length λ as a function of $V_0 - V$ for 370 measurements from 20 different tubes. Each point corresponds to the average λ (and associated standard deviation) for measurements with the same velocity. The continuous line corresponds to the one parameter weighted non-linear fit using Eq. 5.33, with $k_u^0 = 0.42\,\mathrm{s}^{-1}$ (Vale et al., 1996) and $V_0 = 0.6\,\mu\mathrm{m/s}$. Each weight is given by the normalized inverse of the variance associated to that point. The only fit parameter is k_b/D and its best fitting value is $4.7 \pm 0.5\,\mu\mathrm{m}^{-2}$. Using $D = 1.0 \pm 0.5\,\mu\mathrm{m}^2/\mathrm{s}$ leads to $k_b = 4.7 \pm 2.4\,\mathrm{s}^{-1}$. We have further checked that reasonable variations of k_u^0 do not affect significantly this value. (Adapted from Ref. (Leduc et al., 2004)).

between $0.4\,\mu\text{m} < \lambda < 1.8\,\mu\text{m}$ (Fig. 5.13E). The comparison of these values with the theoretical predictions of Eq. 5.33 allows the determination of the binding rate k_b of kinesin on microtubules in a one parameter fit, provided that we know D, V_0.

The average velocity in far from threshold conditions, i.e. for $\rho_\infty \simeq 10\,\rho_\infty^{min}$ (same tension $\sigma \simeq 2\,10^{-4}$ N/m), measured over twenty different experiments where a single tube was pulled from the vesicle, was $V \simeq 0.12 \pm 0.04\ \mu\text{m/s}$. The growth velocity is the velocity of kinesins effectively pulling the tube. It is smaller than the velocity obtained in a bead assay, which corresponds to the velocity of kinesins at vanishing load, $V_0 = 0.6 \pm 0.1\,\mu\text{m/s}$. Bead assays were performed in the same experimental context as tube assays (molecular motors from the same batch, microtubule network obtained with the same protocol, same buffers and ATP concentration) and the measured velocity is in good agreement with data by other groups (Cappello et al., 2003; Block et al., 2003).

Using FRAP [7] experiments, it was possible to measure the diffusion constant D of the biotinylated lipid-streptavidin-kinesin in the membrane, $D = 1.0 \pm 0.5\,\mu\text{m}^2\,\text{s}^{-1}$. The velocity V_0 is obtained from the velocity measured in bead assays in absence of external load. As discussed in the beginning of section 5.3.1, the friction force exerted on the bound motors moving along the tube is given, according to Einstein's law, by $K_B T V_0/D$. Using the experimentally measured values for D and V_0, this force is $K_B T V_0/D \simeq 2.4 \cdot 10^{-3}$pN, totally negligible compared to the stall force of kinesins. Using the value of the detachment rate at vanishing force, $k_u^0 = 0.42\,\text{s}^{-1}$ (Vale et al., 1996), and $V_0 = 0.6\,\mu\text{m/s}$, we can estimate the value of k_b by fitting the experimental values of the decay length λ to Eq. 5.33. We obtain the value of the binding rate k_b in a tubular geometry similar to *in vivo* conditions:

$$k_b = 4.7 \pm 2.4\,\text{s}^{-1}\,. \tag{5.52}$$

Away from threshold, for $\rho_\infty \simeq 10\,\rho_\infty^{min}$ (same tension), we can also calculate the number of motors at the tip without any adjustable parameter. Using flux balance (Eq. 5.27; represented in Fig. 5.8b) we find

$$n_b \simeq 24\,. \tag{5.53}$$

Both the number of motors pulling the tube at threshold (Eq. 5.50) and far from the threshold (Eq. 5.53) are rather small. Fluctuations may thus play an interesting role in the process. The average velocity of the tube is obtained from the expression $V = V_0(1 - F_0/f_s n_b)$. Using the estimated number of motors, we obtain an average tube velocity in conditions far from threshold of

$$V \simeq 0.49\ \mu\text{m/s}\,. \tag{5.54}$$

[7] FRAP stands for "Fluorescence Microscopy After Photobleaching". This technique allows the measurement of the diffusion coefficient of a fluorescent component. It consists in measuring the recovery of fluorescence intensity in a previously photobleached zone. The time needed for the fluorescence component to invade the photobleached region allows the determination of its diffusion constant.

This value differs from the measured average tube velocity. This is due to the fact that our mean-field description does not account for any interaction between the motors and, in particular, it does not account for the excluded volume interactions of the motors at the tip. In section 5.4 we analyze the growth of tubes using numerical simulations and show that motor fluctuations and mutual interactions are essential to understand both the organization of the motors pulling the tube and the growth properties like the average tube velocity.

In the description above we have considered that the bound motors outside the tip do not exert any significant force on the tube. This is indeed legitimate: a conservative estimate of the friction force close to the threshold is $2\pi r_0 \rho_\infty (K_B T/D) L \lesssim 10^{-4} F_0 \ll F_0$ (in which we have chosen the tube length L to be a few times the tube radius r_0). Away from threshold, this force is estimated to be $\lesssim 10^{-1} F_0 < F_0$, which is again negligible and justifies our previous assumptions.

5.3.2 Long tubes

The analysis developed in the previous section is valid for tubes with a total length smaller that the characteristic length scale of force increase (see section 5.2.2). We have shown that for $L < L_c$ it is possible to perform a quantitative study of tube extraction by molecular motors. When the tube length exceeds this characteristic length L_c, the tube force can no longer be considered as constant and the dynamics of tube extraction is strongly influenced by the force increase. For long single tubes or large tube networks, this increase in tube force is crucial and reveals several dynamical regimes that arise from the collective dynamics of the motors pulling the tube.

In this section we describe theoretically the dynamics of membrane tube extraction in conditions where the tube force is not constant. Upon tube growth, the tension of the vesicle increases due to the increasing length of the tube (see section 5.2.2). As a result, the force that the motors must overcome to pull the tube increases during tube extraction. We couple the cooperative dynamics of the motors pulling the tube to the dynamics of the tube growth, and analytically determine the possible dynamical regimes. We show that the interplay between tube extension and motor dynamics give rise to highly non-linear oscillations in the tube length. There exist two possible dynamical regimes: membrane tubes may either stall at a certain length or oscillate between minimal and maximal lengths. The theoretical results are in good qualitative agreement with the experimental observations.

The work we present in this section is still in progress and some results are preliminary. The simplified description below pretends to understand the experimental observations at a qualitative level. We are currently developing a more elaborate quantitative analysis, which will be published soon (Campas et al., 2006d).

Theoretical description

Unlike the case of short tubes where we described in detail the dynamics of the motors on the vesicle, along the tube and at the tip of the tube, here we reduce the dynamics of the tube to an effective dynamics for the motors at the tip.

Once the motors have been able to pull out a membrane tube of length L, the magnitude of the restoring tube force $F(L)$ is a function of the tube length L. The relation between the tube force and length is given by Eqs. 5.5 and 5.7 for vesicles in the entropic and elastic regimes respectively. For the time being, we do not specify any particular functional form for $F(L)$. The motors at the tip of the tube apply a total force F_M to pull the tube and any variation in the tube length leads to a friction force F_F. For short enough tubes, we have shown above that the friction force can be safely neglected and the tube force is balanced by the force of the motors at the tip, so that $F_M = F(L)$. In general, this is not the case and the force balance must include the friction force explicitely. Assuming for simplicity that the tube force is not affected by the friction along the tube [8], force balance reads

$$F_M - F(L) + F_F = 0 \,. \tag{5.55}$$

The tube motion is opposed by the hydrodynamic friction of the tube with the surrounding fluid. Knowing the viscosity η of the surrounding fluid, we can estimate the order of magnitude of such friction force to be $\sim 2\pi\eta L\dot{L}$, with $\dot{L} \equiv dL/dt$ being the tube velocity. This force can only be relevant for the dynamics of the tube if it on the order of the tube force. Using typical values for the tube force (~ 20 pN) and knowing the measured value of the tube velocity during a tube retraction ($\sim 100\ \mu\text{ms}^{-1}$; see below and Ref. (Rossier et al., 2003)), this friction force is only relevant if the tube length is of hundreds of microns. Indeed, this hydrodynamic friction is typically small compared to the fluid-like drag force, $F_{F,M}$, due to the bound motors along the tube, which reads

$$F_{F,M} = \xi_m L \left(V_0 - \dot{L}\right) \,, \tag{5.56}$$

where $\xi_m = \rho_b K_B T/D$ is the motor friction coefficient per unit length and ρ_b the bound motor density. During tube growth ($0 < \dot{L} < V_0$) or in case the tube stalls ($\dot{L} = 0$), the drag force of the motors along the tube is in the direction of tube growth, meaning that the motors along the tube contribute to pull the tube with a force of order $\sim \xi_m L V_0$. Using typical values for the motor density ρ_b and tube force, this term is only important for tube lengths about 100 μm. The relevant length scale in the system is the characteristic length of force variation L_c, which is about $20\mu m$ (see section 5.2.2). Therefore, friction effects can be totally neglected during tube growth as long as the tube length does not reach values larger than 10^2 μm. On the other hand, when the tube retracts back to the vesicle, the tube velocity is much larger ($\dot{L} \sim 10^2\ \mu\text{ms}^{-1}$) and the friction of motors along the tube is not only relevant but essential. Indeed, tube retraction takes place because of the lack of motors pulling the tube at the tip, and the force F_M nearly vanishes. When this situation takes place, the only force left to balance the tube force is the friction force. Therefore, as friction is only relevant for large tube velocities $|\dot{L}| \gg V_0$, force balance (Eq. 5.55) can be expressed as

$$\xi_m L\dot{L} = F_M - F(L) \,. \tag{5.57}$$

[8] A more detailed analysis should account for the variation of the tube force along its length due to local friction forces along the tube.

The latter equation states that for motor forces at the tip F_M larger than the tube force $F(L)$, the tube grows ($\dot{L} > 0$), whereas if the motors at the tip cannot apply large enough forces to sustain the tube ($F_< F(L)$), the tube retracts.

The total motor force, F_M, results from the collective action of a number n_b of bound motors at the tip. If each single motor at the tip applies an average force f_m and assuming the motors to be independent from one another, the total motor force at the tip is $F_M = n_b f_m$. The motors at the tip move thus with a force-dependent velocity, V, which can be approximated by $V = V_0\left(1 - F_M/n_b f_s\right)$. At mean-field level, the velocity of the tube $\dot{L}$ corresponds to the velocity of the motors pulling the tube at the tip, so that $\dot{L} = V$. Rewriting force balance (Eq. 5.57) with the explicit dependence of the motor force F_M on the tube velocity $\dot{L}$, one obtains an equation for the tube velocity, which reads

$$\frac{\dot{L}}{V_0} = \frac{n_b - \frac{F(L)}{f_s}}{n_b + \frac{\xi_m V_0 L}{f_s}} \,. \tag{5.58}$$

If the number of motors at the tip n_b is large enough, the force applied to each motor is almost negligible and $\dot{L} \to V_0$. On the contrary, when the motors at the tip are not able to sustain the applied force ($n_b \to 0$), the tube retracts with velocity $\dot{L} = -F(L)/\xi_m L$.

In order to fully describe the dynamics of the tube we must account for the dynamics of the motors at the tip, which has already been discussed in section 5.3.1. We remind here that the dynamics of the number of bound motors at the tip can be written, from conservation arguments (Eq. 5.9), as

$$\frac{dn_b}{dt} = \hat{J}_b(L) - k_u(n_b) n_b \,, \tag{5.59}$$

where $k_u(n_b)$ is the detachment rate of the motors at the tip (Eq. 5.10). The flux of bound motors entering the tip region, $\hat{J}_b(L)$, is given by $\hat{J}_b(L) = (V_0 - \dot{L})\rho_b(L)$, and depends on the value of the bound motor density $\rho_b(L)$ at the tube-tip boundary. Although we have shown above that the motor density depends on the position along the tube and is larger in the vicinity of the tip, for the sake of simplicity, we assume here a uniform density of bound motors along the tube. Indeed, at leading order, the bound motor density along the tube is given by

$$\rho_b = 2\pi r \rho_\infty \frac{k_b}{k_b + k_u^0} = \frac{4\pi^2 \kappa \rho_\infty}{F(L)} \frac{k_b}{k_b + k_u^0} \,, \tag{5.60}$$

where the dependence of ρ_b on the tube force $F(L)$ arises from the dependence of the tube radius r on the membrane tension σ.

This simplified description of the bound motor density along the tube decouples the dynamics of the motors along the tube and those at the tube tip, and the equations above specify a two dimensional dynamical system for the variables n_b and L. As there is a one-to-one correspondence between the tube length L and the tube force F, we use n_b and F as variables. Scaling the tube length with the processivity length

of the motors $l_p \equiv V_0/k_u^0$, so that $\tilde{L} = L/l_p$, the relation between the normalized tube force $\tilde{F} \equiv F/F_0$ and $\tilde{L}$ can be written as $\tilde{L} = \beta g(\tilde{F})$, where $\beta \equiv L_c/l_p$ is the ratio between the characteristic length scale L_c of force variation and l_p, and $g(\tilde{F})$ is the function that defines how the dimensionless tube length $\tilde{L}$ increases with the normalized force $\tilde{F}$. For a vesicle in the entropic regime, $g(\tilde{F}) = 2\tilde{F}\ln\left(\tilde{F}\right)$ (Eq. 5.5), whereas for a vesicle in the elastic regime, $g(\tilde{F}) = \tilde{F}\left(\tilde{F}^2 - 1\right)$ (Eq. 5.7). Defining the normalized number of bound motors at the tip as $\tilde{n}_b \equiv n_b f_s/F_0$, the dynamics of the system is given by

$$\begin{aligned}
\frac{d\tilde{n}_b}{d\tau} &= \frac{\gamma e^f}{\tilde{F}}\frac{\tilde{F} + \tilde{n}_\xi(\tilde{F})}{\tilde{n}_b + \tilde{n}_\xi(\tilde{F})} - \exp\left(f\frac{\tilde{F} + \tilde{n}_\xi(\tilde{F})}{\tilde{n}_b + \tilde{n}_\xi(\tilde{F})}\right)\tilde{n}_b\,, \\
\frac{d\tilde{F}}{d\tau} &= A(\tilde{F})\frac{\tilde{n}_b - \tilde{F}}{\tilde{n}_b + \tilde{n}_\xi(\tilde{F})}\,,
\end{aligned} \tag{5.61}$$

where $\tau \equiv k_u^0 t$ is the time in units of $(k_u^0)^{-1}$ and $f \equiv f_s a/K_B T$ is a dimensionless parameter that quantifies the influence of the force on motor detachment. The parameter γ, defined as

$$\gamma \equiv \frac{4\pi^2 \kappa l_p f_s e^{-f}}{F_0^2}\frac{k_b}{k_b + k_u^0}\rho_\infty = \frac{\rho_\infty}{\rho_{\infty,2}^{min}}\,, \tag{5.62}$$

corresponds to the ratio of the initial surface density of motors on the vesicle, ρ_∞, and the threshold density $\rho_{\infty,2}^{min}$ (Eq. 5.32) found in section 5.3.1. Finally, the functions $\tilde{n}_\xi(\tilde{F})$ and $A(\tilde{F})$, which characterize the effects of friction and force increase respectively, are given by

$$\tilde{n}_\xi(\tilde{F}) \equiv \gamma e^f \tilde{\xi}\beta\frac{g(\tilde{F})}{\tilde{F}}\,, \qquad A(\tilde{F}) \equiv \left[\beta\frac{dg(\tilde{F})}{d\tilde{F}}\right]^{-1}\,, \tag{5.63}$$

where $\tilde{\xi} \equiv K_B T V_0/D f_s$ corresponds to the ratio of the motor friction $K_B T/D$ and the friction f_s/V_0.

The dynamical system in Eq. 5.61, together with the definitions above fully specify the dynamics of the tube. Note that there are only four dimensionless parameters that influence the dynamics, namely γ, β, $\tilde{\xi}$ and f. While $\tilde{\xi}$ and f are intrinsic motor parameters, the value of γ can be tuned by changing the motor density ρ_∞, and β can be changed by varying the characteristic length L_c, which depends on the radius of the vesicle R.

Stability analysis

In order to find out the different dynamical regimes, we perform a stability analysis of the dynamical system in Eq. 5.61. There is a single fixed point $\{\tilde{n}_b^c, \tilde{F}^c\}$ [9], given by

[9] For an introduction to dynamical systems, see Ref. (Guckenheimer and Holmes, 1990).

$$\tilde{n}_b^c = \sqrt{\gamma}\,, \qquad \tilde{F}^c = \sqrt{\gamma}\,, \tag{5.64}$$

that corresponds to the situation in which the tube velocity strictly vanishes ($\dot{L} = 0$, or $\dot{F} = 0$ equivalently) and the flux of bound motors reaching the tip region exactly balances the motor detachment flux at the tip, so that $dn_b/dt = 0$. There are not always solutions of Eq. 5.64. The length of the tube must be larger than zero. The value $F = F_0$, corresponding to vanishing tube length ($L = 0$), sets a minimal value of γ below which tubes cannot be extracted from the vesicle. This threshold value is given by $\tilde{F}^c = 1$ which corresponds to $\gamma = 1$ or, equivalently,

$$\rho_\infty = \rho_{\infty,2}^{min}\,. \tag{5.65}$$

We thus recover here the existence of a threshold in tube extraction, which we discussed in section 5.3.1. This threshold corresponds to the "stall regime" (Eq. 5.32), in which case the condition specifying the threshold is $dL/dt = 0$, which is fulfilled by definition at the fixed point. Note however that in order to find out the proper expression for the threshold density, one must perform the limit of vanishing length $L \to 0$ and analyze whether the condition of flux balance ($dn_b/dt = 0$) is more restrictive than the condition of zero tube velocity. This limit corresponds to the analysis performed for short tubes in section 5.3.1. We shall show below, when analyzing the stability of the fixed point, that it is also possible to recover the "flux limited regime".

We now study the stability of the system at linear level. The linearized dynamics for the perturbations $\delta\tilde{n}_b \equiv \tilde{n}_b - \tilde{n}_b^c$ and $\delta\tilde{F} \equiv \tilde{F} - \tilde{F}^c$ close to the fixed point read

$$\frac{d}{dt}\begin{pmatrix}\delta\tilde{n}_b\\ \delta\tilde{F}\end{pmatrix} = \underbrace{\begin{pmatrix} e^f\frac{(f-2)\tilde{F}^c-\tilde{n}_\xi\left(\tilde{F}^c\right)}{\tilde{F}^c+\tilde{n}_\xi\left(\tilde{F}^c\right)} & -e^f\frac{f\tilde{F}^c+\tilde{n}_\xi\left(\tilde{F}^c\right)}{\tilde{F}^c+\tilde{n}_\xi\left(\tilde{F}^c\right)} \\ \frac{A\left(\tilde{F}^c\right)}{\tilde{F}^c+\tilde{n}_\xi\left(\tilde{F}^c\right)} & -\frac{A\left(\tilde{F}^c\right)}{\tilde{F}^c+\tilde{n}_\xi\left(\tilde{F}^c\right)} \end{pmatrix}}_{\Lambda_c}\begin{pmatrix}\delta\tilde{n}_b\\ \delta\tilde{F}\end{pmatrix}\,, \tag{5.66}$$

where the matrix Λ_c specifies the linearized dynamics around the fixed point, and its stability is given by the real part of the eigenvalues of Λ_c (Guckenheimer and Holmes, 1990). The eigenvalues can be expressed in terms of the trace, $\mathrm{Tr}(\Lambda_c)$, and determinant, $\mathrm{Det}(\Lambda_c)$, which are given respectively by

$$\begin{aligned}\mathrm{Tr}(\Lambda_c) &= \frac{e^f\left[(f-2)\tilde{F}^c-\tilde{n}_\xi\left(\tilde{F}^c\right)\right]-A\left(\tilde{F}^c\right)}{\tilde{F}^c+\tilde{n}_\xi\left(\tilde{F}^c\right)}\,,\\ \mathrm{Det}(\Lambda_c) &= \frac{2e^f A\left(\tilde{F}^c\right)}{\tilde{F}^c+\tilde{n}_\xi\left(\tilde{F}^c\right)}\,.\end{aligned} \tag{5.67}$$

The stability analysis can thus be done studying $\mathrm{Tr}(\Lambda_c)$ and $\mathrm{Det}(\Lambda_c)$. The determinant of Λ_c is always positive because the tube force is an increasing function of the tube length, so that $dg\left(\tilde{F}^c\right)/d\tilde{F} > 0$ $\left(A\left(\tilde{F}^c\right) > 0\right)$, and the stability of the fixed point is entirely given by $\mathrm{Tr}(\Lambda_c)$. When $\mathrm{Tr}(\Lambda_c) < 0$ the fixed point is stable, meaning that

the membrane tube grows until a length $L = L_c g\left(\sqrt{\gamma}\right)$ and stalls there. Any small perturbation, either in the number of bound motors or the tube length, relaxes back to the same state. On the other hand, when $\mathrm{Tr}(\Lambda_c) > 0$ the fixed point is unstable, and any perturbation drives the system away from the fixed point. The transition from stable to unstable regimes is given by $\mathrm{Tr}(\Lambda_c) = 0$, which leads to

$$(f-2)\tilde{F}^c = e^{-f} A\left(\tilde{F}^c\right) + \tilde{n}_{\xi}\left(\tilde{F}^c\right) \ . \tag{5.68}$$

In case $f < 2$, there are no solutions for the latter equation, and the system is always stable ($\mathrm{Tr}(\Lambda_c) < 0$). Indeed, the parameter f was used in section 5.3.1 to distinguish between the two possible threshold regimes. We argued that in case $f < 2$, the "stall regime" is the actual threshold regime, whereas for $f > 2$ the "flux limited regime" provides the right threshold. Here we can review that finding. For $f < 2$ the system is always stable, meaning that the flux of motors reaching the tip is able to balance the detachment flux of motors at the tip. In this case, the condition of vanishing tube velocity ($dL/dt = 0$) is more limiting and the threshold is specified by Eq. 5.32. On the contrary, for $f > 2$ there may exist unstable regimes. The system is unstable when the flux of bound motors reaching the tip region is not able to compensate the motor detachment flux, leading to the detachment of all motors at the tip and the retraction of the tube. The condition of flux balance determines the threshold value in the "flux limited regime". This limit can also be recovered in the present description by setting $dn_b/dt = 0$ in Eq. 5.61 and $\tilde{F} = 1$, corresponding to the limit in which the tube force is constant and equal to F_0. The existence of stable solutions for the equation $\hat{J}_b(L) = k_u(n_b)$ specifies the threshold value, which is given by Eq. 5.30.

Oscillations in tube length

In case the system is above the threshold value, tubes can be extracted from the vesicle. As discussed above, if the fixed point is stable, tubes grow and eventually stall at a length $L = L_c g\left(\sqrt{\gamma}\right)$. On the contrary, when the fixed point is unstable any perturbation drives the system away from the fixed point. The dynamics of the system in the unstable regime is governed by full non-linear original dynamical system (Eq. 5.61).

Numerical integration of the dynamical system (Eq. 5.61) in the linearly unstable regime leads to sustained oscillations of the tube length (Fig.5.14b). This oscillatory behavior is in good qualitative agreement with the experimental observations (Fig.5.14a). The experiments were performed by C. Leduc using the experimental set-up described in section 5.1. The oscillations are composed of a growth phase and a fast retraction phase separated by a rapid switch (Fig.5.14). The motor attachment/detachment kinetics sets the time scale for the switching between growth and retraction phases, and is much shorter than the characteristic time scale of tube growth. This difference in time scales explains the sawtooth shape of the oscillations. The origin of the oscillations is the interplay between the collective force-dependent detachment of motors at the tip and the variation of the tube force with its length. Once the tube is pulled out of the vesicle, the tube growth induces progressively an

increase of vesicle tension. As a result, the motors at the tip must overcome increasing forces upon tube extraction. At some point, the force becomes too large and the detachment events at the tip cannot be equilibrated by the flux of motors reaching the tip region. There is then a sudden loss of motors (Fig.5.14c). In the absence of motors to pull the tube, this retracts suddenly until a point where the force is low enough to allow again for tube growth. The velocity of the tube in the retraction phase is very large, because the friction along the tube is small. Although it is not possible to measure such large velocities in these experiments, we can determine a lower bound for the absolute value of the retraction velocity of $|\dot{L}| = 50\ \mu$m/s. This value is consistent with the measured values of tube retraction velocities at similar values of the vesicle tension (Rossier et al., 2003).

The numerically obtained oscillations in Fig. 5.14b are in good qualitative agreement with the experimental observations (Fig. 5.14a). Unfortunately, it was not possible to determine the precise value of all parameters in the experiments where oscillations were observed. Although we use the known values of all known parameters, the values of the vesicle radius and ρ_∞ used to perform the numerical integration do not necessarily correspond to those in the experiments. Moreover, the dynamical system in Eq. 5.61 is very stiff, and its numerical integration is difficult. In order to overcome this problem, we have artificially added a constant contribution to friction $\tilde{n}^0_\xi$ ($\tilde{n}_\xi \to \tilde{n}_\xi + \tilde{n}^0_\xi$) so that the retraction phase is slower. Although this method reduces the stiffness of the dynamical system and allows its numerical integration, it also modifies the dynamics of the retraction phase. In particular, the amplitude and period of the oscillations are affected by the value of $\tilde{n}^0_\xi$. In spite of the intrinsic stiffness of the dynamical system, our simplified description does not properly account for the physics of the retraction phase. We are currently working to understand the mechanism that stops a retracting tube.

Dynamical regimes

The possible dynamical regimes of the system depend on four dimensionless parameters: γ, β, $\tilde{\xi}$ and f. Using the experimental values for D, V_0 and f_s (see discussion in section 5.3.1), it is possible to estimate the dimensionless motor friction $\tilde{\xi}$ to be $\tilde{\xi} \simeq 4.1\,10^{-4}$. In a typical experiment, there are several vesicles in the same observation chamber with different radius, R, ranging approximately from 1 μm to 15 μm. Moreover, the initial surface density of motors on the vesicle, ρ_∞ can be varied in the experiments. Therefore, we analyze the dynamical regimes of the system as a function of γ and β, corresponding to variations in ρ_∞ and R respectively. Although the parameter f can also be estimated from f_s and a to be $f \simeq 2$, we vary it slightly around this value to see its effect on the dynamical regimes.

In Fig. 5.15a we plot the different dynamical regimes as a function of the parameters γ and β, for vesicles in the entropic (Fig. 5.15a.1) and elastic regimes (Fig. 5.15a.2) and $f = 2.03$. The transition between stable and oscillatory regimes corresponds to a Hopf bifurcation and is given by the solution of Eq. 5.68. Oscillations are more likely to appear close to threshold. These oscillations correspond in

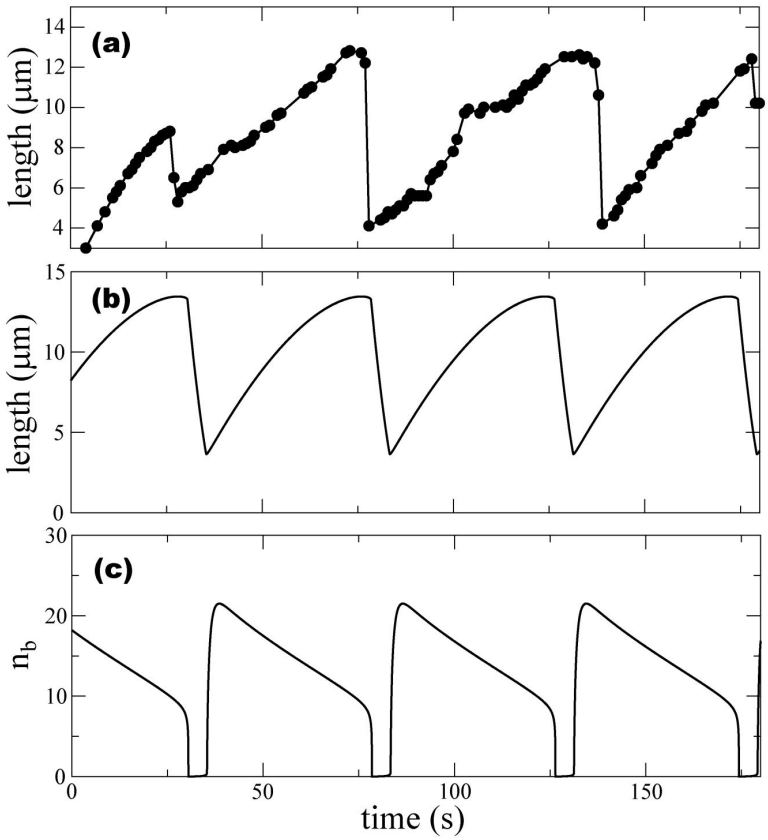

Fig. 5.14. Oscillations of a membrane tube. (a) Example of the tube oscillations observed experimentally. Length of the tube as a function of time, obtained by determining the position of the tube tip in each frame. (Experiments performed by C. Leduc). (b-c) Numerically obtained time evolution of the tube length (b) and number of bound motors at the tip (c), in the unstable regime. Parameters: $\gamma = 7.3$, $\tilde{\xi} = 4.1\,10^{-4}$, $f = 2.3$ and $\beta = 1.73$. The time scale is set by $k_u^0 = 0.42\ \mathrm{s}^{-1}$, the length scale by $l_p = 1.43\ \mu$m and the scale for the number of bound motors by $F_0/f_s = 3.3$. An extra constant contribution to friction ($\tilde{n}_\xi \to \tilde{n}_\xi + 0.55$) was artificially added to allow the numerical integration, because the dynamical system is too stiff otherwise.

most cases to the full retraction of the tube back to the vesicle and the subsequent initiation of tube growth. This feature is in qualitative agreement with the experimental observations for vesicles in conditions close to threshold. Indeed, if the motor density ρ_∞ is below the threshold value, oscillations in the vesicle shape are also observed. Although the motors are not able to pull membrane tubes below threshold, the vesicle is deformed due to the action of the motors. The force acting on the motors increases as the vesicle is increasingly deformed. When the force acting on the motors is too large, the motors pulling at one point of the vesicle detach and the vesicle relaxes. These oscillations in vesicle shape below threshold can be understood by the same

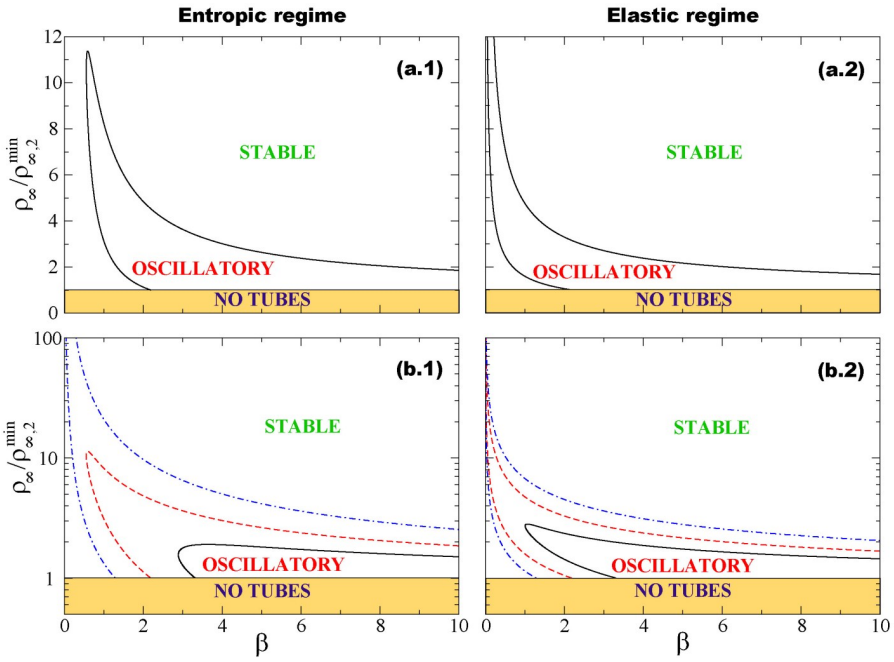

Fig. 5.15. Dynamical regimes as a function of the parameters $\gamma = \rho_\infty/\rho_{\infty,2}^{min}$ and $\beta = L_c/l_p$. In all cases the dimensionless motor friction parameter is $\tilde{\xi} = 4.1\,10^{-4}$, which corresponds to the experimentally measured value. The figures on the left correspond to a vesicle in the entropic regime, so that $g(\tilde{F}) = 2\tilde{F}\ln(\tilde{F})$, and those on the right correspond to a vesicle in the elastic regime, i.e. $g(\tilde{F}) = \tilde{F}(\tilde{F}^2 - 1)$. (a) Dynamical regimes for both entropic (a.1) and elastic (a.2) regimes of the vesicle and $f = 2.03$. (b) Dynamical regimes for both entropic (b.1) and elastic (b.2) regimes of the vesicle and different values of f: $f = 2.02$ (continuous line), $f = 2.03$ (dashed line) and $f = 2.5$ (dashed-dotted line). Note the strong dependence of the size of the oscillatory region on f.

instability mechanism described above for the oscillations in tube length. On the other hand, for large values of the surface density of motors ρ_∞ ($\rho_\infty \gg \rho_{\infty,2}^{min}$), stable states are predominant. Indeed, if a large number of motors are available, the flux of bound motors reaching the tip region is considerable and the system is, in general, more stable. Above the minimal motor density allowing tube extraction both stable and oscillatory states typically exist. For small enough and large enough values of β, tubes are stable. In between, there is a range of values of β for which the tubes oscillate. For clarity, in Fig. 5.16 we plot the dynamical regimes as a function of ρ_∞ and the radius of the vesicle, R, for a vesicle in the entropic regime and $f = 2.03$. Close to threshold, oscillations are expected for almost all the vesicle radius tested experimentally. When the motor density is increased slightly above the threshold value ($\rho_\infty \gtrsim \rho_{\infty,2}^{min}$), the range of vesicle radii for which oscillations should be observed is very small. This result is in qualitative agreement with the experimental observa-

tions as the oscillatory behavior was never observed for very small ($R \simeq 1\ \mu$m) or very large ($R \simeq 15\ \mu$m) vesicles.

The oscillatory region in the parameter space is strongly dependent of the parameter f, for vesicles in both the entropic and elastic regimes (Figs. 5.15b.1, b.2 respectively). As discussed above, for $f < 2$ there is not oscillatory region at all (Eq. 5.68), and the size of the oscillatory region rapidly increases as f is increased above $f = 2$. The existence of oscillations in the experiments suggests that $f > 2$, corresponding to $f_s a > K_B T$. Using the experimentally measured values of $f_s \simeq 6$ pN and $a \simeq 1.3$ nm for conventional kinesin motors (Visscher et al., 1999; Schnitzer et al., 2000), one obtains $f \simeq 2$. However, recent experiments on conventional kinesin report larger values of the stall force, $f_s \simeq 7$ pN (Carter and Cross, 2005; Nishiyama et al., 2002), that lead to $f \simeq 2.2$. Unfortunately, a quantitative characterization of the oscillations has been proved difficult experimentally. Indeed, tube oscillations are rarely observed, suggesting that the oscillatory region in the parameter space is small, in accordance with our predictions for values of f close to $f = 2$ (Fig. 5.16).

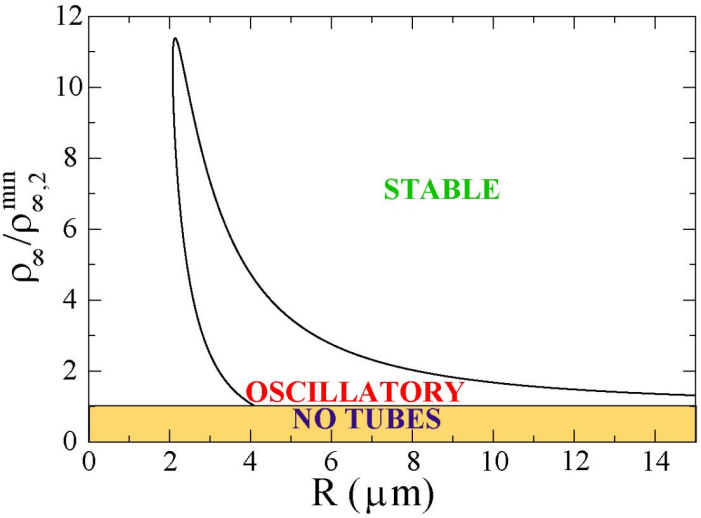

Fig. 5.16. Dynamical regimes for a vesicle in the entropic regime as a function of the motor density ρ_∞ and the vesicle radius R ($f = 2.03$ and $\tilde{\xi} = 4.1\,10^{-4}$). The conversion of β to R requires the expression of the characteristic length of force increase in the entropic regime L_c^{ent} (Eq. 5.6), and the parameters: $\kappa = 10 K_B T$, $l_p = 1.2\ \mu$m, $F_0 = 5$ pN.

Our results concerning the dynamical regimes are in good qualitative agreement with the experimental observations. It is thus likely that the instability mechanism we propose, where the oscillations arise from the interplay between the collective force-dependent motor kinetics and the force increase upon tube extraction, is reasonable. On the other hand, using the experimentally measured values for the parameters, the oscillations obtained from the theoretical description in this section do not match

the amplitude of the observed oscillations. We believe that our simplified description does not capture the mechanism that stops a membrane tube undergoing a retraction. We are currently extending this work to better understand the behavior of oscillating tubes.

5.4 Simulations

In the last section, we described, at mean-field level, how molecular motors dynamically associate at the tip of membrane tubes and collectively generate the necessary force to pull the tube. Although this approach already accounts for several important experimental observations, like the existence of a threshold in tube extraction or the oscillatory behavior, it cannot answer other important questions. In particular, the solutions of the mean-field analysis show that the actual number of motors pulling the tube can be as low as 4, suggesting a crucial role of the fluctuations. Moreover, the mechanism by which motors are able to cooperate and apply large forces requires the analysis of their mutual interactions and organization at the tip. In this section, we address these questions using continuous-time Monte Carlo simulations of the process of tube extraction.

5.4.1 Implementation of the simulation

Kinesin motors walk along microtubules by a sequence of discrete steps (see chapter 1). A single motor jumps from a given tubulin dimer to a neighboring one with a certain rate. Conventional kinesin motors are highly biased, meaning that the rate at which the motors step forward to the next tubulin dimer is much larger than that at which the motors step backward (at vanishing load). We adopt this discrete microscopic approach in the simulations and neglect, for simplicity, the backward stepping of the motors. Note that at large length scales and long time scales, this stochastic discrete motion can be well described using a coarse-grained continuum theory. This continuum approximation of motor motion was used in the previous section, as we were interested in the dynamics of membrane tubes at time and length scales larger than those of individual motor stepping.

We consider a single protofilament of a microtubule and describe it as a one dimensional lattice, composed of individual sites (Fig. 5.17a). The size of each site is ℓ and reflects the periodicity of the filament (tubulin dimers). The membrane tube is composed of N sites, where the site numbered 0 determines the boundary with the vesicle and site N locates the very tip of the tube. A motor at a given site can either be bound to or unbound from the microtubule. When bound to the microtubule, the motor can step forward to the next site, if empty, with a rate k_f or detach from the filament at a rate k_u [10]. The unbound state represents motors attached to the tube, but not to the microtubule, and therefore many motors can be placed in this state

[10] The particular choice for the rates in the different regions of the tube is discussed below.

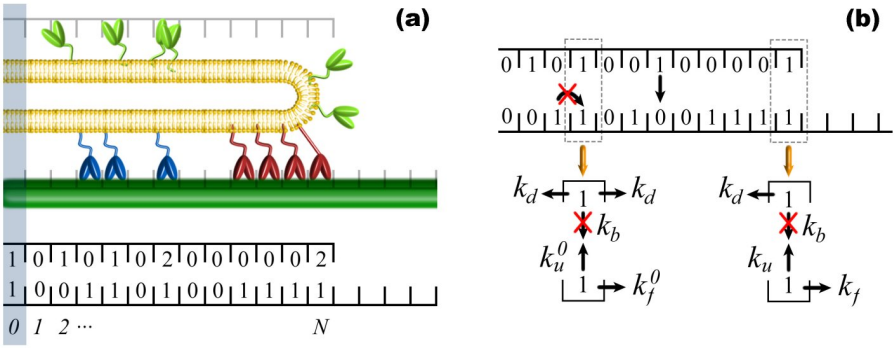

Fig. 5.17. (a) Sketch of a growing tube (top) and its coded representation in the simulations (bottom). The boxes along the microtubule (dark green) represent binding sites for motors. The tube (yellow) is also discretized, using the same one dimensional lattice as for the microtubule. The sites are labeled from 0 to N, with 0 and N corresponding respectively to the left boundary (e.g. tube-vesicle boundary) and to the position of the leading motor, which defines the position of the tube tip. In the coded representation, the number in each site represents the number of motors occupying that site. Along the microtubule, the sites may be either empty or occupied by one bound motor (light blue and red) at most, which corresponds respectively to occupation numbers 0 and 1 in the code. Along the tube, each site may be occupied by several unbound motors (light green), corresponding to an integer occupation number in the code. (b) Possible transition rates of bound and unbound motors. There are 5 possible motor transitions at a given location along the tube: forward motion of bound motors (with rates k_f^0 and k_f respectively for bound motors along the tube or at the tip), bound motor detachment (with rates k_u^0 and k_u respectively for bound motors along the tube or at the tip), unbound motor attachment (with rate k_b) and forward and backward unbound motor diffusion (with rate k_d in both cases). The particular choice for the rates is discussed in the main text.

at a given spatial position [11]. Unbound motors diffuse along the tube with diffusion constant D and stochastically attach to the microtubule at a rate k_b in case there is no bound motor at that site. In the present discretized system, the diffusion of the motor along the tube is characterized by a diffusion rate $k_d = D/\ell^2$, no matter whether the motor diffuses forward or backward as the diffusion process is symmetric. In Fig. 5.17b we sketch the possible transitions that motors can undergo, each one of them characterized by a rate. Besides diffusion, unbound motors move also as a consequence of the tube motion. This unbound motor movement is described below, when discussing the rules determining the tube dynamics.

Each site contains all the information of a given position, namely the motors at that spatial location, their states and their associated rates. The rates may depend on the location along the microtubule and can also change over time. The reason to allow for spatio-temporal variations of the rates is that, in several biological situations,

[11] Although excluded volume effects also exist on the surface of the tube, the number of unbound motors in this state is typically small as $k_b >> k_u^0$, and one can safely assume no restriction for the number of unbound motors.

spatio-temporal force fields are applied to the motors, leading to spatial and temporal changes of the forward and detachment rates of motors. The case of tube extraction is a particularly simple example as the rates of the motors along the tube (those that do not apply force) are constant in space and time. It is only close to the tip, where motors generate the force to pull the tube, that the rates depend on both space and time (see below).

This type of non-equilibrium systems, where self-propelled particles (like motors) undergo stochastic transitions, are generically called self-driven diffusive systems. There are several examples that have been extensively studied in the literature in simplified conditions (Lipowsky et al., 2001; Parmeggiani et al., 2003). Most of these studies use discrete space and time Monte Carlo simulations as the transition rates of the particles are constant quantities. The principal drawback of this approach is that either the rates or their range of variation have to be known *a priori* in order to set the time step of the simulation. There are systems in which the rates may depend on the configuration of the system at a given time and their values may be difficult to know *a priori*. Although the discrete space and time Monte Carlo methods can be adapted to simulate the particular case of tube extraction by motor proteins, it is more suitable to use continuous-time Monte Carlo simulations, where the rates can be varied during the simulation with no constrains.

We have adapted the Gillespie Algorithm for chemical reactions (Gillespie, 1976), which was originally thought for spatially homogeneous systems, to the case of particle transitions with spatio-temporal dependent rates. The idea behind the simulations is very intuitive. Every particle (motors) can undergo several transitions, each one of them characterized by a certain transition rate. The time for each transition to occur is a stochastic variable distributed exponentially, with a characteristic time scale equal to the inverse of the transition rate. In order to know which transition takes place in the system and the time it takes to occur, one calculates the stochastic time at which each one of all possible transitions would occur. The smallest of these times determines the reaction that takes place. In spite of its simplicity, the straightforward implementation of this algorithm is not optimal. In Ref. (Gillespie, 1976) it is shown that the probability distribution for the time of a transition to occur (no matter which one) and the probability distribution for the transition that takes place can be decoupled. Using this result, there exists a more efficient method to implement the algorithm (Gillespie, 1976). We adapt here this algorithm (know as Gillespie Algorithm) to the case of spatially extended systems with time dependent transition rates.

The system is characterized by a rate matrix $k_{i,j}$, where $i \in [0,N]$ specifies the site and $j \in [0,r-1]$ the motor transition (r being the number of possible motor transitions; $r = 5$ in the present case). We order the transitions as follows: $k_{i,0} = k_f(i)$, $k_{i,1} = k_u(i)$, and $k_{i,2} = k_b(i)$, $k_{i,3} = k_{i,4} = k_d(i)$. Note that the rate matrix does not contain information about the motors occupying the sites. In order to account for the actual potential transitions, we define a global array in the system, a_l, with $l \in [0,Nr]$, that characterizes the rates of all possible potential transitions, and it is defined as the number of motors that can undergo a particular transition times the rate of that transition: $a_{ir} = n_b(i)k_{i,0}$, $a_{ir+1} = n_b(i)k_{i,1}$, $a_{ir+2} = n_u(i)k_{i,2}$, $a_{ir+3} = n_u(i)k_{i,3}$ and

$a_{ir+4} = n_u(i)k_{i,4}$, where $n_b(i) \in [0,1] \subset \mathbb{N}$ and $n_u(i) \in \mathbb{N}$ are, respectively, the number of bound and unbound motors at site i (occupation numbers). Regardless of the internal order of the array a_l, it can be now seen as the array of all possible potential transition rates, l varying from 0 to Nr, which is the total number of possible transitions in the system. Once the potential transitions rates are given, we define the global transition rate as

$$k_g \equiv \sum_{l=0}^{Nr} a_l \,. \tag{5.69}$$

Unlike discrete-time Monte Carlo simulations, where the time step of the simulation is set *a priori*, here it is necessary to know the time Δt at which the next transition takes place. This time is a stochastic variable distributed exponentially with a characteristic time scale $1/k_g$. Note that this time does not specify a particular transition of a certain motor, but only determines how long we have to wait to see a motor (no matter which) performing a transition. The time Δt is obtained by taking an exponentially distributed random number, with $1/k_g$ as the characteristic time scale of the exponential distribution (Gillespie, 1976). The actual transition that takes place is a stochastic variable distributed uniformly and is calculated as follows. Generate a stochastic number y distributed uniformly in the range $[0,k_g]$ and define m as an integer number in the range $[0,Nr]$. The value of m that specifies the transition that occurs is the largest value of $m \in [0,Nr]$ that fulfills the following inequality:

$$\sum_{l=0}^{m} a_l < y \,. \tag{5.70}$$

The actual site i at which the transition takes place and the particular transition j, are given respectively by the integer part and the module of m/r.

The simulation evolves as follows. The system is initialized in a configuration with an initial number M_i of consecutive bound motors, the first one defining the position of the very tip of the tube, so that the length of the tube N is $N = M_i$. Then, the rate matrix is calculated, and the array a_l is obtained from the system configuration and the rates. The value of the global transition rate k_g is calculated for the initial configuration. Then, the following steps are repeated until a time t_{max}:

- (step 1) Determine the stochastic time Δt at which the next transition occurs, the site i at which the transition takes place and the actual transition j.
- (step 2) The transition is performed if allowed by excluded volume interactions and the time t is updated to $t + \Delta t$.
- (step 3) The transition rates $k_{i,j}$ are then updated with the new configuration (it is not necessary to update all transition rates in the system, except if these depend explicitely on time).
- (step 4) The array a_j is updated with the new configuration and rates.
- (step 5) The global transition rate k_g is updated.
- (step 6) Go back to step 1.

So far, we have described the algorithm without specifying the transition rates of the motors. Indeed, this part of the algorithm determines the transitions of the

motors, given the rate matrix and a particular configuration, but does not specify the dynamics of tube growth. The dynamics of the tube is specified by the rates of the motors under applied load in the vicinity of the tube tip, and by a set of special rules for the growth events. We can thus study the mechanism by which motors cooperate to pull the tube by analyzing the growth dynamics of the tube with different motor organizations at the tip and different ways of cooperation between the motors.

The boundary conditions and the dependence of the rate matrix on the position and configuration of the system are thus essential features to determine the growth process. The left boundary (Fig. 5.17a) characterizes the contact of the tube with the vesicle and controls the fluxes of the motors getting in and out of the tube. The transition rates of the motors under applied load (close to the tube tip; right boundary) affect critically the growth dynamics and are discussed in detail below.

Transition rates along the tube

The motors in this region are not subject to any force and their rates are constant regardless the position and time (Fig. 5.18a). A bound motor moves forward with rate $k_f = V_0/\ell$ and detaches at a rate $k_u = k_u^0$ (Fig. 5.18b). In the unbound state, the motors diffuse at a rate $k_d = D/\ell^2$ and attach to the microtubule at a rate k_b. Using the experimentally measured values of the different parameters (see chapter 1 and discussion in section 5.3.1), the values for the rates of motors along the tube are: $k_f = 75\ \mathrm{s}^{-1}$, $k_u^0 = 0.42\ \mathrm{s}^{-1}$, $k_b = 4.7\ \mathrm{s}^{-1}$ and $k_d = 15625\ \mathrm{s}^{-1}$ ($\ell \simeq 8$ nm).

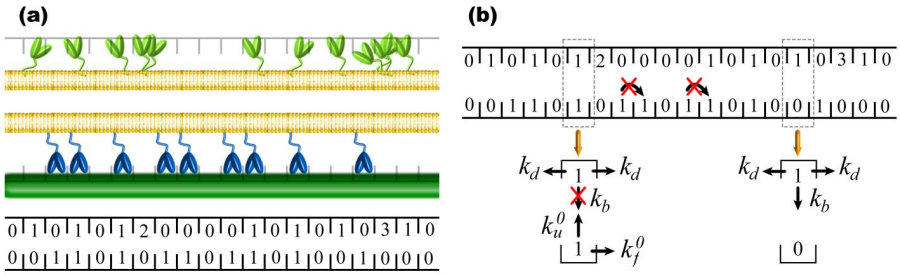

Fig. 5.18. (a) Sketch of a portion of the tube (top; the boundaries are not shown) and the coded representation for this particular motor configuration (bottom). (b) Particular choice of the transition rates for motors along the tube. An unbound motor in a given site can attach to the corresponding site along the microtubule if empty (with rate k_b), and diffuse to the neighboring sites along the tube (with rate k_d). A bound motor at a given site can step forward to the next site provided it is empty (with rate k_f^0), and detach from the microtubule to the corresponding site along the tube (with rate k_u^0).

Vesicle-tube contact (left boundary)

The boundary with the vesicle is characterized by special rules that account for the boundary conditions (Fig. 5.19). This boundary is constituted solely of the site numbered 0 (Fig. 5.17) which is not a part of the tube itself and acts only as a control site for the fluxes getting in and out of the tube. The rates at this site are different from all the sites that constitute the tube as these must account for the fluxes of motors entering and leaving the tube. In order to fix the motor fluxes at this position, we impose an occupation number of 1 in both the bound and unbound states, so that $n_b(i=0)=1$ and $n_u(i=0)=1$ (Fig. 5.19b). The rate at which bound motors enter the tube is given by the flux of bound motors, J_b, at this boundary (site 0). When a motor is stochastically introduced into the system through the bound state, the occupation number at site 1 is increased by one ($n_b(i=1)=0 \rightarrow n_b(i=1)=1$) provided it is empty, and the occupation number at site 0 remains $n_b(i=0)=1$ (Fig. 5.19b). Therefore, the bound state of site 0 constitutes a source of motors that enter the tube at rate J_b.

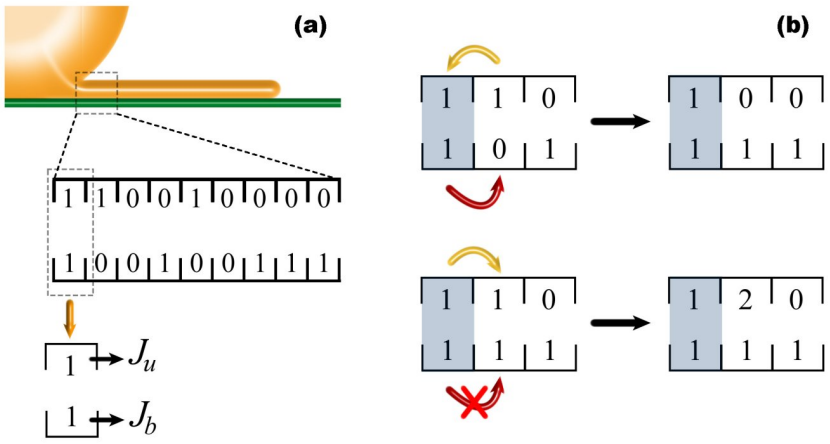

Fig. 5.19. (a) Sketch of the tube-vesicle boundary (top) and a detail of the tube in the vicinity of this boundary showing an arbitrary motor configuration in the coded representation (bottom). The site numbered 0 constitutes the tube-vesicle boundary, and the occupation numbers for both bound and unbound states at this site are fixed to $n_b(i=0)=n_u(i=0)=1$. The bound and unbound fluxes of motors entering the tube are J_b and J_u respectively. (b) Possible motor transitions at the boundary. Only the boundary site 0 and the two first sites of the tube are shown. The site constituting the boundary (site 0) is shown in gray. Bound motors cannot enter the tube if a bound motor is occupying the site 1, and an unbound motor at site 1 leaves the tube if it transits to site 0 (top). A bound motor can enter the tube at site 1 if empty and unbound motors can enter the tube at site 1 with no restriction in the previous occupation number at this site (bottom).

The control of the flux in the unbound state is more complex as it depends on the velocity V of the tube, which is set by the own dynamics of the whole system and not known *a priori*. As in the bound state, we impose an unbound motor flux, J_u, at site 0, which corresponds to the flux of unbound motors entering the tube. This flux depends on the average velocity of the tube V and cannot be known *a priori*. In order to overcome this problem, we initially assume the velocity of the tube to be V_0 when considering the unbound motor flux at site 0, and run the simulation. We determine the actual average velocity V and run the simulation again with the new value of V. Repeating this procedure recursively, the value of the unbound motor flux converges to the actual value set by the the own dynamics of the tube. In our particular problem only to recursions are needed to obtain the actual value of J_u. There also exists a flux of unbound motors leaving the tube at site 0. When an unbound motor at site 1 transits to the left (site 0), we consider this unbound motor to leave the tube (Fig. 5.19b). Therefore, the unbound state at site 0 acts both as source and sink of unbound motors. There are several ways by which unbound motors can leave the tube. A motor at site 1 which diffuses to site 0 is considered to leave the tube. However, when the tube retracts, many unbound motors can leave the tube simultaneously, as we shall explain below.

Although the actual values for the bound and unbound motor fluxes depend on the details of the contact between the tube and the vesicle, we use here a simplified description where the motor fluxes entering the tube, expressed in the laboratory reference frame, read

$$J_b = \rho_b^\infty V_0 \,, \qquad J_u = \rho_u^\infty V \,. \tag{5.71}$$

These expressions for the bound and unbound motor fluxes entering the tube, J_b and J_u respectively, only account for the convective components of the fluxes. We have shown in section 5.3.1 that once a tube is pulled, there is a central region of the tube in contact with the microtubule which is characterized by the homogeneous equilibrium densities ρ_b^∞ and ρ_u^∞ given by Eq. 5.44. In this region of the tube there is no net diffusive unbound motor flux. Therefore, our particular choice for the fluxes in Eq. 5.71 provides a good description of the tube from the region where the average motor densities are the equilibrium ones to the tip of the tube and can properly account for the growth of the tube. During the initial stages of tube extraction, the bound and unbound motor densities at the contact with the vesicle are given by the equilibrium densities, which in this case read: $\rho_b^\infty = 2\pi r_0 \rho_\infty \left(k_b/(k_b + k_u^0)\right)$ and $\rho_u^\infty = 2\pi r_0 \rho_\infty \left(k_u^0/(k_b + k_u^0)\right)$ (see section 5.3.1). In this case, the motor flux entering the tube is given by Eq. 5.71. Note that there is also a diffusive flux of unbound motors toward the vesicle. In the simulations, we account for this unbound motor flux by removing from the tube the unbound motors that reach the left boundary by diffusion.

Using the experimentally measured values for the parameters, the unbound motor flux is negligible compared to the bound motor flux. Therefore, the simulations provide a fairly good description of the system when the bound motor flux entering the system can be expressed in the form of Eq. 5.71, which is the case for both the initial process of tube extraction and tube growth.

Tube tip (right boundary)

This region specifies the growth dynamics of the tube and it is thus of crucial importance. In order to study the differences in tube growth that arise from different motor organizations at the tip and different ways of cooperation between the motors, we propose three different scenarios. By comparing the results of the simulations for these different cases with the experimental data, we aim at understanding how motors do cooperate and organize to pull the tube.

There are general rules that can be established for the tube dynamics, independently of the organization and cooperation of the motors at the tip. If the bound motor at site N (the very tip of the tube) steps forward, the tube grows by on site ($N \rightarrow N+1$). On the other hand, if the leading motor at site N detaches from the microtubule, there is no bound motor to sustain the tube at the tip and the tube instantaneously moves backward to closest site containing a bound motor (Fig. 5.20). Indeed, the instantaneous tube retraction is legitimate as the time needed for the tube to retract is much smaller than the time for forward motor stepping. When the tube moves either forward or backward, the bound motors along the tube remain at their respective sites as they are bound to the microtubule and the drag force applied on each one of them arising from the tube motion is negligible (see section 5.3.1). On the contrary, the motors in the unbound state follow the motion of the tube because the viscosity of the membrane is larger than the bulk viscosity. Therefore, when the tube moves forward or backward all the unbound motors along the tube move accordingly (Fig. 5.20). Note that some of the unbound motors located in the vicinity of the left boundary (tube-vesicle boundary) leave the tube as a result of a tube retraction.

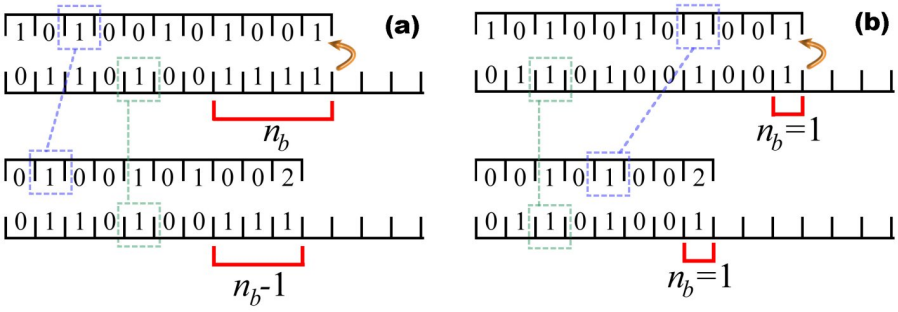

Fig. 5.20. Tube retraction caused by the detachment of the leading motor. A portion of the tube in the vicinity of the tube tip is shown in the coded representation used in the simulations. Two different motor configurations are shown (a,b). Configuration before the detachment of the leading motor (top) and resulting configuration after detachment (bottom). The tube retracts up to the position of the closest bound motor. The bound motors along the tube do not change their positions upon retraction (light green dashed box). Unbound motors are dragged by the tube and change their positions accordingly upon retraction (light blue dashed box). The number of consecutive bound motors at the tip is n_b.

Once the general rules for the tube motion are specified, we describe the different scenarios concerning the cooperation and organization of motors in the vicinity of the tip (Fig. 5.21).

Cluster tip

This scheme intends to model two important features, namely the coordination of the motors and their ability to transmit the forces when they are in contact to each other.

In this scenario, the first n_b consecutive bound motors share the force to pull the tube (Fig. 5.21a). This situation models the case in which the motors are able to "transmit" the force to each other when they are in contact in a row-like configuration. Moreover, this particular scheme highlights a possible coordination between the motors: when the first motor in the cluster (the leading motor, placed at site N) steps forward, the other motors in the cluster step also forward (Fig. 5.21a). The n_b consecutive motors at the tip can thus be seen as a compact cluster able to apply forces larger than the individual motors. Note however that the number of motors constituting the cluster, n_b, is not fixed. It is a stochastic variable that depends on the kinetics of the motors.

The forward stepping rate, $k_f(n_b)$, and detachment rate, $k_u(n_b)$, of the motors in the cluster are affected by the tube force and given respectively by

$$k_f(n_b) = \frac{V_0}{\ell}\Theta\left(1 - \frac{F}{n_b f_s}\right), \qquad k_u = k_u^0 \exp\left(\frac{Fa}{K_B T}\frac{1}{n_b}\right), \tag{5.72}$$

where $\Theta(z)$ is the Heaviside step function. We impose a vanishing forward rate in case the force applied on the motor is larger than f_s in order to account for recent experimental observations on conventional kinesin (Carter and Cross, 2005). The remaining rates, k_b and k_d, are the same than for the motors along the tube and were discussed above.

Variable tip

This scheme emphasizes the capacity of the motors to transmit the forces when they are in contact, but the motors do not have any coordination mechanism; they are totally independent from one another.

Similarly to the previous scheme, the first n_b consecutive bound motors share the force to pull the tube (Fig. 5.21b), highlighting the transmission of forces by motors in contact. The absence of coordination between the motors is manifest in the motion of the first motor. When this steps forward, the remaining motors in the cluster do not follow it and remain at their respective sites (Fig. 5.21b).

The expressions for the transition rates of the motors are the same than in the previous scheme. In particular, the force-dependent rates, k_f and k_u, are given by Eq. 5.72. Note however that although the expression is the same, the dynamics of the stochastic variable n_b is totally different and, as a consequence, the dynamics of the tube differs also significantly from the "cluster tip" scheme. Consider, for instance, the forward stepping of the leading motor (Fig. 5.21b). Unlike in the "cluster tip" scheme (Fig. 5.21a), when this situation takes place the leading motor must sustain the tube alone, increasing considerably its detachment rate.

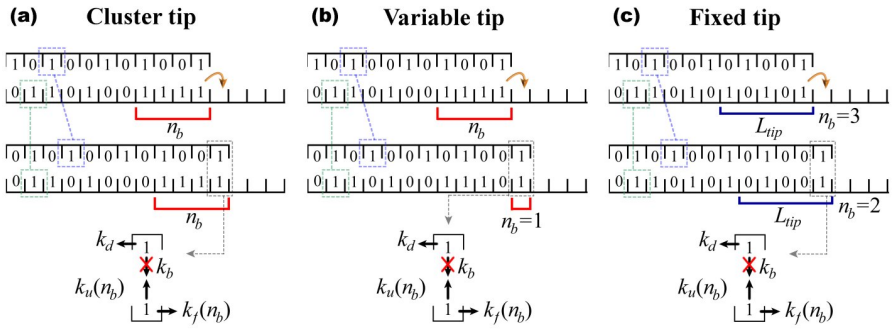

Fig. 5.21. Dynamics of tube growth for the three different organizations of motors pulling the tube at the tip. A portion of the tube in the vicinity of the tube tip is shown in the coded representation used in the simulations. Configuration before the forward stepping of the leading motor (top) and resulting configuration after the motor step (bottom). In all cases, when the tube grows, the unbound motors along the tube follow the motion of the tube accordingly (light blue dashed box). On the contrary, the bound motors along the tube remain at their positions (light green dashed box). (a) Cluster tip: The forward stepping of the leading motor is followed by all the consecutive motors constituting the tip (red line). (b) Variable tip: The forward stepping of the consecutive motors constituting the tip (red line) is independent. (c) A number n_b of bound motors in the tip region of size L_{tip} (blue line) act collectively to pull the tube, and their forward stepping is independent.

Fixed tip

In contrast to the previous scenarios, the present scheme models the case where the motors cannot transmit the forces to each other when they are in contact and no coordination exists between them. Only the motors which apply normal forces to the membrane can contribute to pull the tube. The curvature of the tip of the tube defines then a region of fixed size L_{tip} (or N_{tip} sites of size ℓ equivalently) where the motors can apply normal forces to the membrane, no matter whether they are consecutive or not (Fig. 5.21c). This model introduces a parameter, the number of sites N_{tip} where the motors can contribute to pull the tube. Typical values for the curvature of the tube at the tip ($\sim 1/r_0$) suggest $N_{tip} \in [1,4]$ (corresponding to radius of curvature in the range $r_0 \simeq 8-32$ nm). We analyze below the differences in tube growth for different values of the size of the tip.

The number of bound motors, n_b, in the tip region is a stochastic variable that can vary in the range $[1,N_{tip}]$. The fact that motors cannot transmit the forces to each other is manifest in different configurations sketched in Fig. 5.21c. For example, consider the case where the tip region is constituted of four sites ($N_{tip} = 4$) and besides the necessary bound motor at site N (leading motor), there is only another motor in the tip region placed in the site numbered $N-3$. Both motors contribute to pull the tube in spite of being two sites with no bound motors between them. Moreover, in case there is a bound motor at the site numbered $N-4$ (outside the tip region), and thus in contact with the last motor in the tip region, this motor does not

contribute to pull the tube. The dynamics of the motors in the tip region are totally independent from one another, meaning that no coordination between the motors exists.

The expressions for the transition rates of the motors are the same than in the two previous schemes. Again, the difference stems in the dynamics of the number of bound motors n_b due to the different rules described above.

5.4.2 Organization of motors at the tip

Once the rates of the motors are specified for all the sites along the tube and the rules for the tube dynamics are established, the simulation can be performed. In order to gain insight on the organization and cooperation mechanism of the motors that pull the tube, we analyze different quantities that characterize tube extraction and growth and compare them to the experimental observations. The simulations in this section are done for short tubes ($L < L_c$), in which case the tube force F_0 can be considered as constant.

There are two main quantities that can be compared at a quantitative level to the results of the simulation. First, the maximal membrane tension (or tube force), for a given motor concentration on the vesicle, above which no tubes can be extracted and, second, the average growth velocity of the tube.

Threshold in tube extraction

As shown in section 5.3.1, there exists a range of parameters for which molecular motors cannot extract membrane tubes from the vesicle. In particular, for a given motor density on the surface of the vesicle ρ_∞, there exists a maximal tension σ_{max} (or maximal tube force $F_{max} = 2\pi\sqrt{2\kappa\sigma_{max}}$ equivalently) above which the motors are not able to pull tubes from the vesicle.

In the simulations, the maximal tube force F_{max} for a given value of the density ρ_∞ is determined as follows. We set the surface density of motors ρ_∞ to a certain value and impose a tube force F_0 much larger than the threshold force for the value of ρ_∞ used. As we do not know *a priori* the threshold force F_{max} resulting from the simulations, we initially set a force F_0 larger than the theoretical threshold force obtained in section 5.3. The system is initialized with a certain number of bound motors, M_i. We set this number to a large enough value ($M_i \simeq 20$) to insure the initial tube growth. If the initial number of bound motors were too small, it could be more limiting than the value of the surface density of motors, and would lead to artifacts. Typically, the tube initially grows (as it has enough bound motors at the tip) and, in case the force is too large, it retracts until its length vanishes. We repeat this process 200 times for the same values of F_0 and ρ_∞ and if all tubes retract, we lower the force and repeat the process again for the same value of ρ_∞. As the force is progressively lowered, there exists a value of the force for which at least one tube does not retract and grows with finite average velocity. This force is the maximal force F_{max} above which no tube can be extracted. Still for the same value of ρ_∞ we repeat the whole

process (20 times) and obtain different values of F_{max} that allow a statistical treatment of the data.

We perform the simulations just described for different values of ρ_∞. In Fig. 5.22 we plot the average value of F_{max} (and its standard deviation) as a function of ρ_∞ for the different schemes of motor organization described above. The maximal force F_{max} saturates for large surface density of motors. This result is independent of the scheme used, but the saturation value depends strongly on the motor organization at the tip. One could expect this result for the "fixed tip" scenario as there is an upper bound for the number of bound motors that pull the tube. The reason why the maximal force saturates for the two other schemes is the intrinsic detachment/attachment kinetics of motors. The force is developed by the n_b consecutive bound motors at the tip and, as soon as a motor in this compact cluster detaches, the number n_b is reduced. The equilibrium of motor fluxes sets an average number of consecutive motors at the tip and, as a result, the cluster cannot develop arbitrarily large forces. Note that the saturation of the maximal force at large values of ρ_∞ is not related to the fact that the flux of bound motors entering the tube is bound by the motion of the motor at site 1. Indeed, motors cannot enter the tube if site 1 is occupied and, although J_b may be larger than V_0/ℓ, the rate of forward motion of the motor at site 1 sets an upper bound to the flux of bound motors entering the system. However, even if a macroscopic high density phase (traffic jam) exists along the microtubule, meaning that almost all the sites are occupied by bound motors, the number of consecutive bound motors at the tip is small due to their attachment/detachment kinetics, and the maximal force is consequently small. This phenomenon is studied in more detail below.

The maximal force F_{max} is also constant for small values of ρ_∞ (Fig. 5.22). For such values of the tube force, the initial number of motors M_i is sufficient to extract the tube and keep pulling it. Therefore, no matter how much the density ρ_∞ is lowered, the maximal force that the motors can perform saturates because the initial number of motors is fixed to the same value in all cases. Reducing the initial number of motors M_i confirms this explanation as the saturation of F_{max} for small values of ρ_∞ takes place at smaller values of both the force and ρ_∞. Note that at vanishing ρ_∞, the flux of motors entering the tube J_b strictly vanishes. However, the tube can be extracted by the initial bound motors in case the tube force is similar to the stall force of single kinesins ($f_s \simeq 6$ pN).

The experimental data establishes that for a tube force of $F_0 \simeq 27.5 \pm 2.5$ pN, the threshold density is $\rho_\infty^{min} \simeq 200 \pm 100\ \mu\mathrm{m}^{-2}$. It is important to realize that this value corresponds to the minimal surface density of motors tested experimentally at which tubes are pulled from the vesicle. At a value of $\rho_\infty \simeq 100\ \mu\mathrm{m}^{-2}$ no tubes are pulled from the vesicle. Therefore, the actual value of the minimal density at which tubes are extracted lies within the range $100 - 200\ \mu\mathrm{m}^{-2}$. When comparing the numerical and experimental results, the experimental value of the threshold is not a specific point but rather a region of forces and densities due to the experimental uncertainty (Fig. 5.22a). Note that the minimal density ρ_∞^{min} at a given force F_0 measured experimentally, is equivalent to a maximal force $F_{max} = F_0$ for a motor density $\rho_\infty = \rho_\infty^{min}$.

The value of the maximal force F_{max} obtained in the simulations is below the experimentally measured value $F_{max} = 27 \pm 2.5$ pN at values of ρ_∞ in the range

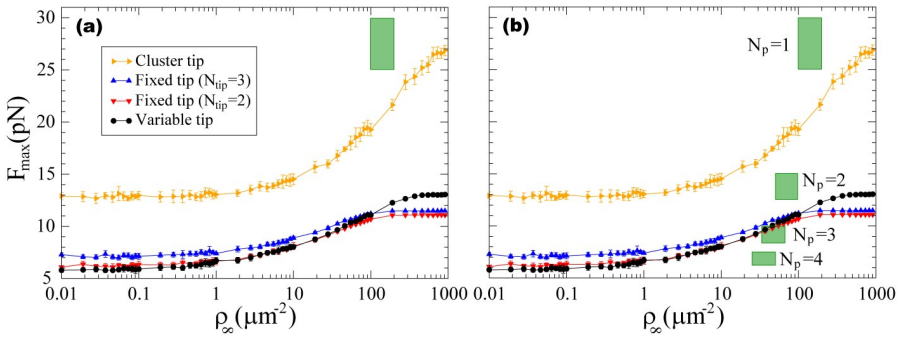

Fig. 5.22. Maximal force F_{max} as a function of the surface motor density on the vesicle ρ_∞, for the different motor organizations at the tip: "Variable tip" (circles), "Fixed tip" ($N_{tip} = 2$; triangles down), "Fixed tip" ($N_{tip} = 3$; triangles up) and "Cluster tip" (triangles right). The parameters in the simulations are those measured experimentally: $\ell = 8$ nm, $k_b = 4.7$ s^{-1}, $k_u^0 = 0.42$ s^{-1}, $a = 1.4$ nm, $f_s = 6$ pN, $V_0 = 0.6$ μms^{-1}, $D = 1$ μm^{2}s^{-1} and $\kappa = 10 K_B T$. (a) The experimentally measured value of the threshold is represented by a green rectangle, due to the experimental uncertainty. If only one protofilament is used by the motors, the results of the simulations for any motor organization do not agree with the measured value. (b) Comparison of the experimental and numerical results when several protofilaments are used simultaneously by the motors. The experimentally measured value of the threshold that must be compared with the simulations is ρ_∞/N_p and F_0/N_p, i.e. the corresponding values per protofilament. The measured threshold for different values of the number of protofilaments are shown. For 3 protofilaments ($N_p = 3$), the simulations agree with the experimental observations within the error.

$100\ \mu\text{m}^{-2} < \rho_\infty < 200\ \mu\text{m}^{-2}$, for any motor organization scheme (Fig. 5.22a). The reason is that the simulations consider only a single protofilament, while more protofilaments are likely to be used by the motors. Although the membrane tube couples the motor dynamics on different protofilaments, as a first approximation, we assume the different protofilaments to be independent as far as motor dynamics is concerned. The experimental values that have to be compared to the simulations are not directly the ones given above. If bound motors use a number N_p of protofilaments when moving along the microtubule, the flux of motors entering the system is shared among these protofilaments, so that the flux per protofilament is J_b/N_p. As the flux is proportional to ρ_∞ and variations in the motor flux correspond to changes in ρ_∞, the value of the motor density that must be used to compared to the simulation results is ρ_∞/N_p. Similarly, the force F_0 is shared among the motors in the different protofilaments, so that the force that the motors pulling the tube along a single protofilament must overcome is F_0/N_p.

With a single protofilament, the simulations do not agree with the measured value for the threshold (Fig. 5.22a). If bound motors use 2 protofilaments, the measured value of the threshold does not agree neither with the simulations (Fig. 5.22b). For a number of protofilaments larger than 3 ($N_p > 3$), the same result is found and the

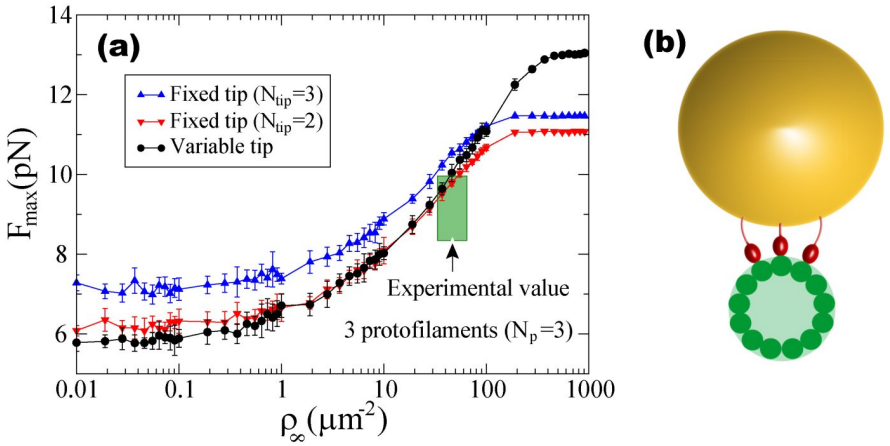

Fig. 5.23. (a) Maximal force F_{max} as a function of the surface motor density on the vesicle ρ_∞, for the different motor organizations at the tip: "Variable tip" (circles), "Fixed tip" ($N_{tip} = 2$; triangles down) and "Fixed tip" ($N_{tip} = 3$; triangles up). We consider that 3 protofilaments are simultaneously used by bound motors ($N_p = 3$). The experimentally measured value of the threshold that must be compared with the simulations is ρ_∞/N_p and F_0/N_p, and lies then within the values represented by the green rectangle due to the experimental uncertainty. The only two schemes that agree with the experimental data are "Variable tip" and "Fixed tip" ($N_{tip} = 2$). The parameters in the simulations are those measured experimentally and are the same than in Fig. 5.22. (b) Schematic representation of a front view of the tube (orange) and the microtubule (light green) using approximately the right proportions. The radius of the tube ($r_0 \simeq 20$ nm) is about twice the radius of a microtubule. The motors (red) have a head of about 5 nm and the motor tail is about 15 nm. Indeed, the kinesin motors used in the experiments are conventional kinesins with a truncated tail, much shorter than the normal tail of conventional kinesins. The sketch suggests that at most three protofilaments (dark green) are likely to be simultaneously used by bound motors (red), due to geometric constraints.

experimentally measured value of the threshold does not fit the results of the simulations neither (Fig. 5.22b). However, in case bound motors use simultaneously 3 protofilaments, the maximal force F_{max} obtained in the simulations for the schemes "variable tip" and "fixed tip" (with $N_{tip} = 2$) agrees with the measured value of the threshold within the experimental error (Figs. 5.22b and 5.23a). Indeed, from geometric considerations knowing the radius of both the tube and the microtubule we estimate that no more than 3 protofilaments can be used at the same time (Fig. 5.23b). For any number of protofilaments, the scheme "cluster tip" does not fit the experimental data within the error. As this is the only scenario that contains a coordination of the motors, our results suggest that the motors pulling the tube behave independently. We thus conclude that bound motors use 3 protofilaments simultaneously and act independently to pull the tube.

The maximal force F_{max} does not however distinguish between the two remaining possible schemes, namely "variable tip" and "fixed tip". We now use the experimen-

tal measure of the average growth velocity of the tube to distinguish between these two scenarios.

Average growth velocity

The very tip of the tube is determined by the position of the leading bound motor at site N. When this motor steps forward, the tube increases its length by one site and, in case the leading motor detaches, the tube retracts until the position of the closest bound motor. The time evolution of the variable N traces the trajectory of the tube $N(t)$, or $L(t) = \ell N(t)$ equivalently. The slope of $L(t)$ corresponds to the average tube velocity.

We first analyze the average tube velocity at threshold. As described above, the force F_{max} is the force, for a given value of ρ_∞, at which at least one tube can be extracted. We determine the average growth velocity of this tube and repeat the process to obtain enough statistics. In Fig. 5.24a we plot the average tube velocity as a function of ρ_∞ for the two schemes left ("variable tip" and "fixed tip" with $N_{tip} = 2$). Note that the tube force is not the same along the curve. Being at threshold, the tube force is F_{max} and thus different for each value of ρ_∞. Below a surface motor density of about $\rho_\infty \simeq 1\ \mu\text{m}^{-2}$, the two schemes show similar tube velocities. Indeed, for low forces both schemes should behave similarly as there is no need for a large number of consecutive bound motors n_b to pull the tube. The dispersion of the data for low densities (low forces) is large as the number of bound motors necessary to pull the tube is very small ($n_b \simeq 1-2$) and the fluctuations in the tube trajectory are large. For densities above $\rho_\infty \simeq 10\ \mu\text{m}^{-2}$ (Fig. 5.24b), the dispersion is much smaller and the two schemes show clearly different average tube velocities. For the "variable tip" scheme, the tube velocities are larger than for the "fixed tip" scheme with $N_{tip} = 2$. This is so because the latter scheme has a limited number of sites where the motors can apply forces, whereas in the "variable tip" scheme larger bound motor clusters can be stochastically created.

The average tube velocity can be determined experimentally close to threshold. The initial motor density at the surface of the vesicle ρ_∞ was set to $\rho_\infty \simeq 200 \pm 100\ \mu\text{m}^{-2}$, corresponding to the value tested experimentally closest to threshold at a tube force of $F_0 \simeq 27.5 \pm 2.5$ pN, and the average velocity of the tubes growing in this conditions was determined. As the system is close to threshold, very few tubes are observed; tubes were extracted only from approximately 10% of the vesicles in the chamber, whereas in far from threshold conditions, tubes are observed for nearly all vesicles. In spite of the low number of tubes close to threshold, when a tube is extracted its average velocity is finite and can be measured by determining the slope of its trajectory. The average value, $\bar{V}$, of the average tube velocity V measured for 9 different tubes close to threshold, is

$$\bar{V} \simeq 0.11 \pm 0.05\ \mu\text{ms}^{-1}\ . \tag{5.73}$$

As discussed above, the value of ρ_∞ that has to be compared to the simulation results is ρ_∞ / N_p. Note however that the velocity is not affected by the number of protofilaments considered, as we assume the different protofilaments to be independent.

The measured value of the average tube velocity is consistent with the one obtained for the "variable tip" scheme (Fig. 5.24b). The smaller velocities for the "fixed tip" scheme with $N_{tip} = 2$ that result from its limited number of pulling motors, do not fit the experimental data within the error (Fig. 5.24b). Moreover, the velocity of tubes at threshold for the "Cluster tip" scheme is above the experimentally measured value, confirming that this scheme is not in agreement with the observations.

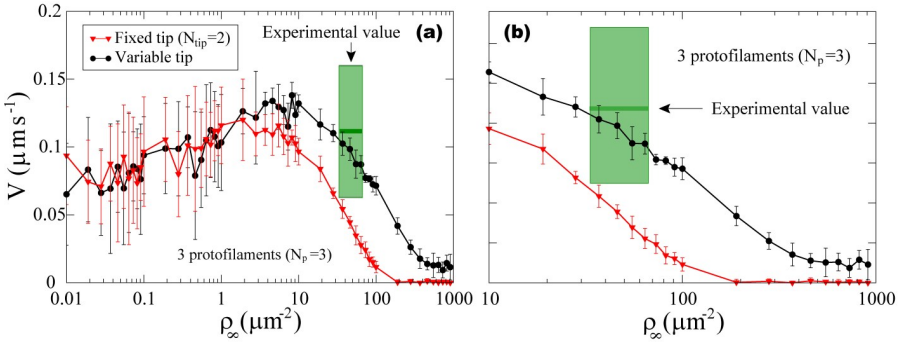

Fig. 5.24. Average tube velocity V as a function of the surface motor density on the vesicle ρ_∞ for different motor organizations at the tip: "Variable tip" (circles) and "Fixed tip" ($N_{tip} = 2$; triangles down). We consider that 3 protofilaments are simultaneously used by bound motors ($N_p = 3$). The experimentally measured value of the threshold that must be compared with the simulations is ρ_∞/N_p and F_0/N_p. The experimental value of the average velocity V that must be compared with the simulations is the direct measure of the velocity, no matter the number of protofilaments, and is represented by the green rectangle due to the experimental uncertainty. Only the "Variable tip" scheme agrees with the experimental data within the error. The parameters in the simulations are those measured experimentally and are the same than in Fig. 5.22. (b) Same than in (a) for the range of densities where the fluctuations in the tube velocity are small.

The velocity of tubes in far from threshold conditions was also measured (see discussion in section 5.3.1). For the same tube force ($F_0 \simeq 27.5 \pm 2.5$ pN) the surface motor density ρ_∞ was increased 10 times over the threshold density for this force ($\rho_\infty \simeq 2000\ \mu\text{m}^{-2}$). The average value, $\bar{V}$, of the average tube velocity V measured for 27 different tubes is

$$\bar{V} \simeq 0.12 \pm 0.04\ \mu\text{ms}^{-1}\ . \tag{5.74}$$

There is thus a very weak dependence of the average tube velocity on the surface density of motors. This result is also found in the simulations of tube growth for the "variable tip" scheme. Using the same parameters than in the experiments and considering that 3 protofilaments are used simultaneously by bound motors, the average value, $\bar{V}$, of the average tube velocity obtained in the simulations for 500 tubes is

$$\bar{V} \simeq 0.127 \pm 0.005\ \mu\text{ms}^{-1}\ , \tag{5.75}$$

confirming the scheme "variable tip" as the most plausible type of motor organization at the tip, because it agrees with all experimentally measured quantities within the experimental error. Note that the average tube velocity obtained in the simulations, which is in good agreement with the experimental measure, is much smaller than the mean-field prediction (section 5.3.1). The organization of the motors at the tip and their mutual interactions are thus important to understand the growth of membrane tubes.

The results presented suggest that motors cooperate by transmitting the forces to each other when in contact in spite of behaving independently from one another. In Fig. 5.25 we sketch the tip of a growing tube with the motor organization that our analysis suggests.

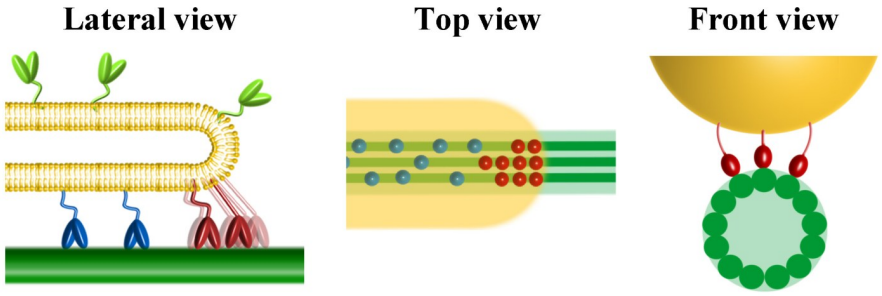

Fig. 5.25. Schematic representation of the organization of motors pulling a membrane tube. Lateral, top and front views are shown. Bound motors (blue and red) can use three different protofilaments (dark green) to pull the membrane tube (orange). The motors applying the force to sustain the tube at the tip are shown in red, whereas the other bound motors are shown in blue.

Number of motors at the tip

Having established the "variable tip" scheme as the most plausible one, we now study the distribution and average number of motors, $\bar{n}_b$, pulling the tube. As discussed above, the motors contributing to the force to pull the tube are the first n_b consecutive motors at the tip in the "variable tip" scheme. Due to the stochastic motor transitions, the number n_b is a stochastic variable. During tube growth, the variable n_b can be tracked as a function of time and its statistical properties can be determined.

We simulate the growth of a tube in far from threshold conditions, using the experimentally measured values for the parameters. The tube force and surface motor density imposed in the simulations are, respectively, the force per protofilament, $F_0/N_p \simeq 9.1$ pN, and the motor density per protofilament, $\rho_\infty/N_p \simeq 300\ \mu\text{m}^{-2}$ ($N_p = 3$). Upon tube growth, we obtain the number of consecutive motors at the tip as a function of time, $n_b(t)$. In order to obtain the average number of motors pulling the tube, $\bar{n}_b$, as a function of time, we repeat the simulation of tube growth

for several independent tubes and perform an ensemble average at each given time. In Fig. 5.26a we plot the average number of pulling motors during tube extraction. Interestingly, it is constant in time and small, $\bar{n}_b \simeq 2.8$. This number corresponds to the average number of pulling motors per protofilament. As three protofilaments are used simultaneously and independently, we estimate the average number of motors pulling the tube in the conditions specified above to be

$$\bar{n}_b \simeq 8.4\,. \tag{5.76}$$

This number is smaller than the one obtained for the same conditions in the mean-field study developed in section 5.3.1, where an average number of 24 motors was estimated to pull the tube. Such discrepancy between the mean-field prediction and the results of the simulations shows that the motor organization and mutual interactions at the tip are important to understand the process of tube extraction.

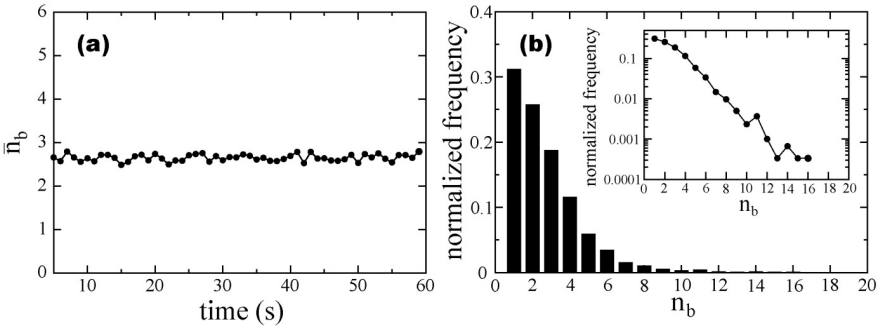

Fig. 5.26. Average number (a) and probability distribution (b) of pulling motors at the tip for a single protofilament. The parameters in the simulations are those measured experimentally in far from threshold conditions (normalized to the number of protofilaments N_p used by bound motors, when necessary; $N_p = 3$): $F_0/N_p \simeq 9.1$ pN, $\rho_\infty/N_p \simeq 300\,\mu\text{m}^{-2}$, $k_b = 4.7\,\text{s}^{-1}$, $k_u^0 = 0.42\,\text{s}^{-1}$, $V_0 = 0.6\,\mu\text{ms}^{-1}$, $f_s = 6$ pN, $D = 1\,\mu\text{m}^2\text{s}^{-1}$, $\kappa = 10K_BT$, $\ell = 8$ nm and $a = 1.4$ nm. (a) The average number of motors pulling the tube, $\bar{n}_b$, is constant in time. The total number of motors pulling the tube for three independent protofilaments is $\bar{n}_b \simeq 8.4$. (b) The probability distribution (normalized frequency) for the number n_b of consecutive motors at the tip (pulling motors) shows a rapid decay at small number of motors. The inset in (b) shows the probability distribution in logarithmic scale, and suggests an exponential decay with n_b for $n_b \gtrsim 3$.

In order to characterize the statistical properties of the number of motors n_b, we determine its probability distribution. In Fig. 5.26b we show the normalized frequency histogram (probability distribution) of n_b, calculated using an ensemble average over 3000 independent runs. The probability distribution does not change in time, in agreement with our previous result concerning the average number of motors. Although the tube is pulled by an average number of motors $\bar{n}_b \simeq 2.8$, there is a finite probability that much larger motor clusters transiently form. The most frequent

case corresponds to an isolated motor pulling the tube, and the probability of larger motor cluster decreases rapidly with the number of motor in the cluster. Clusters of more than about 7 motors hardly occur. Although the decrease of the probability density is consistent with an exponential decrease (inset in Fig. 5.26b), we cannot rule out a long-tail decrease at large values of n_b. We are currently studying analytically this behavior using a master equation approach.

The probability distribution $\rho_{n_b}(n_b)$ can be used to calculate statistical quantities, like the average number of pulling motors or the average tube velocity, that we obtained above in a different way. Using the expression for the velocity of the tube for a given number of motors at the tip, $V(n_b) = V_0(1 - F_0/n_b f_s)$, the average tube velocity, $\bar{V}$ reads

$$\bar{V} = V_0 \sum_{n_b=1}^{\infty} \rho_{n_b}(n_b) \left(1 - \frac{F_0}{f_s n_b}\right) . \tag{5.77}$$

Note that the average velocity cannot be calculated by direct substitution of the average number of pulling motors $\bar{n}_b$ in the expression for V, i.e.

$$\bar{V} \neq V_0 \left(1 - \frac{F_0}{f_s \bar{n}_b}\right) . \tag{5.78}$$

The constant average number of pulling motors obtained in the simulations is in contrast with the mean-field prediction in section 5.3.1, where the number of motors increased slowly in time. The reason is that in the simulations a traffic jam develops in the close vicinity of the tip, and the assumption of low motor density used in the mean-field analysis no longer holds. The average size of this jam is typically small ($10 - 20$ sites) and cannot be observed by the fluorescence microscopy measurements discussed above, but is still larger than the average size $\bar{n}_b$ of the motor cluster pulling the tube, which is of about 3 motors per protofilament. The size of the jam increases with time as there is a net flux of motors toward the tip. However, the number of consecutive motors at the tip is much smaller and constant. Indeed, the attachment/detachment kinetics sets an average number of consecutive motors and, even if a macroscopic traffic jam develops upstream from the tip, the actual number of motors pulling the tube is very small due to detachment events. In spite of the constant average number of motors pulling motors and constant average tube velocity, there is no steady state for the motor density profile along the tube because of the net flux of motors toward the tip. We discuss below the formation of macroscopic jams upstream from the tip region.

5.4.3 Motor density during tube growth

In the mean-field description of the system, we considered the bound motors moving along the microtubule to be in the dilute limit (low density phase). This assumption, which simplifies considerably the mathematical analysis, was done because the experimental data suggested in most conditions a low density phase of motors (see section 5.3.1). However, when the concentration of motors is increased, like in the

vicinity of the tube tip, this approximation no longer holds. Generically, there are several nonlinear phenomena in traffic that arise from the mutual interactions between the particles (motors in our case). In this section we focus on the motor density during tube growth and describe the accumulation of motors upstream from the tube tip. All the simulations of tube growth in this section are done using the "variable tip" scheme, as we have shown above that it is the most plausible one.

The simulations account for the dynamics of individual motors, which undergo elementary transitions. However, when analyzing the motor density field, we are interested in length scales much larger than the size of a single site ℓ ($\ell \simeq 8$ nm for a microtubule). Indeed, using optical microscopy the minimal observable length scale is about $150-200$ nm due to the diffraction limit, meaning that no length scales below this limit can be resolved. The fluorescence intensity along the tube measured experimentally corresponds to the sum of bound and unbound motor densities. Note however that the total motor density, given by the sum of bound and unbound motor densities, can be well approximated by the density of bound motors because the attachment rate k_b is much larger than the detachment rate at zero force k_u^0 ($k_b/k_u^0 \simeq 10$; see section 5.3.1). We thus focus on the time evolution of the bound motor density field in what follows. In order to obtain the density field from the binary data resulting from the simulations, different techniques can be used. We briefly describe two of the commonly used procedures and comment the one we use:

- *Smoothing*. The smoothing procedure consists in substituting the binary value of the occupation number at a given site by the average value of the occupation number over a certain number of sites. If the averaging is done in a window of $2m+1$ sites, the value of the average occupation number (bound motor density), $\rho_b(i)$, at site i reads

$$\rho_b(i) = \frac{1}{2m+1} \sum_{k=i-m}^{i+m} n_b(k) \,, \tag{5.79}$$

  where $i \in [m, N-m-1] \subset \mathbb{N}$, $k \in [0, N-1] \subset \mathbb{N}$, and $n_b(k)$ is the occupation number of the bound state at site k, which takes the value 0 if the site is empty and 1 in case it is occupied. Note that if the original system contains N sites, the smoothed system has $N-2m$ sites.
- *Averaging*. The averaging technique consists in renormalizing the size of the unit cell and substitute the binary values of the occupation number at the original sites for the average occupation number in the renormalized unit cell. If the original system contains N sites of length ℓ and the averaging is done over m sites, the averaged system has N/m unit cells ("sites") of length $m\ell$ [12]. The average occupation number (motor density), $\rho_b(i)$, at a renormalized cell i, reads

$$\rho_b(i) = \frac{1}{m} \sum_{k=0}^{m-1} n_b(im+k) \,, \tag{5.80}$$

[12] The integer number N and m should be commensurate. In case they are not, it is necessary to crop a small portion of the system to make them commensurate.

where $i \in [0, N/m-1] \subset \mathbb{N}$ and n_j is the occupation number at the original site j, with $j \in [0, N-1] \subset \mathbb{N}$.

Both techniques act as a high-frequency noise filter, preventing large fluctuations at very short length scales. The main difference between them is the size of the resulting unit cell. While the smoothing technique conserves the size of the unit cell, the averaging procedure changes it from the original size of a site to the size of the averaged region. We present here the data after filtering it with the averaging technique because the resulting size of the unit cell closely corresponds to the experimental resolution of fluorescence microscopy (1 pixel = 134 nm).

Growth of short tubes

For short enough tubes ($L < L_c \sim 20\ \mu$m) the tube force does not increase much during tube extraction and can be considered as constant, with a value $F_0 = 2\pi\sqrt{2\sigma\kappa}$. We simulate the growth of short tubes and analyze, at qualitative level, the density field of bound motors upstream from the tip.

In Fig. 5.27a,b we show the time evolution of the bound motor density field upon tube growth, for different values of ρ_∞. In case both the flux of motors entering the tube and the tube force are small ($\rho_\infty/N_p = 10\ \mu\text{m}^{-2}$ and $F_0/N_p = 4$ pN; Fig. 5.27a), the accumulation of motors upstream from the tube tip is small and evolves slowly in time. In this case, the average density field decays exponentially away from the tip with a decay length λ which is in agreement with the mean field analysis in section 5.3.1. However, even in the case of a small net motor influx, at long times ($t > 10^2$ s) there is a jamming of motors at the tip that progressively invades the system. For a large net motor influx ($\rho_\infty/N_p = 100\ \mu\text{m}^{-2}$ and $F_0/N_p = 4$ pN; Fig. 5.27b), this jamming of motors occurs very quickly ($t \sim 10$ s) and the exponential decay of the density profile in the vicinity of the tip is not observed.

An example of the time evolution of the motor density field obtained experimentally is shown in Fig. 5.27c. The density field presents an accumulation of motors at the tip, which does not evolve much during the observation time. The density field decays exponentially from the tip, in agreement with the mean-field analysis and the simulation results for low motor influx. However, the time scale to generate a micron-sized jam of motors at the tip is longer than that obtained in the simulations. We interpret this disagreement as an overestimation of the flux of motors entering the tube in the simulations. Indeed, the bound motor flux, J_b, depends on the details of the tube-vesicle contact and, in particular, on the existence of a connection region where the tube is not in contact with the microtubule. The simulations are done assuming a constant flux, as given by Eq. 5.71. In case there is a connection region, the flux of bound motors entering the tube is smaller (Eq. 5.44) and could be overestimated in the simulations.

The small density inhomogeneities along the tube obtained in the simulations (Fig. 5.27a) are not observed in the experiments (Fig. 5.27c). Unlike the simulations, where only one protofilament is considered, the experimental density profile corresponds to the total motor density, i.e. the average density of motors moving on

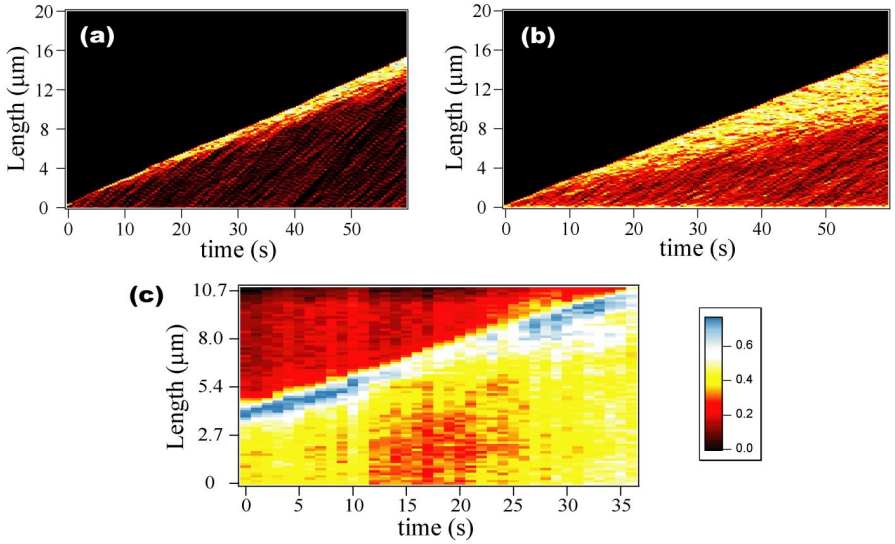

Fig. 5.27. (a-b) Space-time plots corresponding to the time evolution of the bound motor density field along the tube obtained from the simulations ($F_0/N_p = 4$ pN). The parameters are: $\ell = 8$ nm, $k_b = 4.7\,\mathrm{s}^{-1}$, $k_u^0 = 0.42\,\mathrm{s}^{-1}$, $a = 1.4$ nm, $f_s = 6$ pN, $V_0 = 0.6\,\mu\mathrm{ms}^{-1}$, $D = 1\,\mu\mathrm{m}^2\mathrm{s}^{-1}$ and $\kappa = 10 K_B T$. (a) Low flux of bound motors entering the tube ($\rho_\infty/N_p = 10\ \mu\mathrm{m}^{-2}$). (b) Large bound motor influx ($\rho_\infty/N_p = 100\ \mu\mathrm{m}^{-2}$). (c) Experimentally measured fluorescence intensity plot as a function of position along the tube path and time. (Experiments by C. Leduc).

different protofilaments. It is thus likely that the small density inhomogeneities on individual protofilaments are averaged out to some extent.

Growth of long tubes

In the previous simulations, the tube force was assumed to be constant during tube extraction. This approximation holds for short tubes, but as tubes grow further the force increase becomes important and can eventually stall tube growth. While the underlying reason of tube stall is clearly the force increase, note that, in contrast to the analysis presented in section 5.3, here there exists a maximal force that the motors can perform. When the tube grows up to a length where the force reaches the maximal force that the motors can develop, the tube necessarily stalls.

In order to analyze at a qualitative level the effect of the tube stall on the density field, we artificially impose the force increase to take place over a length scale ($\sim \mu$m) shorter than that expected theoretically ($\sim 20\ \mu$m; see section 5.2), because the simulation of long tubes is computationally demanding. We simulate the tube growth with a tube force that increases linearly with the tube length at a rate of 1 pN/μm and an initial tube force of 2 pN. The resulting space-time plots for low ($\rho_\infty/N_p = 10\ \mu\mathrm{m}^{-2}$) and large ($\rho_\infty/N_p = 100\ \mu\mathrm{m}^{-2}$) bound motor influx are shown

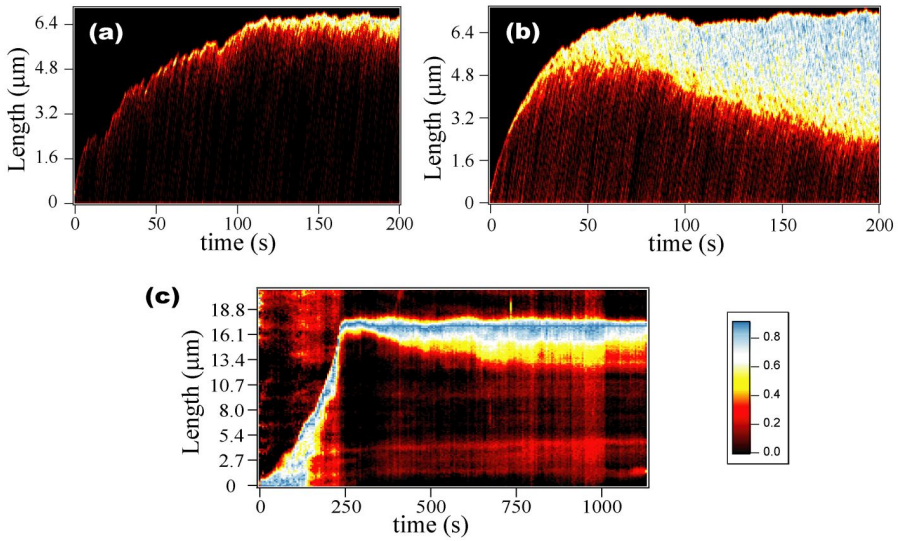

Fig. 5.28. (a-b) Space-time plots corresponding to the time evolution of the bound motor density field along the tube obtained from the simulations. The tube force increases with the tube length at a force-rate increase of 1 pN/μm and an initial tube force $F_0 = 2$ pN. The parameters are: $\ell = 8$ nm, $k_b = 4.7\,\mathrm{s}^{-1}$, $k_u^0 = 0.42\,\mathrm{s}^{-1}$, $a = 1.4$ nm, $f_s = 6$ pN, $V_0 = 0.6\,\mu\mathrm{ms}^{-1}$, $D = 1\,\mu\mathrm{m}^2\mathrm{s}^{-1}$ and $\kappa = 10 K_B T$. (a) Low flux of bound motors entering the tube ($\rho_\infty/N_p = 10\,\mu\mathrm{m}^{-2}$). (b) Large bound motor influx ($\rho_\infty/N_p = 100\,\mu\mathrm{m}^{-2}$). (c) Experimentally measured fluorescence intensity plot as a function of position along the tube path and time. After tube stall, there is an accumulation of motors that progressively develops upstream from the tip, in agreement with the results from the simulations (a-b). In contrast to the simulations, where the net motor influx is constant, experimentally, the size of the high motor density phase saturates at very long times ($\sim 10^3$ s). (Experiments by C. Leduc).

in Fig. 5.28a,b respectively. For the fluxes of bound motors that we represent, the tube grows until it stalls at a certain length. However, for large tube forces and low motor influx, the tube can undergo large and repeated retractions, similar to the oscillations described in section 5.3.2. Note that the length at which the tube stalls does not depend strongly on the motor influx (Fig. 5.28a,b). This is so because the motor attachment/detachment kinetics at the tip sets an average number of consecutive motors that sustain the tube, independent of how big is the traffic jam of motors upstream from the tip. Therefore, as the average number of motors pulling the tube in both cases is almost the same, the maximal force that this small cluster of bound motor performs is very similar and the tube stalls nearly at the same length. When the tube stalls, the motors dynamically accumulate upstream from the tip and a high density phase progressively invades the system, with a time scale that depends on the motor influx.

The tube stall has indeed been observed experimentally (Fig. 5.28c). In agreement with the results of the simulations, the tube grows until it reaches a certain

length, where it stalls and a high density phase of motors progressively develops upstream from the tip. For time scales $\sim 10^2$ s, the front separating the high and low density phases moves upstream with nearly constant velocity, similarly to the simulations, indicating that the flux of motors entering the tube is constant. However, for time scales $\sim 10^3$ s the size of the high motor density phase at the tip evolves very slowly in time and eventually stops growing. In this particular experiment, different tubes were pulled simultaneously from the same vesicle, implying that motor depletion on the vesicle is likely to be important. We interpret the observed saturation of the size of the high density phase upstream from the tip as due to the depletion of motors on the vesicle, which leads to a smaller motor flux entering the tube for long time scales $\sim 10^3$ s.

5.4.4 Traffic of interacting motors: density inhomogeneities

In the previous section we described the evolution of the motor density field upon tube growth, focusing our analysis on the motor accumulation upstream from the tip. However, even in the absence of any boundary (like the tube tip) inducing the motor accumulation, simply the presence of mutual motor interactions can generate large density inhomogeneities (traffic jams). In this section we study the large scale traffic of motors far away from the boundaries, focusing our analysis on the inhomogeneities of the motor density field. We analyze both the case in which only excluded volume interactions between the motors exist and the situation where interactions beyond excluded volume affect the motor dynamics. We show that the experimental observations are consistent with effective attractive interactions between the motors.

Several experimental observations suggest that interactions between motors are important to understand their behavior at large scales. Kinesin motors attach to microtubules in a non-homogeneous way in absence of ATP (Vilfan et al., 2001). An homogeneous attachment would be expected in the absence of interactions. These experiments suggest the existence of short-range interactions between motors in absence of ATP. Other experiments (Muto et al., 2005) suggest long-range interactions between the motors, as the attachment of motors onto microtubules depends on the configuration and movement of the motors already bound to the microtubule at a distance of about a micron. Recent experiments using the monomeric kinesin KiF1a (Nishinari et al., 2005) show the existence of large inhomogeneities in the motor density along a microtubule in the presence of ATP. These motor accumulations cannot be explained in the absence of interactions. There is thus growing evidence that the interactions between motors (monomeric or dimeric) are crucial to understand their large scale traffic properties.

In addition to the already mentioned experimental observations suggesting mutual motor interactions beyond excluded volume, new *in vitro* experiments performed by Wouter Roos and Giovanni Cappello (Institut Curie) suggest that the detachment and attachment rates of individual motors are, respectively, reduced and enhanced in presence of neighboring motors (Roos et al., 2006).

Theoretical approaches

Several works have addressed the traffic properties of elementary self-propelled particles in many different systems. We briefly comment the different approaches.

The motion of biased random walkers has been extensively studied (Spohn, 1991; Schmittmann and Zia, 1995; Derrida, 1998). In particular, the asymmetric exclusion process (ASEP) considers the motion of particles that cannot overtake each other along a one dimensional lattice. The elementary particles may step forward and backward with different rates. Most of the studies focus on the steady-state properties of the system (Schmittmann and Zia, 1995). In particular, the variation of the motor fluxes entering and leaving the system at the boundaries leads to phase transitions, which are known as boundary-induced phase transitions (Derrida, 1998).

One of the most studied examples of traffic of self-propelled particles is the vehicular and pedestrian traffic (Helbing, 2001; Chowdhury et al., 2000; Nagel, 1996; Lighthill and Whitham, 1955). The community studying vehicular traffic focuses more on the inhomogeneities of the vehicle density field, which are of clear practical importance. Even in the steady state, the density field may show important inhomogeneities. Many interesting non-equilibrium phenomena appear in these systems, like the spontaneous appearance of traffic jams (known as "phantom traffic jams"), the existence of density waves that can move both upstream and downstream, traffic breakdowns and synchronized traffic flow. Several models are used to explain the observed behavior. Microscopic models account for the detailed interaction between vehicles and build the macroscopic behavior from the interaction rules between individual vehicles. More macroscopic approaches using coarse-grained descriptions have been introduced to describe the observed spatio-temporal pattern formation that arises from the mutual vehicle interactions. Finally, computational in-lattice simulations have been shown to be very successful in reproducing the main features of real vehicular traffic (Nagel, 1996).

More recent works have directly addressed the traffic of molecular motors at large scales (Lipowsky et al., 2001; Parmeggiani et al., 2003). These studies mainly focus on the steady-state properties of the average density field, in a similar way than TASEP studies, but including also the motor attachment/detachment kinetics. We discuss some of the main results from these works below.

In this section we analyze the effect of mutual motor interactions on motor density spatio-temporal patterns, like traffic jams and density waves. To this end, we use a similar approach than in Ref. (Parmeggiani et al., 2003), but include the effect of mutual motor interactions in the motor kinetics. However, instead of analyzing the boundary induced phase transitions in the steady state or the steady state properties of traffic themselves, we focus on the density inhomogeneities arising from the collective behavior of interacting motors, in a similar way as the studies on vehicular traffic.

Simulations of motor traffic

Far from the tip and the boundary with the vesicle, the average density profile is characterized by constant bound and unbound motor densities, ρ_b^∞ and ρ_u^∞ respectively

(see section 5.3.1). As the simulations of tube growth are computationally heavy and we are interested in the density inhomogeneities far from the boundaries, where the average motor density is constant, we simulate a portion of the tube with constant average bound and unbound motor densities. To this end, the simulations are done using periodic boundary conditions.

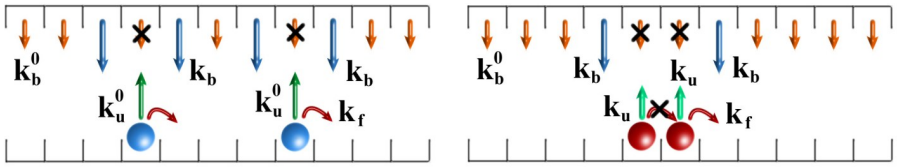

Fig. 5.29. Possible motor transition rates for different motor configurations. Rates for bound motors with empty neighboring sites (left) and rates for motors in contact (right). The mutual motor interactions are effectively taken into account in the configuration-dependent attachment and detachment rates. The attachment rate to sites neighboring already bound motors k_b is, in general, different than the attachment rate k_b^0 to sites with empty neighboring sites. The detachment rate of bound motors with empty neighboring sites k_u^0 is also different, in general, than the detachment rate of bound motors with at least one motor in its neighboring sites, k_u. In addition, motors move forward to the next site, if empty, with rate $k_f = V_0/\ell$.

The unbound state is characterized by a constant motor density ρ_u^∞, and we neglect the diffusive flux of unbound motors ($k_d = 0$; Fig. 5.29). Indeed, as the diffusion time scale to neighboring sites along the tube, k_d^{-1}, is much shorter than the other time scales in the system, the fluctuations of the motor density in the unbound state are smeared out very quickly. The motors in the bound state can detach from the microtubule and step forward to the next site, if empty. Only contact interactions are assumed between the motors, so that a motor is only affected by the presence of motors in its neighboring sites. The effect of mutual motor interactions is effectively taken into account in the attachment and detachment rates (Fig. 5.29). A motor occupying a site with empty neighboring sites detaches from the microtubule at a rate k_u^0, whereas if one of its neighboring sites is occupied by another motor, it detaches at a rate $k_u \equiv \delta k_u^0$ [13]. The dimensionless parameter δ quantifies the strength of the interaction. While a value $\delta = 1$ means that the detachment rate is not affected by the presence of neighboring motors (only excluded volume interactions), values $\delta > 1$ and $\delta < 1$ correspond to enhanced and reduced detachment rates in presence of neighboring motors, respectively. Similarly, the attachment rate to a site with empty neighboring sites is k_b^0, whereas in case one of the neighboring sites is occupied, the attachment rate is $k_b = \gamma k_b^0$. Values $\gamma > 1$ and $\gamma < 1$ indicate, respectively, enhanced and reduced attachment rates in presence of neighboring motors. We refer to the cases $\delta \neq 1$ and $\gamma \neq 1$ as preferential detachment and preferential attachment

[13] We assume for simplicity the cases where only one neighboring site is occupied and both neighboring sites are occupied to be equivalent.

respectively. The case $\gamma > 1$ and $\delta < 1$ corresponds to effective attractive interactions between the motors, whereas the case where $\gamma < 1$ and $\delta > 1$ corresponds to effective repulsive interactions.

Changes in the average unbound motor density ρ_u^∞ correspond to changes in the time scale for motor attachment. At very low unbound motor densities the motor attachment flux onto sites along the microtubule is small, whereas for high unbound motor densities, the motor attachment flux is large. Note that unlike the previous simulations, where k_b was the rate at which an individual motor attached to the microtubule, here the attachment rate corresponds to the total flux of motors that can attach to a given site. As the unbound motor density is constant, it is just a redefinition of the binding rate: $k_b \rho_u^\infty \ell \to k_b$.

In addition to attachment and detachment events, motors step forward and backward in general. We focus on the motion of strongly biased motors, for which the forward motor stepping rate $k_f = V_0/\ell$ is much larger than the backward stepping rate (e.g. conventional kinesin), and neglect the backward motor stepping, as previously assumed. Although it is likely that mutual motor interactions affect all transition rates (k_u, k_b and k_f) we assume for simplicity that the forward rate is not modified by the interactions; we only address here the traffic of motors in presence of preferential attachment/detachment kinetics. In Fig. 5.29 we sketch the motor transition rates that specify the dynamics of the system. So as to make clear the differences in traffic properties arising from mutual motor interactions, we first present the results in absence of preferential motor kinetics.

Motor traffic with only excluded volume interactions

The steady-state properties of motor traffic with only excluded volume interactions have been addressed by several works (Chowdhury et al., 2000; Lipowsky et al., 2001; Parmeggiani et al., 2003). Unlike the case we consider here, most of the works focus on the effects of the boundary conditions on the steady-state density field. When motors which can only step forward enter the left boundary at a rate α and leave the system at the right boundary at a rate β, and no attachment/detachment kinetics is present, the system is called *Totally Asymmetric Exclusion Process* (TASEP) (Derrida, 1998). Varying the parameters α and β, different steady-state phases appear, namely a low density density phase, a high density phase and a maximal current phase. However, there is no coexistence between different phases. When attachment/detachment kinetics is added, the competition between TASEP and Langmuir kinetics, changes the phase diagram and a coexistence between high and low density phases appears (Parmeggiani et al., 2003).

Our aim here is not to study the boundary-induced phase transitions of the steady-state density field, but rather the inhomogeneities of the steady-state density field. To this end, we perform the simulations in a ring geometry (periodic boundary conditions), and in presence of only excluded volume interactions ($\delta = 1$ and $\gamma = 1$).

In Fig. 5.30 we show the spacetime plots of the bound motor density field for $\delta = 1$, $\gamma = 1$ and average bound motor densities below and above $\bar{\rho}_b/\rho_s = 0.5$

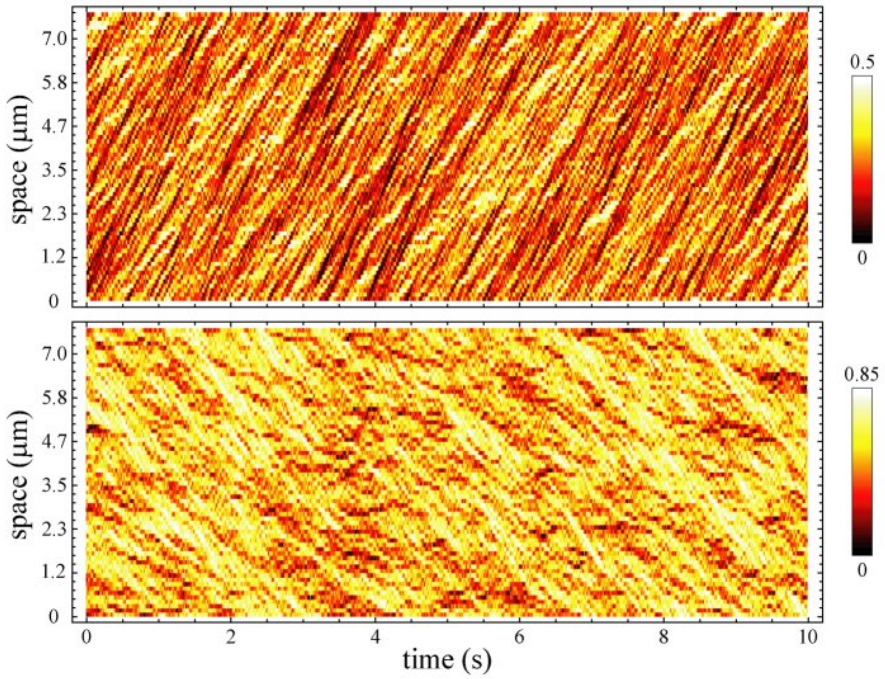

Fig. 5.30. Bound motor density inhomogeneities obtained by numerical simulation. Space-time plots corresponding to the steady state bound motor density field in a portion of the tube, for average motor densities of $\bar{\rho_b}/\rho_s = 0.25$ (a) and $\bar{\rho_b}/\rho_s = 0.6$ (b). The density scale is color coded and different in (a) and (b) to increase the contrast. Below (above) an average motor density of 0.5 the density inhomogeneities move downstream (upstream). The parameters are: $\ell = 8$ nm, $k_u^0 = 1\ \mathrm{s}^{-1}$ $V_0 = 0.6\ \mu\mathrm{ms}^{-1}$. The average value of the bound motor density field is given by the ratio k_b/k_u^0: (a) $k_b/k_u^0 = 0.33$ and (b) $k_b/k_u^0 = 1.5$.

($\rho_s \equiv 1/\ell$ being the saturation density). There are small density inhomogeneities that move downstream if the average value of the bound motor density is below 0.5. On the other hand, for an average motor density above 0.5 the density inhomogeneities move upstream. Note that the motors do not reverse the direction of motion; they always move downstream. However, for $\bar{\rho_b}/\rho_s > 0.5$ the density field shows density waves moving upstream, similarly to the density waves observed in vehicular traffic. This is a well-known result and can be explained by a simple mean-field description of the density field which accounts for dependence of the bound motor velocity on the local density of motors on the microtubule (Lighthill and Whitham, 1955; Helbing, 2001; Nagel, 1996). These small density inhomogeneities, known as kinematic waves (small traffic jams), are constantly created and destroyed by fluctuations and never lead to major differences of density values around the average density. The typical size of the jams is small (~ 10 sites) and their lifetime is short, on the time scale of motor detachment, k_u^{-1}.

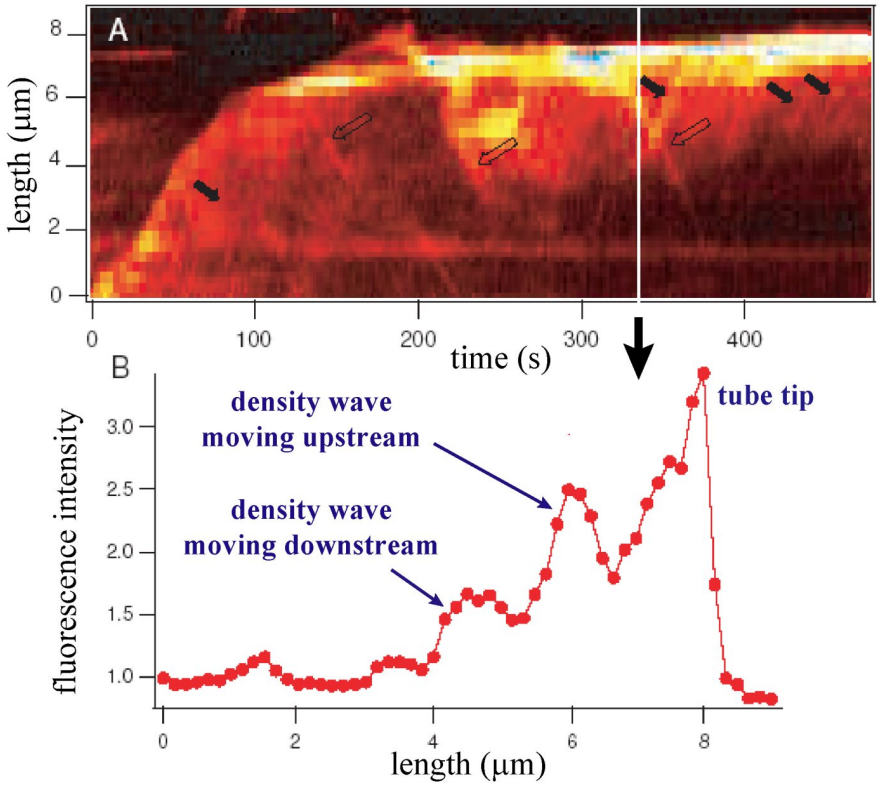

Fig. 5.31. Fluorescence intensity inhomogeneities along a membrane tube. The surface density of motor on the vesicle was set to $\rho_\infty = 10\,\rho_\infty^{min}$. (A) Space-time plot of a growing tube showing the time evolution of the fluorescence intensity along the tube. As the binding sites of kinesin motors are labeled, the intensity field corresponds to the motor density along the tube. There are density inhomogeneities moving downstream (filled arrows) and upstream (empty arrows). The inhomogeneities moving upstream are created close to the tube tip, where the average motor density is high. (B) Intensity profile normalized to the homogeneous fluorescence intensity far away from the tip, at the time specified by the white vertical line in (A). (Figure by C. Leduc; Ref. (Leduc, 2005)).

In Fig. 5.31a we show an example of the experimentally observed time evolution of the motor density profile along the tube. These experiments were done by C. Leduc (Institut Curie) using the experimental set-up described in section 5.1. There are strong density inhomogeneities that travel either downstream or upstream, as can be observed in the space-time plot. The density profile at one given time (Fig. 5.31b) shows that the density inhomogeneities that move downstream are those with small average motor density, while those moving upstream are characterized by large average motor densities, in accordance with the results of the simulations above. How-

ever, in spite of the apparent qualitative agreement between the simulations and the experimental data, the density inhomogeneities observed experimentally are more robust than those in the simulations. Both the lifetime and the size of the inhomogeneities observed experimentally are larger than those in the simulations (Fig. 5.30). Moreover, the inhomogeneities are stronger in the experiments, meaning that the motor density inside a motor jam is substantially larger than the average motor density along the microtubule (Fig. 5.31). In contrast, the traffic jams obtained in the simulations show only small differences in motor density with respect to the average value of the motor density field. Fig. 5.32a shows the space-time plot of the steady-state density field for an average steady-state density $\bar{\rho}_b/\rho_s \simeq 0.25$ and only excluded volume interactions between the motors ($\delta = 1$ and $\gamma = 1$). Unlike the simulations shown in Fig. 5.30, where only 10 s were simulated in order to highlight the inhomogeneities, Fig. 5.32a shows the time evolution of the bound motor density field for a similar time scale than in the experiments. The density inhomogeneities are hardly observable at these time scales ($\sim$ minutes) as the lifetime of the traffic jams is about $k_u^{-1} \simeq 2$ s. We conclude that the density inhomogeneities observed experimentally cannot be understood with only excluded volume interactions between the motors.

Motor traffic in presence of preferential attachment/detachment kinetics

We now show that mutual motor interactions beyond excluded volume can induce the appearance of large traffic jams with long lifetimes. To this end, we simulate the dynamics of the system in a ring geometry in presence of preferential attachment/detachment kinetics.

When $\gamma < 1$ and $\delta > 1$, the density field is even more homogeneous than in absence of preferential kinetics ($\gamma = 1$ and $\delta = 1$), consistent with the fact that configurations of motors in contact are prevented on average. On the contrary, if $\delta < 1$ and $\gamma > 1$ large density inhomogeneities appear. In Fig. 5.32b we show the time evolution of the motor density field for a steady state average density about $\bar{\rho}_b/\rho_s \simeq 0.25$, and effective attractive interactions between the motors ($\gamma = 10$ and $\delta = 0.1$). Even for a low average motor density on the microtubule ($\bar{\rho}_b/\rho_s \simeq 0.25$), micron-sized traffic jams develop. For this value of the average motor density, the traffic jams move downstream and their lifetime is in the order of several tenths of seconds, in accordance with the experimental observations (Fig. 5.31). In case the attachment rate is slightly increased, leading to an average motor density on the microtubule about $\bar{\rho}_b/\rho_s \simeq 0.35$, there are traffic jams moving both downstream and upstream (Fig. 5.32c). While upstream moving jams are typically associated with regions of large enough average density, the downstream moving jams develop in regions of low average motor density. Indeed, the experiments show density waves moving both downstream and upstream, the latter occurring in the region closer to the tip of the membrane tube, where the average density is large, in qualitative agreement with our results.

These findings suggest that mutual motor interactions beyond excluded volume, affecting the attachment/detachment motor kinetics, could be at the origin of the observed motor traffic jams along the microtubule. We are currently working to un-

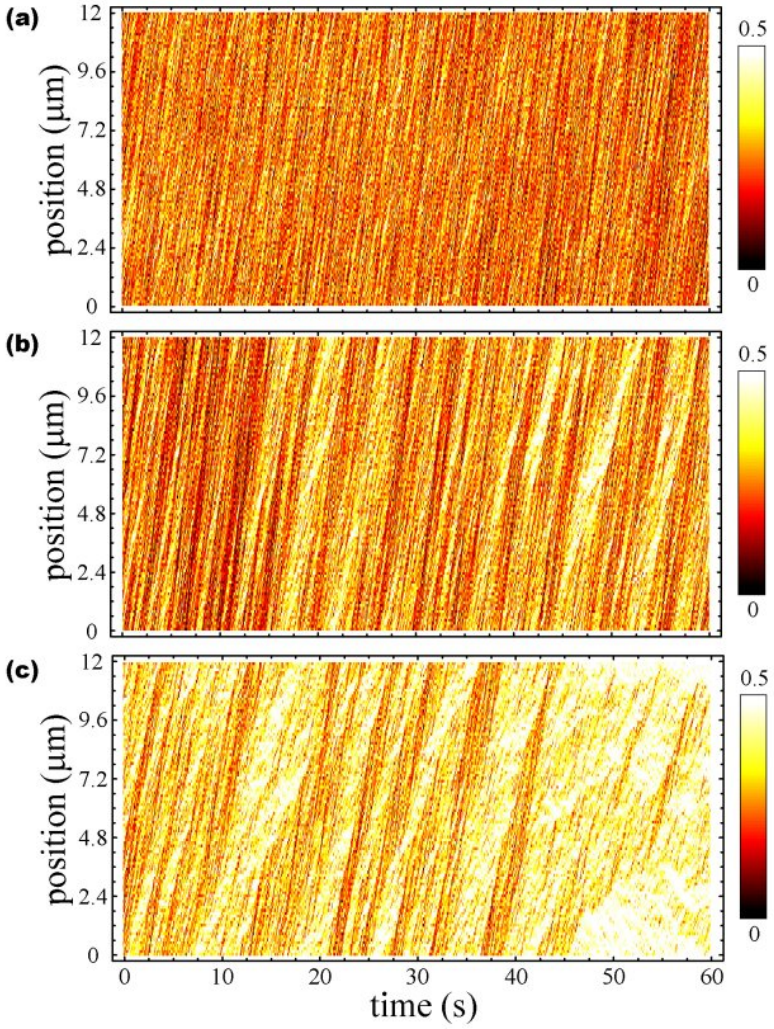

Fig. 5.32. Time evolution of the motor density field in absence (a) and presence (b-c) of preferential attachment/detachment kinetics. In all cases, the kinetic parameters of isolated motors are those of conventional kinesin at saturating ATP concentration: $V_0 = 0.6\ \mu\text{ms}^{-1}$ and $k_u^0 = 0.5\ \text{s}^{-1}$. The attachment rate k_b^0 is different in each case, so that the average steady-state motor density is similar in the cases shown. The time and space scales are similar to those in the experiments (Fig. 5.31). (a) Motor traffic in presence of only excluded volume interactions between the motors; no preferential motor kinetics ($\gamma = 1$ and $\delta = 1$; $\bar{\rho}_b/\rho_s = 0.25$). (b-c) Motor traffic in presence of preferential attachment ($\gamma = 10$) and detachment ($\delta = 0.1$). The values $\gamma > 1$ and $\delta < 1$ correspond to effective attractive interactions between the motors. Large density inhomogeneities (traffic jams) are apparent and move downstream for a low enough average density (b; $k_b^0 = 0.0205\ \text{s}^{-1}$ so that $\bar{\rho}_b/\rho_s \simeq 0.25$) and both downstream and upstream above a threshold average density (c; $k_a^0 = 0.021\text{s}^{-1}$ so that $\bar{\rho}_b/\rho_s \simeq 0.35$).

derstand at quantitative level the effect of interactions in the large scale traffic of motors (Campas et al., 2006c; Roos et al., 2006).

5.5 Conclusions

In this chapter we have described in detail the mechanism by which molecular motors act collectively to pull membrane tubes. We have shown that the collective behavior of motors is essential to understand the dynamics of tube extraction. Our analysis shows that several important physical magnitudes, like the membrane tension or the motor concentration, are essential to monitor tube extraction. Moreover, by comparing at quantitative level the theoretical results to the experimental data, we have been able to estimate kinetic parameters of individual kinesin motors.

Our findings highlight the physical constraints that living cells must deal with in the process of intracellular transport. We briefly describe below our main results and comment their biological relevance and the possible mechanisms that cells may use to control the physical magnitudes that monitor tube extraction.

We have shown that the collective force-dependent detachment kinetics of motors is responsible for both the threshold in tube extraction and the oscillations in tube length. The existence of a threshold is important in that it shows that cells can switch transport on or off when needed. This could be done via two different strategies. The first mechanism involves the control of the local density of motors attached to the membrane, either by regulating the number of available motors, or by regulating the number of motor binding sites on the membrane. The concentration of active motors inside specialized membrane domains would then be an important feature for the understanding of the secretory pathway regulation. The second strategy involves the control of membrane tension. Tension can be changed very rapidly and globally on a membrane providing thus a very fast way to monitor tube growth.

The biological functionality, if any, of membrane tube oscillations remains however unclear. Although tube retractions followed by a recovery of tube growth are observed *in vivo* (Waterman-Storer and Salmon, 1998), no sustained oscillations of membrane tubes have been reported. In any case, when a tube network, like the endoplasmic reticulum, extends inside the cell, the tension increase (if the tension is not fixed by membrane reservoirs) would couple the tube formation in distant regions of the cell; if tube growth from a given organelle is promoted in a particular direction, the tension increase of the organelle would prevent the formation of tubes in other directions. Regardless of the biological function of the oscillations in tube extraction, the mechanism responsible for the oscillatory instability is of clear biological relevance. There exist very many situations in living cells in which motor proteins work in large groups in order to develop the necessary forces to induce motion at cellular scales. It is thus likely that the same oscillatory instability exists in these situations. Indeed, in chapter 8 we analyze the movement of chromosomes in mitosis and show that the collective dynamics of motor proteins is essential to understand both chromosome motion and positioning. In particular, the same oscillatory instability exists and explains the oscillatory behavior of chromosomes throughout mitosis.

Our results concerning the organization of motors at the tip of growing tubes suggest that motor proteins need to simultaneously use several protofilaments to generate the forces required for tube extraction. We have shown that the attachment/detachment kinetics of motors sets a small average number of working motors per protofilament at the tube tip. This finding establishes limits on the forces that motors can develop when pulling a membrane tube. It is possible that living cells use other proteins to create motor aggregates that would rigidly couple the motors and allow the generation of larger forces. The organization and mutual motor interactions at the tip of a growing tube or, in general, when motors pull on a fluid membrane are thus important. In chapter 6 we analyze in more details the collective force generation of motors pulling on fluid membranes and extend these results.

Finally, the experiments performed by C. Leduc concerning the motor traffic along the tube showed that large motor inhomogeneities (traffic jams) appear spontaneously. Our theoretical results show that these density inhomogeneities cannot arise solely from excluded volume interactions between the motors. Moreover, we show that micron-sized traffic jams, similar to those observed experimentally, appear as a consequence of mutual motor interactions beyond excluded volume. Together with Giovanni Cappello and Wouter Roos (Institut Curie) we are studying the formation of motor density inhomogeneities caused by mutual motor interactions. The preliminary results suggest that the attachment/detachment kinetics of individual motors is affected by the presence of other motors, leading to a clustering effect (Roos et al., 2006). It is possible that the spontaneous formation of traffic jams have important consequences for the long range traffic in the crowded conditions of the cell. Indeed, several neurodegenerative diseases have been associated to anomalies in the traffic along axons (Aridor and Hannan, 2000; Aridor and Hannan, 2002). It would be interesting to explore whether the nonlinear phenomena in traffic, due to mutual motor interactions, is at the origin of some of these diseases.

6

Cooperative dynamics of interacting molecular motors

The analysis in chapter 5 suggested that molecular motors pulling a membrane tube can transmit forces to each other when they are in contact in a row-like configuration. In this chapter we analyze the physical mechanism of collective force generation when motors pull on a fluid membrane, and show that it differs significantly from the collective behavior of rigidly or elastically connected motors. Although the collective behavior of rigidly coupled motors is important in many biological situations (Bray, 1992) (muscle contraction, flagellar beating,...), there are other situations in which the motors cannot transmit the forces to each other through the cargo at which they are attached. This latter case occurs, for instance, when motors pull on a fluid membrane.

The collective behavior of molecular motors plays a crucial role in many biological phenomena ranging from intracellular and intra-flagellar transport to axonal transport (Alberts et al., 2004; Bray, 1992; Howard, 2001). Molecular motors are often classified according to their processivity (Leibler and Huse, 1993). Processive motors rarely unbind from the track on which they are moving; they perform best when working in small groups and are therefore referred to as "porters". Non-processive motors unbind from the track frequently, they work best in large groups and are referred to as "rowers". Examples of "porters" are kinesin motors which move along microtubules, while classical myosin motors which move along actin filaments are examples of "rowers" (Leibler and Huse, 1993).

The classification of motors into "porters" and "rowers" is based on their behavior when connected to a rigid or elastic cargo. The strong coupling between processive motors leads to an effective friction which results from motors which cannot move because other motors are bound to the track (Leibler and Huse, 1993; Vale et al., 1989). A strong coupling between the motors indeed exists for a microtubule pushed by kinesin motors that are bound to a surface (Howard, 2001). It is also important for describing myosin motors acting in skeletal muscles. The abundance of such systems has inspired several theoretical studies of the collective behavior of strongly coupled motors (Julicher and Prost, 1995; Vilfan et al., 1998).

In many cases, however, this description in terms of rowers and porters is not adequate since the motors are not rigidly attached to the cargo. An important class

of systems where this happens is when motors, such as kinesin, move along microtubules carrying a load which is a lipid membrane, an ubiquitous situation in living cells. This occurs, for example, when kinesins or dyneins carry a vesicle along a microtubule (Howard, 2001). Moreover, we have shown in chapter 5 that kinesin motors moving along a microtubule act collectively to pull membrane tubes from a vesicle (Leduc et al., 2004).

When motors are rigidly attached to the cargo being transported there is a strong coupling between the motors, as the motion of one motor affects the dynamics of the other motors. Although this strong coupling does not exist for motors not rigidly attached to the cargo (e.g. attached to a fluid membrane), in this case the dynamics of the motors is affected by the presence of other motors. Mutual motor interactions can thus play an important role in the collective behavior of motors pulling of fluid membranes. Indeed, there are several experimental observations that suggest the existence of interactions between the motors (Vilfan et al., 2001; Muto et al., 2005; Nishinari et al., 2005).

A part of the work that we present in this chapter can be found in Ref. (Campas et al., 2006b).

6.1 Theoretical description

We study theoretically the collective behavior of N processive motors pulling a tube out of a membrane and acting against the force needed to extract it (Derenyi et al., 2002; Powers et al., 2002) (Fig. 6.1a). For simplicity, the tube force F is considered as constant. A fluid membrane can only exert a force on the motors at the leading edge of the tube where the normal to the surface has a component in the direction of motor motion. For simplicity we assume here that all the force is transmitted to the leading motor (Fig. 6.1a). Although we focus on the process of membrane tube extraction due to its simplified geometry, the present treatment is a reasonable approximation for motors carrying a vesicle (Fig. 6.1b). In this case, the forces opposing motion would arise from the movement of the vesicle in the crowded environment of the cell.

We consider the collective behavior of the motors as a function of the applied force, F, the number of motors, N, and the effective interactions (defined as the combined effect of the microscopic details of the system on the transition rates in a coarse-grained description) between the motors. We show that the force-velocity curve $V_N(F)$ strongly depends on the interactions between motors and differs significantly from the mean-field treatment where independent motors equally share the force, leading to $V_N(F) = V_1(F/N)$. Moreover, we find that beyond a certain number of motors, the force-velocity curves are all indistinguishable for practical purposes. While the interactions do not play any role in the absence of external force, their effect becomes clearly visible as F increases. The analysis is first carried out assuming that motors do not detach from the filament. We then use numerics to show that under experimentally relevant conditions our results are not modified even in the presence

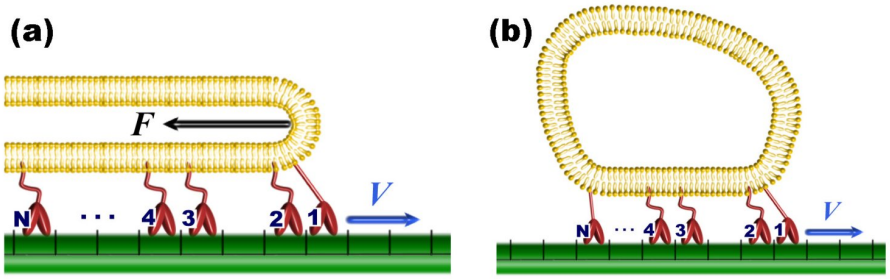

Fig. 6.1. Sketch of the system. (a) N motors pulling a membrane tube from a vesicle. The force, F, required to extract the tube, is assumed to act only on the leading motor (labeled 1). The remaining motors move in the absence of any applied force. At long time scales, all motors move at the same mean velocity V. (b) N motors carrying a small vesicle. In this case, the forces opposing the movement would arise from the friction of the vesicle in the crowded environment of the cell, and are not depicted here.

of force-dependent motor detachment. Finally we explore how the effective interactions in the coarse-grained description arise from a more microscopic two-state model.

In a coarse-grained description of the system we first model the motors as interacting biased random-walkers moving along a one-dimensional lattice. A similar approach has been used to study the traffic of motor proteins with excluded volume interactions (Lipowsky et al., 2001; Parmeggiani et al., 2003). We first assume that the motors are fully processive and never unbind from the filament that acts as a track. All lengths are expressed in units of the lattice constant, ℓ, which characterizes the filament period [1]. Each site can be occupied by one motor at most, which can move to a neighboring site if empty. We label the motors with an index $\mu = 1 \ldots N$, with 1 labeling the leading motor on which the force is exerted (Fig. 6.1a). The dynamics of the motors is specified by the hopping rates defined in Fig. 6.2 where the boxes represent sites on the lattice and a ball with index μ indicates that the site is occupied by motor μ.

The model is a generalization of the disordered exclusion model introduced in Ref. (Evans, 1996), which includes modifications of the rates due to nearest-neighbor interactions between the motors. The particular choice for the hopping rates in our description is $p_\mu = p$, $v_\mu = v$, $q_\mu = q$ and $u_\mu = u$ for $\mu \geq 2$ (Fig. 6.2b), whereas the rates of the leading motor ($\mu = 1$) depend on the external force (Fig. 6.2c) [2]. According to Kramers rate theory (van Kampen, 2004), we write $p_1 = pe^{-f\delta}$, $q_1 = qe^{f(1-\delta)}$ and $v_1 = ve^{-f\delta}$, where f is the force in units of K_BT/ℓ (K_BT being the thermal energy). The dimensionless parameter $0 < \delta < 1$ characterizes the position

[1] The length ℓ should in principle be the elemental step size of a motor. We define it as the filament period because the step size of several types of motor proteins coincides with the size of the filament periodicity.

[2] We assume for simplicity that the N-motor problem can be described with the same rates as the two motor case; we ignore higher order correlations on the rates.

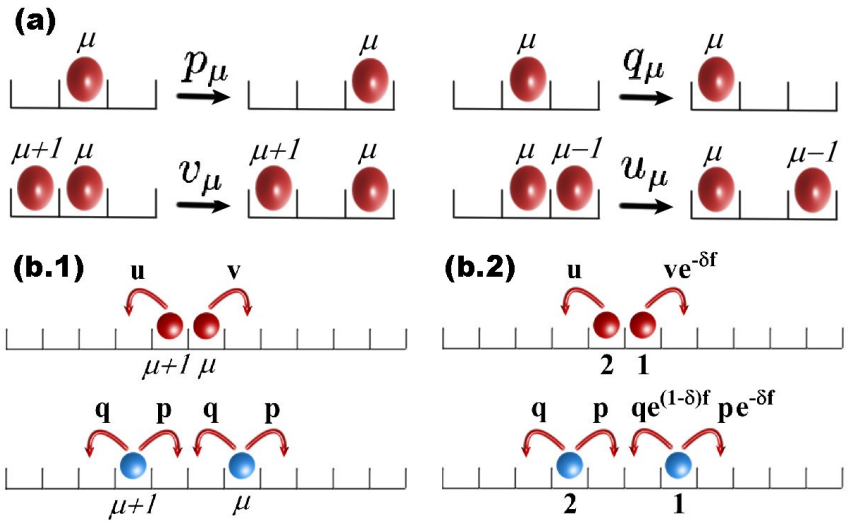

Fig. 6.2. Possible motor transitions and associated rates. The boxes and balls represent lattice sites and motors respectively. (a) General scheme for the transition rates. The rates can be different for each motor and can also depend on whether the motor is isolated or in contact with another motor. (b) Particular choice for the motor transition rates in our analysis. Transition rates for motors sustaining no load (b.1; $\mu \geq 2$) and rates for the leading motor (b.2; $\mu = 1$). The effect of the interactions is effectively taken into account in different transition rates for isolated motors and motors in contact.

of the energy barrier associated to the forward transition. For single conventional kinesin motors, this exponential dependence of the forward and backward rates on the force has indeed been observed experimentally (Nishiyama et al., 2002; Carter and Cross, 2005). Attractive effective interactions correspond to reduced hopping rates ($v < p$, $u < q$) and repulsive effective interactions to increased hopping rates ($v > p$, $u > q$). We refer to the case in which the motors do not change their individual rates when they are in contact ($v = p$ and $u = q$) as neutral.

6.1.1 Single motor

Before describing the motor collective behavior, we first study the motion of a single motor as a biased random walker. In the long-time limit, the average velocity of the motor, V_1, is given by[3]

$$V_1 = p_1 - q_1 = p\exp(-f\delta) - q\exp(f(1-\delta)) \ , \tag{6.1}$$

where the velocity is in rate units as all lengths are scaled with ℓ. After expressing the time in p^{-1} units, the force-velocity relation $V_1(f)$ depends only on two dimensionless parameters, namely δ and p/q. The parameter δ quantifies which of the rates

[3] The subscript stands for the number of motors being considered.

(forward or backward) is more affected by the load. A value $\delta = 0.5$ means that both rates are equally affected by the force, whereas a value $\delta = 0.9$ indicates that the forward rate is much more affected by the force than the backward rate. On the other hand, the parameter p/q characterizes the bias of the motor. Large values for p/q mean that the motor steps forward much more frequently than backward.

The force-velocity relation in Eq. 6.1 has two points of particular interest, namely the velocity at vanishing force, V_0, and the force at which the velocity vanishes, f_s (stall force). Using Eq. 6.1, the expressions for V_0 and f_s as a function of the motor transition rates read

$$V_0 = p - q\,, \qquad f_s(1) = \ln(p/q)\ . \tag{6.2}$$

In Fig. 6.3 we plot the force-velocity curves for different values of the parameter δ and compare them to the force-velocity curves for 2 motors. Recent single molecule experiments directly measure the forward and backward transition rates as a function of the applied load for single conventional kinesin motors (Nishiyama et al., 2002; Carter and Cross, 2005). We compare the experimental data of these works to our theoretical results in section 6.3.1.

6.1.2 Two motor problem

Before addressing the general case of N motors, it is instructive to first consider a system with only two motors. This case may be solved exactly in the long-time limit. Defining the variable k as the number of empty sites between the two motors, the dynamics of the system are given by the one-step stochastic process for the variable k. The probability, $\rho_k(t)$, of finding the motors k ($k \geq 2$) sites apart at time t is specified by the master equation

$$\frac{d\rho_k(t)}{dt} = (p+q_1)\rho_{k+1}(t) + (p_1+q)\rho_{k-1}(t) - (p_1+p+q_1+q)\rho_k(t)\ . \tag{6.3}$$

When the two motors are in contact, $k = 0$, or separated by only one site, $k = 1$, the dynamics is different and the master equations for this cases read

$$\begin{aligned} \frac{d\rho_0(t)}{dt} &= (p+q_1)\rho_1(t) - (v_1+u)\rho_0(t)\,, \\ \frac{d\rho_1(t)}{dt} &= (v_1+u)\rho_0(t) + (p+q_1)\rho_2(t) - (p_1+p+q_1+q)\rho_1(t)\ . \end{aligned} \tag{6.4}$$

The steady-state solution for the probability, ρ_k, can be obtained by writing a recursion relation for the probabilities, and reads

$$\rho_k = \frac{(p-q)-(p_1-q_1)}{(u+v_1)+(p-q)-(p_1-q_1)}\,\frac{v_1+u}{p_1+q}\left(\frac{p_1+q}{p+q_1}\right)^k\,, \tag{6.5}$$

where the probabilities satisfy the normalization condition, $\sum_{k=0}^{\infty}\rho_k = 1$. For any finite force the probability of finding the motors k sites apart decays as $\left[(p_1+q)/(p+q_1)\right]^k$.

The average number of sites between the two motors is therefore finite and decreases with the force.

Since the motors can not overtake each other, their average velocities are equal and can be found, for example, by writing the equation of motion for their center of mass. If the leading motor is at site i and the second motor at site j ($j < i$), the number of empty sites between them is $k = i - j - 1$, and the position of the center of mass, x, is $x = (i+j)/2$. The probability, $\rho_{CM}(x,t)$, that the center of mass is at position x at time t is given by

$$\begin{aligned}\frac{d\rho_{CM}(x,t)}{dt} &= \rho_0(t)\Big[v_1\rho_{CM}(x-\frac{1}{2},t)+u\rho_{CM}(x+\frac{1}{2},t)-(v_1+u)\rho_{CM}(x,t)\Big] \\ &+ \big(1-\rho_0(t)\big)\Big[(p_1+p)\rho_{CM}(x-\frac{1}{2},t)+(q_1+q)\rho_{CM}(x+\frac{1}{2},t) \\ &- (p_1+p+q_1+q)\rho_{CM}(x,t)\Big]\,, \end{aligned} \tag{6.6}$$

where $\rho_0(t)$ is the probability that the motors are in contact ($k = 0$) at time t. As we are interested in the behavior at large length scales (larger than the size of a site), we expand the probability for the position of the center of mass up to first order to get

$$\begin{aligned}&\frac{\partial\rho_{CM}(x,t)}{\partial t}+\frac{\partial\rho_{CM}(x,t)}{\partial x}\left[\frac{1}{2}\rho_0(t)(v_1-u)+\frac{1}{2}\big(1-\rho_0(t)\big)\big(p_1-q_1+p-q\big)\right] \\ &+\frac{\partial^2\rho_{CM}(x,t)}{\partial x^2}(\cdots)+\cdots=0\,. \end{aligned} \tag{6.7}$$

The drift term specifies the average velocity of the center of mass in this coarse-grained description [4]. In the long-time limit, the average velocity of the motors reads

$$V_2 = \frac{v_1(p-q)+u(p_1-q_1)}{(v_1+u)+(p-q)-(p_1-q_1)}\,, \tag{6.8}$$

where we have used the expression previously found for ρ_0 as a function of the rates. The stall force of two motors is obtained from Eq. 6.8 by setting $V_2 = 0$, and reads

$$f_s(2) = \ln\left(\frac{pv}{qu}+\frac{p}{q}-\frac{v}{u}\right)\,. \tag{6.9}$$

The stall force is not necessarily twice the stall force of a single motor. It is a function of the rates ratio v/u, which depends on the interactions between the motors, and can be either larger or smaller than $2\,f_s(1)$ depending on whether $v/u > p/q$ or $v/u < p/q$ respectively. Two interacting motors can thus develop forces larger than the sum of their individual contributions. Although the stall force depends on the effective interactions as these determine the transition rates v and u, it does not depend on the type of interactions; the same stall force can be obtained for both attractive and repulsive interactions as long as the ratio v/u has the same value.

[4] The second order corresponds to the diffusive term and provides the diffusion coefficient for the two motor system as a function of the elemental transition rates.

The velocity V_2 is plotted for various values of v and u in Fig. 6.3 where, for clarity, we set $v/u = p/q$, so that $f_s(2) = 2f_s(1)$. The general shape of the force-velocity curve is highly sensitive to the interactions. For strong enough attractive interactions the velocity of two motors is smaller than that of a single motor up to a certain value of the force, at which the two motors become faster than a single motor. An experimental signature of this type is a clear demonstration of attractive interactions between the motors. In the neutral case, i.e. when the motor transition rates are not modified for motors in contact ($v = p$ and $u = q$), the velocity of two motors is always larger than that of a single motor. This is due to the fact that the second motor rectifies the movement of the leading one, by not allowing some of its backward transitions. For repulsive effective interactions, the presence of the second motor just behind the leading one, not only prevents some of its backward transitions, but also enhances its forward rate ($v > p$). As a result, the velocity of two motors with effective repulsive interactions is larger than in the neutral case.

6.1.3 N motor problem

Exact solution for the neutral case

We now turn to the general case with N motors. Using the results of Ref. (Evans, 1996), an exact expression of the velocity can be obtained in the neutral case where $v = p$ and $u = q$ on a ring geometry. In the limit where the number of vacancies in front of the first motor ($\mu = 1$) is infinite, the periodic boundary conditions do not influence the results. On a ring geometry, the steady-state weight, $f(n_1,\ldots,n_N)$, of a configuration where particle μ has n_μ sites with no motors in front of it, is a product measure

$$f(n_1,\ldots,n_N) = \prod_{\mu=1}^{N} g_\mu^{n_\mu} \,, \tag{6.10}$$

$$g_\mu = \left[\sum_{i=0}^{N-1} \frac{1}{p_{\mu-i}} \prod_{j=\mu+1-i}^{\mu} \frac{q_j}{p_j}\right] \left[1 - \prod_{k=1}^{N} \frac{q_k}{p_k}\right]^{-1} .$$

It is convenient to work in the a grand-canonical ensemble where the number of empty sites in the system is allowed to fluctuate. Namely, define the grand-partition sum $G(z) = \sum_{L=0}^{\infty} Z_{L,N} z^L$ where L is the number of empty sites on the track, $z = g_N$ is the fugacity and $Z_{L,N}$ is the sum over the weights of configurations with L empty sites and N occupied sites. In Ref. (Evans, 1996) it is shown that the velocity of the motors is equal to the fugacity. Moreover, it has been shown (Evans, 1996) that when the leading motor ($\mu = 1$) is slower, in the limit $L \to \infty$ and N finite, the distance between the first ($\mu = 1$) and last ($\mu = N$) particles is finite. In this limit, the value of the fugacity is given by the pole of $G(z)$ which is closest to the origin. Inserting the rates of our description (Fig. 6.2) in Eq. 6.11, one finds

$$V_N = p \frac{\left[1 - e^f (q/p)^N\right] [1 - q/p]}{e^{f\delta} [1 - q/p] + e^f [q/p - (q/p)^N]} \,. \tag{6.11}$$

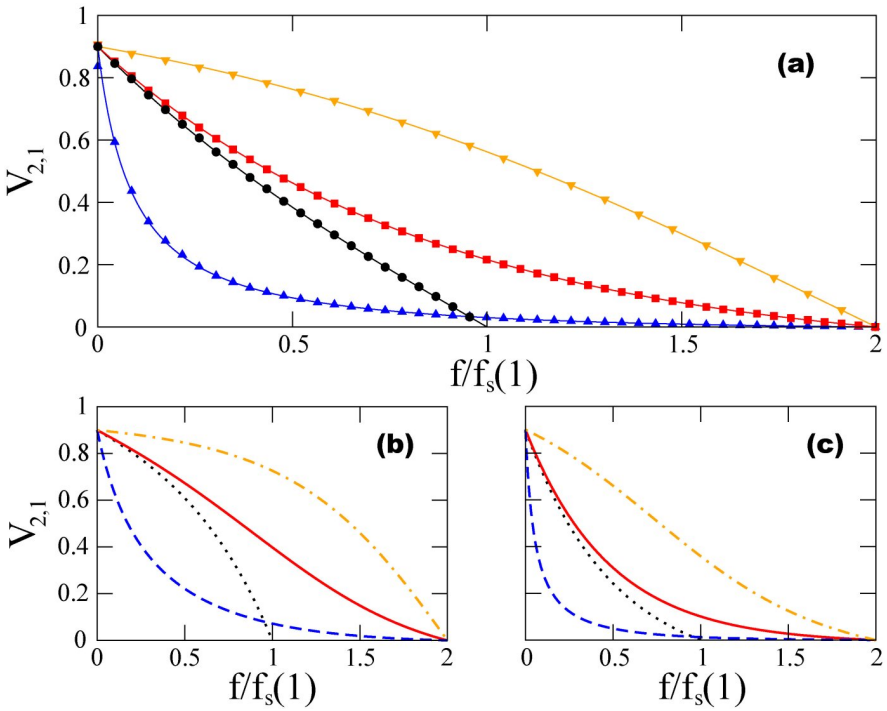

Fig. 6.3. Force-velocity curves of 2 motors in the limits of attractive, repulsive and neutral interactions. In all cases $p = 1.0$ and $q = 0.1$. (a) $\delta = 0.5$, (b) $\delta = 0.1$, (c) $\delta = 0.9$. Analytical solutions (lines) and Monte Carlo simulations (symbols; only in (a)). The rates v and u are: $v = 0.1, 1.0, 10.0$ and $u = 0.01, 0.1, 1.0$ for attractive (dashed line; triangle up (a)), neutral (continuous line; square (a)) and repulsive (dashed-dotted line; triangle down (a)) interactions respectively. The velocity-force curve for a single motor is also plotted for comparison (dotted line; circle (a)). The ratio $v/u = p/q$ so that $f_s(2) = 2 f_s(1)$. All rates are in units of p.

In the neutral case, for any number of motors $f_s(N) = N f_s(1)$ (Fig. 6.6a). The force-velocity curves for 10 and 20 motors are shown in Fig. 6.4, together with the results from the simulations for comparison (see section 6.2). The agreement between the analytical and numerical results is excellent.

In the absence of force, the velocity is independent of the number of motors and given by $V_0 = p - q$. The slope of the force-velocity curve for vanishing forces is negative and converges exponentially fast with N to $-(1 - q/p)[q + (p - q)\delta]$. The larger the number of motors the smaller the absolute value of the slope (Fig. 6.5a). For large N and f the motors form a dense cluster which can move only through the exponentially slow (in N and f) process of a vacancy entering at one end of the cluster and exiting at the other. As a consequence, for any number of motors

$$N \gg 1 + \frac{1}{\ln(p/q)} , \tag{6.12}$$

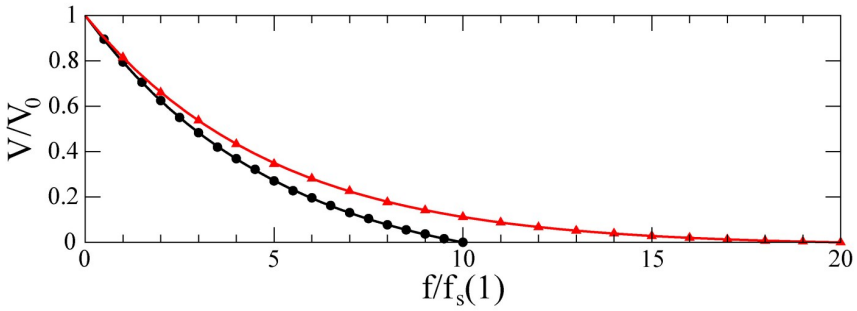

Fig. 6.4. Force-velocity curves for 10 (circle) and 20 (triangle up) motors, and neutral interactions ($v = p$ and $u = q$). The rates $p = 1$ and $q = 0.8$ correspond to weakly biased motors. All rates are in units of p.

the force-velocity curves are indistinguishable for all practical purposes (Fig. 6.5a,b). For weakly biased motors ($p/q = 2$), this saturation effect becomes noticeable at about 7 motors (Fig. 6.5a). However, for strongly biased motors ($p/q = 10^2$), the saturation effect is already present for 2 motors (Fig. 6.5b). These results imply that it is not possible to estimate the number of kinesin motors pulling on a vesicle or a membrane tube from the force-velocity curve measured experimentally. Even in the neutral case, the force-velocity curve is significantly different from the commonly used mean-field prediction where the motors share equally the load, leading to $V_N(F) = V_1(F/N)$ (Fig. 6.5c,d). For highly biased motors like conventional kinesin, this discrepancy is noticeable even for a number of motors as small as two and becomes dramatic for increasing number of motors (Fig. 6.5d).

The saturation effect has important consequences for the stall force. Although for the neutral case the stall force increases linearly with the number of motors ($f_s(N) = N f_s(1)$), the velocity reaches negligible values at forces much smaller than $N f_s(1)$. In Fig. 6.5b we compare the force-velocity curves of 2 and 10^2 motors. They differ only for velocity values below approximately $10^{-2}V_0$. The velocity of 100 is negligible already at the stall force of two motors, but only vanishes strictly at $f = 100 f_s(1)$. Thus, for neutral interactions between strongly biased motors, the apparent stall force is essentially independent of the number of motors for $N \geq 2$.

General solution close to stall force

In the vicinity of the stall force, when the motion of the motors is exponentially slow in their number, the velocity can be obtained in the presence of interactions if $p \gg q$, $p \gg u$ and $v \gg u$. In this limit, the motors form a compact cluster with no vacancies in the middle. The movement in either direction occurs by propagation of a vacancy from one end to the other. The velocity is then equal to the difference between the rate of motion of the tightly bound motors to the right and the rate of motion to the left. To leading order, the rate at which the motors move to the right is given by the hopping rate of the first motor, v_1, to the right times the product of the probabilities

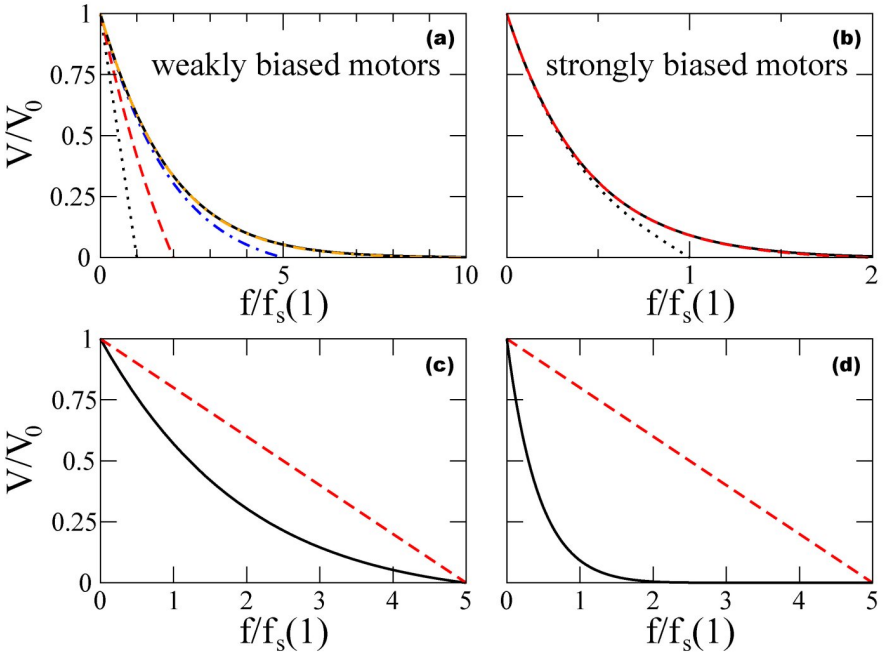

Fig. 6.5. (a-b) Force-velocity curves for different number of motors and neutral interactions, showing the saturation of the force-velocity curves for different motor bias. (a) Weakly biased motors with rates: $p = 1$ and $q = 0.5$. Force-velocity curves for: $N = 1$ (dotted line), $N = 2$ (dashed line), $N = 5$ (dashed-dotted line), $N = 10$ (dashed-double-dotted line) and $N = 100$ (continuous line). (b) Highly biased motors with rates: $p = 1$ and $q = 0.01$. Force-velocity curves for: $N = 1$ (dotted line), $N = 2$ (dashed line) and $N = 100$ (continuous line). (c-d) Comparison of the force-velocity curves ($N = 5$) obtained in the neutral case (Eq. 6.11; continuous line) and those obtained from a simple mean-field analysis in which the motors equally share the load ($V/V_0 = 1 - F/Nf_s(1)$; dashed line). (c) Weakly biased motors: $p = 1$ and $q = 0.5$. (d) Strongly biased motors: $p = 1$ and $q = 0.01$. All rates are in units of p and $\delta = 0.5$.

that the other motors move to the right. The probability that particle $\mu = 2$ moves to the right is given by $v/(v+q_1) \simeq v/q_1$ near the stall force. Similarly, in this limit for strongly biased motors, the other motors move with probability 1 to the right. A close argument for the rate at which the cluster moves to the left gives

$$V_N = v\frac{v_1}{q_1} - u\frac{u}{p}\left(\frac{u}{v}\right)^{N-3} . \tag{6.13}$$

The latter expression is in agreement with the general result for two motors (Eq. 6.8) and with the result for N motors in the neutral case (Eq. 6.11). The normalized stall force for N motors in this limit is then

$$\frac{f_s(N)}{Nf_s(1)} = \frac{\ln(v/u)}{\ln(p/q)} - \frac{1}{N}\left(\frac{\ln(v/u)}{\ln(p/q)} - 1\right) . \tag{6.14}$$

As for two motors, the stall force only depends on the ratios of the rates v/u and p/q. If $v/u > p/q$ the normalized stall force per motor increases with the number of motors and saturates at a value larger than 1 for many motors. It has the opposite behavior when $v/u < p/q$.

6.2 Simulations

6.2.1 Monte Carlo simulations of interacting motors

The results presented in the last section for N motors hold only for neutral interactions. In order to test the effect of different type of interactions between motors on our results, we have performed continuous time Monte Carlo simulations. The simulations are implemented in similar way than those developed for the process of membrane tube extraction described in chapter 5. The general implementation procedure is detailed in section 5.4.1.

We have first performed simulations for the cases described in the previous sections. In Fig. 6.3a we compare the analytical and numerically computed force-velocity curves for two motors and different effective interactions. The numerical and analytical force-velocity curves for 10 and 20 motors in the case of neutral interactions are shown in Fig. 6.4. In all cases, the numerical and analytical results are in perfect agreement.

We have performed simulations for different types of effective interactions and number of motors, in order to determine the influence of attractive and repulsive effective interactions in the previous results. Similarly to the case of two motors, the stall force is only a function of the rate ratios p/q and v/u (Fig. 6.6b). Both attractive and repulsive interactions lead to the same value of the stall force provided that the rate ratios p/q and v/u have the same values for both type of interactions. When $v/u = p/q$ the stall force always satisfies $f_s(N) = N f_s(1)$ as expected (Fig. 6.6a). In case $v/u > p/q$, the stall force is larger than the sum of the individual contributions of the motors ($f_s(N) > N f_s(1)$), and for $v/u < p/q$ the stall force is smaller than $N f_s(1)$ (Fig. 6.6b). Thus, depending on how the interactions affect the transition rates for motors in contact, an ensemble of N motors can, in principle, develop forces larger than the sum of their individual contributions.

Similarly to the neutral case, for any given type of interaction the force-velocity curves are all indistinguishable above a certain number of motors. In the presence of strong enough attractive interactions the velocity is smaller than that of a single motor for small forces but becomes larger at larger forces, as in the case of two motors. The force-velocity curves for different number of motors cross the force-velocity curve of 1 motor at the same point (Fig. 6.7a). Moreover, for a given force, the velocity shows a non-monotonous behavior as a function of N until it saturates. The force-velocity curves collapse if $N \gtrsim 7$ ($p/q = 10$; Fig. 6.7a). In the presence of repulsive interactions, the velocity V_N is always larger than the velocity of 1 motor and the force-velocity curves become nearly identical if $N \gtrsim 7$ ($p/q = 10$; Fig. 6.7b).

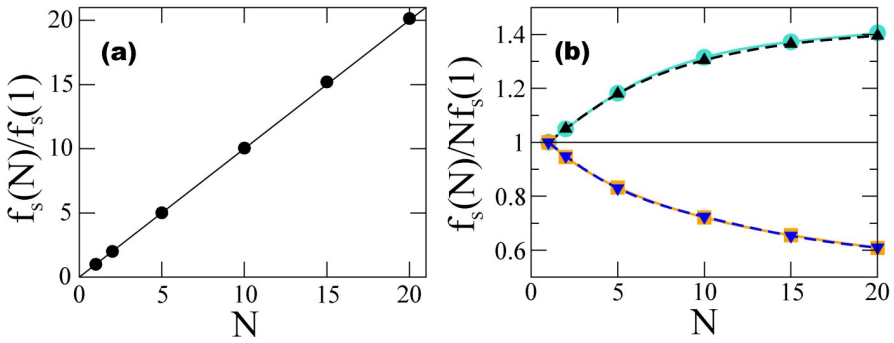

Fig. 6.6. Stall force of N motors. (a) Stall force in the case of neutral interactions ($v = p$ and $u = q$) as a function of the number of motors. Numerical simulations (circle) are compared to the theoretical prediction, $f_s(N) = N f_s(1)$ (continuous line). (b) Stall force as a function of N for various types of interactions. Both for attractive ($v = 0.7$, $u = 0.5$; circles) and repulsive ($v = 1.54$, $u = 1.1$; triangles up) interactions, the value of the stall force, $f_s(N)$, is the same and larger than $N f_s(1)$ as $v/u = 1.4 > p/q$. When $v/u = 1.1 < p/q$, $f_s(N) < N f_s(1)$ and it has also the same value for both attractive ($v = 0.55$, $u = 0.5$; squares) and repulsive ($v = 1.21$, $u = 1.1$; triangles down) interactions. All rates are in units of p and $\delta = 0.5$. Note that the stall force does not depend on the particular value of δ.

Experimentally one should expect a force-velocity curve independent of the number of motors if a few motors act collectively. The number of motors at which the force-velocity curves become indistinguishable depends on the motor bias. The comparison between the velocities of many and one motor could serve as an experimental test to sort out attractive from repulsive interactions.

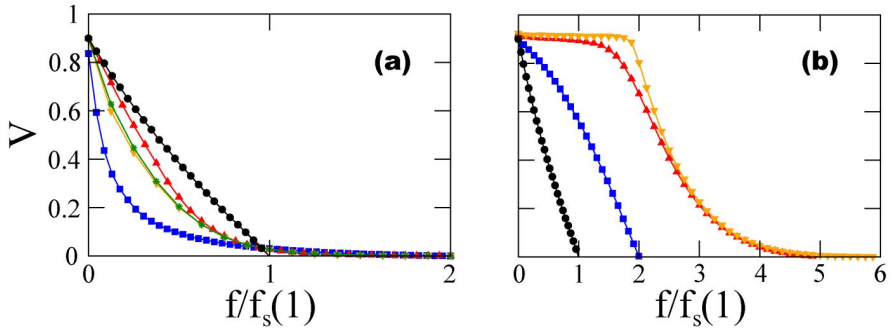

Fig. 6.7. (a) Force-velocity curves in the case of attractive interactions between strongly biased motors ($p = 1, q = 0.1, v = 0.1, u = 0.01$) for 1 (circles), 2 (squares), 5 (triangles up), 10 (triangles down) and 20 (star) motors. (b) Force-velocity curves in the case of repulsive interactions between strongly biased motors ($p = 1, q = 0.1, v = 10, u = 1$) for 1 (circles), 2 (squares), 5 (triangles up) and 10 (triangles down) motors; All rates are in units of p and $\delta = 0.5$.

As discussed above for the neutral case, the collapse of the force-velocity curves implies that the apparent stall force can be much smaller than that at which the velocity strictly vanishes, because the velocity reaches negligible values way below stall force. In particular, for strong enough attractive interactions the apparent stall force for a system with an arbitrarily large number of motors, may be similar (or even smaller) than the stall force of a single motor.

6.2.2 Effect of motor detachment/attachment kinetics

We now study the influence of the motor processivity by including the attachment/detachment kinetics in the simulations. We introduce an unbound state with a constant motor density, so that motors can attach to any site (behind the leading motor) at a constant rate, a_0. The motors bound to the filament unbind at a constant rate d_0, except for the leading motor, which detaches with a force-dependent rate $d = d_0 \exp(f\delta_d)$ (where δ_d is a length, expressed in ℓ units, characterizing the activated process). In Fig. 6.8 we define the motor transition rates that specify the dynamics. Although it is likely that the detachment rate of the other motors is also influenced to some extent by the load applied to the leading motor, here we consider the extreme case where the load only affects the rates of the leading motor, as this is the case where detachment may influence most our previous results.

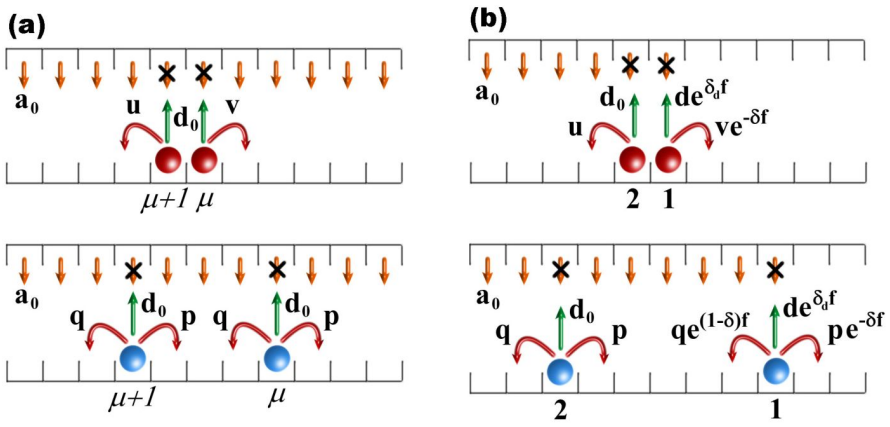

Fig. 6.8. Possible motor transitions and associated rates in the presence of detachment. The boxes and balls represent lattice sites and motors respectively. The unbound state is represented by inverted boxes. Transition rates for motors sustaining no load ((a); $\mu \geq 2$) and rates for the leading motor ((b); $\mu = 1$). Configurations where the motors are isolated and in contact are shown.

In presence of attachment/detachment kinetics, the number of motors in the system is not fixed. However, there is always a cluster of consecutive motors that forms dynamically behind the leading motor. The average number of motors in the cluster,

n, depends on the applied force. In Fig. 6.9 we compare the force-velocity curves in the presence and absence of attachment/detachment kinetics for the neutral case. For typical values of the rates for conventional kinesin motors (see discussion below), detachment events do not modify the force-velocity curve, as long as the number of motors clustered behind the leading motor remains large enough (Fig. 6.9, inset). For both neutral and attractive interactions, the effect of detachment on the force-velocity curves is negligible. Detachment events can however significantly affect the force-velocity curve only for strongly repulsive interactions at large forces.

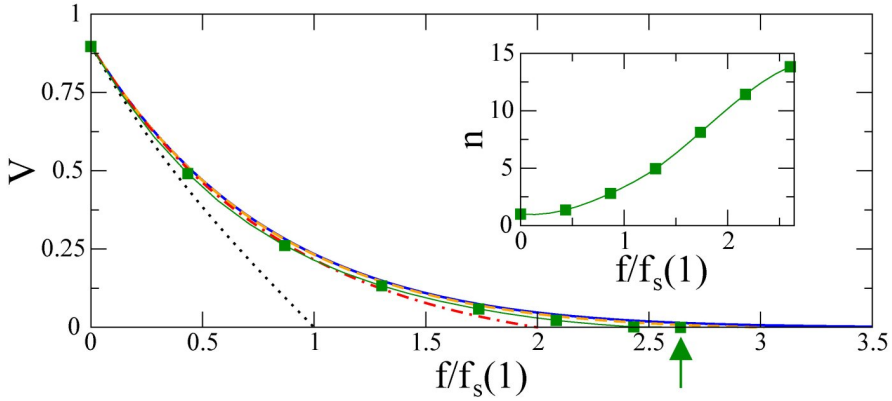

Fig. 6.9. Force-velocity curves in the case of neutral interactions (Eq. 6.11) for 1 (dotted line), 2 (dashed-dotted line), 3 (dashed line) and 100 (continuous line) motors. The force-velocity curve obtained by numerical simulation in presence of detachment/attachment kinetics is also shown (squares). The arrow corresponds to the stall force in presence of attachment/detachment kinetics. The inset shows the evolution of n with the force; Parameters: $p = v = 1$, $q = u = 0.1$, $\delta = 0.5$, $a_0 = 0.01$, $d_0 = 5.6\,10^{-3}$, $\delta_d = 0.16$. All rates are in units of p.

The main effect of motor detachment is to lower slightly the average velocity, as a consequence of detachment events associated to the leading motor. While this effect is totally negligible at small forces, where the average velocity is much larger than its reduction due to detachment, it becomes critical for small average velocities. As a result, the value of the stall force is substantially influenced by detachment. However, as discussed above, the relevant measure of the stall force is the apparent stall force, for which the velocity becomes negligible. In Fig. 6.9 we show that although the stall force may change considerably due to motor detachment, the apparent stall force remains nearly unchanged in the case of attractive and neutral interactions. Hence, detachment events set the value of the stall force to about the value of the apparent stall force in absence of detachment. For strongly repulsive interactions, detachment events can modify substantially the force-velocity curve and, as a consequence, the apparent stall force can also be changed.

6.2.3 Motor internal states

In the previous discussion, the nature of the effective interaction between motors was assumed. Two-states models (Julicher et al., 1997) are generic descriptions that consider, at a coarse-grained level, some of the internal states of the motor and allow for a more detailed analysis of the effective interactions. We now show that for these models, one expects non-neutral interactions at long times and large length-scales. For simplicity, we use the example of a two-state model (Julicher et al., 1997) (Fig. 6.10a). In the strongly bound state (1) the motor feels the sawtooth potential, $W_1(x)$, with a period ℓ, an amplitude $5K_BT$ and a short segment of the sawtooth of length $a = 0.2\ell$. In the weakly bound state (2) the potential $W_2(x)$ is constant. The motors change from state 1 to state 2 and vice-versa with local excitation rates $\omega_1(x)$ and $\omega_2(x)$ respectively. The transition rates, in arbitrary units, are given by

$$\omega_1(x) = \frac{\Omega}{\alpha\sqrt{\pi}} \exp[-(x \mod \ell)^2/\alpha^2] , \qquad \omega_2(x) = 0.2 , \tag{6.15}$$

where $\Omega = 2$ and $\alpha = 0.05\ell \ll a \ll \ell$. We assume only hard core interactions between the motors. The repulsive potential chosen is the shifted repulsive part of a Lennard-Jones potential vanishing at $y > 2^{1/6}\sigma = 1.68\ell$ (y being the distance between the motors), with an amplitude $\varepsilon = 0.05K_BT$. The interaction range is $\sigma = 1.5\ell$. We have carried out simulations with a wide range of σ, from values smaller than the lattice constant to those presented here with no change in the qualitative nature of the results. We have also verified that our results remain qualitatively the same upon changing the details of the model.

We numerically simulate the model using Langevin dynamics for the motors. The equations for motor μ in state s_μ read

$$\xi \frac{dx_\mu}{dt} = -\frac{dW_{s_\mu}(x_\mu)}{dx} - \frac{d}{dx_\mu} \sum_{\kappa \neq \mu} U(x_\mu - x_\kappa) + F\delta_{\mu,1} + \eta, \tag{6.16}$$

where F is the external opposing force, and $\xi = 50$ is the dimensionless friction coefficient of the motor. The random force is described by the noise term $\eta = r\xi\sqrt{\frac{6K_BT}{\xi dt}}$, where r is a random number taken from a uniform distribution from -1 to 1. These equations are coupled to standard Monte Carlo steps for the transitions between the bound states 1 and 2. Initially, the N motors are placed randomly at distances exceeding $2^{1/6}\sigma$, so that the interaction energy $U(y)$ vanishes. Throughout the simulation, we follow the position of the first motor and determine its velocity at long times.

The force-velocity curve obtained from the simulations for 20 motors is plotted in Fig. 6.10b. Since the parameters were chosen so that the stall force of one motor is small, the force-velocity relation is nearly linear for a small number of motors (Fig. 6.10b, inset). Increasing the number of motors reveals the non-linearities. The comparison between the general shape of the curve for 20 motors (Fig. 6.10b) with the ones obtained from the coarse-grained model (Fig. 6.4), suggests that the existence of two internal states for the motors leads to effective repulsive interactions.

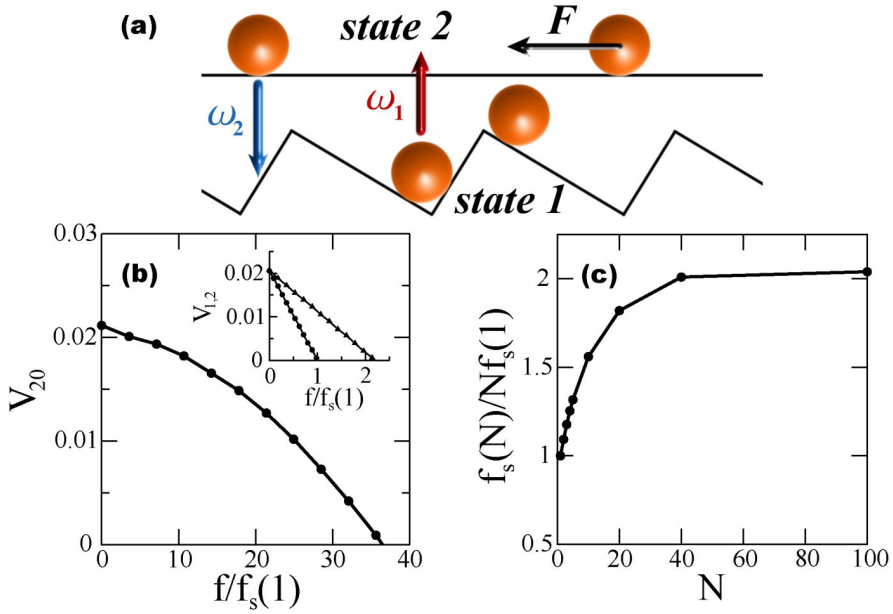

Fig. 6.10. (a) Sketch of the two-state model. (b-c) Simulation results for motors with two internal states (two-state model) and only excluded volume interactions. (b) Velocity-force curve for 20 motors. The inset shows the velocity-force relation for 1 (circles) and 2 (triangles up) motors. (c) Stall force as a function of the number of motors. The value of the stall force is larger than $N f_s(1)$.

The stall force is plotted in Fig. 6.10c as a function of the number of motors. For a given N, it is larger than $N f_s(1)$, indicating that the effective rates for forward and backward movement in the equivalent coarse-grained model are such that $v/u > p/q$. As the number of motors is increased this effect becomes more important and saturates for large N. Overall, these results are consistent with those obtained from the lattice model with effective repulsive interactions between the motors.

6.3 Discussion

The theoretical analysis developed in this chapter provides several predictions that could be tested experimentally. In the description above, we have varied the different parameters in order to understand the possible qualitatively different behaviors in the system. However, it is important to use experimentally measured values for the parameters, in order to provide predictions that could be directly assessed experimentally. In this section, we first discuss the motion of single conventional kinesin motors in the view of recent experimental data and obtain the values of several kinetic parameters of conventional kinesin. We then discuss the predictions of our description for conventional kinesin motors pulling on fluid membranes.

6.3.1 The motion of individual kinesin motors

Recent experimental works (Nishiyama et al., 2002; Carter and Cross, 2005) have studied the motion of single kinesin motors from a point of view similar to ours. We briefly describe some of the experimental results in Ref. (Carter and Cross, 2005) and compare them to the theoretical predictions for a single biased random walker under an external load, F (see section 6.1.1).

In Ref. (Carter and Cross, 2005) the authors tracked the motion of a single kinesin motor under an externally applied load, F. They measured the dwell time distribution and the average dwell time as a function of the load, for both forward and backward motor steps. The dwell time is defined as the time between two consecutive steps. Therefore, the average dwell time for forward (backward) steps, τ_f (τ_b), corresponds to the inverse of the rate for forward (backward) motor stepping in our description, i.e. $p_1 = 1/\tau_f$ ($q_1 = 1/\tau_b$). This correspondence holds for saturating ATP concentrations, in which case the time for an ATP molecule to bind the active site of the motor is not limiting. We restrict our discussion to this case.

If detachment events are not counted in the statistics, as done in Ref. (Carter and Cross, 2005), the ratio, R, of forward and backward steps is given by

$$R = \frac{p_1}{q_1} = \frac{p}{q} \exp\left(-\frac{F\ell}{K_B T}\right) . \tag{6.17}$$

In Ref. (Carter and Cross, 2005) the authors measured the ratio of forward and backward steps as a function of the external force. The data shows a very good agreement with a single exponential fit, with $p/q \simeq 8\,10^2$ and $\ell/K_B T \simeq 0.95$ pN^{-1}. Kinesin motors are thus strongly biased, as indicates the large value of p/q [5]. In the same experiments, the authors measured the step size, ℓ, to be $\ell \simeq 8$ nm for all values of the applied force. The value of ℓ obtained from the measured value of the coefficient in the exponential $\ell/K_B T$ is puzzling. One would expect to obtain the same value for ℓ, i.e. $\ell \simeq 8$ nm reflecting the periodicity of the microtubule. Instead, using the measured value $\ell/K_B T \simeq 0.95$ pN^{-1} one obtains 3.9 nm, almost exactly half the size of the kinesin step. The theory provides an independent check for the value of ℓ, the stall force, which reads

$$F_s = \frac{K_B T}{\ell} \ln\left(\frac{p}{q}\right) . \tag{6.18}$$

Using the experimentally measured value for the motor bias, $p/q \simeq 8\,10^2$, and a value of 3.9 nm for ℓ, one obtains $F_s \simeq 7$ pN. This value is in agreement with the value of the stall force for kinesins measured by several groups (Visscher et al., 1999; Schnitzer et al., 2000; Block et al., 2003). Everything seems consistent but the value of ℓ. However, the description of the motor as a bias random walker does not take into account the existence of the two motor domains of kinesins. Before performing the step, both heads must be attached to the microtubule because the motor would detach otherwise. Assuming that the two heads share equally the applied load, the

[5] From the data in Ref. (Nishiyama et al., 2002) one obtains $p/q \simeq 220$. Although they differ nearly by a factor of four, they both indicate that kinesin motors are highly biased.

kinetic events for forward and backward stepping would only be affected by half the load applied on the motor. In this case, the force per head, F_h, affecting the motor forward and backward kinetics is $F_h = F/2$. As a consequence, the ratio, R, is given by

$$R = \frac{p_1}{q_1} = \frac{p}{q} \exp\left(-\frac{F\ell}{2K_BT}\right) . \tag{6.19}$$

Comparing this expression to the experimental data, the value of the motor bias remains unchanged as only concerns the motion of the motor under vanishing load, but the coefficient in the exponential is $\ell/2K_BT \simeq 0.95\ \mathrm{pN}^{-1}$, leading to $\ell \simeq 7.8$ nm. Moreover, the stall force is $F_s = (2K_BT/\ell)\ln(p/q) \simeq 7$ pN. Therefore, assuming the two motor heads to share equally the load removes the internal inconsistency.

Once we know the bias of the motor and the fact that the forward/backward kinetics is affected only by half of the applied load, we are interested in the experimental value of δ and $V_0 = \ell(p-q) \simeq \ell p$. The value of the forward stepping rate at zero load is the inverse of the dwell time for forward stepping at vanishing load. From the data in Ref. (Carter and Cross, 2005) we obtain $\tau_f \simeq 0.015$ s ($p \simeq 66.7\ \mathrm{s}^{-1}$). Then, the velocity at vanishing load is $V_0 \simeq \ell p \simeq 534\ \mathrm{nm\,s}^{-1}$, which is consistent with the known values for the velocity of conventional kinesin at vanishing load and saturating ATP concentrations (Visscher et al., 1999; Block et al., 2003). In order to obtain the value of δ is necessary to know the force dependence of the dwell time for either forward or backward motor stepping. Theoretically, the dwell time for forward stepping reads

$$\tau_f(F) = \frac{1}{p_1} = \frac{1}{p} \exp\left(\frac{F\,\delta\ell}{2K_BT}\right) . \tag{6.20}$$

Experimentally, the results in Ref. (Carter and Cross, 2005) show an exponential dependence on the force with a value of the coefficient in the exponential, $\delta\ell/2K_BT$, of $0.57\ \mathrm{pN}^{-1}$, which leads to $\delta \simeq 0.6$.

The analysis performed here with the experimental data in Ref. (Carter and Cross, 2005) can also be done for the data in Ref. (Nishiyama et al., 2002) and similar results are obtained. In particular, it is also necessary, for the same reasons, to take into account the existence of two motor heads and assume that these share the external load.

In the previous discussion, detachment events were not considered. The kinetic parameters that characterize motor force-dependent detachment, d_0 and δ_d, are also known experimentally for conventional kinesin (Schnitzer et al., 2000; Vale et al., 1996). Theoretically, the detachment rate reads

$$d(F) = d_0 \exp\left(\frac{F\,\delta_d\ell}{K_BT}\right) . \tag{6.21}$$

Note that ℓ only appears in the latter expression because it sets the length units, not for a physical reason, as was the case for forward and backward rates. The force that appears in the exponential is the external load applied on the motor. As far as detachment is concerned, it is not necessary to discuss whether the force is the external

load or the load per motor head, because it only redefines δ_d but leaves the results unchanged. However, it is more probable that the motor detaches when performing a step as there is only one head attached to the microtubule which has to sustain all the load. In this case, the force F would correspond to the external load. The exponential dependence of the detachment rate on the load agrees with the experimental data, with values $d_0 \simeq 0.42\ \mathrm{s}^{-1}$ (Vale et al., 1996) and $\delta_d \simeq 0.16$ (Schnitzer et al., 2000).

6.3.2 Collective behavior of interacting kinesins

In this section we discuss the results presented in this chapter for the collective behavior of interacting motors using the kinetic parameters of conventional kinesin motors. In Fig. 6.11 we compare the force-velocity curves of two motors and a single motor and show that the collapse of the force-velocity curves in the neutral case takes place already for two motors ($N = 2$). Due to the strong bias of conventional kinesin motors, the force-velocity curves of one and two motors are very similar down to almost negligible values of the velocity, if only neutral interactions exist between the motors. For strongly attractive interactions the velocity of two motors is smaller than that of one motor and becomes larger at an interaction dependent point. However, the velocity of two motors is negligible even at forces below the stall force of a single motor. For repulsive interactions the velocity of two motors is always larger than that of a single motor. These results suggest that in the case of strongly biased motors like conventional kinesin, for any type of interactions there exist two force-velocity curves for practical purposes: the force-velocity curve for a single motor and a common force-velocity curve for many motors. For neutral interactions, the similarity between these two force-velocity curves, suggests that only one common force-velocity curve would be observable for any number of motors.

These results show that the velocity of many kinesins becomes negligible at very small forces. The physical picture presented here strongly suggests that our qualitative results will remain largely unchanged if the motors use several protofilaments. It is indeed necessary that motors use several protofilaments to develop large forces when carrying a cargo. Although using different arguments, in chapter 5 we showed that the use of three protofilaments was needed in order to pull a membrane tube from a tensed vesicle.

Motor attachment/detachments events are, in general, very important to understand the collective dynamics of the system. We have shown in chapter 5 that force-dependent detachment is at the origin of the threshold in tube extraction and the oscillatory behavior. The aim of this chapter is not to describe these dynamic instabilities but rather the consequences of the motor collective behavior in the force-velocity curves, far from these instabilities. We have shown using numerical simulations that detachment events do not influence much the force-velocity curves, if several motors are clustered behind the leading one (section 6.2.2). The reason stems in the different time scales for forward motor stepping and detachment. Below the stall force of a single motor, there is a separation of time scales; the time scale for forward mo-

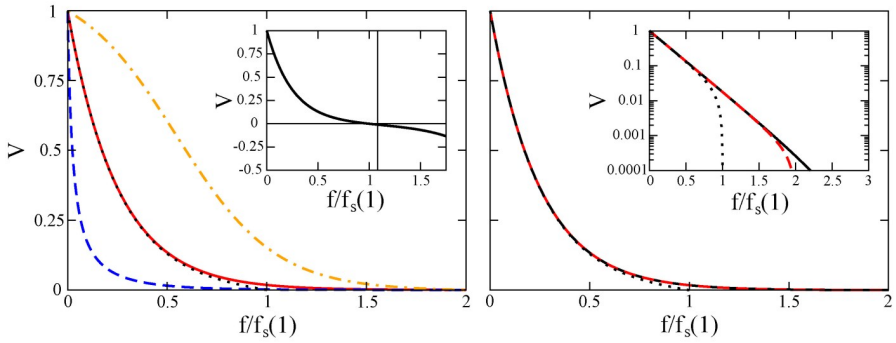

Fig. 6.11. Force-velocity curves for the parameters of single kinesin motors (see section 6.3.1). All rates are in units of p ($p = 1.0$), $p/q = 800$ and $\delta = 0.6$. (a) Force-velocity curves of 2 motors (Eq. 6.8) in the limits of attractive, repulsive and neutral interactions. The velocity-force curve for a single kinesin motor is also plotted (dotted line). The rates v and u are: $v = 0.1, 1.0, 10.0$ and $u = 0.01, 0.1, 1.0$ for attractive (dashed line), neutral (continuous line) and repulsive (dashed-dotted line) interactions respectively. The ratio $v/u = p/q$ so that $f_s(2) = 2f_s(1)$. The inset shows the force-velocity curve for a single kinesin motor for a larger range of forces. (b) Force-velocity curves for several motors and neutral interactions (Eq. 6.11). Single motor (dotted line), 2 motors (dashed line) and 100 motors (continuous line). The force-velocity curves in the case of neutral interactions and any number of motors are almost indistinguishable, for the parameters of kinesin motors. The inset shows the force-velocity curves in logarithmic scale. Appreciable differences between the force-velocity curves for 1 and 2 motors are found at velocities $\sim 10^{-2}V_0$. The differences between 2 motors and 100 motors are only appreciable at velocities $\sim 10^{-4}V_0$.

tor stepping [6] lies within $0.5s$ (at stall force) and $0.01s$ (at vanishing force) whereas the time scale for motor detachment is between $0.3s$ (at stall force) to $2s$ (at vanishing force). It is only for forces larger than the stall force of one motor that the time of motor detachment becomes similar to that for forward motor movement. As a result, the effects of detachment are negligible below $f_s(1)$. The situation above $f_s(1)$ is different. The force influences more the forward motor stepping rate than the detachment rate, as can be seen in the values for δ and δ_d. Therefore, the velocity reaches negligible values before detachment events can considerably influence the force-velocity curve. Note that this is not the case for strongly repulsive interactions, and detachment events considerably change the force-velocity curve.

6.4 Conclusions

We have shown in using various models of molecular motors that the collective behavior of motors pulling on fluid membranes depends on their dynamic interactions

[6] We use for the discussion the values of conventional kinesin (Schnitzer et al., 2000; Vale et al., 1996; Carter and Cross, 2005).

and is very different from both the mean field prediction and from the behavior of rigidly or elastically coupled motors. The present study provides several results that can be quantitatively compared to experiments where a bead is exerting a force on a single motor moving in front of several other motors. The comparison between such experiments and our results would allow the determination of the effective interactions between motors. Moreover, this treatment is a reasonable approximation for kinesin motors carrying a vesicle subject to the friction forces that arise from its motion in the crowded environment of the cell. Any estimation of the number of motors pulling a vesicle from the force-velocity curve is questionable because of the collapse of the force-velocity curves (Snider et al., 2004).

Acknowledgments

The theoretical work in this chapter has been done in close collaboration with Y. Kafri. In particular, the analytical calculations for the neutral case considering N motors have been entirely performed by him. The simulations of the ratchet model presented in section 6.2.3 have been done by K. Zeldovich. I warmly thank them for the interesting and fruitful discussions we had. I specially thank Y. Kafri for introducing me the world of zero-range processes.

Part III

Eukaryotic cell division

7

Introduction

All cells reproduce by dividing into two daughter cells. The process of cell division consists in the duplication of the material in a cell (both the genome and the cytoplasm) and the subsequent physical division into two genetically identical cells. Bacteria constitute the simplest example of cell division as they do not have nucleus and only contain a single chromosome. Eukaryotic cells are more complex; they contain several chromosomes that have to be duplicated, moved and separated in a coordinated way. The necessary machinery to perform these tasks is far more sophisticated than in bacteria, and it involves both biochemical signals that regulate the process and different motor proteins responsible for the force generation at molecular scales [1].

Multicellular organisms (composed of many eukaryotic cells), like us, require a constant generation of new cells to simply survive. The duplication of an eukaryotic cell is achieved by the nuclear division (mitosis), followed by the cytoplasmic division (cytokinesis). Mitosis is composed of several phases (mitotic phases) which correspond to different stages of the division process, separated by important events (Fig. 7.1 and 7.2). It is possible to identify the stage of the division process from the microtubule organization and chromosome positioning and structure (Fig. 7.1). The first sign that a cell initiates the nuclear division is the condensation of DNA into the chromosomes. We shortly describe the sequence of events that constitute each one of the mitotic phases:

- *Prophase*. At this initial stage of the division process, the two attached copies of each already replicated chromosome (called sister chromatids), start a compaction process named DNA condensation (Fig. 7.1A). At the same time, outside the nucleus, the microtubules organize radially from each one of the two centrosomes, generating two microtubule asters that interact with each other and start the assembly of the mitotic spindle (Figs. 7.1B and 7.2a).

[1] For a general introduction to cell division, see Refs. (Alberts et al., 2004; Bray, 1992). A more detailed description can be found in Refs. (Mitchison and Salmon, 2001; Wittmann et al., 2001; Karsenti and Vernos, 2001; Sharp et al., 2000b; Scholey et al., 2003; Gadde and Heald, 2004).

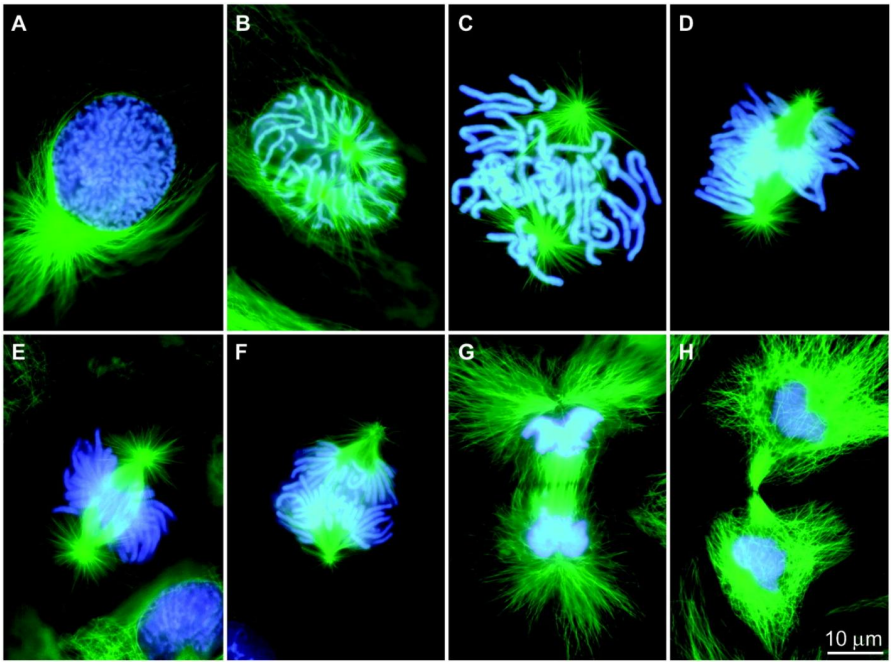

Fig. 7.1. Fluorescence micrographs of a Newt Lung cell undergoing mitosis. Microtubules are shown in green and chromosomes in blue. (A) Early prophase: the chromosomes start the condensation process and there is still a single microtubule aster. (B) Prophase: The two microtubule asters separate apart and the chromosomes have already condensed. (C) Prometaphase: The nuclear envelope has been degraded and the chromosomes interact with the microtubules in the spindle. (D) Chromosome congression (late prometaphase): the chromosomes move toward the midplane between the two spindle poles. (E) Metaphase: All chromosomes are properly positioned and the metaphase plate and the mitotic spindle displays the characteristic fusiform shape. (F) Anaphase A (chromosome segregation): the sister chromatids separate and move toward opposite spindle poles. (G) Telophase: A nuclear membrane starts to assemble around each of the two sets of chromosomes located at the poles and the chromosomes begin the decondensation process. (H) Cytokinesis: A contractile actin ring (not visible) contracts at the cell midplane and divides the cytoplasm. (Adapted from Ref. (Rieder and Khodjakov, 2003)).

- *Prometaphase*. The nuclear envelope breakdown establishes the initiation of this stage. As the nuclear membrane progressively degrades, the microtubules emanating from the centrosomes are able to interact with the chromosomes (Figs. 7.1C and 7.2b). This interaction provides the necessary forces to drive chromosome motion. Chromosomes progressively move towards the midplane between the two poles in a process called chromosome congression (Fig. 7.1D).
- *Metaphase*. This stage is composed of several important events. The microtubules extending from both poles interact through the action of many proteins and form the characteristic fusiform spindle (Fig. 7.1E). This bipolar self-

organized structure mediates the propagation of forces necessary for chromosome motion. At this stage, chromosomes are placed at the mitotic plate and, although the process is highly dynamic, it reaches a steady state (Figs. 7.1E and 7.2c). After a short delay to make sure that all chromosomes are properly located at the mitotic plate (spindle checkpoint), the sister chromatids lose their physical connection, setting the initiation of anaphase.

- *Anaphase*. The sister chromatids separate apart and move to opposite spindle poles (Anaphase A; Figs. 7.1F and 7.2d). The mitotic spindle elongates, increasing the separation between the spindle poles (Anaphase B; Fig. 7.2e).
- *Telophase*. The two identical sets of sister chromatids arrive at the spindle poles, where they remain and start the decondensation process. A nuclear envelope assembles around each one of the sets of chromosomes located at the poles, completing the process of nuclear division (Figs. 7.1G and 7.2f).

At this point, in spite of having two nucleus, the cell is not yet divided. It is necessary to physically split the cytoplasm. This process is called *cytokinesis* and is achieved by the assembly of an actin ring in the midplane of the cell that progressively contracts until the cell pinches off into two new daughter cells, each one with a nucleus (Figs. 7.1H and 7.2e,f).

Eukaryotic cells a have very complex machinery to perform the tasks described above. Spindle assembly and the interaction of the chromosomes with the spindle involve many different proteins (Alberts et al., 2004; Wittmann et al., 2001). In particular, microtubules and motor proteins play a crucial role in the generation of the forces needed to drive mitotic movements. Before addressing the process of spindle assembly, we briefly describe the mechanism by which chromosomes interact with the mitotic spindle in a typical vertebrate cell. Although plant cells divide by a similar sequence of events, the mechanism by which this is done is different than for mammalian cells (Alberts et al., 2004).

7.1 Chromosome-spindle interaction

The interaction of chromosomes with spindle microtubules takes place both at the kinetochore and at the chromosome arms (Fig. 7.3). Many different proteins mediate this interaction and, in particular, several motor proteins in the kinetochore region have been shown to play an important role in the motion of the chromosome (Rieder and Salmon, 1998; Gadde and Heald, 2004) (Fig. 7.3b). The kinetochore is a complex protein assembly, located at the centromere region of the chromosome, to which spindle microtubules attach (kinetochore microtubules), forming a microtubule bundle (kinetochore fiber) that tightly connects the chromosome to a spindle pole. Each sister chromatid contains a kinetochore, and the two sister kinetochores in a chromosome face opposite directions, enhancing the probability that a chromosome attaches to both spindle poles.

Unfortunately, the molecular organization of the kinetochore is not fully understood, and the molecular force generators in the kinetochore have not yet been precisely characterized. However, regardless of the internal kinetochore organization, it

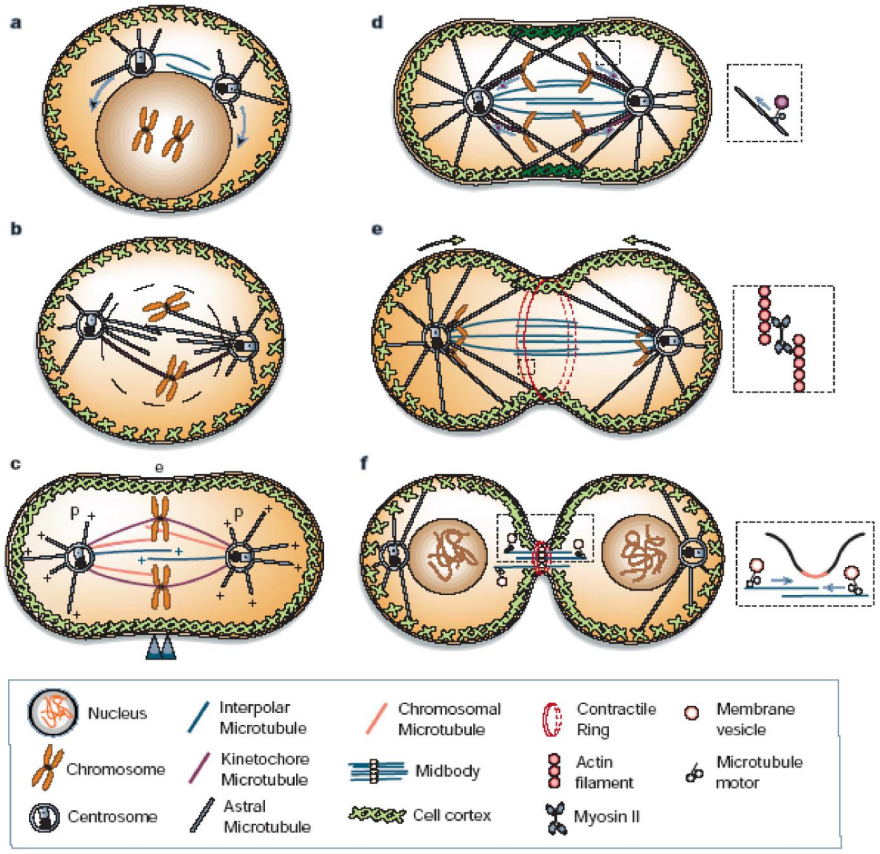

Fig. 7.2. Sketch of the mitotic phases and cytokinesis. (a) Prophase, (b) prometaphase, (c) metaphase, (d) anaphase A, (e) anaphase B and initiation of cytokinesis, (f) telophase and cytokinesis. The events that take place at every stage are described in the main text. (Adapted from Ref. (Scholey et al., 2003)).

has been shown that it applies a force on the chromosome directed toward the spindle pole to which it is connected (Nicklas, 1983). The molecular origin of this force remains under debate, but both minus-end directed motors (cytoplasmic dynein (Sharp et al., 2000a)) and microtubule depolymerization (Koshland et al., 1988) are thought to be provide the dominant contributions. Micromanipulation experiments in meiotic spindles have shown that the forces developed by the kinetochore are in the nanoNewton range and that the poleward chromosome velocity decreases almost linearly with the applied force (Nicklas, 1983). However, experimental observations in mitotic spindles suggest that the kinetochore may switch between phases of poleward force generation and phases where it generates no force (neutral states) (Khodjakov et al., 1999).

The interaction of a chromosome with the astral microtubules in the spindle is mediated by chromokinesin motors attached to the chromosome arms (Fig. 7.5b). These plus-ended directed motors have been shown to be responsible for the polar ejection force, which drives the chromosome away from the poles (Levesque and Compton, 2001; Kapoor and Compton, 2002; Brouhard and Hunt, 2005). The chromosome motion arises from the tug-of-war between the two opposing forces acting on the chromosome, namely the kinetochore force and the polar ejection force. A detailed analysis of chromosome movement is done is chapter 8 (see also Ref. (Campas and Sens, 2006)), where we extend the discussion on the forces acting on the chromosome.

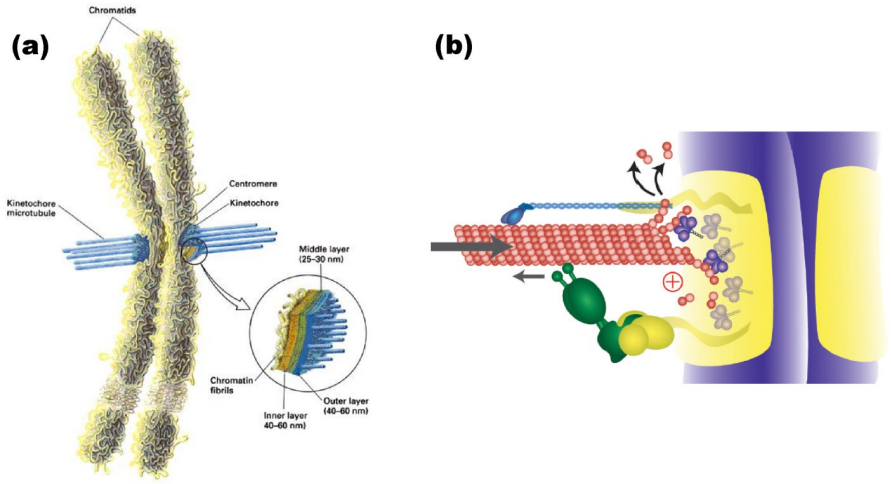

Fig. 7.3. (a) Interaction of a chromosome with the microtubules in the mitotic spindle; only the microtubules associated with the kinetochores are shown. (Figure taken from the website http://www.utexas.edu/courses/utgeneticstamu/kinetchr.htm). (b) Sketch of the kinetochore and some of its components. Dynein motors (green) move toward the minus ends of microtubules, generating a poleward force on the chromosome. Motors with depolymerizing activity (Kin1; purple) induce microtubule depolymerization at their plus ends. A plus-ended directed motor, CENP-E is also shown (light blue). (Modified from Ref. (Gadde and Heald, 2004)).

7.2 Mitotic spindle assembly

The mitotic spindle (Fig. 7.4a) is composed of two microtubule asters that interact with each other mainly through motor proteins. The microtubules in the spindle are typically classified in three groups, depending on their dynamic properties and the interactions they have with other components of the spindle. Kinetochore microtubules are those that associate with the chromosome kinetochores and are involved in the

process of chromosome movement and positioning (label 1 in Fig. 7.4b). This type of microtubules forms a bundle (kinetochore fiber) that associates to kinetochores and firmly connects the chromosome to a spindle pole. Interpolar microtubules are those microtubules in the asters that interact with the microtubules from the opposite aster (label 2 in Fig. 7.4b). These are mainly involved in the process determining the spindle morphology and mediate the interactions between the spindle poles. The rest of microtubules are defined as astral microtubules (label 3 in Fig. 7.4b) and are involved in many processes, like chromosome movement, the separation of spindle poles and the three dimensional orientation of the mitotic spindle in the cell.

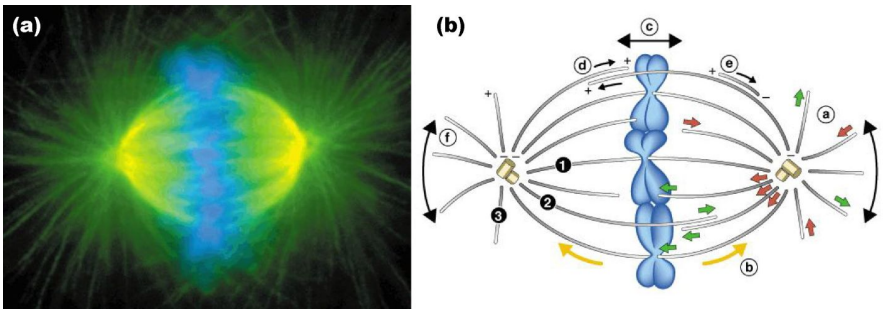

Fig. 7.4. Spindle structure and dynamics. (a) Fluorescence photograph of the mitotic spindle at metaphase. Microtubules are shown in green, chromosomes in blue and TPX2 (a spindle pole component) in red. When microtubules and TPX2 are present, the overlapping appears yellow. (b) Sketch of the mitotic spindle at metaphase. Different subpopulations of microtubules: kinetochore microtubules (1), interpolar microtubules (2) and astral microtubules (3). Several dynamic processes take place in the spindle: microtubule dynamic instability (a; green arrows show growing and shrinking microtubules), poleward microtubule flux (b; yellow arrows), chromosome motion (c), motor-driven antiparallel interpolar microtubule sliding (d), dynein dependent minus-ended microtubule transport (e) and orientation movements of the spindle poles (f). (Modified from Ref. (Wittmann et al., 2001)).

The precise mechanism responsible for the spindle organization and remodeling during mitosis remains unclear, but there is a general consensus that the mitotic spindle arises from the self-organization of microtubules and motor proteins (Mitchison and Salmon, 2001; Wittmann et al., 2001; Karsenti and Vernos, 2001; Nedelec et al., 2003; Hyman and Karsenti, 1996). In order to reorganize the microtubules, there exist motor proteins able to crosslink pairs of microtubules and slide them with respect to one another (Wittmann et al., 2001; Sharp et al., 2000b; Scholey et al., 2003). In mixtures of microtubules and bipolar motors, this motor-induced motion of microtubules leads to the overall self-organization of the system (Fig. 7.5a). Several spatiotemporal patterns appear spontaneously at large scales as a result of this process, as has been shown experimentally (Nedelec et al., 1997; Surrey et al., 2001). Moreover, numerical simulations indicate that bipolar structures, similar to the mitotic spindle, can arise from the interactions of bipolar motors and microtubules (Nedelec,

2002). However, the spindle organization *in vivo* is mediated by many different motor proteins and their specific roles in the assembly process are not fully understood. Fig. 7.5b shows a sketch of the mitotic spindle together with some of the motors involved in the assembly process and their specific functions. Plus-ended directed bipolar motors of the BimC family slide antiparallel interpolar microtubules (label *b* in Fig. 7.5b), generating a force that separates apart the spindle poles. Minus-ended directed kinesins (Kin C) are thought to generate an inward force in the spindle (label *c* in Fig. 7.5b). Cytoplasmic dyneins (associated with dynactin and NuMA) crosslink microtubules and move toward the minus ends of microtubules, focusing the spindle poles (label *d* in Fig. 7.5b). Cortical dyneins are responsible for spindle orientation and spindle pole separation during Anaphase B (label *a* in Fig. 7.5b). Finally, chromokinesin motors, attached to the chromosome arms, are mainly involved in chromosome movement (label *e* in Fig. 7.5b).

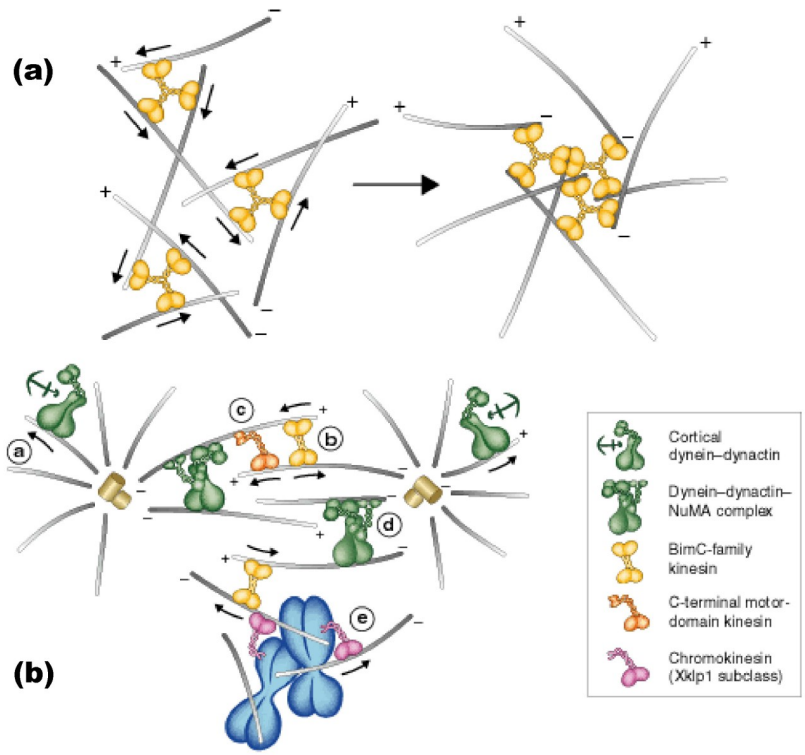

Fig. 7.5. (a) Sketch of the self-organization process in motors and microtubule mixtures. Motor complexes able to crosslink microtubules and move along them can organize randomly distributed microtubules into aster-like structures. (b) Sketch of the mitotic spindle and some of the motor proteins involved in the organization process. The specific function of the different motor proteins is described in the main text. (Adapted from Ref. (Wittmann et al., 2001)).

Besides the organization of microtubules by motor proteins, the chromosomes themselves are also thought to be important for the spindle assembly. It has been reported that a substantial fraction of the microtubules in meiotic and plant mitotic spindles are nucleated at the chromosomes and subsequently organized by molecular motors (Karsenti and Vernos, 2001; Hyman and Karsenti, 1996). According to these observations, the spindle would result from the self-organization of motors, microtubules and chromosomes.

Spindle dynamics and regulation

The different events just described must be tightly coordinated to avoid any mistake. There exist several biochemical signals that exquisitely regulate the division process and assure its proper progression (Alberts et al., 2004). In spite of the importance of these biochemical networks, it is clear that forces must be developed in order to induce the observed movements. The aim of the study in chapter 8 (see also Ref. (Campas and Sens, 2006)) is to understand how the force generation at molecular level translates in the large scale chromosome motion, and in chapter 9 (see also Ref. (Campas et al., 2006a)) we analyze the stability of the mitotic spindle at metaphase.

Most of the works devoted to the understanding of the cell division process focus either on the physical properties or the biochemical signaling. However, it is very likely that both processes influence each other, meaning that not only the biochemical reactions influence the elementary force generators, but also that the forces involved induce or modify biochemical events. Indeed, there are some experimental observations that suggest an important role of such force-feedback to control biochemical signaling (Nicklas, 1997; Pinsky and Biggins, 2005). The spindle checkpoint, which ensures that sister chromatids separate apart only when all chromosomes are properly positioned at the metaphase plate, is thought to be controlled by the tension between sister kinetochores (Nicklas et al., 1998; Logarinho et al., 2004). Within this framework, the overall spindle dynamics would result from the self-organization of biochemical networks and spatio-temporal force generation.

8

Chromosome movement and positioning in mitosis

During mitosis chromosomes show a very complex sequence of coordinated movements (Alberts et al., 2004; Bray, 1992). Just after the nuclear envelope breakdown, the microtubules extending from both spindle poles interact with the chromosomes. Generally, a microtubule from one of the spindle poles contacts laterally one of the two sister kinetochores and the chromosome quickly slides along it toward this pole (Hayden et al., 1990; Rieder and Alexander, 1990). This initial rapid sliding is thought to be due to dynein motors located at the outer region of the kinetochore. As the chromosome moves poleward, a bundle of microtubules (kinetochore fiber) associates to the kinetochore facing the pole (Rieder, 1990), providing a firm connection between this spindle pole and the chromosome, which is then said to be mono-oriented as it is only connected to one spindle pole (Figs. 8.1 and 8.3a). In animal cells, a mono-oriented chromosome moves towards and away from the pole in a periodic fashion (Bajer, 1982; Rieder et al., 1986; Skibbens et al., 1993; Levesque and Compton, 2001) (Fig. 8.2). This oscillatory movement, which persists during chromosome congression, metaphase and early anaphase (Skibbens et al., 1993; Rieder and Salmon, 1998), is driven by the forces acting on the chromosome. Its quantitative description can thus provide important insights on the generation of large scale motion from molecular forces in cell division.

There exist two main opposed forces acting on the chromosome during mitosis. The protein complex kinetochore associated to the chromosome is known to apply a force on the chromosome directed toward the pole of the microtubule aster (poleward force). Although the exact molecular origin of this force remains unclear, the main contributions to this force are thought to be due to cytoplasmic dyneins (Sharp et al., 2000a) and microtubule depolymerization in the kinetochore (Koshland et al., 1988). On the other hand, several experimental observations have shown the existence of forces that eject the chromosomes away from the pole (away-from-the-pole force, or polar ejection force). The molecular origin of this force has been recently elucidated. Chromokinesin motors are plus-ended kinesin motors (Yajima et al., 2003) which associate with the chromosome arms (Tokai et al., 1996) and generate the polar ejection force (Levesque and Compton, 2001; Yajima et al., 2003; Kapoor and Compton, 2002; Brouhard and Hunt, 2005). While individual chromokinesin motors generate

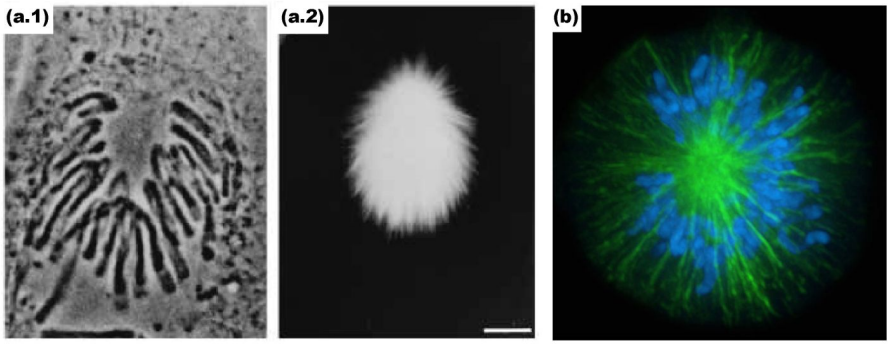

Fig. 8.1. Monopolar spindles with mono-oriented chromosomes, which locate at a certain distance from the pole. (a.1) Phase contrast and (a.2) immunofluorescence (tubulin labeled fluorescently) micrographs of a Newt lung cell prometaphase monopolar spindle. Chromosomes positioned toward the sides of the spindle are located closer to the pole (a.1), due to the lower microtubule density in these regions (a.2). (Modified from Ref. (Cassimeris et al., 1994)). (b) Fluorescence image of a single microtubule aster (monaster). Microtubules are shown in green and the DNA in blue. (Figure taken from the website of the Compton Lab: http://dms.dartmouth.edu/compton).

forces in the picoNewton range (Yajima et al., 2003; Brouhard and Hunt, 2005), typical values for the forces driving mitotic movements are of several nanoNewtons (Nicklas, 1983). Chromokinesin motors must thus work in large groups so as to influence chromosome motion. These motors play a crucial role in both chromosome motion and positioning, as a drastic reduction of their number suppresses the oscillations and induces the chromosome to move closer to the pole (Levesque and Compton, 2001).

Chromosome movement arises from the tug-of-war between the polar ejection force and the poleward kinetochore force. The polar ejection force has an intrinsic dynamic origin as is created collectively by the chromokinesins and depends thus strongly on their intrinsic kinetics. Generically, the collective behavior of motor proteins can give rise to dynamical instabilities (Julicher and Prost, 1997). However, the existence of a dynamical instability does not necessarily imply periodic oscillations in space if it is not coupled to a spatial degree of freedom. We argue that such coupling is provided by the interaction of chromokinesins with the astral microtubules in the spindle which, due to their aster-like distribution, constitute a position dependent substrate for motor binding. Thus, chromokinesin binding events onto spindle microtubules allow the chromosome to sense its position in the spindle. We show that the coupling between the dynamical instability of a collection of motors and the morphology of the mitotic spindle leads to well defined spatial oscillations.

All the available models for the oscillatory movement of the chromosome (often referred to as “kinetochore directional instability” (Skibbens et al., 1993)) have as a common feature that the kinetochore somehow controls the switching between poleward and away from the pole phases (Murray and Mitchison, 1994; Rieder and

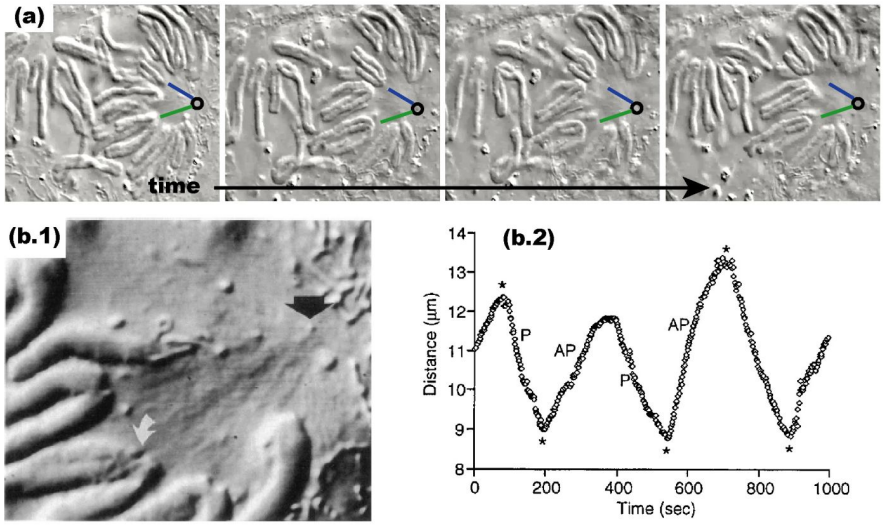

Fig. 8.2. Oscillations of mono-oriented chromosomes. (a) Snapshots showing the motion of mono-oriented chromosomes during prometaphase in a Newt lung cell. The circle indicates the position of the pole and the bars show the initial chromosome-to-pole distance for two chromosomes. For increasing times, chromosomes move away and towards the pole. (Adapted from a film in Ref. (Rieder and Khodjakov, 2003)). (b.1) DIC image of mono-oriented chromosomes in a Newt lung cell. The black and gray arrows indicate the position of the pole and the kinetochore respectively. (b.2) Motion of the chromosome in (b.1), showing the characteristic sawtooth-shaped oscillations. The chromosome move toward and away from the pole with phases of nearly constant velocity separated by abrupt changes in direction (*) (Modified from Ref. (Inoue and Salmon, 1995)).

Salmon, 1994; Khodjakov et al., 1999; Joglekar and Hunt, 2002). Unfortunately, little is known about the kinetochore and there is no explanation for the mechanism at the origin of this hypothetic switching. Although the chromosome oscillatory behavior has been reproduced by some models (Khodjakov et al., 1999; Joglekar and Hunt, 2002), these works do not provide any explanation for the oscillations as the spatial dependence of the polar ejection force is postulated. We introduce in this chapter a unifying framework in which chromosome movement, positioning and congression can be explained on the same physical basis.

In addition to the oscillatory chromosome motion, there are several biological situations where similar oscillations are observed, like the periodic motion of the spindle poles in mitosis (Grill et al., 2005), the contraction of muscle fibers by ensembles of myosin motors (Bray, 1992; Huxley and Simmons, 1971; Murase, 1992; Vilfan and Duke, 2003) and the ciliary and flagellar beating (Bray, 1992; Murase, 1992; Camalet and Julicher, 2000). It is thus important to understand the origin of the oscillatory instability associated to the motion of individual chromosomes.

8.1 Theoretical description

In order to precisely assess the role of chromokinesins in chromosome motion and positioning, we study the balance of forces on a mono-oriented chromosome (Fig.8.3a). While the present analysis aims at understanding the motion of mono-oriented chromosomes in prometaphase, it can be readily extended to the case of bi-oriented chromosomes, which we address in section 8.2.3.

Force Balance

Without loss of generality, all forces are written as being applied to the chromosome. The motion of the chromosome is written in the reference frame of the pole, with r being the chromosome-to-pole distance (Fig. 8.3b). Chromosome motion occurs at lengths ($\sim \mu$m) and velocity scales ($\sim 0.01 - 0.1\ \mu\mathrm{m\,s}^{-1}$) for which inertial effects are negligible (low Reynolds number). As discussed above, the chromosome is subject to two main forces, namely the poleward kinetochore force, F_K, and the polar ejection force, F_{AP} (away-from-the-pole force). Any mismatch between these two forces induces the motion of the chromosome, which is opposed by a friction force (Fig. 8.3b). The balance of forces on the chromosome reads

$$F_{AP} - F_K - \xi \dot{r} = 0\,, \tag{8.1}$$

where $\dot{r} \equiv dr/dt$ is the chromosome velocity (t being the time). We assume a viscous-like friction force, with a friction coefficient, ξ, which may, in principle, depend on the chromosome position and velocity. In the present context there are several contributions to friction, which occurs both within the kinetochore and on the chromosome arms. The hydrodynamic drag associated to the chromosome motion through the intracellular environment is of order $\sim 6\pi\eta L|\dot{r}| \sim 10^{-1}$ pN ($L \sim 5\mu$m and $\eta \sim 10^{-2}$ Pa s being the typical chromosome size and solution viscosity respectively), and is about one order of magnitude smaller than the typical forces of single motor proteins ($\sim$pN; see chapter 1). Therefore, chromosome motion is most probably hindered by other phenomena. Both chromokinesin attachment/detachment events from the microtubules and the increasing microtubule density near the pole may generate a friction force on the chromosome arms. In the kinetochore, the friction is likely to arise from microtubule polymerization/depolymerization and the activity of molecular motors (Inoue and Salmon, 1995). A precise modeling of the kinetochore force and friction would require the detailed knowledge of its molecular organization, which is not currently available. As a first step to elucidate the consequences of chromokinesin collective behavior on chromosome motion, both the kinetochore force and the global friction parameter are taken as constant in what follows. The implications and limits of this approximation are analyzed in section 8.2.

Although chromokinesins have been shown to generate an away-from-the-pole force on the chromosome, one could expect other contributions to this force. This possibility has been ruled out by several experimental observations. It is now clear

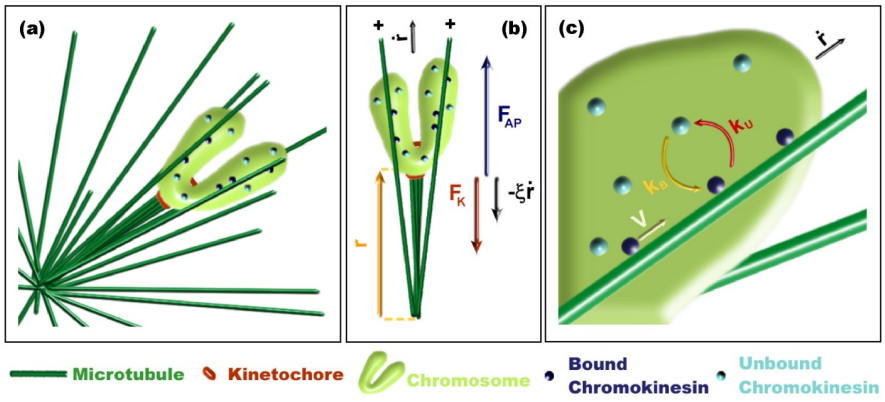

Fig. 8.3. Schematic representation of a mono-oriented chromosome. (a) Sketch of a microtubule aster (dark green) interacting with a single chromosome (light green). The kinetochore (red) is connected to the pole through a bundle of microtubules. Chromokinesin motors, permanently attached to the chromosome arms, may be bound to a microtubule (dark blue dots) or unbound (light blue dots). (b) Forces driving chromosome motion: the kinetochore poleward force, F_K (red), the polar ejection force created by the chromokinesins bound to the microtubule aster, F_{AP} (dark blue), and the friction force opposing motion, $-\xi\dot{r}$ (black). The chromosome position relative to the pole (orange arrow) is r and its velocity is $\dot{r}$. (c) Binding/unbinding kinetics of chromokinesin motors, with rates k_b and k_u respectively. In the bound state, chromokinesins move toward the plus end of microtubules with a velocity V.

that microtubule polymerization in the kinetochore does not contribute to the away-from-the-pole force as the centromere is stretched during both poleward and away-from-the-pole phases (Waters et al., 1996; Khodjakov and Rieder, 1996). On the other hand, the polymerization of astral microtubules against the chromosome could, in principle, generate a substantial away-from-the-pole force (see chapter 1). However, this is not likely to be the case as it has been shown that the inhibition of chromokinesins induces the collapse of the chromosome onto the pole (Levesque and Compton, 2001). These observations strongly suggest that the forces due to microtubule polymerization on the chromosome are much weaker than those generated by chromokinesins. Moreover, no other redundant mechanisms able to push the chromosomes away from the pole are known to exist besides chromokinesins (Levesque and Compton, 2001). Based on all these experimental observations, we consider the away-from-the-pole force to be solely created by the binding and displacement of chromokinesin motors on the microtubule aster (Fig.8.3a-c).

Note that this description focuses on the motion of the chromosome as a whole and does not provide information on its internal stress. In particular, it cannot account for the amount of centromere stretch, i.e. the distance between sister kinetochores, during chromosome motion. In order to reproduce the experimental observations in this respect (Waters et al., 1996; Khodjakov and Rieder, 1996), both internal degrees of freedom of the chromosome and the precise distribution of forces within the chromosome should be considered. However, the internal response (stretch) of

the chromosome to the forces does not influence the motion of the chromosome as a whole, and it is not included here.

Chromokinesin kinetics

The away-from-the-pole force is generated by ensembles of chromokinesin motors located at the chromosome arms. It is important to realize that the polar ejection force is of inherent dynamic origin as it arises from the kinetics of the force generators, the chromokinesins. In order to understand the properties of the away-from-the-pole force, we describe the coupling between the forces and the motor kinetics.

We consider N chromokinesins permanently attached to the chromosome arms. They stochastically attach to and detach from microtubules with average binding and unbinding rates k_b and k_u respectively (Fig. 8.3c). At one given time, only an amount n of all available chromokinesins is bound to the microtubules in the aster and able to contribute to the away-from-the-pole force. Generically, the time evolution of the number of bound chromokinesins may be written as

$$\frac{dn}{dt} = k_b(N-n) - k_u n \,. \tag{8.2}$$

A binding event involves the encounter of a motor and a microtubule. The binding rate k_b takes into account both the probability of the encounter and the attachment probability per unit time of the motor onto a neighboring microtubule. The higher the concentration of microtubules, the easier it is for a motor to find an attachment site, hence the binding rate k_b is larger in denser regions of the microtubule aster. In an isotropic monopolar spindle (Fig. 8.3a) the microtubule concentration, ρ_{MT}, decreases away from the pole as [1]

$$\rho_{MT}(r) = \frac{N_{MT}}{4\pi r^2} \,. \tag{8.3}$$

The probability of finding a microtubule at a distance r from the pole is given by the microtubule density at that position, and the binding rate of chromokinesins onto spindle microtubules reads

$$k_b(r) = k_b^0 S_{ch}\, \rho_{MT}(r) \,, \tag{8.4}$$

where k_b^0 is the attachment rate of chromokinesins onto a neighboring microtubule and S_{ch} is the effective chromosome surface that interacts with spindle microtubules [2]. For typical spindle morphologies, the microtubule density decreases away from the pole and, as a result, the binding rate $k_b(r)$ is a decreasing function of

[1] Strictly speaking, Eq. 8.3 is valid for infinitely long microtubules. For practical purposes, it can be used as long as the microtubule length does not limit the motion of the chromosome.

[2] In this description, the size of the chromosome is assumed to be small compared to the chromosome-to-pole distance. A more detailed description should account for the spatial variations of the binding rate along the chromosome arms.

the chromosome position. Note that neither the poleward nor the away-from-the-pole forces depend explicitly on the chromosome position. All spatial information is contained in the binding rate $k_b(r)$, and reflects the morphology of the microtubule spindle.

Once a motor is bound to a microtubule, its velocity and unbinding rate are strongly influenced by the motor load (see chapter 1). If the n bound chromokinesins are independent from one another, they equally contribute the total ejection force, F_{AP}, so that each motor applies a fraction F_{AP}/n of the total ejection force on the chromosome. The load felt by each motor is thus F_{AP}/n by the Newton's third law. Motor unbinding can be seen as a stochastic process that necessitates the passage of an energy barrier, which is reduced in the presence of an applied force (see chapter 1). Kramers Theory (Kramers, 1940; van Kampen, 2004) relates the applied load to the motor unbinding rate k_u according to: $k_u = k_u^0 \exp[F_{AP} a/nK_BT]$, where k_u^0 is the unbinding rate at vanishing load, a is a phenomenological length and K_BT is the thermal energy. This exponential sensitivity to the applied force has been observed for conventional kinesin (Schnitzer et al., 2000) ($k_u^0 \simeq 0.5\ \mathrm{s}^{-1}$ (Vale et al., 1996) and $a \simeq 1.3$ nm (Schnitzer et al., 2000)) and also for myosin motors ($k_u^0 \simeq 6.2\ \mathrm{s}^{-1}$ and $a \simeq 1.3$ nm (Veigel et al., 2003)). The velocity of a motor decreases with a force opposing motor movement and vanishes at a particular stall force f_s. For conventional kinesin, the force-velocity relationship is nearly linear (Visscher et al., 1999; Block et al., 2003). For the sake of simplicity, we adopt such linear relationship $V = V_0(1 - F_{AP}/nf_s)$, with no substantial influence on our results. The present description of the force-dependent motor kinetics is the same than in chapter 5, which was first introduced in chapter 1.

Equations for the chromosome dynamics

Identifying the chromosome velocity $\dot{r}$ with the chromokinesins velocity V on microtubules and combining the equations above, we obtain a self-contained set of two coupled equations for the time evolution of the chromosome position r and the number of bound motors n:

$$\begin{aligned} \dot{n} &= k_b(r)(N-n) - k_u^0 \exp\left(f \frac{n_s + n_\xi}{n + n_\xi} \right) n \,, \\ \dot{r} &= V_0 \frac{n - n_s}{n + n_\xi} \,, \end{aligned} \tag{8.5}$$

where $n_s \equiv F_K/f_s$ is the number of bound motors at which away-from-the-pole and poleward forces exactly balance, $n_\xi \equiv \xi V_0/f_s$ characterizes the global chromosome friction, and $f \equiv f_s a/K_BT$ quantifies the sensitivity of motor unbinding to an external load. We have further checked that allowing for a mismatch between the velocities of the chromosome and the chromokinesins leaves our conclusions unchanged.

8.1.1 Chromosome positional stability

Close to the pole the microtubule density is high, many chromokinesins are attached to the microtubules and the polar ejection force is large enough to move the chromosome away from the pole. Far from the pole microtubules are scarce, the polar ejection force is weak as very few chromokinesins are bound to the microtubules, and the chromosome moves poleward due to the kinetochore force. Somewhere in between, there exists a point where the system remains still (fixed point). It corresponds to a number of bound chromokinesins n_s and to a chromosome position r_s, given implicitly by

$$k_b(r_s) = \frac{k_u^0 e^f n_s}{N - n_s} \,, \tag{8.6}$$

for which chromokinesin attachment and detachment fluxes exactly compensate. If the kinetochore force is so large that even all N motors applying the force f_s are not able to equilibrate the kinetochore force F_K ($n_s > N$), the velocity is always negative, and the chromosome collapses onto the pole. This situation is indeed observed *in-vivo* if the total number of chromokinesins is reduced by a large amount (Levesque and Compton, 2001). Chromosome oscillations in native conditions suggest that $N > n_s$, and we restrict our analysis to this case in what follows.

The fixed point may be stable, in which case the chromosome stalls at a distance r_s from the pole, or unstable, leading to permanent chromosome oscillations (see section 8.1.2). Stability is lost when the fluxes of motor attachment and detachment are not able to compensate. While the attachment flux is mostly dependent on the chromosome position, the detachment flux is highly sensitive to the amount of bound motors, and the more so for small chromosome friction, in which case $k_u \sim \exp(n_s/n)$. The system becomes unstable when the detachment of one or a few motors sufficiently increases the force per remaining motor to induce the dramatic unbinding of them all.

In order to understand the influence of the different parameters on the positional stability of the chromosome, we perform a linear stability analysis of Eq. 8.5. The linearized dynamics of the perturbations $\delta n \equiv n - n_s$ and $\delta r \equiv r - r_s$ close to the fixed point are given by

$$\frac{d}{dt}\begin{pmatrix}\delta n\\ \delta r\end{pmatrix} = \underbrace{\begin{pmatrix} k_u^0 e^f \left[f \frac{n_s}{n_s+n_\xi} - \frac{N}{N-n_s}\right] \frac{\partial k_b(r_s)}{\partial r}\,(N-n_s) & \\ \frac{V_0}{n_s+n_\xi} & 0 \end{pmatrix}}_{\Lambda} \begin{pmatrix}\delta n\\ \delta r\end{pmatrix} . \tag{8.7}$$

The matrix Λ specifies the linearized dynamics of the system around the fixed point, and its stability is obtained from the eigenvalues of Λ or, equivalently, from its trace and determinant, which read

$$\mathrm{Det}(\Lambda) = -V_0 \frac{\partial k_b(r_s)}{\partial r} \frac{N-n_s}{n_s+n_\xi} \,, \tag{8.8}$$

$$\mathrm{Tr}(\Lambda) = k_u^0 e^f \left[-\frac{n_s}{N-n_s} + f\frac{n_s}{n_s+n_\xi} - 1 \right] .$$

The determinant is always positive if enough motors are available ($N > n_s$) and for a decreasing concentration of microtubules away from the pole ($\partial_r k_b(r) < 0$). If $\mathrm{Tr}(\Lambda) < 0$, the fixed point is stable and any perturbation relaxes back to the fixed point. If $\mathrm{Tr}(\Lambda) > 0$, perturbations are enhanced, driving the system away from the fixed point. The condition $\mathrm{Tr}(\Lambda) = 0$ sets the boundary between stable and unstable regimes. For the range of parameters satisfying

$$\frac{n_\xi}{N} < \frac{n_s}{N}\left(f - 1 - f\frac{n_s}{N}\right) \,, \tag{8.9}$$

the fixed point is unstable. Eq. 8.9 shows that the dynamical state of the chromosome is controlled by three parameters: f, n_s/N and n_ξ/N. There exists a force-sensitivity threshold for the motors ($f = 1$) below which the system is never unstable. Although the value of f is not known for chromokinesins, it is estimated to be $f \simeq 2$ for conventional kinesin (Schnitzer et al., 2000). We plot the range of stability for $f = 2$ in Fig. 8.4a.

The linear analysis only specifies the condition leading to an unstable regime, but does not provide information about the evolution of the system in the unstable regime. In next section we analyze the non-linearities and show that once the system is linearly unstable, it always evolves towards a limit cycle of the non-linear system.

8.1.2 Oscillatory behavior

Far from the fixed point, the evolution of the system is governed by the full non-linear coupled equations (Eq. 8.5). In order to understand how the oscillations appear, it is thus necessary to study the non-linearities. To this end, we study the possible qualitatively different scenarios by analyzing the nullclines[3].

The dynamical evolution of the system is graphically represented by trajectories in phase space, which combines information on the chromosome position and the number of bound chromokinesins (Fig. 8.4b,c). Each point $\{n, r\}$ of this two-dimensional space represents a possible configuration of the system, with the chromosome at a distance r from the pole and a number n of chromokinesins bound to the microtubule aster. It is instructive to analyze the location of all points satisfying $\dot{n} = 0$ ($n-$nullcline) and of all points satisfying $\dot{r} = 0$ ($r-$nullcline). The $r-$nullcline (dashed line in Fig. 8.4b,c) represents all points where the chromosome velocity vanishes, and the $n-$nullcline (solid line) represents points where the chromokinesin binding and unbinding fluxes exactly balance, so that $\dot{n} = 0$. The intersection of the

[3] For a general introduction on dynamical systems and bifurcation theory see Ref. (Guckenheimer and Holmes, 1990).

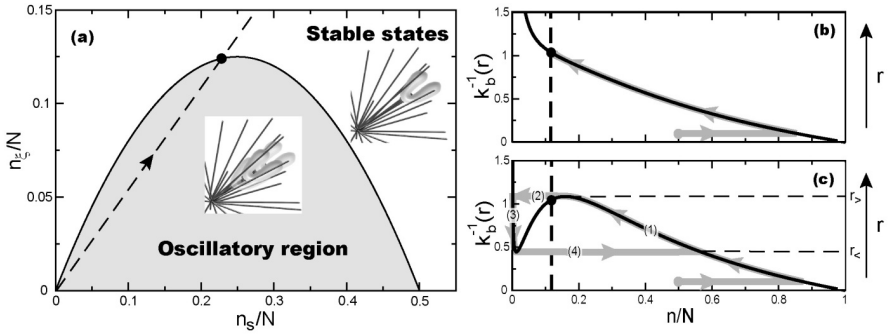

Fig. 8.4. Dynamical regimes of chromosome motion. (a) Parameter space showing the stable and oscillatory states of the chromosome. The continuous line corresponds to the transition between stable and oscillatory regimes, as given by Eq. 8.9 ($f = 2$). A stable chromosome remains still at a fixed distance from the pole, whereas an oscillating chromosome moves toward and away from the pole in a periodic fashion. Increasing n_s and n_ξ corresponds to increasing kinetochore force and chromosome friction, respectively. Decreasing the total chromokinesin number N (arrow) eventually leads to the disappearance of oscillations at $N = N_c$ (filled circle; Eq. 8.11). (b-c) Stable and oscillatory trajectories in the phase space of the dynamical system in Eq. 8.5. Each point corresponds to a given number of bound motors n and chromosome position r ($k_b^{-1}(r)$, equivalently). The r-nullcline (dashed line) and n-nullcline (solid line) intersect at the fixed point (filled circle). The phase trajectories (thick gray line) start from an (arbitrary) initial condition (gray circle). (b) Stable regime: the n-nullcline is monotonous, and the systems evolves toward the (stable) fixed point. (c) Oscillatory regime: the n-nullcline is non-monotonous, the fixed point is unstable and the system follows a limit cycle corresponding to periodic oscillations of the chromosome between the extreme positions $r_<$ and $r_>$. Parameters: $f = 2$, $n_s/N = 0.115$ (b-c); $n_\xi/N = 0.152$ (b) and $n_\xi/N = 0.052$ (c).

two nullclines defines the fixed point. Right (left) to the $r-$nullcline, the away-from-the-pole force is larger (smaller) than the poleward force, the chromosome velocity is positive (negative) and the chromosome moves away from the pole (poleward). Similarly, the points lying below (above) the $n-$nullcline characterize states for which the chromokinesin binding flux is larger (smaller) than the unbinding flux, corresponding to an increase (decrease) of the number of bound motors.

Motor binding and unbinding is typically much faster than chromosome motion. As a consequence, the number of bound motors quickly adapts to the number that equilibrates the attachment and detachment fluxes for a given chromosome position. After this fast equilibration, the system always tries to remain in a boundary layer around the $n-$nullcline. The initial evolution from an arbitrary starting point is thus characterized by a nearly horizontal line in the phase space, corresponding to the fast equilibration of motor binding and unbinding, with very little chromosome motion. The chromosome moves significantly only after the $n-$nullcline is reached, and the trajectory in the phase space (thick gray line in Fig. 8.4b,c) attempts to follow this line up to the fixed point. This can only be achieved if the trajectory dictated by the $n-$nullcline is compatible with the balance of forces (Eq. 8.1). It requires that

the number of bound motors that equilibrates the attachment/detachment fluxes decreases for increasing chromosome-to-pole distances (i.e. the $n-$nullcline must have negative slope at the fixed point). For the system to be unstable, the $n-$nullcline must be non-monotonous and the fixed point must be located in the region of positive slope, a condition specified by Eq. 8.9. The n-nullcline is non-monotonous in the range of parameters given by

$$\frac{n_\xi}{N} < \frac{1}{2}\left(\frac{f}{4}-1\right) + \frac{1}{2}\sqrt{\left(\frac{f}{4}-1\right)^2 + f\frac{n_s}{N}}\,. \tag{8.10}$$

This condition is always fulfilled by the range of parameters leading to a linearly unstable fixed point (Eq. 8.9). Thus, when the fixed point is linearly unstable, the n-nullcline is non-monotonous and the trajectories of the system in the phase space circle around the fixed point in a limit cycle (Fig. 8.4c). Although it is essential to take into account the non-linear system to understand the oscillatory behavior, the transition from stable to unstable fixed point (Eq. 8.9) specifies the transition from a linearly stable regime to a non-linear oscillatory regime (Hopf bifurcation (Guckenheimer and Holmes, 1990)). The existence of a limit cycle can also be shown formally using the Poincaré-Bendixon Theorem (Guckenheimer and Holmes, 1990) [4].

Fig. 8.4b shows the time evolution of the system (thick gray line) toward a stable fixed point from an (arbitrary) initial condition (open circle). First, the number of bound motors quickly increases until it reaches the $n-$nullcline. As the system is placed to the right of the $r-$nullcline, the away-from-the-pole force is larger than the kinetochore force and the chromosome moves away from the pole. The number of bound motors that balances the motor attachment/detachment fluxes decreases for increasing chromosome-to-pole distances (the $n-$nullcline has always negative slope). As a consequence, when the chromosome moves away from the pole there is always the possibility to balance the motor fluxes. The chromosome can thus smoothly reach the position r_s, where it stalls.

Fig. 8.4c shows the trajectory around an unstable fixed point. The evolution is similar to the stable case up to the region where the slope of the $n-$nullcline is positive, at which point the balance of motor fluxes cannot be fulfilled with the chromosome velocity dictated by force balance. After the fast initial motor equilibration to the value dictated by the $n-$nullcline for that chromosome position, the system lies in the right-hand-side of the $r-$nullcline and the chromosome moves away from the pole (label 1 in Fig. 8.4c). When the chromosome reaches a distance $r_>$, the detachment flux of motors becomes too large and the chromosome should then move toward the pole, where the attachment flux of motors is larger, in or-

[4] It is actually easy to show that the phase space flux crossing a closed curve around the fixed point changes its sign depending on how close the curve is from the fixed point. In particular, when the closed curve is in the vicinity of the unstable fixed point, the phase space flux emanates from the fixed point, in accordance with the linear analysis. On the contrary, when the closed curve around the linearly unstable fixed point is far from it, the phase space flux is in the inward direction. In this case, the only solution is the existence of a limit cycle around the fixed point.

der to balance the fluxes (positive slope of the $n-$nullcline). As the chromosome is moving away from the pole, it is unable to move closer to the pole to equilibrate the motor attachment/detachment fluxes. The system can not fulfill the requirements on both the velocity and the balance of motor fluxes at the same time. This situation results in the dramatic unbinding of nearly all bound motors at the position $r_>$ (label 2 in Fig. 8.4c), corresponding approximately to the local maximum of the $n-$nullcline. As a consequence, the away-from-the-pole force nearly vanishes and the chromosome moves poleward to a region of higher microtubule density, where the chromokinesin attachment flux is sufficient to compensate its detachment flux (label 3 in Fig. 8.4c). Close to the pole, the scenario is reversed and the chromosome is ejected away from the pole by a dramatic chromokinesin binding at a position $r_<$, which can be well approximated by the local minimum of the $n-$nullcline (label 4 in Fig. 8.4c). This scheme repeats over time and the trajectory in phase space circles around the fixed point following a limit cycle, which corresponds to periodic chromosome oscillations between its minimal ($r_<$) and maximal ($r_>$) positions.

In Fig. 8.4a we represent the different dynamical regimes of chromosome motion. A reduction of the total number N of available chromokinesins has the effect of moving the system along a straight line in the parameter space (arrow in Fig. 8.4a), and to eventually exit the oscillatory regime. We predict that the oscillations should cease below a minimal number of chromokinesins, N_c, given by

$$N_c = \frac{f n_s^2}{(f-1)n_s - n_\xi} \,. \tag{8.11}$$

Although for clarity reasons we have presented the analysis of the system (Eq. 8.5) using the chromosome-to-pole distance r and the number of bound chromokinesins n as variables, it is more convenient to use the binding rate k_b as a variable instead of r. The results are obviously equivalent no matter the variables used, but choosing k_b and n as variables allows to perform both the linear and non-linear analysis without specifying any particular functional form for the binding rate $k_b(r)$ (or $\rho_{MT}(r)$ equivalently). Therefore, all the results concerning the dynamical state of the chromosome do not depend on the morphology of the microtubule aster, as long as it decreases away from the pole.

8.2 Discussion

In this section we compare the theoretical results to different experimental observations and show that the theoretical framework developed above can explain chromosome positioning, movement and congression, on the same physical grounds.

8.2.1 Positioning and oscillations of mono-oriented chromosomes

Chromosome oscillations are a very generic behavior observed during the division of many animal cells. This ubiquity is consistent with our analysis, which predicts oscillations for a wide range of motor and kinetochore parameters (Fig. 8.4a). Numerically computed chromosome motion in the unstable regime (Fig. 8.5a) displays the

characteristic sawtooth shaped oscillations observed *in-vivo* (Skibbens et al., 1993) (Fig. 8.5c), indicating that the system switches suddenly between phases of nearly constant velocities. Changing the various parameters leads to changes in amplitude, period, and symmetry of the oscillations, but it has a little effect on their sawtooth shape. This is a signature of the fact that chromokinesin kinetics is much faster than the viscous motion of the chromosome. Indeed, the time scale of the oscillation ($\sim$min) is controlled by the net force and the effective viscous friction on the chromosome, while the switching between phases occurs over a much shorter time scale, characteristic of motor binding/unbinding ($\sim$sec).

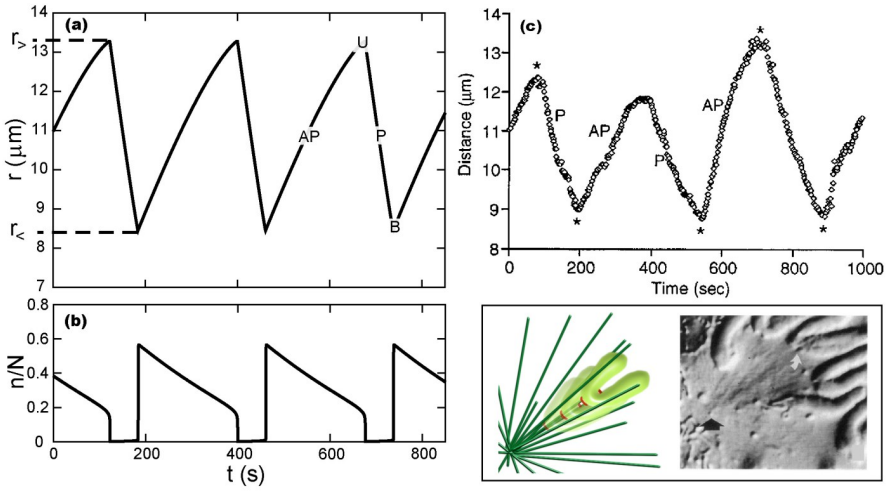

Fig. 8.5. Chromosome oscillations. Time evolution of the chromosome position (a) and the number of bound chromokinesins (b) obtained by numerical integration of Eq. 8.5. The theoretical analysis reproduces and explains the sawtooth shape of the oscillations observed *in vivo* (c; adapted from Ref. (Inoue and Salmon, 1995)). The chromosome periodically oscillates between phases of poleward and away-from-the-pole motion with nearly constant velocities. The sudden switches from poleward to away-from-the-pole motion correspond to a dramatic chromokinesin binding (B) and unbinding (U) events. For the sake of simplicity, the microtubule distribution in the aster is assumed to be isotropic (Eq. 8.3 and 8.4). The parameters are $V_0 = 2.38\ \mu$m/min (Skibbens et al., 1993), $k_u^{(0)} = 1.65\ \text{s}^{-1}$ (obtained from the processivity length $l_p \equiv V_0/k_u^0$ of chromokinesins; $l_p \simeq 24$ nm (Yajima et al., 2003)) and $f = 2$ (Schnitzer et al., 2000). The parameters $k_b(r) = 266/(r(\mu\text{m}))^2\ \text{s}^{-1}$, $n_s/N = 0.115$, $n_\xi/N = 0.052$, are chosen to reproduce the amplitude, period and average chromosome-to-pole distance of the *in vivo* oscillations in (c). The box shows a sketch of an oscillating chromosome (left) and the DIC image of the chromosome showing the oscillations in (c) (right; modified from Ref. (Inoue and Salmon, 1995)).

The oscillations proceed as follows (Fig. 8.5). Close to the pole, the high density of microtubules results in the binding of a large number of motors (Fig. 8.5b), driving the chromosome away from the pole at a velocity close to their maximum velocity V_0.

We argue that the velocity of the away-from-the-pole motion is a direct quantitative estimate of the chromokinesin velocity at vanishing load ($V_0 \simeq 2\ \mu$m/min in Newt lung cells (Rieder et al., 1986; Skibbens et al., 1993)). Indeed, chromosome arm fragments cut by laser microsurgery move away from the pole with the same velocity as the full chromosome in the away-from-the-pole phase (Rieder et al., 1986), in spite of being only subject to the hydrodynamic drag, a much weaker friction force. As the chromosome moves away from the pole, the density of microtubules decreases and eventually reaches a value at which the attachment flux is too low to compensate the motor detachment flux. The remaining bound motors then detach rapidly (Fig. 8.5b) and the chromosome switches to poleward movement. The poleward phase occurs with almost no motors attached to the microtubule aster and the chromosome moves toward the pole with a constant velocity $-F_K/\xi$. The cycle is completed when the chromosome reaches a region of high enough microtubule density, where many motors abruptly attach and eject the chromosome. The ratio of away-from-the-pole and poleward velocities, approximately given by n_ξ/n_s, characterizes the symmetry of the oscillations. Symmetric oscillations are obtained for $n_\xi \simeq n_s$ and $f > 2$. In case $f < 2$, all states that fulfill $n_\xi \simeq n_s$ are stable and only asymmetric oscillations can be obtained.

The friction of the system ξ and the kinetochore force F_K are difficult to modify experimentally. On the other hand, the total number N of chromokinesins in the chromosome arms can be altered *in-vivo*. As discussed in section 8.1.2, there exist a critical number of chromokinesins N_c (Eq. 8.11), independent of the aster morphology, below which no oscillations should be observed. This result is in good agreement with the experimental observations in Ref. (Levesque and Compton, 2001), which are discussed below. For $N < N_c$, the chromosome is stable and located at a fixed distance to the pole (Fig. 8.6). The stable chromosome position depends crucially on the morphology of the microtubule aster, as observed experimentally (Rieder et al., 1986). It corresponds to a microtubule density where chromokinesin binding onto microtubules equilibrates their unbinding (Eq. 8.6), and increases continuously with increasing number of chromokinesins. Our results indicate that oscillations of finite amplitude start at the critical point ($N = N_c$) [5], and that increasing the number of chromokinesins further increases both the mean chromosome position and the amplitude of the oscillations (Fig. 8.6).

Important changes in chromosome positioning have been observed upon changes of the morphological properties of the microtubule aster (Ault et al., 1991; Cassimeris et al., 1994). In our framework, the stable position of the chromosome and the average distance to the pole of an oscillating chromosome depend strongly on the aster morphology, as can be seen in the expression for the fixed point (Eq. 8.6). Therefore, a morphological variation of the microtubule aster changes the average chromosome-to-pole distance and the amplitude of the oscillations, but does not change the dynamical state of the chromosome. In particular, an increase of the

[5] For most values of the parameters, the transition from stable to oscillatory behavior is specified by a subcritical Hopf bifurcation, leading to oscillations of finite amplitude at the critical point.

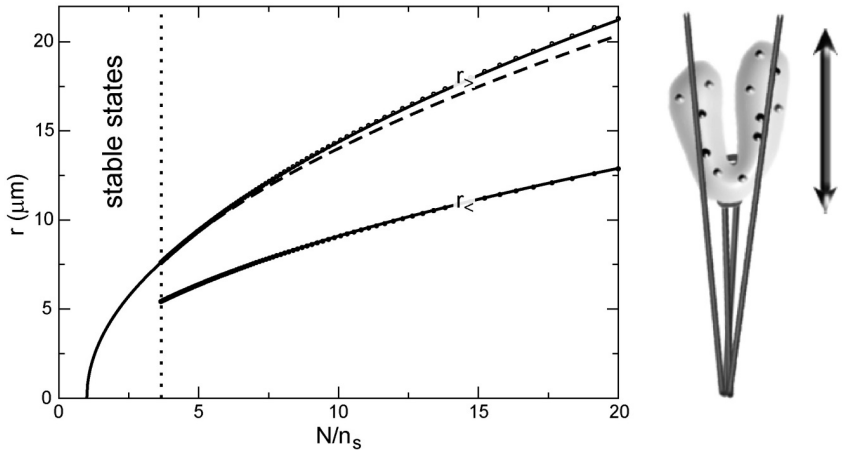

Fig. 8.6. Dependence of the amplitude of the oscillations with the total number N of chromokinesins associated to the chromosome arms. The kinetochore properties are fixed ($n_\xi/n_s = 0.45$) and the total number of motors N varies, so that the system follows a straight line in the parameter space (Fig. 8.4a). There is a critical number of motors N_c (dotted line) at which the system transits from a stable to an oscillatory regime. Below N_c, the stable chromosome position moves away from the pole with increasing N. Above N_c, both the position of the unstable fixed point (dashed line) and the amplitude of the chromosome oscillations increase with N. The numerically computed maximal and minimal positions of the chromosome during the oscillations are shown (circles). The maximum and minimum of the $n-$nullcline (Fig. 8.4c) provide a good analytical approximation for the two extreme positions of the chromosome during the oscillations ($r_>$ and $r_<$ respectively; continuous lines for $N > N_c$). For increasing average chromosome-to-pole distance, the amplitude of the oscillations becomes larger and the oscillations become more noticeable. The sketch of the chromosome on the right represents the geometry of the system.

microtubule density leads to both larger average chromosome-to-pole distance and larger amplitude of the oscillations. This result is in good agreement with the observation that the amplitude of the oscillations increases with the average chromosome-to-pole distance (Cassimeris et al., 1994). However, the precise manner in which these quantities increase with an increasing microtubule density depends strongly on the functional form $k_b(r)$. Note that a drastic increase in the microtubule density modifies also the global friction acting on the chromosome. In particular, if the microtubule aster is extremely dense, the friction coefficient is too high and chromosome oscillations are prevented. On the other hand, the depolymerization of astral microtubules prevents the generation of polar ejection forces and the chromosome moves toward the pole. Both results are confirmed by experimental observations (Ault et al., 1991).

8.2.2 Implications for chromosome congression

Experimentally, vastly reducing the number of chromokinesins (but presumably not entirely suppressing them) leads to the disappearance of the oscillations of mono-oriented chromosomes and their collapse onto the centrosome, while not preventing bi-oriented chromosomes to congress to the metaphase plate (Levesque and Compton, 2001) (Fig. 8.7). This observation agrees favorably with our results (section 8.2.1). Forces in mitosis are typically of order 1nN (Nicklas, 1983). With this estimate for the kinetochore force, along with typical values for the average chromosome-to-pole distance and the amplitude and period of the oscillations in Newt lung cells (Rieder et al., 1986; Skibbens et al., 1993), we estimate a total number $N \simeq 1500 - 5000$ of chromokinesins on the chromosome arms, and a critical number $N_c \simeq 600 - 700$ above which oscillations are expected. We thus predict that inhibition of 60% to 90% of the chromokinesins would be sufficient to suppress oscillations. Indeed, it has been observed experimentally that the inhibition of at least 90% of chromokinesins suppresses chromosome oscillations (Levesque and Compton, 2001) (Fig. 8.7A,B). This shows that a significant number of chromokinesins may remain attached to the arms of non-oscillating chromosomes (~ 100). The magnitude of the away-from-the-pole force is substantially reduced upon a drastic inhibition of chromokinesins, and the non-oscillating chromosome locates closer to the pole, as observed experimentally (Levesque and Compton, 2001) (Fig. 8.7C). For such chromosomes, the probability that a microtubule from the opposite spindle pole contacts the unattached sister kinetochore and the chromosome becomes bi-oriented is much lower. This explains why several chromosomes in chromokinesin depleted cells remain close to one pole and never become bi-oriented during the division process. However, if by chance, one of these chromosomes becomes bi-oriented, the kinetochore forces toward each pole cancel each other to a large extent, and the polar ejection force of the remaining chromokinesins may be sufficient to allow for chromosome congression, as observed in experimentally (Levesque and Compton, 2001) (Fig. 8.7C). Indeed, it has been shown that chromokinesins are essential for congression and proper chromosome alignment at the metaphase plate in several organisms (Antonio et al., 2000; Funabiki and Murray, 2000).

8.2.3 The motion of bi-oriented chromosomes

The description of mono-oriented chromosome motion can be directly extended to the case of bi-oriented chromosomes. A bi-oriented chromosome is connected to both spindles poles by kinetochore fibers attached to the sister kinetochores. The chromosome is thus subject to opposing kinetochore forces and polar ejection forces from both microtubule asters (Fig. 8.8). For the sake of simplicity, we consider a one dimensional geometry and the opposing kinetochore forces to be equal and constant, similarly to the case of mono-oriented chromosomes. With these assumptions, the kinetochore forces cancel out for each chromosome position. Note that assuming equal opposing kinetochore forces implies the kinetochore fiber to be fully developed in both kinetochores. This is unlikely to be the case for congressing chromosomes

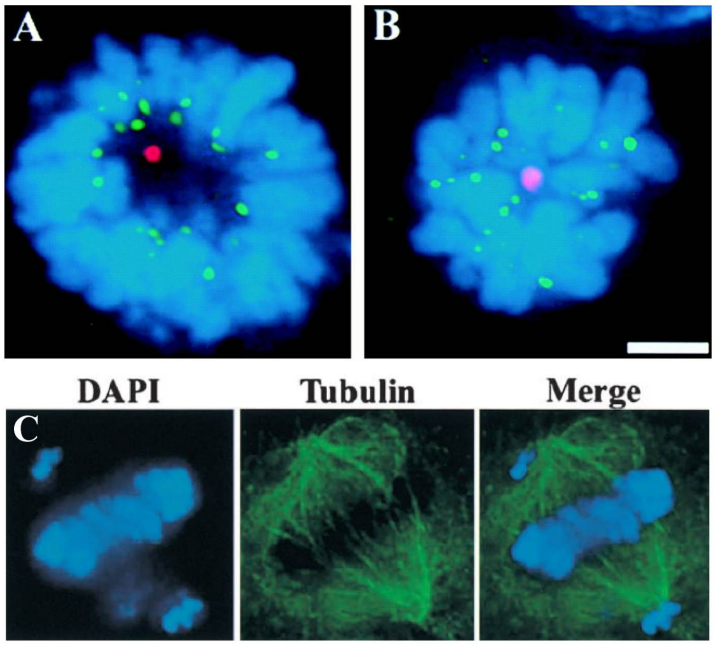

Fig. 8.7. (A-B) Effects of chromokinesin Kid inhibition on mono-oriented chromosomes in vertebrate-cultured cells. Cells were injected with Eg5-specific antibodies to induce monopolar spindles (see chapter 9). Fluorescence photographs: the centrosome is shown in red, CENP-E (kinetochore component) in green and DNA in blue. (A) Cells injected only with Eg5-specific antibodies. The gap between the spindle pole and the chromosomes is clearly visible. Chromosomes oscillated toward and away from the pole, and were located at an average distance of 10 μm from the pole. (B) Cells injected with Eg5-specific and Kid-specific antibodies. The injection of Kid-specific antibodies reduces by more than 90% the number of Kid chromokinesins associated to the chromosome arms. The chromosomes moved poleward and approached very close to the pole (no gap between the pole and the chromosomes is visible). The chromosomes did not display oscillations after Kid inhibition. Bar, 10 μm. (C) Failure of chromosome congression in some cells injected with Kid-specific antibodies. Fluorescence images showing the DNA (blue) and microtubules (green). From left to right: DNA, microtubules and merge (DNA and microtubules). Some chromosomes remain very close to the pole and never become bi-oriented. (Adapted from Ref. (Levesque and Compton, 2001)).

and we thus restrict our analysis to chromosomes with fully formed kinetochore fibers, like those in metaphase. Unlike the poleward kinetochore forces, the polar ejection forces implicitly depend on the chromosome position in the spindle via the dependence of the chromokinesin binding rate on the local microtubule density.

The forces responsible for chromosome motion in mitosis may be probed by micromanipulation experiments investigating the influence of an external force on the motion and positioning of chromosomes. In addition to the forces discussed above, we consider the action of an external force, F_{ext}, acting on the chromosome and dis-

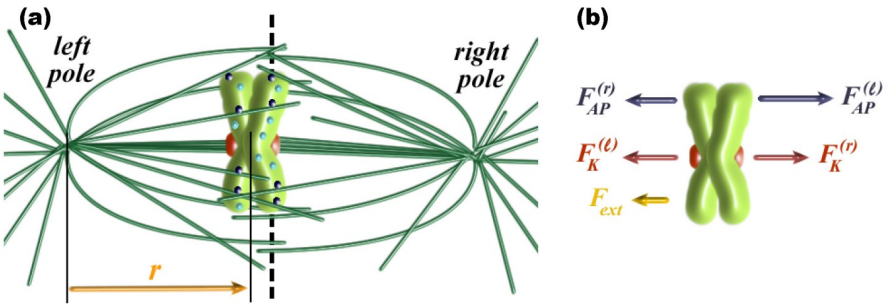

Fig. 8.8. (a) Sketch of a bi-oriented chromosome. The microtubules (dark green) from both asters interact with a single chromosome (light green). Each sister kinetochore (red) is connected to a different pole through a bundle of microtubules. Chromokinesin motors, permanently attached to the chromosome arms, may be bound to a microtubule (dark blue dots) or unbound (light blue dots). The chromosome position relative to the left pole is r (orange arrow). (b) Forces acting on the bi-oriented chromosome: the opposing kinetochore poleward forces, $F_K^{(\ell)}$ and $F_K^{(r)}$ (red), the polar ejection forces created by the chromokinesins bound to the microtubules of the left and right asters, $F_{AP}^{(\ell)}$ and $F_{AP}^{(r)}$ respectively (dark blue), and the external force, F_{ext} (orange).

cuss the effect of such a force on the position and motion of a bi-oriented chromosome [6]. An additional external force, F_{ext}, applied to a mono-oriented chromosome in the direction of the pole, merely modifies the effective value of the kinetochore force to $F_K + F_{ext}$ and shifts the chromosome motion accordingly. We analyze below the effect of the external force on bi-oriented chromosomes.

In a monopolar spindle, the spatial variation of the chromokinesin binding rate follows the spatial distribution of microtubules in the aster and is given by the function, $k_b(r)$ (Eq. 8.4). In a bipolar spindle, characterized by a distance L between the spindle poles, the chromokinesins attach to microtubules associated to both spindle poles (Fig. 8.8). The chromokinesin motors attached to microtubules associated to the left pole, generate a polar ejection force, $F_{AP}^{(\ell)}$, directed toward the right pole. The chromokinesins attached to microtubules associated to the right pole, generate a polar ejection force, $F_{AP}^{(r)}$, that opposes the polar ejection force from the left pole. Force balance on a bi-oriented chromosome reads

$$F_{AP}^{(\ell)} - F_{AP}^{(r)} - F_{ext} - \xi \dot{r} = 0 \,, \tag{8.12}$$

where r is the position of the chromosome with respect to the left pole, $\dot{r}$ is the chromosome velocity and F_{ext} is an external force directed toward the left pole.

We consider a total number, N, of chromokinesins to be permanently attached to the chromosome arms. Unlike the situation when only one microtubule aster is

[6] An external force can be applied on the chromosome using, for instance, a microneedle. These experiments have been done for chromosomes in meiotic (Nicklas, 1983) and mitotic (Skibbens and Salmon, 1997) spindles.

present, the chromokinesins can now attach to microtubules from the two microtubule asters forming the mitotic spindle. Due to their attachment/detachment kinetics, at one given time, a number n_ℓ of chromokinesins is bound to microtubules from the left aster, and a number n_r is bound to microtubules associated to the right aster. Assuming the chromokinesins to behave independently from each other and to share the total load, the total ejection force produced by the chromokinesins bound to the microtubules from the left (right) pole is $F_{AP}^{(\ell)} = n_\ell f_\ell$ ($F_{AP}^{(r)} = n_r f_r$), where f_ℓ (f_r) is the force felt by a chromokinesin bound to a microtubule from the left (right) aster. We assume a linear force-velocity relation for a single chromokinesin and write $V_\ell = V_0(1 - f_\ell/f_s)$, for the chromokinesins associated to microtubules from the left pole. The motion of the chromosome away from the left pole is driven by the chromokinesins associated to microtubules from this pole, so that $V_\ell = \dot{r}$. Similarly, the velocity of chromokinesins associated to the microtubules of the right pole is $V_r = V_0(1 - f_r/f_s)$ and, as they are responsible for the movement of the chromosome toward the left pole, $V_r = -\dot{r}$.

Writing the kinetics of the chromokinesins bound to microtubules of each aster in the same way than for a mono-oriented chromosome (Eq. 8.2), and using the equations above, we obtain a dynamical system for the time evolution of the number of chromokinesins bound to microtubules from the left and right asters, n_ℓ and n_r respectively, and the chromosome position, r, which reads

$$\begin{aligned}
\frac{dn_\ell}{dt} &= k_b(r)(N - n_\ell - n_r) - k_u^0 \exp\left(f(1-\dot{r})\right) n_\ell \,, \\
\frac{dn_r}{dt} &= k_b(L-r)(N - n_\ell - n_r) - k_u^0 \exp\left(f(1+\dot{r})\right) n_r \,, \\
\frac{dr}{dt} &\equiv \dot{r} = V_0 \frac{n_\ell - n_r - F_{ext}/f_s}{n_\xi + n_\ell + n_r} \,.
\end{aligned} \tag{8.13}$$

The parameters f and n_ξ are already defined in Eq. 8.5, and the function $k_b(r)$ is given by Eq. 8.4. Note that we have assumed the same morphology for both microtubule asters. However, as the center of the right aster is placed at distance L from the left one, the binding rate to microtubules associated to the right aster is $k_b(L-r)$, with $L-r$ being the distance of the chromosome to the right pole.

Similarly to the case of mono-oriented chromosomes, for bi-oriented chromosomes there is a position, r_s, for which the chromosome velocity vanishes and the attachment flux of chromokinesins is equilibrated by their detachment flux on each aster (fixed point). The fixed point may be stable, in which case the chromosome remains still at position r_s, or unstable. We first analyze the stable case and discuss below how the system evolves in the unstable regime. Equilibration of chromokinesin attachment and detachment fluxes on each aster ($\dot{n}_\ell = 0$ and $\dot{n}_r = 0$) at the position r_s leads to

$$n_{r,s} = N \frac{k_b(L-r_s)}{k_b(L-r_s) + k_b(r_s) + k_u^0 e^f} \,, \qquad n_{\ell,s} = N \frac{k_b(r_s)}{k_b(L-r_s) + k_b(r_s) + k_u^0 e^f} \,, \tag{8.14}$$

where $n_{\ell,s}$ and $n_{r,s}$ are the number of chromokinesins bound to left and right asters respectively, that equilibrate the attachment and detachment fluxes on each aster for $\dot{r} = 0$. The position r_s depends on the external force applied on the chromosome and reads

$$\frac{F_{ext}}{N f_s} = \frac{k_b(r_s) - k_b(L - r_s)}{k_b(L - r_s) + k_b(r_s) + k_u^0 e^f} \,. \tag{8.15}$$

The latter expression implicitly specifies the possible stable chromosome position, r_s, as a function of the external force applied on the chromosome, F_{ext}. In absence of external load, the chromosome is positioned at a distance $r_s = L/2$, due to the symmetry of the bipolar spindle. As expected, bi-oriented chromosomes in native conditions are positioned in the metaphase plate.

When an external force is applied on the chromosome, its displacement from the mitotic plate (located at $L/2$) is linearly proportional to the external force even for fairly large displacements, due to the symmetry of the bipolar spindle. Mathematically, this arises from the existence of an inflexion point for the right-hand-side of Eq. 8.15, so that the quadratic term in the expansion near the midplane vanishes. In Fig. 8.9a we represent the number of chromokinesins bound to microtubules of the left and right asters as a function of the stable position r_s. For forces $F_{ext} > 0$ ($F_{ext} < 0$), the chromosome is positioned closer to the left (right) pole, where the polar ejection force from the left (right) aster is larger and can balance both $F_{AP}^{(r)}$ ($F_{AP}^{(\ell)}$) and F_{ext}. The stable chromosome position, given by Eq. 8.15, is represented in Fig. 8.9b for various aster-like microtubule distributions. The linear relationship between the external force and the stable chromosome position is valid almost up to values of the external force at which the chromosome collapses onto one pole: $F_{ext} \simeq N f_s$. According to the estimate for the number of chromokinesins that we obtained in section 8.2.2 ($N \sim 10^3$), and using typical values for the stall force of motors ($\sim$pN), this force is in the nanoNewton range.

The relation between the external force and the chromosome position could be directly measured in micromanipulation experiments. This situation has to some extent been realized experimentally in Ref. (Hays et al., 1982) by analyzing the metaphase stable position of multivalent chromosomes, i.e. those chromosomes with more than two kinetochores. In this case, the excess number of kinetochores generate an extra force toward one of the poles. The resulting chromosome displacement with respect to the metaphase plate has indeed been reported to be proportional to the excess number of kinetochores, in agreement with the results of our analysis.

Bi-oriented chromosomes correctly locate at the mitotic plate if the net force toward each pole increases with the distance to the pole. Östergren (Ostergren, 1951) proposed a long time ago that the kinetochore force F_K increases (linearly) with the length of the kinetochore fiber. We argue that this "traction fiber model", which was originally introduced before the discovery of chromokinesin, should be understood in the more general sense. Rather than the kinetochore force, it is the net poleward force, i.e. the difference of the kinetochore and polar ejection forces ($F_K^{(i)} - F_{AP}^{(i)}$, for $i = r, \ell$), that increases with the distance to the pole. Our results show that the increase of the net poleward force is related to a decreasing polar ejection force away

from the center of the microtubule aster. The symmetry of a bipolar spindle ensures that chromosomes correctly locate at the mitotic plate, where polar ejection forces from each pole balance. This idea is supported by several experimental observations which show that chromokinesins are essential for proper chromosome alignment at the metaphase plate in several organisms (Antonio et al., 2000; Funabiki and Murray, 2000).

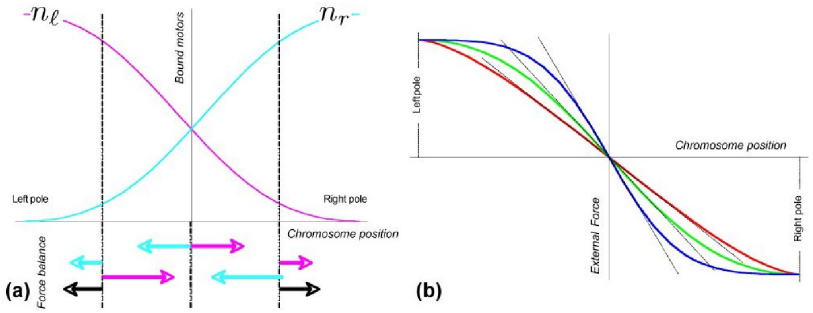

Fig. 8.9. (a) Number of chromokinesin motors bound to microtubules of the left (pink) and right (turquoise) asters. The balance of polar ejection forces and the external force (black) is also represented for two symmetrical chromosome positions. (b) Stable chromosome position as a function of the external force. The chromosome displacement with respect to the spindle midplane varies linearly with the external force almost up to the chromosome collapse onto one of the poles. The different curves are for power-law decreases of microtubule density with distance from the pole, $k_b(r)/(k_u^0 e^{-f}) = r^{-\beta}$, with $\beta = 1.5$ (red) $\beta = 2$ (green) and $\beta = 3$ (blue). (Figure: Pierre Sens).

Oscillatory behavior

In many organisms, bi-oriented chromosomes also display the oscillatory behavior described above for mono-oriented chromosomes. We now show that the tug-of-war between the opposing polar ejection forces of the two microtubule asters, also leads to sawtooth shaped oscillations like those observed *in vivo* for bi-oriented chromosomes (Skibbens et al., 1993). The positional stability of a bi-oriented chromosome does not depend on the kinetochore force because it does not play any role in this description. Instead, the length of the spindle L and the external force can affect the dynamical state of the chromosome. Similarly to mono-oriented chromosomes, the fixed point may either be stable or unstable. In the stable regime, chromosomes evolve from an arbitrary initial position toward the stable position given by Eq. 8.15 and remain there. In order to find out the behavior of a bi-oriented chromosome in the unstable regime, we numerically integrate the dynamical system in Eq. 8.13. Fig. 8.10a shows the time evolution of the chromosome position in the unstable regime for $F_{ext} = 0$. In the absence of an external force, the chromosome oscillates around the mitotic midplane located at $L/2$. The oscillations are highly non-linear

and display the characteristic sawtooth shape previously found for mono-oriented chromosomes, with phases of constant velocity interrupted by sudden switches in direction. In this case however, the symmetry of the bipolar spindle ensures symmetric oscillations in the absence of external force. When the chromosome is moving away from the left pole, the number of chromokinesins bound to microtubules of the left aster is larger than that attached to microtubules of the right aster ($n_\ell \gg n_r$). The polar ejection force created by the left aster is thus larger than that of the right aster, explaining the movement toward the right pole (Fig. 8.10a,b). As the chromosome progressively approaches the right pole, the number n_ℓ decreases because the density of microtubules of the left aster diminishes. At the same time, the attachment rate of chromokinesins to microtubules from the right aster increases. This situation eventually leads to the simultaneous abrupt detachment of the chromokinesins bound to the left aster and attachment of chromokinesins to the right aster (Fig. 8.10b). As a result, the polar ejection force generated by the right aster becomes larger than that from the left aster, and the chromosome moves away from the right pole. The situation is reversed when the chromosome is close enough to the left pole. Chromokinesins detach suddenly from the right aster, and their abrupt attachment to the left aster ejects the chromosome away from the left pole. This scheme is repeated over time, leading to periodic oscillations of the chromosome around the mitotic midplane.

Our results show that both mono- and bi-oriented chromosomes may display highly non-linear oscillations, in agreement with the experimental observations. In Fig. 8.10c we show the motion of a chromosome throughout the division process. Oscillations are present in almost all mitotic phases, from prometaphase to anaphase A. In particular, bi-oriented chromosomes oscillate around the mitotic plate during metaphase (Skibbens et al., 1993).

The presence of an external force acting on an unstable chromosome modifies the characteristics of the oscillations. If a force directed toward the left (right) pole, $F_{ext} > 0$ ($F_{ext} < 0$), is applied on a bi-oriented oscillating chromosome, its average distance to the left pole is reduced (Fig. 8.11). Moreover, the amplitude, period and symmetry of the oscillations are affected. While the change in the symmetry of the oscillations depends on the direction of the force, the amplitude and period depend on the magnitude of the force but not on its direction. In particular, both period and amplitude are reduced in presence of an external force. The typical sawtooth shape of the oscillations remains however largely unchanged.

The present analysis on the motion of bi-oriented chromosomes shows that even in the extreme case where the kinetochore forces do not play any role in the dynamics, chromosome oscillations arise from the tug-of-war of the opposing polar ejection forces from the two microtubule asters.

8.2.4 Mechano-sensitivity of the kinetochore

Similarly to chromokinesins, it is most likely that the force-producing entities responsible for the kinetochore force are themselves force-sensitive (Skibbens et al., 1995). A more detailed description of the force generation within the kinetochore, which involves microtubule depolymerization (Koshland et al., 1988; Inoue and

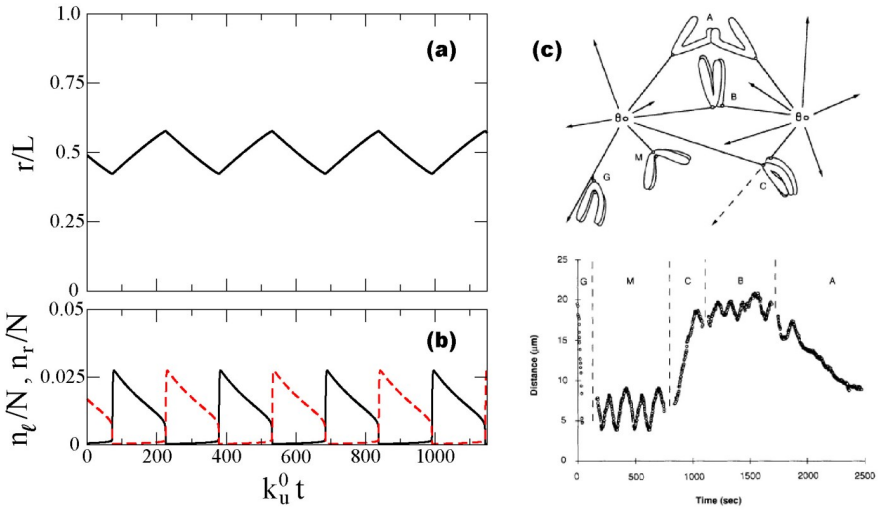

Fig. 8.10. (a-b) Bi-oriented chromosome oscillations in absence of external force ($F_{ext} = 0$). Time evolution of the chromosome position (a) and the number of chromokinesins bound to the left (continuous line) and right (dashed line) microtubule asters (b), obtained by numerical integration of Eq. 8.13. The chromosome oscillates around the mitotic midplane at $L/2$. The oscillations display the characteristic sawtooth shape and are symmetric as a consequence of the symmetry of the bipolar spindle. Parameters: $f = 2$, $L/l_p = 800$, $n_\xi/N = 0.002$ and $N_{MT} k_b^0 S_{ch}/4\pi l_p^2 k_u^0 = 4\,10^3$. (c) Chromosome motion in different stages of mitosis. (Top) Schematic illustration of the different stages of chromosome movements during mitosis in Newt lung cells: G, gliding; M, mono-oriented; C, congression of a bi-oriented chromosome toward the mitotic midplane; B, bi-oriented chromosome; A, anaphase A poleward movement. (Bottom) kinetochore-to-pole distance as a function of time, showing that sawtooth-shaped oscillations are present in almost all stages of the division process. (Adapted from Ref. (Skibbens et al., 1993)).

Salmon, 1995) and cytoplasmic dynein motors (Sharp et al., 2000a), is required to account for some features of the chromosome behavior. The mechanism proposed here for the away-from-the-pole force generation by chromokinesins, based on the motor collective dynamics, can be extended to the poleward force generation by any force-sensitive element in the kinetochore (e.g. dynein motors).

In this extended description, the kinetochore force, F_K, is no longer constant. It is instead specified by the dynamics of the force generators in the kinetochore. For the sake of simplicity, we consider the force generators in the kinetochore to be dynein motors. Note however that microtubule polymerization/depolymerization in the kinetochore can also be described in the same framework (Joglekar and Hunt, 2002). We assume a total number of dyneins, N_d, in the kinetochore which can be bound to or unbound from the kinetochore microtubules (K-fiber). At each time t there is a number n_d of dyneins bound to kinetochore microtubules, generating a poleward force, $F_K = n_d f_d$, where f_d is the force generated by a single bound

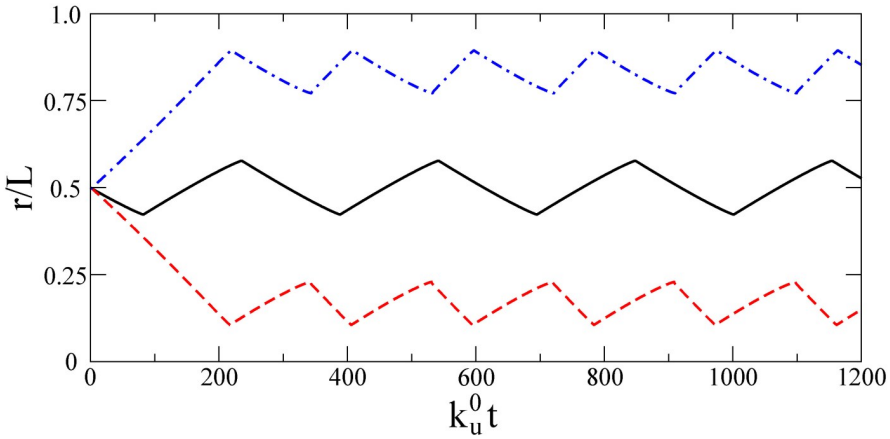

Fig. 8.11. Bi-oriented chromosome oscillations in presence of an external force F_{ext}. The motion in absence of external force is shown as reference (continuous line). For an external force $F_{ext}/N f_s = 0.02$, directed toward the left pole, the chromosome oscillates around an average position closer to the left pole and the oscillations are no longer symmetric (dashed line). The reversed situation happens for a force $F_{ext}/N f_s = -0.02$, of equal magnitude but directed toward the right pole (dashed-dotted line). Parameters: $f = 2$, $L/l_p = 800$, $n_\xi/N = 0.002$ and $N_{MT} k_b^0 S_{ch}/4\pi l_p^2 k_u^0 = 4\,10^3$.

dynein motor. We assume a linear force-velocity relation for dynein motors and write $V_d = V_0^d(1 - f_d/f_s^d)$, where V_0^d is the velocity of dynein at vanishing load and f_s^d its stall force. As dynein motors move poleward and they induce the poleward motion of the chromosome, we identify $\dot{r} = -V_d$. Force balance on the mono-oriented chromosome is given by Eq. 8.1. It is now necessary to write the dynamics of the poleward kinetochore force, as we did for chromokinesins. The time evolution of the number of dynein motors bound to kinetochore microtubules is given by

$$\frac{dn_d}{dt} = k_b^d(N_d - n_d) - k_u^d n_d \,, \tag{8.16}$$

where k_b^d and k_u^d are, respectively, the attachment rate of dyneins onto kinetochore microtubules and their detachment rate. Similarly to chromokinesins, the detachment rate for dynein motors depends exponentially of the applied load, so that $k_u^d = k_{u,0}^d \exp(f_d a_d/K_B T)$, with a_d being a length characterizing the effect of the force on detachment and $k_{u,0}^d$ the dynein detachment rate at vanishing load.

The equations written so far for the force generation by dynein motors in the kinetochore are the same than for chromokinesins on the chromosome arms. The difference in their dynamics is that the attachment rate of dyneins onto kinetochore microtubules does not depend on the microtubule density in the aster, as dyneins are located in the kinetochore and move along the kinetochore fiber. Therefore, k_b^d is a constant parameter. The dynamics of dynein motors are not coupled to any spatial degree of freedom and, as a consequence, there is no difference between a chromo-

some positioned close to the pole or far from it, as far as the kinetics of dyneins is concerned. Indeed, several experimental observations show that chromokinesin inhibition leads to defects in the positioning of bi-oriented chromosomes (Antonio et al., 2000; Funabiki and Murray, 2000), suggesting that chromokinesins provide the spatial information that allows the chromosome to sense its position in the spindle.

Using Eqs. 8.1, 8.2, 8.16, we get the following dynamical system for the time evolution of the number of chromokinesins bound to astral microtubules, n, the number of dyneins bound to kinetochore microtubules, n_d, and the position of the chromosome r:

$$\begin{aligned}
\dot{n} &= k_b(r)(N-n) - k_u^0 \exp\left(f\left(1-\frac{\dot{r}}{V_0}\right)\right) n \,, \\
\dot{n}_d &= k_b^d(N_d-n_d) - k_{u,0}^d \exp\left(f_d\left(1+\frac{\dot{r}}{V_0^d}\right)\right) n_d \,, \\
\dot{r} &= V_0 \frac{n - n_d \frac{f_s^d}{f_s}}{n + n_d \frac{f_s^d}{f_s}\frac{V_0}{V_0^d} + \frac{\xi V_0}{f_s}} \,,
\end{aligned} \tag{8.17}$$

where $f_d \equiv f_s^d a_d / K_B T$ characterizes the force-sensitivity of dynein detachment events.

The stability analysis done in section 8.1 can also done for the dynamical system in Eq. 8.17, and similar results are found. There exist stable states for which the chromosome stalls at a fixed position from the pole (given by the fixed point of Eq. 8.17) and also an oscillatory region. The aim of the present analysis is to show that similar highly non-linear oscillations can also appear when the kinetochore is force sensitive. In Fig. 8.12a.1 we show the numerically computed time evolution of the chromosome position in the unstable regime. Similarly to the case where the kinetochore is not force-sensitive, the chromosome oscillates toward and away from the pole, with phases of nearly constant velocity. Based on experimental observations, it has been argued that the kinetochore switches between a force producing state in the poleward phase and a neutral state, in which it does not apply any force, during the away-from-the-pole phase (Khodjakov et al., 1999). The existence of a neutral state can be naturally explained by the collective detachment of dyneins induced by their force dependent detachment kinetics. In Fig. 8.12a.2 we show the time evolution of the number of bound chromokinesins and bound dyneins. During the away-from-the-pole phase most dyneins are detached and, therefore, the poleward force is negligible, explaining the existence of neutral states during away-from-the-pole motion (Khodjakov et al., 1999).

Although this extended description, which takes into account the possible force-sensitivity of the kinetochore allows to reproduce more experimental observations, it introduces a large number of unknown parameters without bringing substantial improvement to our qualitative understanding of the oscillations. There is, however, one limiting situation that clearly highlights the crucial role of chromokinesins. Even in the hypothetic case that chromokinesins were not force sensitive ($f = 0$), the coupling between the instability associated to the kinetochore and the spatial informa-

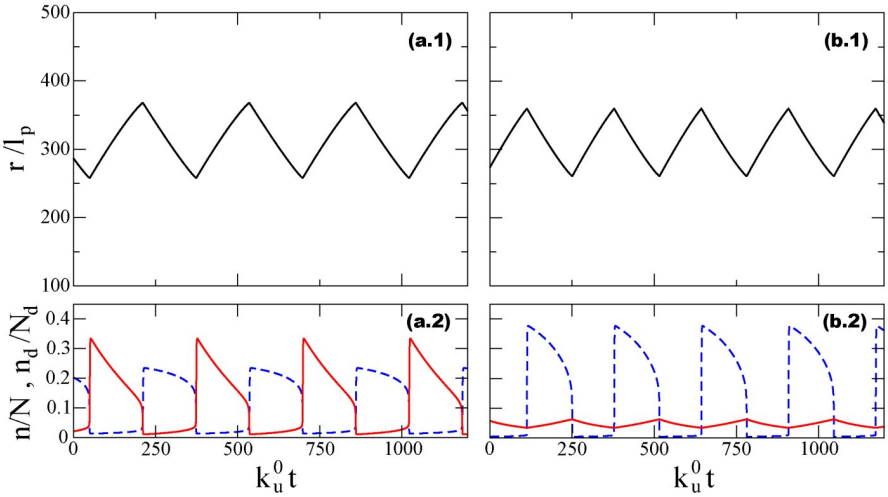

Fig. 8.12. Chromosome oscillations for a mechano-sensitive kinetochore. Time evolution of the chromosome position (a.1, b.1) and the number of bound chromokinesins (continuous line in a.2 and b.2) and bound dyneins (dashed line in a.2 and b.2) obtained by numerical integration of Eq. 8.17. Note that the number of dyneins during the away-from-the-pole phase is negligible, leading to a very small poleward force as the chromosome moves away from the pole and explaining the existence of neutral states. (a) Chromosome oscillations when both dyneins and chromokinesins are force sensitive, with $f_d = 2.0$ and $f = 2.0$. Parameters: $N f_s/N_d f_s^d = 1$, $V_0/V_0^d = 1$, $k_b^d/k_u^0 = 0.5$, $k_u^0/k_{u,0}^d = 1$, $\xi V_0/N f_s = 0.05$ and $N_{MT} k_b^0 S_{ch}/4\pi l_p^2 k_u^0 = 5\,10^4$. (b) Chromosome oscillations when chromokinesin motors are not force-sensitive ($f = 0$), and dyneins in the kinetochore are force-sensitive ($f_d = 3.0$). Although chromokinesins are insensitive to the force, their number oscillates because different positions in the aster lead to different attachment rates. Parameters: $N f_s/N_d f_s^d = 1$, $V_0/V_0^d = 1$, $k_b^d/k_u^0 = 1$, $k_u^0/k_{u,0}^d = 1$, $\xi V_0/N f_s = 0.001$ and $N_{MT} k_b^0 S_{ch}/4\pi l_p^2 k_u^0 = 4.5\,10^3$.

tion provided by the attachment kinetics of chromokinesins, also leads to similar chromosome oscillations (Fig. 8.12b). We emphasize that the essential ingredients for chromosome oscillations are the position-dependent chromokinesin attachment rate (providing spatial information via the microtubule density in the aster) and the collective force-dependent detachment kinetics of the motors, regardless whether the latter are chromokinesin, dynein, or both.

The results in this section show that chromokinesins are essential motors for chromosome positioning and motion during prometaphase and metaphase, as they allow the chromosome to sense its position in space through their position-dependent binding onto spindle microtubules.

8.3 Conclusions

In summary, we have presented a unifying framework in which chromosome movement, positioning and congression can be explained on the same basis. It is a self-contained description where chromosome motion and positioning arise from the interaction of chromokinesins on the chromosome arms with the astral microtubules in the mitotic spindle. This study demonstrates the importance of cooperativity between force-generating molecular motors in the production of large-scale chromosome movements. It shows that the dynamic nature of the forces produced by ensembles of motor proteins leads to unexpected chromosome behavior, such as the oscillations observed *in-vivo*. It also identifies the chromokinesin attachment kinetics on astral microtubules as the mechanism that provides positional information to the chromosome, and it illustrates the crucial role of the polar ejection force for chromosome congression. We propose that congression is due to the weakening of the polar ejection forces as the chromosome moves away from the pole, which is in turn due to a decrease of microtubule density away from the center of the microtubule aster. The results are consistent with the currently available experimental data, and provide a quantitative estimate for the *in vivo* chromokinesin velocity at vanishing force. We make further predictions that are experimentally testable, such as the existence of a minimal number of chromokinesins below which the chromosomes should not oscillate.

Our work highlights the essential role of chromokinesins in chromosome positioning and motion, but a better understanding of the kinetochore is also of capital importance to obtain a detailed description of chromosome movements during mitosis.

Acknowledgments

The work in this chapter has been done in close collaboration with Pierre Sens. We thank E.D. Salmon for his interesting remarks and T. Kapoor and K. Kruse for fruitful discussions.

9

Dynamic stability of spindle-like structures

The collective action of motor proteins is not only important for the chromosome movement and positioning but also for the assembly of the mitotic spindle. In this chapter we study the role of motor cooperativity in the stability of spindle structures, like the mitotic spindle.

Living cells display many structures that arise from the self-organization of polar filaments and motor proteins (Alberts et al., 2004). Several *in vitro* studies have shown that mixtures of kinesin motors and microtubules can spontaneously develop complex spatio-temporal patterns (Nedelec et al., 1997; Surrey et al., 2001). These self-organization processes are essential for eukaryotic cell division (Wittmann et al., 2001; Hyman and Karsenti, 1996) (see chapter 7). During mitosis, motor proteins organize microtubules in a bipolar structure, the mitotic spindle, which serves as a scaffold to transmit the necessary forces for chromosome segregation (Mitchison and Salmon, 2001) (Fig. 7.4). The spindle consists of two microtubule asters that overlap in the central region. The microtubules, with their minus-ends located at the aster poles, are crosslinked by different motor proteins (Sharp et al., 2000b; Wittmann et al., 2001) (Fig. 7.5b). Among all the motor proteins involved, one particular type of motors, the plus-ended bipolar kinesins (Eg5 or Klp61F of the BimC family), has been shown to be essential for the spindle stability. A decrease in their concentration below a certain threshold value causes the spindle collapse (Kapoor et al., 2000; Miyamoto et al., 2004), and their total inhibition prevents bipolar spindle formation (Goshima and Vale, 2003). In addition, Eg5 motors have been shown to drive the microtubule poleward flux (Miyamoto et al., 2004) and homolog motors to induce the formation of (interpolar) microtubule bundles (Sharp et al., 1999). Based on these experimental observations, we analyze in this chapter the role of bipolar motors in the stability of pre-assembled spindles.

Bipolar motors are composed of two connected units, each one composed of two motor domains. Both units can move simultaneously and independently on microtubules (Kapitein et al., 2005). These motors are able to crosslink microtubules (Sharp et al., 1999) and slide them with respect to each other when they are in an antiparallel configuration (Kapitein et al., 2005), like in the central region of the spindle (Figs. 7.5b, 9.1 and 9.2a,c). As a result, the motors produce an outward force

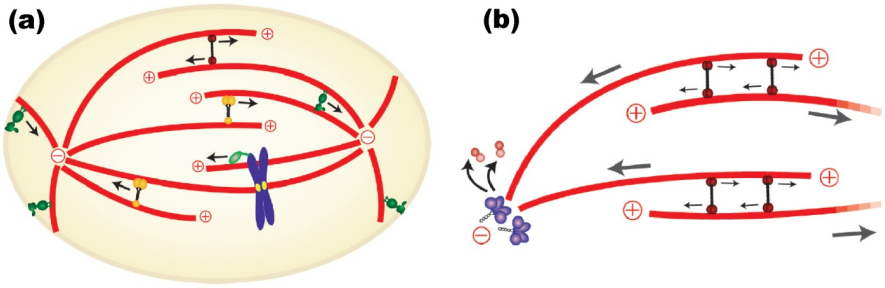

Fig. 9.1. (a) Sketch of the mitotic spindle showing the distinct activities of some motor proteins. Plus-end (red) and minus-end (yellow) directed crosslinking motors. Cytoplasmic dynein (green) on the cortex can pull on astral microtubules and focus the minus-ends of microtubules into the poles. Chromokinesins (light green) are bound to chromosomes and move toward the plus-ends of microtubules. (b) Microtubule poleward flux induced by the motion of plus-end directed crosslinking bipolar motors (Eg5 or Klp61F of the BimC family; red) and minus-end microtubule depolymerization induced by a pole-localized motor with depolymerizing activity (KinI, purple). (Modified from Ref. (Gadde and Heald, 2004)).

along the spindle axis and generate a microtubule flux toward the poles (Miyamoto et al., 2004). The forces involved in mitosis are in the nanoNewton range (Nicklas, 1983). Since individual Eg5 motors cannot exert forces larger than a few picoNewtons (Valentine et al., 2006), their collective action is required to ensure the stability of the mitotic spindle. At metaphase, this dynamic structure reaches a steady state with microtubules of constant length undergoing permanent treadmilling (Mitchison et al., 2004; Miyamoto et al., 2004), i.e. polymerizing at the plus end and depolymerizing at the minus end (Fig. 9.1b). We refer to this microtubule treadmilling as microtubule poleward flux because it is the common terminology in the mitosis research field.

The theoretical study of motors and microtubule mixtures has been recently addressed using continuum coarse grained descriptions (Kruse et al., 2004; Kruse and Julicher, 2000; Lee and Kardar, 2001), which have elucidated the basic self-organizing principles. Other theoretical works describe the system at a less coarse-grained level and consider the microtubules as rigid rods that can be moved and the action of the motors (Aranson and Tsimring, 2005; Liverpool and Marchetti, 2003). These descriptions are mainly focused in understanding the spatio-temporal patterns that arise from the self-organization in out-of-equilibrium systems. However, the coupling between the force-dependent motor kinetics and the local forces in self-organized structures has not been addressed. We have seen in the previous chapters that the coupling between local forces and motor kinetics is essential to understand some of the instabilities. In this chapter, we study the dynamic stability of antiparallel arrays of microtubules under the action of longitudinal forces, in the presence of bipolar molecular motors able to collectively hold the structure by stochastically crosslinking the filaments. We analyze the effects of the motor kinetics on the sta-

bility of the structure, and show that several phenomena observed in eukaryotic cell division can be understood on the same physical grounds.

9.1 Theoretical description

In order to understand the basic physical mechanisms controlling the stability of a spindle, we concentrate on a simplified geometry. We consider a pair of antiparallel microtubules (or an antiparallel microtubule bundle) of constant length, under the action of an inward force F (Fig. 9.2a). In the steady state, there is a region of length ℓ where the antiparallel filament array overlaps (overlapping region). The motors in this region can crosslink antiparallel microtubules and slide them in opposite directions, generating an outward force that balances the applied force F. We assume the antiparallel microtubule sliding to be the only mechanism generating the poleward microtubule flux, as observed experimentally (Miyamoto et al., 2004). The microtubule sliding generates a net microtubule flux toward the poles, which requires a permanent treadmilling of the microtubule lattice in order to maintain a steady state (Fig. 9.1b). Although the microtubule polymerization velocity at the plus-end and depolymerization at the minus-end are, in general, different than the sliding velocity generated by the motors, we assume that the polymerization rates adapt to the sliding velocity. This assumption is based on the observation that the spindle length and morphology do not significantly vary upon changes of the microtubule turnover velocity (Miyamoto et al., 2004). Indeed, there are several motor proteins with depolymerizing activity (e.g. KinI and MCAK) that associate to minus and plus ends of microtubules and could modify the dynamics of the microtubule ends (Fig. 9.1b) [1]. With this assumption concerning the adaptation of the microtubule polymerization/depolymerization dynamics to the sliding velocity induced by the motors in the overlapping region, the system can reach a steady state with microtubules of constant length and a net microtubule flux toward the poles.

Outside the overlapping region, there are two regions of length L (non-overlapping regions; see Fig. 9.2a) where motors cannot apply forces to sustain the spindle due to the parallel configuration of the microtubules. Since we concentrate on the spindle stability and do not address the mechanisms that determine L and ℓ, we consider them as given parameters.

Non-overlapping region

The motors in the non-overlapping region can be either bound to a microtubule or freely diffusing in the bulk (Fig. 9.2b). We assume a constant bulk motor density,

[1] One could also describe the dynamics of plus and minus microtubule ends and derive an equation for the spindle length. However, such a description would require a detailed knowledge of both the polymerization/depolymerization dynamics of spindle microtubules and the activity of the motors associated to the microtubule ends. Unfortunately, this knowledge is not currently available.

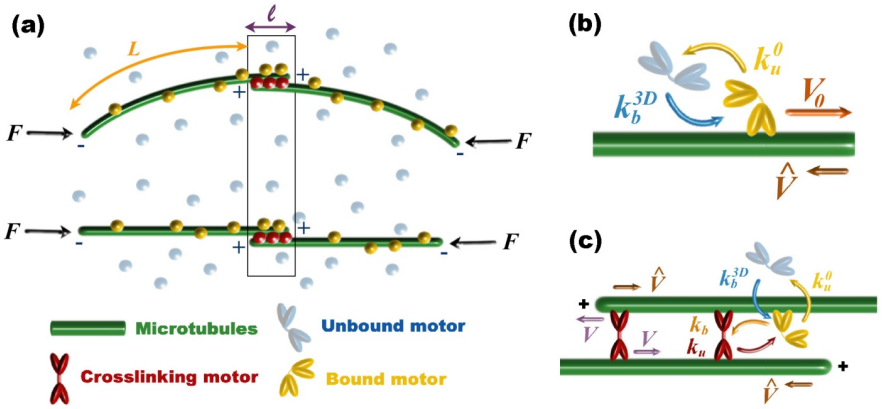

Fig. 9.2. (a) Antiparallel array of microtubules under the action of a longitudinal force F. Buckled and non-buckled arrays are shown. The minus and plus ends of microtubules are depicted as $-$ and $+$ respectively. Motors are represented by dots. In the non-overlapping region of length L there are no antiparallel filaments and the motors are not subject to any force. The motors in the overlapping region of length ℓ sustain the structure by crosslinking and sliding antiparallel filaments. (b-c) Possible kinetic events of a motor in the non-overlapping region (b) and in the overlapping region (c). The velocities V and $\hat{V}$ are the crosslinking motor velocity and the microtubule poleward velocity respectively.

ρ_{3D}, and consider the motors in the bulk to attach onto microtubules at a rate k_b^{3D}. Once a motor is bound to a microtubule, it moves convectively with an average velocity V_0 (motor velocity at vanishing load; see chapter 1) toward the plus-end of the microtubule and detaches at a rate k_u^0 (detachment rate at vanishing force). The approximation of constant bulk motor density is reasonable for typical spindle lengths ($L_s \sim 5\ \mu$m) as the motor bulk concentration equilibrates over time scales, of order $\sim L_s^2/D \simeq 1$ s ($D \sim 10\ \mu\text{m}^2\,\text{s}^{-1}$ being the diffusion constant of the motors in the bulk), shorter than the time scale of convective motor movement along microtubules, of order $\sim L_s/V_0 \simeq 100$ s, for typical values of the motor velocity ($V_0 \simeq 50\ \text{nm}\,\text{s}^{-1}$ for Eg5 motors (Kapitein et al., 2005; Valentine et al., 2006)). At the mean field level, the dynamics of the bound motor density, $\rho(s,t)$, can then be expressed as (Lipowsky et al., 2001; Parmeggiani et al., 2003)

$$\partial_t \rho(s,t) + \partial_s J(s,t) = -k_u^0 \rho(s,t) + k_b^{3D} \rho_{3D}\,, \tag{9.1}$$

where s is the position along the microtubule as measured from the microtubule minus ends and $J(s,t)$ is the flux of bound motors. For simplicity, we assume the bound motors to be in a low density phase[2] and write $J(s,t) = \rho(s,t)(V_0 - \hat{V})$ in the laboratory reference frame. The velocity $\hat{V}$ corresponds to the turnover velocity of microtubules toward the poles, induced by the sliding of antiparallel microtubules in the overlapping region (Fig. 9.2b,c).

[2] This is to say that the density of bound motors is low enough so that the interactions between them can be neglected.

Overlapping region

In the central overlapping region, bipolar motors can be either in a crosslinking state or in a bound state. In the former state both motor units are attached to a pair of antiparallel microtubules, sliding them in opposite directions and supporting a fraction of the total force F. As a result, the crosslinking motors move with a force-dependent velocity V (Fig. 9.2c). Based on recent experimental observations on Eg5 (Valentine et al., 2006), we use a linear-force velocity relation and write $V = V_0(1 - f_m/f_s)$, where f_m is the load applied on the motor and f_s its stall force. The value of the stall force has not yet been measured for Eg5 but it is estimated to be about $f_s \simeq 7pN$ (Valentine et al., 2006). We describe the collective dynamics of the motors holding the structure in the same way than in chapters 5 and 8. We consider a number n_c of independent crosslinking motors to equally share the total applied force, so that $f_m = F/n_c$. As the poleward microtubule movement is driven by the sliding of microtubules generated by these motors, we identify $\hat{V} = V$ (Fig. 9.2c). Each unit of a motor in the crosslinking state can detach at a force-dependent rate $k_u(f_m) = k_u^0 \exp(f_m b/K_B T)$ (Kramers theory (van Kampen, 2004); see chapter 1), where b is a length in the nanometer scale characterizing the activated process and $K_B T$ the thermal energy. After the detachment of one motor unit, the bipolar motor is only bound to one microtubule and unable to apply force. Such a motor can either detach the bound motor unit left at a rate k_u^0 and diffuse into the bulk, or re-attach the unbound motor unit at a rate k_b and become a crosslinking motor again. The motors in the bulk can also attach directly to the microtubules in the overlapping region at a rate k_b^{3D}.

The relevant variable being the number of motors sustaining the spindle, we neglect their spatial distribution in the overlapping region. Accordingly, the equations for the average number of crosslinking and bound motors, n_c and n_b respectively, read

$$\begin{aligned} \frac{dn_c}{dt} &= k_b n_b - k_u(n_c) n_c \,, \\ \frac{dn_b}{dt} &= 2J(L,t) + k_b^{3D} \rho_{3D} \ell + k_u(n_c) n_c - \left(k_u^0 + k_b\right) n_b \,, \end{aligned} \tag{9.2}$$

where $J(L,t)$ is the convective flux of bound motors reaching the overlapping region from each non-overlapping region, with L being the arclength of a microtubule from its pole to the overlapping region (Fig. 9.2a). The value of $J(L,t)$ is determined by the solution of Eq. 9.1. Specifying a zero-flux boundary condition at the poles, $J(s = 0,t) = 0$, the steady-state solution for the density field of bound motors is

$$\rho(s) = \frac{k_b^{3D} \rho_{3D}}{k_u^0} \left[1 - \exp\left(-s \frac{k_u^0}{V_0 - \hat{V}} \right) \right] . \tag{9.3}$$

Note that the velocity $\hat{V}$ is not a parameter; it is fixed by the coupled dynamics of the motors in the overlapping and non-overlapping regions. When the motor processivity length, $l_p \equiv V_0/k_u^0$, is smaller than the characteristic spindle length ($l_p \ll L$),

the flux $J(L,t)$ is fixed by the exchange of motors between the microtubule and the bulk (Langmuir kinetics) and determined by a constant bound motor density, $\rho = k_b^{3D}\rho_{3D}/k_u^0$, in the steady state. Indeed, typical values for L are about several microns long for most cell types, while Eg5 motors are not very processive ($l_p \simeq 67$ nm (Valentine et al., 2006; Kapitein et al., 2005)) [3]. In this case the dynamics of n_c and n_b are decoupled from the density of motors close to the poles. Therefore, for relevant values of the parameters ($l_p \ll L$) our results do not depend on the boundary condition for the bound motor density field at $s = 0$.

Equations for the motor dynamics

In order to understand which are the relevant parameters controlling the stability of the spindle, we scale the variables as follows. The quantities $\tilde{n}_c \equiv n_c/\tilde{F}$ and $\tilde{n}_b \equiv n_b/\tilde{F}$ are the normalized numbers of crosslinking and bound motors respectively. The natural scale for the number of motors is set by $\tilde{F} \equiv Fb/K_BT$, i.e. the ratio of the force F and the characteristic detachment force K_BT/b. The relevant dimensionless lengths are $\tilde{L} \equiv fL/l_p$ and $\tilde{\ell} \equiv f\ell/l_p$, where the parameter $f \equiv f_s b/K_BT$ quantifies the sensitivity of motor detachment to force. Asymmetry in motor attachment/detachment events at vanishing load is characterized by $\gamma \equiv k_b/k_u^0$ and the time is scaled with k_u^0 ($t \to \tau \equiv tk_u^0$). Finally, the most relevant parameter, δ, which accounts for the strength of the motor flux reaching the overlapping region, is defined as

$$\delta \equiv \frac{\rho_{3D} k_b^{3D} l_p}{\tilde{F} f k_u^0} \frac{k_b}{k_u^0} \,. \tag{9.4}$$

With these definitions, we rewrite Eq. 9.2 to get

$$\begin{aligned} \frac{d\tilde{n}_c}{d\tau} &= \gamma\tilde{n}_b - \exp\left(\frac{1}{\tilde{n}_c}\right)\tilde{n}_c \,, \\ \frac{d\tilde{n}_b}{d\tau} &= \frac{\delta}{\gamma}\left[\frac{2}{\tilde{n}_c}\left(1-\exp(-\tilde{L}\tilde{n}_c)\right)+\tilde{\ell}\right] + \exp\left(\frac{1}{\tilde{n}_c}\right)\tilde{n}_c - (1+\gamma)\tilde{n}_b \,. \end{aligned} \tag{9.5}$$

Although the original system (Eq. 9.2) depends on all motor kinetic parameters and the parameters characterizing the spindle morphology (L and ℓ), the scaled system depends only on four dimensionless parameters. The stability of the system will thus depend on these four combinations of the original parameters at most.

9.1.1 Stability of spindle-like structures

The existence of antiparallel microtubule arrays under an external load F is determined by the balance between motor attachment and detachment fluxes, as given by the steady state solutions (fixed points), $\{n_c^f, n_b^f\}$, of Eq. 9.5, which read

[3] New experiments on Eg5 motors indicate that the processivity length of Eg5 motors might be about a micron (T. Kapoor, personal communication).

$$\tilde{n}_b^f = \frac{\exp\left(1/\tilde{n}_c^f\right)\tilde{n}_c^f}{\gamma}\,, \qquad \delta = \frac{\exp\left(1/\tilde{n}_c^f\right)(\tilde{n}_c^f)^2}{2\left[1-\exp\left(-\tilde{L}\tilde{n}_c^f\right)\right]+\tilde{\ell}\tilde{n}_c^f}\,, \tag{9.6}$$

There always exists a critical value, δ_m, below which there are no solutions of Eq. 9.6. This situation corresponds to an attachment flux of crosslinking motors that can not balance their detachment flux, leading to the loss of all crosslinking motors and inducing the spindle collapse. Associated to the critical point δ_m, there is a minimum number of crosslinking motors, $\tilde{n}_c^m$, necessary to sustain a spindle, which is given implicitly by

$$1+\left[\tilde{n}_c^m\left(2+\tilde{L}\tilde{n}_c^m\right)-1\right]\exp\left(-\tilde{L}\tilde{n}_c^m\right) = \tilde{n}_c^m\left[2+\frac{\tilde{\ell}}{2}\left(\tilde{n}_c^m-1\right)\right]\,. \tag{9.7}$$

The actual value of δ_m is obtained by substituting $\tilde{n}_c^f$ in Eq. 9.6 by the solution of Eq. 9.7, so that

$$\delta_m = \frac{\exp\left(1/\tilde{n}_c^m\right)(\tilde{n}_c^m)^2}{2\left(1-\exp\left(-\tilde{L}\tilde{n}_c^m\right)\right)+\tilde{\ell}\tilde{n}_c^m}\,. \tag{9.8}$$

In order to determine the stability of the structures, we perform a linear stability analysis of the solutions of Eq. 9.6. We thus study the stability of the structure with respect to fluctuations in the number of motors sustaining it.

Stable spindles exist above a critical value δ_c. The precise expression for this critical point δ_c depends on the ratio, γ, between motor attachment/detachment rates at vanishing load. For values of k_b and k_u^0 such that

$$\gamma > \gamma_c \equiv \frac{\exp\left(1/\tilde{n}_c^m\right)\left(1-\tilde{n}_c^m\right)}{\tilde{n}_c^m} - 1\,, \tag{9.9}$$

the transition from an unstable array to a stable spindle corresponds to a saddle-node bifurcation at $\delta_c = \delta_m$, given by Eq.9.8. On the other hand, if $\gamma < \gamma_c$, this transition corresponds to a global bifurcation (saddle-connection [4]) at a value δ_c slightly larger than δ_m (Fig. 9.3a). In the limiting case where $L \gg l_p$ and $\ell \ll l_p$, the expressions for δ_m and γ_c reduce to

$$\delta_m = \frac{e^2}{8} \simeq 0.92\,, \qquad \gamma_c = e^2 - 1 \simeq 6.39\,. \tag{9.10}$$

As discussed above, in most relevant situations $L \gg l_p$, but ℓ may typically be larger than l_p. In this case, for $\tilde{\ell} \gtrsim 6.62$ the value of γ_c is negative, meaning that for any value of the ratio k_b/k_u^0, the value of δ_c is given by Eq. 9.8. Regardless of the value of γ, the same qualitative scenario is observed as δ is varied and we restrict the following discussion to the regime $\gamma > \gamma_c$ without loss of generality.

The threshold value, δ_c, depends only on the minimal number of motors $\tilde{n}_c^m$ (Eq. 9.8), which is a function of only $\tilde{L}$ and $\tilde{\ell}$. Thus, δ_c depends solely on $\tilde{L}$ and $\tilde{\ell}$. Typically $L \gg l_p$ and δ_c becomes independent of L (Fig. 9.3b), while ℓ modifies δ_c

[4] See Ref. (Guckenheimer and Holmes, 1990) for an introduction to bifurcation theory.

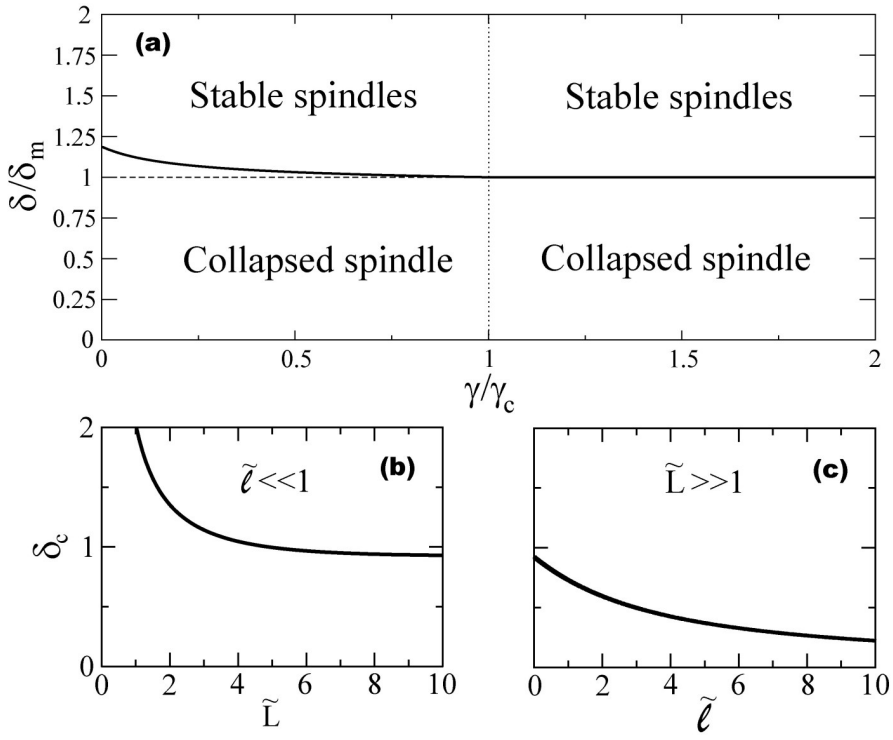

Fig. 9.3. (a) Stability of an antiparallel microtubule array as the parameters δ and γ are varied, for the limiting case where $L \gg l_p$ and $\ell \ll l_p$. The continuous line represents the critical value δ_c that specifies the transition between stable and collapsed spindles. Above γ_c, the transition takes place at $\delta_c = \delta_m$ (dashed line; Eq. 9.8). Below γ_c, the numerically computed value of δ_c is slightly larger than δ_m. In both cases, the same qualitative behavior is obtained as δ is varied. (b-c) Dependence of the critical value δ_c on $\tilde{L}$ and $\tilde{\ell}$ in the limiting cases where $\tilde{\ell} \ll 1$ (b) and $\tilde{L} \gg 1$ (c).

slightly (Fig. 9.3c). In this limit, the stability does not depend on the characteristic spindle length L and, as a consequence, the spindle morphology and its stability are decoupled. As the motor properties and the lengths L and ℓ are difficult to modify experimentally, δ appears as the natural control parameter for the spindle stability, since it depends both on the applied force, F, and the bulk motor density, ρ_{3D}.

9.1.2 Spindle morphology

The self-organization process of motors and microtubules can induce the formation of microtubule bundles (Nedelec et al., 1997). Such microtubule bundles have been observed during the cell division of several organisms (Sharp et al., 1999; Winey et al., 1995; Mastronarde et al., 1993), and bipolar motors (Klp61F) have been shown

to crosslink the microtubules forming the bundles (Sharp et al., 1999). In this section we derive the shape of an antiparallel microtubule array (interpolar microtubule bundle) from purely elastic arguments.

The bipolar spindle can be decomposed into two half arrays, each one being the mirror image of the other with respect to the mitotic plate. Due to this symmetry, we analyze only the shape of half array, which is composed of a non-overlapping region and one half of the overlapping region (Fig. 9.2a). In case the overlapping region is small compared to the non-overlapping one, the half array can be thought as a rigid rod with bending rigidity B, having one of its edges clamped due to the crosslinking motors in the overlapping region. The clamped edge is located at the mitotic plate and the array is perpendicular to this plane of symmetry. The shape of a rigid rod of bending rigidity B is unique for a given length L and applied force F (Landau and Lifshitz, 1986). In the stability analysis developed above we considered different values of F and L, so that it is, in principle, possible to identify the stable spindle shapes for a given set of parameters. However, as discussed above, for relevant values of the parameters ($L \gg l_p$) the stability of the spindle does not depend on L and there is a degeneracy of shapes for each value of the force F and bulk motor density ρ_{3D} (see section 9.2.1). Such degeneracy suggests that the mechanism fixing the spindle length can be different than the mechanism governing its stability.

Below the buckling force, $F_B = (\pi/2)^2 B/L^2$, the array is simply straight and perpendicular to the mitotic plate. For forces above F_B, the shape of the half array is given by the elastica solutions of a rod of length L with a clamped edge under an applied load F (Landau and Lifshitz, 1986). The shape of the buckled half array can be described by the angle, $\theta(s)$, of the local tangent to the array at the point s with the spindle axis (s being the arclength, measured from the clamped edge). The Euler-elastica equation for a bent rod,

$$B\frac{d^2\theta(s)}{ds^2} + F\sin\theta(s) = 0\,, \tag{9.11}$$

together with the boundary conditions, $\theta(s=0)=0$ and $\theta'(s=L)=0$ ($\theta' \equiv d\theta/ds$), fully specify the shape of the array, which is given implicitly by

$$s = \sqrt{\frac{B}{2F}}\int_0^{\theta(s)} d\theta' \frac{1}{\sqrt{\cos\theta' - \cos\theta_L}}\,. \tag{9.12}$$

$\theta_L \equiv \theta(s=L)$ is the angle of the array with the spindle axis at the spindle pole. For a given set of parameters $\{F,B,L\}$ satisfying $F \geq F_B$, there is a single value θ_L which depends only on the dimensionless combination $L\sqrt{F/B}$. The value of θ_L is an increasing function of $L\sqrt{F/B}$, so that for fixed F and B, the longer the array, the more deformed it is with respect to the straight shape (Fig. 9.4). The observed shapes for the mitotic spindle at metaphase are in qualitative accordance with our theoretical results (see discussion below).

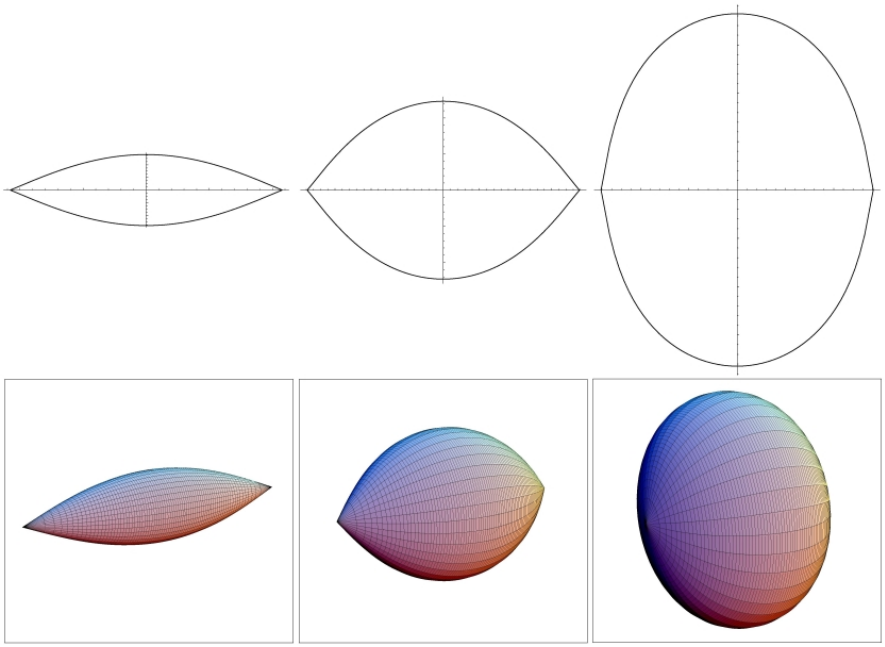

Fig. 9.4. Shape of a microtubule antiparallel array. (Top) Two dimensional representations of the buckled array for a force, $F > F_B$, and increasing array lengths (from left to right). (Bottom) Three dimensional representations of the whole spindle for the arrays on the top, obtained by rotation of the antiparallel array shape around the spindle axis.

9.2 Discussion

In this section we compare the theoretical results above to several experimental observations in eukaryotic cell division.

9.2.1 Collapse of the mitotic spindle

The existence of a critical value δ_c implies that for a microtubule array under the action of a load, F, there exists a minimal motor bulk concentration, ρ_{3D}^{min}, below which no stable spindles are found. Using the definition of δ (Eq. 9.4) and Eq. 9.8, this minimal motor density reads

$$\rho_{3D}^{min} = \frac{k_u^0}{k_b^{3D} l_p} \frac{f \delta_c}{\gamma} \tilde{F} \, . \tag{9.13}$$

When $\rho_{3D} > \rho_{3D}^{min}$ the stable spindle may be either straight or buckled depending on the value of the compressive force, F. For forces below (above) the buckling force F_B of the structure, the stable spindle is straight (buckled). In Fig. 9.5 we plot the structures that can be found as the bulk density of motors and the force applied on

the spindle are varied. Fig. 9.6 shows the experimentally observed collapse of a pre-assembled bipolar spindle after the addition of 50 μM of monastrol, an inhibitor of the bipolar kinesin Eg5. About 5min after the addition of monastrol, the spindle is still bipolar and displays its characteristic fusiform shape (to be compared to Fig.9.4-center). As monastrol progressively inhibits Eg5 motors, the bipolar spindle becomes more deformed (13.8min after monastrol injection; to be compared with Fig.9.4-right), and some interpolar microtubules lose their connection in the central region (16.3 – 19.0min after monastrol injection). At this point, the spindle is still bipolar, but it starts to break up and the microtubules that are no longer hold in the central region by Eg5 motors relax to their straight shape, converting progressively the spindle into a single microtubule aster (27.3min after monastrol injection). These experimental observations suggest the existence of a minimal bulk motor density to sustain the spindle.

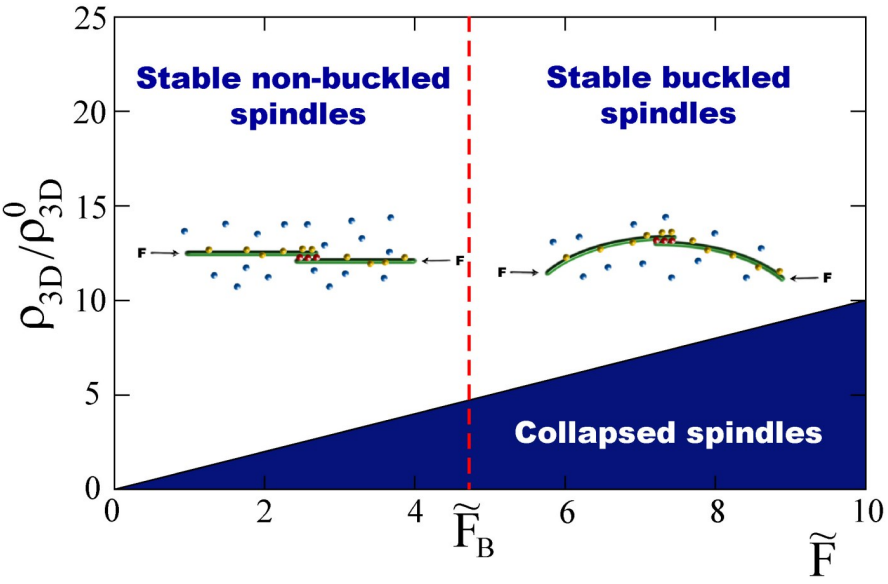

Fig. 9.5. Possible spindle structures as the bulk motor density ρ_{3D} and the force F are varied. The bulk density $\rho^0_{3D} \equiv \delta_c f (k^0_u)^3 / k^{3D}_b V_0 k_b$ sets the density units. Above $\rho^{min}_{3D}(F)$, buckled (straight) stable spindles exists for $F > F_B$ ($F < F_B$). Below $\rho^{min}_{3D}(F)$ no stable spindles exist. The insets show sketches of straight and buckled stable arrays.

More recently, it has been shown that the progressive inhibition of Eg5 motors leads to the collapse of the spindle at a finite bulk motor density (Miyamoto et al., 2004). Moreover, the total inhibition of homolog motors (Klp61F) has been shown to prevent bipolar spindle formation *in vivo* (Goshima and Vale, 2003), in accordance with our predictions.

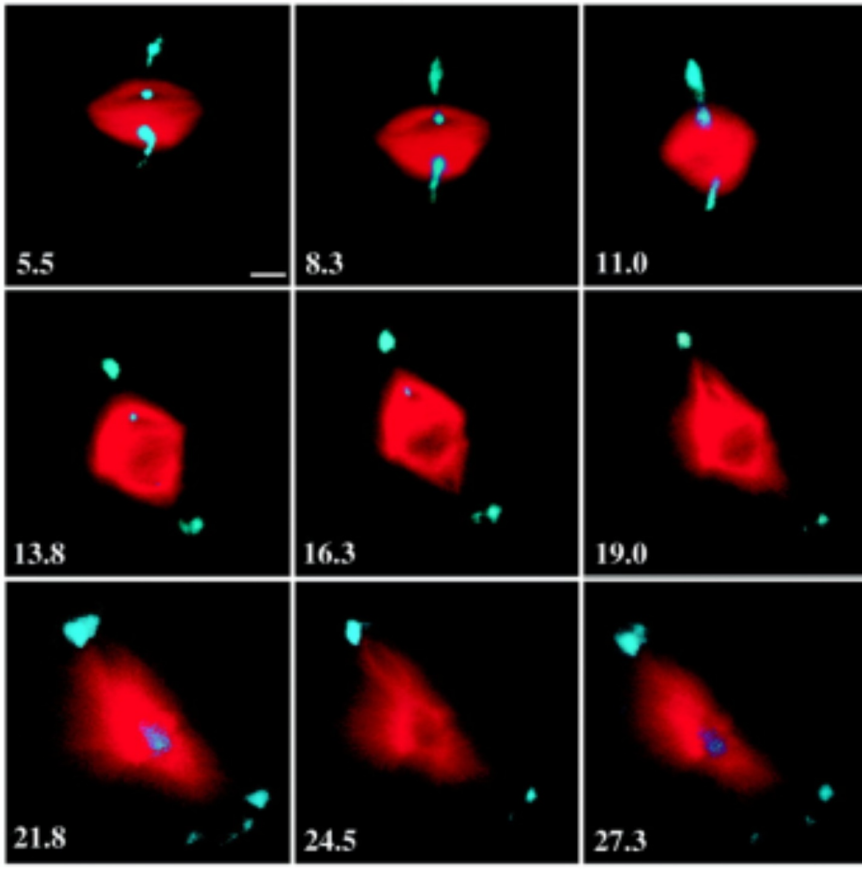

Fig. 9.6. Collapse of a pre-assembled bipolar spindle induced by monastrol, an inhibitor of Eg5 motors. 50 μM of monastrol were added to bipolar spindles assembled in *Xenopus* egg extract. The time (in minutes) after the addition of monastrol is indicated. Microtubules (red) and DNA (blue) are shown. The spindle is progressively deformed as monastrol inhibits Eg5 motors. After about 16min the spindle starts to break up and, after 27min it has collapsed into a single microtubule aster. Bar, 5 μm. (Adapted from Ref. (Kapoor et al., 2000)).

9.2.2 Interpolar microtubule bundles

Above the threshold density ρ_{3D}^{min}, there is a finite amount of crosslinking motors n_c collectively holding the spindle. In Fig. 9.7a we plot the stable solutions of Eq. 9.6 as a function of the bulk concentration of motors. Increasing values of ρ_{3D} and ℓ leads to larger motor attachment fluxes, that result in a larger amount of crosslinking motors. For a living cell in native conditions, the interpolar microtubules in the spindle are typically buckled (Mitchison and Salmon, 2001) (Figs. 9.6-upper left and 9.8c). Therefore, the force applied on the microtubules is of order F_B which, for single microtubules of 5 μm in length, is about 1 pN. Using this value for the force F, the

number of crosslinking motors leading to a stable antiparallel array turns out to be very small ($n_c \simeq 2$). In this case fluctuations would dominate and, although stable arrays could be transiently formed, their lifetime would be too short (on the time scale of motor detachment). Since the buckling force of a microtubule bundle can be at least one order of magnitude larger[5], stable interpolar microtubule bundles require tenths of crosslinking motors and provide robust spindles with lifetimes over the time scale of the division process. Indeed, the time to break up the antiparallel array is given by the time needed to detach all n_c crosslinking motors holding the array in the overlapping region. For a large enough number of motors, this time increases essentially exponentially with the number of motors $n_b + n_c$ (Klumpp and Lipowsky, 2005).

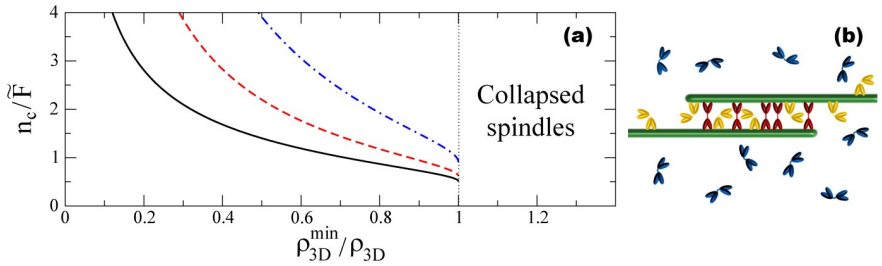

Fig. 9.7. (a) Steady state analytical solutions for the number of crosslinking motors as a function of the bulk density of motors. (b) Sketch of the overlapping region showing a collection of crosslinking motors (red) holding the spindle.

Interpolar microtubule bundles are indeed observed in several organisms during cell division (Mastronarde et al., 1993; Winey et al., 1995; Sharp et al., 1999) (Fig.9.8). Although we do not address here the mechanism by which interpolar microtubule bundles are formed, our analysis predicts that their existence is essential for the stability of the spindle. Indeed, microtubules (or any filament) can only resist compressive forces below or about their buckling force. Interestingly, it has been reported that microtubule bundles are not observed in small mitotic spindles (Winey et al., 1995), for which the microtubule length is about $L \simeq 0.3\ \mu$m, corresponding to buckling forces of several hundreds of picoNewtons.

[5] Assuming the bending rigidity of a microtubule bundle to scale linearly with the number of microtubules in the bundle, the buckling force of an interpolar microtubule bundle composed of ~ 10 microtubules is about tenths of picoNewtons. The approximation of a linear increase of the bending rigidity with the number of microtubules in the bundle is reasonable if the detachment/attachment time scales of the motors crosslinking the microtubules are short compared to the time scale of deformation of the bundle. In this case, there is no shear stress between the microtubules forming the bundle.

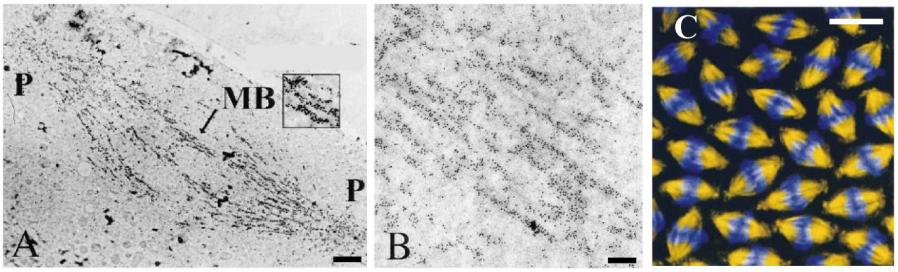

Fig. 9.8. (A-B) Electron microscopy images of a Drosophila spindle at metaphase. 10-nm gold particles are attached to Klp61F motors (Eg5 homologs) that appear as dark dots in the image. The regions with higher density of Klp61F reveal the interpolar microtubule bundles. (A) Klp61F staining pattern on the whole spindle (P, spindle poles; MB, interpolar microtubule bundle). The inset shows a higher magnification of an interpolar microtubule bundle (MB), indicated by an arrow. (B) Higher magnification of the spindle mid-zone. (C) Metaphase spindles in early Drosophila embryos. Confocal images of embryos where tubulin (yellow) and DNA (blue) are stained. Microtubule bundles are more visible in the central region, where the overlap of microtubules and DNA appears white. Bars: (A) 1.3 μm, (B) 320 nm, (C) 7.6 μm. (Modified from Ref. (Sharp et al., 1999)).

9.2.3 Poleward microtubule flux

The speed of the microtubule flux toward the poles is given by the microtubule sliding velocity, $\hat{V}$, induced by the crosslinking motors in the overlapping region, so that $\hat{V} = V$. Thus, the microtubule velocity toward the poles reads

$$\hat{V} = V_0 \left(1 - \frac{F}{n_c f_s}\right) , \tag{9.14}$$

where n_c corresponds to the stable solution for the number of crosslinking motors (Fig. 9.7). In Fig. 9.9a we represent the sliding velocity as a function of ρ_{3D}, for different values of $\tilde{\ell}$. It decreases from its maximal value V_0 as the bulk motor density is decreased, and it is typically finite for the minimal density ρ_{3D}^{min} at which the spindle collapses, as observed experimentally (Miyamoto et al., 2004). At high motor concentrations $\rho_{3D} \gg \rho_{3D}^{min}$, the crosslinking motors move nearly at their maximal velocity, V_0, and the microtubules move poleward at this velocity consequently. As the motors in the non-overlapping regions move at velocity V_0 with respect to the microtubules in the spindle (Fig. 9.2b), they appear static in the laboratory reference frame. This apparent motor stillness has indeed been observed experimentally (Kapoor and Mitchison, 2001). Our analysis predicts that decreasing the bulk motor density ρ_{3D} would allow the observation of motor movement in the spindle. This observation would provide further insight on the understanding of the mitotic spindle structure.

In Ref. (Miyamoto et al., 2004) the authors use (S)-quinazolinone, an Eg5 inhibitor, to progressively reduce the concentration of Eg5 motors and analyze the effects of such reduction on the spindle dynamics. In Fig. 9.9b we show the average microtubule poleward velocity as a function of the drug concentration. The velocity

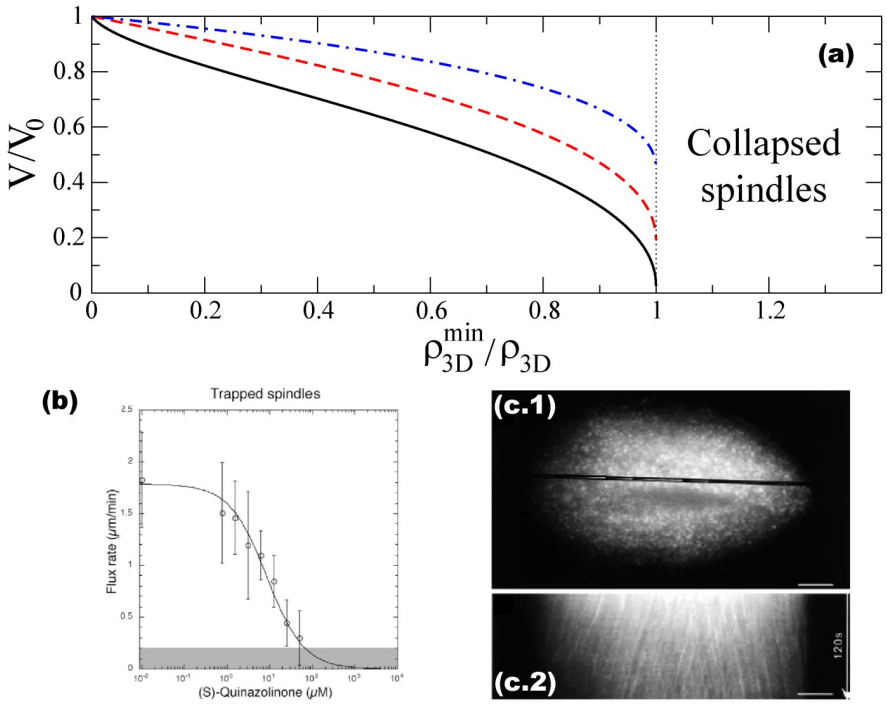

Fig. 9.9. (a) Steady state analytical solutions for the velocity of crosslinking motors (or the microtubule poleward flux velocity equivalently) as a function of the bulk motor density. (b) Effect of a progressive inhibition of Eg5 motors with (S)-quinazolinone. The velocity of microtubules toward the poles is plot as a function of the drug concentration. (Modified from Ref. (Miyamoto et al., 2004)). (c.1) Fluorescence speckle microscopy image of a spindle assembled in *Xenopus* egg extracts, where the tubulin is labeled at low concentrations, giving the spindle this sparkling appearance. The highlighted region across the spindle is used to prepare the space-time plot in (c.2). (c.2) Space-time plot of tubulin speckles. The speckle trajectories characterized by an angle reveal the poleward microtubule movement. Bars, 5 μm. (Modified from Ref. (Kapoor and Mitchison, 2001)).

at vanishing quantities of Eg5-inhibitor saturates to about 2 μm/min, which is about the velocity of Eg5 motors under vanishing load (Miyamoto et al., 2004; Valentine et al., 2006). As the drug concentration is increased, the microtubule poleward velocity decreases until the point where the poleward microtubule flux stalls. However, these experiments are done using trapped spindles in order to avoid the spindle collapse at a finite drug concentration. For spindles in native conditions the microtubule poleward velocity is finite at the motor concentration that leads to the spindle collapse. Unfortunately, the experimentally measured values for the poleward microtubule flux cannot be directly compared to our theoretical results (Fig. 9.9a) because the relation between the drug concentration and the actual concentration of Eg5 motors in the bulk is likely to be non-linear. The only features which are insensitive to

this non-linear scaling are the saturation value of the velocity at large motor concentrations and the value of the velocity at the point where the spindle collapses. Both features are in good qualitative agreement with our results.

9.3 Conclusions

The present approach highlights the importance of force-dependent motor kinetics on the self-organization of microtubules and motors. In these structures there exist internal stresses that arise from the active character of the motors, which crosslink and slide filaments to one another. The stresses that the motors themselves develop affect their own kinetic properties and, in particular, their detachment probability per unit time. The influence of the internal stresses on the motor kinetics may impose restrictive limits to the overall stability of self-organized structures. We have shown in this chapter that this force-feedback is essential to understand the stability of spindle-like structures.

Our study is based on the self-organization of motors and microtubules as the underlying mechanism for spindle assembly. There are however two competing ideas concerning the origin of spindle assembly. One is the self-organization process just mentioned and the other postulates the existence of a spindle matrix, made of an hypothetic unknown protein. Some indirect evidences have been proposed in favor of the spindle matrix hypothesis. In particular, it has been argued that the apparent motor stillness in the spindle suggests the existence of a static spindle matrix, to which the bipolar motors are attached (Kapoor and Mitchison, 2001). The microtubules could, according to this hypothesis, be moved by the motors attached to the matrix. We have given above a different explanation for these observations which is totally compatible with the self-organization of motors and microtubules. Therefore, the observation of motor motion upon a decrease of motor density, as predicted here, would provide strong evidence for the self-organization of motors and microtubules as the underlying principle of mitotic spindle assembly.

The analysis developed in this chapter constitutes a simple framework through which several observations in mitosis, namely the spindle collapse, the microtubule poleward flux, the static appearance of motors in the spindle, and the necessity of microtubule bundles, can be explained on a common physical basis. However, spindle morphogenesis and dynamics is far more complex that the scheme presented here. There are many other proteins that influence the organization processes between motors and microtubules and, in particular, the chromosomes may also play a very important and interesting role.

Acknowledgments

The work described in this chapter has been done in collaboration with Ignacio Pagonabarraga. We thank T. Kapoor, F. Nédélec and K. Kruse for fruitful discussions.

10

General conclusions and perspectives

In this work we have studied how molecular force generators cooperate to develop the forces that drive some cellular movements. All the motility processes addressed have the common feature that ensembles of force generators work cooperatively. Although the coupling between the elementary force generators is distinct in the different cases addressed, they show clear similarities in their dynamics.

We have first addressed the motion of oil drops propelled by an actin comet tail, which closely mimics the propulsion mechanism of the bacteria *Listeria*. The growth of a filamentous actin network on the drop surface generates the necessary forces for motion. The polymerization of an actin filament against an obstacle cannot generate a substantial force if the filament is not somehow held. The crosslinked filaments in an actin network are held together, enabling individual filaments to apply forces upon growth. It is the cooperative action of many growing actin filaments, held together by their entangled network structure, that generates the necessary forces to induce the motion. We have adopted a mesoscopic approach in which the coupling of the growth dynamics of distant filaments is effectively taken into account in the actin gel elasticity. The results of our theoretical analysis are in quantitative agreement with the experimental observations of Hakim Boukellal (Institut Curie). In particular, our study shows that the growth of the actin network generates stresses that push and squeeze the drop along the sides and pull the drop backward at the rear. There are many other actin-based motility processes that may be characterized by a similar stress distribution. The process of phagocytosis is also driven by the growth of an actin network around the object being engulfed (Aderem and Underhill, 1999; Champion and Mitragotri, 2006). Our results could be helpful to understand phagocytic movements, as the pulling stresses may promote the internalization of particles in cells.

Our results concerning the motion of the actin polymerization promoters on the surface of the drop show that the dynamics of the nucleators are essential to understand the propulsion mechanism. It is thus possible that the motion of the polymerization promoters at the leading edge of a crawling cell plays an important role in this complex motility process. Indeed, in adhesion problems, the motion of stickers is crucial to understand the dynamics of the process (Brochard-Wyart and de Gennes,

2002; de Gennes et al., 2003). It would be interesting to perform biomimetic experiments to understand at quantitative level the coupled dynamics of actin polymerization promoters on a fluid interface and the growth of an actin network.

There are many aspects of actin-based motility that remain to be understood. The force generation by individual actin filaments has not yet been well characterized and it is involved in many motility processes. At larger scales, the cooperative dynamics of the entangled actin filaments forming an actin network which grows against an opposing force has not been studied in details neither. It would be interesting to connect our mesoscopic description to more microscopic approaches through a theoretical description at intermediate length scales.

In the second part of the work we have studied several aspects of intracellular traffic. We have first analyzed in details the physics of membrane tube extraction by motors proteins. Although membrane tubes are observed in eukaryotic cells, where they are thought to be involved in transport processes, the mechanism enabling such transport remains unknown. It has been proposed that a gradient of surface tension along a membrane tube, which is set up by connecting compartments with different surface tension, induces a fluid flow inside the tube that drives the transport of material between the compartments (Upadhyaya and Sheetz, 2004). However, there is no direct evidence in favor of this transport mechanism in living cells. It would thus be interesting to study the functionality of membrane tubes *in vivo*, like those composing the endoplasmic reticulum or connecting different organelles.

We have analytically determined the conditions leading to tube extraction and showed that, for a given surface tension of the vesicle, there exists a threshold density of motors on the vesicle below which no tubes can be pulled. Our findings show that the threshold is a direct consequence of the collective force-dependent kinetics of motor proteins. Moreover, we obtained the density profile of motors along the growing tube and estimated the number of motors required to pull it. The motors accumulate dynamically at the tip of a growing tube and, typically, just a few motors ($\sim$ 5-10) work together to extract it. We have shown that the attachment/detachment kinetics of motors sets a small average number of working motors per protofilament at the tube tip. This finding establishes limits on the forces that motors can develop when pulling a membrane tube. It is possible that living cells use other proteins to create motor aggregates that would rigidly couple the motors and allow the generation of larger forces. Our theoretical results are in good quantitative agreement with the experimental observations by Cécile Leduc (Institut Curie). From the comparison between theory and experiments, we have determined the binding rate of kinesins onto microtubules in a geometry close to the *in-vivo* situation.

A more detailed analysis, accounting for the increase of vesicle tension during tube growth, has shown that there exist two possible dynamical regimes. In a stable regime, the tube stalls at a certain length and a micron-sized high density phase of motors progressively develops upstream from the tube tip. There also exists an oscillatory regime where the tube oscillates between minimal and maximal lengths. We have shown that these highly non-linear oscillations have their origin in the collective force-dependent kinetics of the molecular motors pulling the tube. The different dy-

namical regimes described have been observed experimentally by C. Leduc, showing the existence of collective oscillations of processive molecular motors.

We have also studied the collective dynamics of interacting motors pulling on fluid membranes. Both the transport of small vesicles and the extension of membrane tubes in living cells constitute examples of this process. The results obtained differ significantly from simple mean field predictions and from the collective behavior observed for rigidly or elastically coupled motors. Our findings suggest that molecular motors pulling a membrane tube should simultaneously use several protofilaments in order to develop the typical forces required to pull it. This result could also be relevant for motors pulling on transport vesicles in living cells. It would be interesting to test our results using *in vitro* biomimetic experiments where motors carry small vesicles under the action of an applied force. The comparison of our theoretical results to experiments consisting of a bead exerting a force on a single motor moving in front of several other motors, would allow the determination of the interactions between motors.

In living cells, however, transport vesicles have typically motors of different directionalities attached on their surface (Welte, 2004). These vesicles display abrupt changes in direction which are thought to be a consequence of the competing motor activities. It would be interesting to study, both theoretically and experimentally, the dynamics of vesicles being transported collectively by motors with different directionalities. The collective force-dependent kinetics of motors may play a crucial role in the observed changes in direction of the vesicle. It is likely that the coordination of different motor activities results just from their coupled dynamics.

Another important aspect of intracellular transport is the traffic of motor proteins in crowded conditions. We have also analyzed the traffic of motors at large scales, both analytically and numerically (Monte Carlo simulations). Several nonlinear phenomena arise from the mutual motor interactions. In particular, traffic jams develop spontaneously due to the noisy character of the motor kinetics. We predict the appearance of large and long-lived traffic jams, which can move either upstream or downstream, in presence of attractive interactions between the motors that affect their attachment/detachment kinetics. It is possible that the spontaneous formation of traffic jams have important consequences for the long range traffic in the crowded conditions of the cell. Several neurodegenerative diseases are thought to be caused by anomalies in the traffic along axons (Aridor and Hannan, 2000; Aridor and Hannan, 2002). It would be interesting to explore whether the nonlinear phenomena in traffic, due to mutual motor interactions, is at the origin of some of these diseases.

The collective force generation by motor proteins is also essential in cell division. In the last part of our work (part III), we have studied both the movement of chromosomes during mitosis and the stability of spindle-like structures, like the mitotic spindle during metaphase. We have shown that the oscillatory motion of chromosomes results from the interplay between the dynamic instability associated to the collective force-dependent detachment of chromokinesins and the morphology of the spindle, which provides a position-dependent substrate for motor binding. Our analysis also identifies motor binding onto spindle microtubules as the mechanism that allows the chromosome to sense its position in the cell.

It would be interesting to perform experiments in which chromokinesins would be progressively inhibited, in order to test our predictions concerning the transition from oscillatory to stable states, and gain insight on the nature of the polar ejection force. Micromanipulation experiments of single chromosomes would allow to test the effect of external forces on the motion and positioning of the chromosome, and could also provide important hints to understand the forces involved in the division process. *In vitro* biomimetic experiments in which chromosomes were replaced by solid beads covered by chromatin, combined with micromanipulation techniques, would provide an important information to understand several characteristics the polar ejection force.

The relation between the forces driving chromosome motion in mitosis and the biochemical signaling that regulates the division process is also of capital importance. There is growing evidence that the forces involved in chromosome movement can regulate or control the onset of Anaphase (Nicklas, 1997; Pinsky and Biggins, 2005). In particular, the spindle checkpoint, which ensures that sister chromatids separate apart only when all chromosomes are properly positioned at the metaphase plate, is thought to be controlled by the tension between sister kinetochores (Nicklas et al., 1998; Logarinho et al., 2004). It would be interesting to identify the molecular force-sensitive elements able to influence the biochemical signaling and describe the coupled dynamics of chromosomes and biochemical events.

Besides chromosome movement, we have also analyzed the stability of spindle-like structures held collectively by motor proteins. Our results show that the spindle collapse is due to the collective force-dependent detachment kinetics of bipolar motors. Although these results have not been directly tested experimentally, they agree at qualitative level with several observations in eukaryotic cell division. In particular, it has been shown that the mitotic spindle collapses if the concentration of bipolar motors is reduced below a certain threshold value (Miyamoto et al., 2004). Our study of the spindle dynamics does not address the mechanisms that fix the spindle length and morphology. It would be interesting to extend this description and study spindle morphology in more details.

The study of the self-organization processes at the origin of spindle assembly is also of crucial to understand cell division. Our approach highlights the importance of force-dependent motor kinetics on the self-organization of microtubules and motors. In these structures there exist internal stresses that arise from the active character of the motors, which crosslink and slide filaments to one another. The stresses that the motors themselves develop affect their own kinetic properties and, in particular, their detachment probability per unit time. The influence of the internal stresses on the motor kinetics may impose restrictive limits to the overall stability of self-organized structures. It would be interesting to study the self-organization of motors and polar filaments accounting for the force-dependent kinetics of the elementary force generators.

We have shown that similar dynamic instabilities exist in all the cases studied and that these instabilities are a consequence of the collective force-dependent kinetics of the force generators. The saltatory motion of the bacterium *Listeria*, the oscillations in membrane tube extraction, the oscillatory motion of chromosomes during

mitosis, and even the threshold in tube extraction and the threshold characterizing the collapse of the mitotic spindle, have all a very similar origin. There exist very many situations in living cells in which motor proteins work in large groups in order to develop the necessary forces to induce motion at cellular scales. It is thus likely that similar instabilities exist in these situations. For instance, the flagellar and ciliary beating are both driven by ensembles of dynein motors that collectively induce the sliding of microtubules, which leads to the observed beating patterns. It is probable that the oscillatory instability is due to the collective force-dependent detachment kinetics of the motors. Similar behaviors have been observed in other systems involving the collective resistance of molecular bonds to applied forces (Evans, 2001; Evans and Ritchie, 1997; Brochard-Wyart and de Gennes, 2003; Brochard-Wyart and de Gennes, 2002), like in cell adhesion. There are also many physical systems characterized by non-linear friction forces that may display similar instabilities (Urbakh et al., 2004). In biological systems, however, the forces that affect the kinetics of the force generators are those developed by the force generators themselves and, therefore, the instabilities are intrinsic of their collective dynamics. Altogether, our results suggest that several aspects of these motility processes can be understood on a common framework.

The mechanics of cellular movements is important on its own, but the biochemical signaling that regulates the activity of elementary force generators cannot be overlooked. It is clear that biochemical signals can act on the force generators and modify their dynamics. However, there is increasing evidence that the forces driving cellular movements influence, in turn, the biochemical signals and can even modify gene expression (Farge, 2003; Brouzes and Farge, 2004; Nicklas, 1997). This force-feedback couples gene expression and/or the biochemical networks with the mechanical events in living cells. It is thus possible that the coupled dynamics (self-organization) of biochemical networks and the force generating processes are at the origin of some cellular behaviors.

A

Resum en català

Els mecanismes de propulsió responsables dels moviments cel·lulars són potser les obres d'enginyeria més impressionants de la natura. Tot i així, són simplement interaccions entre molècules les responsables d'aquests moviments tan complexes. La pregunta és doncs com s'autoorganitzen les molècules per dur a terme aquestes tasques que requereixen un alt grau de coordinació. Malgrat que la comprensió global del comportament cel·lular està encara lluny del nostre abast, l'estudi d'aspectes particulars dels sistemes biològics pot contribuir a la seva comprensió.

Els biòlegs han fet molt esforços per caracteritzar les proteïnes involucrades en els moviments cel·lulars, per identificar les seves interaccions i per entendre la seva regulació. Aquesta informació és molt important i ha permès explicar diversos aspectes del moviment cel·lular. El descobriment de proteïnes capaces de generar forces a escales moleculars, anomenades proteïnes motores, va aportar una informació essencial per a la comprensió dels moviments cel·lulars. La força creada a nivell molecular per una proteïna és massa petita per tal d'induir el moviment cel·lular per sí sola. Probablement l'exemple més clar és el funcionament dels músculs. Les forces que nosaltres som capaços de crear són aproximadament 12 ordres de magnitud més grans que les forces generades a l'escala molecular. Això és possible perquè les forces necessàries per a la contracció muscular estan generades col·lectivament per grans grups de proteïnes motores. Malgrat que cada una d'aquestes proteïnes desenvolupa una força petita (de l'ordre d'alguns picoNewtons), la suma de totes les contribucions individuals pot generar forces molt més grans. A nivell de la cèl·lula té lloc un fenòmen similar. Les forces necessàries per induir el moviment de la cèl·lula i/o els moviments intracel·lulars són majors que les originades a nivell molecular. Per aquesta raó, l'acció col·lectiva de generadors de força moleculars és essencial per comprendre els moviments cel·lulars.

En aquest treball estudiem a nivell teòric diversos casos de moviments cel·lulars i comparem quantitativament, quan això és possible, els nostres resultats a les observacions experimentals. El treball està dividit en tres parts: primer estudiem el moviments de gotes d'oli propulsades per un cometa d'actina, les quals mimetitzen el mecanisme de propulsió de bacteris com ara *Listeria*. La segona part està dedicada a diversos aspectes del transport intracel·lular. Estudiem el mecanisme físic

pel qual proteïnes motores estiren nanotubs de membrana, el tràfic a gran escala de proteïnes motores i també la generació col·lectiva de força de motors moleculars que estiren membranes fluïdes. En la última part, estudiem el moviment de cromosomes i l'estabilitat del fus mitòtic en la divisió cel·lular eucariota.

El nostre objectiu és entendre com l'acció col·lectiva de generadors de força moleculars dóna lloc a aquests moviments cel·lulars. Com demostrem en el nostre estudi, la combinació de la dinàmica col·lectiva i la cinètica del generadors de força elementals, la qual depèn fortament de la força que ells mateixos generen, dóna lloc a inestabilitats dinàmiques. Així doncs, la dinàmica col·lectiva dels generadors elementals de força és essencial per entendre diversos aspectes dels moviments cel·lulars.

A.1 Generació de força a escala molecular

Tots els moviments cel·lulars tenen el seu origen a l'escala molecular. Existeixen diferents mecanismes que permeten la generació de forces a nivell molecular, la gran majoria dels quals requereixen l'energia provinent de la hidròlisi de nucleòtids, com ara ATP ("Adenosine-TriPhosphate") o GTP ("Guanosine-TriPhosphate").

La major part dels moviments cel·lulars i intracel·lulars involucren filaments de proteïnes i/o proteïnes motores (motors moleculars). Hi ha dos tipus de filaments de proteïnes capaços de generar forces per ells mateixos en el seu procés de creixement. Els filaments d'actina i els microtúbuls són biopolímers amb propietats bioquímiques i físiques diferents que els permeten dur a terme tasques diferents en les cèl·lules. Aquests filaments estan composats d'unitats bàsiques que s'agreguen formant l'estructura unidimensional del filament. Els filaments creixen per l'addició de monòmers a les seves extremitats. És el mateix procés de creixement dels filaments el que genera forces. Quan un filament creix contra un obstable, l'addició de nous monòmers provoca la generació d'esforços interns al filament que empenyen l'obstacle. Les forces generades per la polimerització (creixement) del filament són d'alguns picoNewtons, molt inferiors a les típiques forces a escala cel·lular. Per tal de generar grans forces, els filaments d'actina s'entrellacen mitjançant proteïnes accesòries i formen denses xarxes de filaments. Els filaments de la xarxa poden actuar col·lectivament per generar grans forces i induir moviment.

Malgrat que la polimerització col·lectiva de filaments permet generar forces considerables a l'escala cel·lular, existeix un altre mecanisme que juga un paper importantíssim en la generació de forces. Els motors moleculars són proteïnes capaces de convertir l'energia provinent de la hidròlisi de l'ATP en treball mecànic. Aquestes proteïnes es mouen al llarg de filaments (microtúbuls o filaments d'actina) i generen forces que permeten una bona part dels moviments intracel·lulars i cel·luars. Mentre que les kinesines i dineïnes es mouen al llarg de microtúbuls, les miosines s'associen als filaments d'actina. Quan un motor molecular s'enganxa a l'objecte que ha de transportar i es mou al llarg del filament, li aplica forces d'alguns picoNewtons. Experiments amb motors moleculars individuals han demostrat que aquests típicament generen forces d'alguns picoNewtons. Com hem comentat anteriorment, les forces

a escala cel·lular són molt més grans. Per tal de generar les forces necessàries per induir els moviments cel·lulars, els motors moleculars treballen en grup.

A.2 Moviment de gotes per propulsió basada en actina

Diversos bacteris, com *Listeria*, *Shigella* o *Rickettsia*, desenvolupen un cometa d'actina per generar les forces necessàries que permeten el seu moviment dins la cèl·lula infectada. Els filaments d'actina són polimeritzats a la superfície del bacteri i, mitjançant diverses proteïnes associades a l'actina, creen una densa xarxa de filaments. A escales mesoscòpiques, molt més grans que les escales on es dóna la polimerització i l'entrellaçament dels filaments, aquesta xarxa de filaments d'actina es comporta com un gel elàstic. Quan els filaments d'actina polimeritzen en la superfície del bacteri, una nova capa de gel es crea entre el bacteri i el gel prèviament polimeritzat. El propi creixement del gel genera esforços elàstics en el gel. Així doncs, l'energia provinent de la polimerització del gel, s'emmagatzema de manera transitòria com a energia elàstica del gel. El moviment del bacteri fa que el gel comprimit relaxi en la part posterior del bacteri, alliberant així l'energia elàstica emmagatzemada i generant la força necessària per a la propulsió del bacteri.

Les forces generades en aquest procés són molt més grans que les típiques forces en el món intracel·lular. Com a conseqüència, el bacteri es mou dins la cèl·lula infectada com si es tractés de l'espai lliure, sense que hi hagi cap força capaç de parar el seu moviment letal. És només quan deforma considerablement la membrana cel·lular, que la oposició al seu moviment és important. Tot i així, el bacteri indueix la deformació necessària per tal de ser fagocitat per les cèl·lules adjacents i propagar-se dins el teixit cel·lular.

El bacteri *Listeria* és responsable de diverses malalties, com per exemple la meningitis. Així doncs, la comprensió del mecanisme físic de propulsió és important per tal d'intentar entendre millor com combatre la seva infecció. Malgrat aquesta és una raó prou important per estudiar aquest bacteri, hi ha raons també importants a nivell de recerca bàsica. Les cèl·lules eucariotes es mouen mitjançant un mecanisme de propulsió molt complexe, anomenat en anglès "cell crawling", que involucra la propulsió per actina, l'acció de proteïnes motores i l'adhesió de la cèl·lula sobre un substrat. Desafortunadament, l'estudi del mecanisme de motilitat per polimerització d'actina és altament complicat en cèl·lules eucariotes ja que hi ha molts mecanismes de regulació que poden enterbolir o, fins i tot modificar, la dinàmica del sistema. El bacteri *Listeria* és un candidat idoni per estudiar el moviment basat en la propulsió per polimerització de filaments d'actina, ja que presenta moltes similituds amb el mecanisme de propulsió basat en actina de les cèl·lules eucariotes i, malgrat això, és un sistema molt més simple. En particular, no hi ha motors moleculars i, per tant, la propulsió és deguda simplement al creixement de filaments d'actina.

La motilitat basada en la polimerització de filaments d'actina constituteix un dels mecanismes de generació de forces més utilitzats per les cèl·lules. Tant el procés de fagocitosi com el moviment d'endosomes a nivell intracel·lular es basen també en la polimerització de xarxes d'actina en la superfície de l'objecte propulsat. L'àmplia

varietat de moviments cel·lulars que involucren aquest mecanisme de generació de forces va fer pensar que hauria de ser també possible induir el moviment d'objectes sintètics utilitzant el mateix principi. Experiments on s'indueix la polimerització d'actina en la superfície de petites esferes sintètiques van demostrar que aquestes esferes desenvolupen cometes d'actina i es mouen de manera molt similar al bacteri *Listeria*. Aquests sistemes experimentals, anomenats biomimètics, han permès una comprensió molt més profunda i quantitativa del procés de motilitat basat en actina. Tot i així, aquests estudis no permeten mesurar les forces creades pel cometa d'actina sobre l'objecte que propulsa. Com que són finalment aquestes forces les responsables del moviment, és essencial conèixer en detall el seu origen i la seva magnitud.

Per tal d'esclarir quines són les forces generades pel cometa d'actina, el grup de C. Sykes (Institut Curie) va crear un sistema *in vitro* que permet mesurar directament els esforços generats pel gel d'actina sobre l'objecte propulsat. En aquests experiments s'utilitzen gotes d'oli parcialment cobertes per una proteïna que indueix la polimerització d'actina en la superfície externa de la gota. Quan aquestes gotes s'introdueixen en extractes cel·lulars, un gel d'actina creix inicialment de manera isotròpica en la superfície de la gota esfèrica i l'envolta. Després d'un trencament espontàni de simetria, les gotes desenvolupen un cometa d'actina i es mouen, de la mateixa manera que el bacteri *Listeria*. A diferència del bacteri però, la superfície fluïda de la gota està caracteritzada per una tensió superficial i és, per tant, deformable sota l'acció de forces prou importants, com ara els esforços elàstics que aplica el cometa d'actina sobre la gota. De fet, un cop la gota trenca la simetria esfèrica i es propulsada pel cometa d'actina, la deformació de la gota és clarament visible. Aquesta deformació permet mesurar de manera directa els esforços que el cometa d'actina aplica sobre la gota. L'avantatge d'aquest sistema biomimètic és que permet la mesura i/o control de tots els paràmetres físics importants, com ara la tensió superficial de la gota, la seva velocitat, mida, etc. . ., de manera que els resultats experimentals es poden comparar quantitativament a les prediccions teòriques.

L'objectiu d'aquesta primera part del nostre treball (capítol 3) ha estat comprendre l'origen de la força de propulsió i la distribució de les forces que aplica el cometa d'actina sobre objectes deformables com, per exemple, gotes d'oli. En el nostre estudi analitzem teòricament el moviment d'una gota propulsada mitjançant la polimerització d'actina en la seva superfície. Solucionem el problema de contorn lliure que implica el moviment de la gota, tenint en compte tant l'elasticitat del gel d'actina com la dependència del creixement del gel d'actina en els esforços elàstics del gel. La forma de la gota en l'estat estacionari ve determinada pel balanç entre la força que aplica el gel sobre la gota i la força de restitució deguda a la tensió superficial. El nostre estudi demostra que el gel aplica forces sobre la gota tant en la direcció del moviment com en la contrària. Al darrera de la gota, el gel estira la gota en la direcció contrària al moviment, mentre que l'empeny pels costats. Sorprenentment, la distribució de forces és tal que la força total de propulsió de la gota és estrictament nul·la en cas que tant el gradient de tensió superficial com les variacions de pressió internes de la gota no es tinguin en compte. Aquest resultat té implicacions importants, ja que demostra que la força de propulsió de la gota no es pot mesurar només a partir de la seva forma, com diversos grups havien fet anteriorment. Finalment,

hem comparat a nivell quantitatiu els resultats teòrics amb les dades experimentals. Aquesta comparació ha permès mesurar diversos paràmetres moleculars associats a la polimerització d'actina en superfícies fluïdes, similars a la membrana cel·lular. Apart de determinar la distribució de les forces que aplica el gel sobre la gota, la comparació amb les dades experimentals ha permès obtenir la magnitud d'aquestes forces.

Un estudi més detallat sobre l'origen de la força de propulsió suggereix que el gradient de tensió superficial és el responsable del moviment de la gota. Experimentalment s'observa que la distribució de les proteïnes que indueixen la polimerització d'actina, localitzades en la superfície de la gota, no és uniforme. Existeix una acumulació d'aquestes proteïnes en la part posterior de la gota, i la seva concentració disminueix al llarg del contorn. La tensió superficial depèn de la concentració de proteïnes adsorbides en superfície. Concretament, com més gran és la concentració de proteïnes, més petita és la tensió superficial. La distribució asimètrica de proteïnes de nucleació implica que hi ha un gradient de tensió superficial al llarg del contorn de la gota. Com que és aquest gradient el què propulsa la gota, hem estudiat d'on prové.

Per tal de comprendre l'origen de la distribució asimètrica de proteïnes de nucleació, hem estudiat la seva dinàmica en la superfície de la gota. Aquestes proteïnes poden o bé estar físicament connectades al gel d'actina, o bé movent-se lliurement en la superfície de la gota. El moviment del gel d'actina vers la part posterior de la gota durant el seu desplaçament, fa que les proteïnes connectades al gel d'actina siguin transportades cap a la part posterior de la gota, creant així una acumulació de proteïnes al darrere de la gota. Els nostres resultats indiquen doncs que el moviment de la gota, induït pel gradient de tensió superficial, és el que crea aquest mateix gradient. En altres paraules, el moviment resulta de l'autoorganització de les proteïnes de nucleació i el gel d'actina.

Malgrat l'estudi que presentem referent a la dinàmica dels nucleadors en la superfície de la gota és qualitatiu, estem extenent aquest treball per tal de poder comparar les dades experimentals a les prediccions teòriques.

El nostre estudi ha permès doncs explicar la propulsió de gotes per polimerització d'un gel d'actina. Hem determinat la forma de les gotes i la distribució d'esforços creats pel cometa d'actina de manera quantitativa. Aquests resultats permeten comprendre el mecanisme de propulsió d'endosomes i lisosomes involucrats en el transport intracel·lular, els quals estan propulsats per cometes d'actina i presenten deformacions similars a les predites en la nostra anàlisi.

A.3 Transport intracel·lular

La complexitat de les cèl·lules eucariotes fa que hagin de dur a terme diferents tasques simultàniament. Algunes d'aquestes tasques són necessàriament incompatibles entre elles, com ara la síntesi de proteïnes i la seva degradació. Per tal d'assegurar un cert nivell d'autonomia a les diferents tasques, les cèl·lules eucariotes estan dividides en diversos compartiments limitats per una membrana. Així doncs,

les reaccions bioquímiques que realitzen una certa tasca tenen lloc a l'interior d'un orgànul (compartiment limitat per una membrana) i estan pràcticament aïllades de la resta de la cèl·lula. Malgrat aquest grau d'autonomia que els orgànuls han de mantenir, aquests també han d'interaccionar amb l'entorn cel·lular per tal d'assegurar el bon funcionament global de la cèl·lula. Existeixen diferents mecanismes que s'encarreguen d'aquesta interacció. Els orgànuls contenen proteïnes de membrana que s'encarreguen de l'intervanvi directe de material amb el citosol. Aquest intercanvi involucra només l'orgànul i el seu entorn immediat. Apart d'aquesta interacció local, les cèl·lules han de transportar diferents components, com ara les proteïnes o els lípids, a regions distants dins de la cèl·lula. Per tal de transportar material a llargues distàncies les cèl·lules utilitzen petites vesícules i nanotubs de membrana.

El mecanisme físic de transport es basa en la interacció d'intermediaris de transport (vesícules i tubs de membrana) amb el citoesquelet de la cèl·lula a través de proteïnes motores, les quals es mouen al llarg dels filaments que composen el citoesquelet i propulsen els intermediaris de transport que contenen el material que ha de ser distribuït.

Malgrat el transport per petites vesícules ha estat l'únic mecanisme de transport cel·lular conegut durant dècades, recentment s'ha trobat que xarxes de nanotubs de membrana s'extenen per l'interior de la cèl·lula i permeten la interacció de regions distants de la cèl·lula. L'exemple més clar és el reticle endoplasmàtic, el qual està composant per una xarxa de tubs de membrana. S'ha demostrat que tant els microtúbuls com l'acció de proteïnes motores són necessàris per la formació d'aquests tubs. En absència de microtúbuls o de proteïnes motores, la xarxa de tubs que composa el reticle endoplasmàtic col·lapsa al centre de la cèl·lula. Apart del reticle endoplasmàtic en sí mateix, el transport de material entre l'aparell de Golgi i el reticle endoplasmàtic involucra també nanotubs de membrana. Així doncs, la comunicació intracel·lular requereix l'extensió de xarxes de tubs de membrana. Com si d'una ciutat es tractés, la cèl·lula necessita el permanent transport de material entre regions distants per poder dur a terme les diferents tasques en què es basa el seu funcionament. Si el transport intracel·lular es veu afectat d'alguna manera, les conseqüències poden ser crítiques per la cèl·lula i, fins i tot, per l'organisme. De fet, hi ha diverses malalties neurodegeneratives associades a disfuncions del transport en els axons de les neurones. L'estudi del mecanisme físic de transport pot ajudar a comprendre millor la comunicació intracel·lular.

El nostre estudi referent al transport intracel·lular es focalitza principalment en el mecanisme físic d'extracció de nanotubs de membrana per motors moleculars. En el capítol 5 estudiem com els motors moleculars són capaços de formar tubs de membrana i comparem, a nivell quantitatiu, els resultats teòrics amb experiments *in vitro* realitzats per C. Leduc en el grup de P. Bassereau (Institut Curie). En una segona part estudiem el tràfic de motors moleculars en si mateix, i demostrem que les interaccions mútues entre motors poden induir l'aparació de retencions, similars a les que apareixen en el tràfic de vehicles en carreteres. En vista dels resultats obtinguts, en el capítol 6 analitzem la generació col·lectiva de forces de motors moleculars quan aquests estiren membranes fluïdes, una situació que es dóna tant en l'extracció de

tubs de membrana com en el transport intracel·lular que involucra petites vesícules. A continuació expliquem en més detall els resultats obtinguts.

A.3.1 Extracció de nanotubs de membrana per motor moleculars

Estudis *in vivo* i *in vitro* sobre l'extracció de tubs de membrana van permetre establir que tant les proteïnes motores com els microtúbuls són essencials per a la formació de tubs de membrana. Malgrat això, la complexitat de la composició de la membrana cel·lular i del citosol, no van permetre indentificar els components mínims necessaris per la formació de tubs de membrana. Diferents experiments *in vitro* han demostrat recentment que els motors moleculars poden, per si sols, crear aquests tubs de membrana, sense necessitat de cap altre proteïna accessoria present en la cèl·lula. Al mateix temps es va suggerir que l'acumulació dinàmica dels motors a la punta del tub és el mecanisme que permet la seva extracció. Per tal de demostrar l'existència d'aquesta acumulació, C. Leduc, en el grup de P. Bassereau (Institut Curie), va desenvolupar un sistema *in vitro* on els motor moleculars (kinesines) estan directament enganxats a lípids específics d'una vesícula gegant. Quan aquesta vesícula, recoberta parcialment per kinesines, es posa en contacte amb una xarxa de microtúbuls en presència d'ATP, les kinesines caminen al llarg dels microtúbuls, apliquen forces sobre la membrana de la vesícula i, en certes condicions, estiren tubs de membrana. Fins aquí, aquestes observacions només verifiquen els resultats d'altres grups. La novetat d'aquests experiments és que els lípids als quals estan enganxats els motors moleculars contenen un fluorofor, de manera que la posició dels motors moleculars és accessible mitjançant microscopia de fluorescència. En particular, quan un tub és estirat pels motors, la seva distribució al llarg del tub és mesurable. D'altre banda, aquest sistema biomimètic permet el control de diverses magnituds físiques rellevants, com ara la tensió de la membrana o la densitat de motors en la superfície de la vesícula. Les quantitats que no poden ser controlades, com els parametres cinètics dels motors moleculars, es poden mesurar. Així doncs, en aquests experiments es coneixen els valors de totes les magnituds rellevats i, per tant, les dades experimentals es poden comparar quantitativament als resultats del nostre estudi teòric.

El treball que presentem en el capítol 5 analitza teòricament l'extracció i creixement de tubs de membrana estirats per motors moleculars. Resolem tant analíticament com numèricament (utilitzant simulacions Monte Carlo) la dinàmica dels motors moleculars al llarg d'un tub de membrana i en la superfície de la vesícula. L'estudi analític de la formació inicial de tubs determina la influència de diverses magnituds físiques en el process d'extracció. En particular, demostrem que, com a conseqüència de la dinàmica col·lectiva de motors, existeix un llindar de densitat de motors per sota del qual els motors moleculars no són capaços d'extreure tubs de membrana. Les dades experimentals mostren l'existència d'aquest llindar. A més, la mesura experimental dels diferents parametres físics que controlen el procés permet comparar a nivell quantitatiu les prediccions teòriques amb les dades experimentals. La concordància entre les prediccions teòriques i els resultats experimentals indica que la descripció teòrica realitzada és adient.

L'existència d'un llindar per a l'extracció de tubs posa de manifest el caràcter col·lectiu de la dinàmica dels motors moleculars. El nostre estudi demostra que el llindar és una conseqüència directe de la dependència de la dinàmica col·lectiva dels motors moleculars en la força que sostenen. Això és degut al caràcter no-lineal de l'acoblament entre els motors. Apart de determinar l'origen de la inestabilitat dinàmica responsable de l'existència d'un llindar, també hem determinat la influència de les magnituds físiques rellevants en el valor d'aquest llindar. Concretament, per tensions de membrana petites els motors moleculars poden extreure tubs més fàcilment. Això es tradueix en un valor més petit del llindar de densitat de motors per extreure tubs. El llindar es pot també veure des d'un altre punt de vista. Per una quantitat fixa de motors en la membrana, existeix una tensió de membrana màxima per sobre de la qual els motors no poden extreure tubs.

Aquests resultats emfatitzen els lligams físics amb els quals les cèl·lules han de tractar pel què fa al transport intracel·lular. L'existència d'un llindar en l'extracció de tubs té implicacions biològiques rellevants. En particular, el llindar permetria a les cèl·lules activar o suprimir el transport quan fos necessari. Diverses estratègies permeten diferents tipus de control sobre el transport. El primer mecanisme requereix el control de la densitat local de motors enganxats a la membrana, ja sigui controlant el nombre de motors directament, o modificant el nombre de llocs en la membrana on els motors es poden enganxar. Aquesta estratègia permetria el control local del transport, és a dir, permetria controlar específicament cada una de les vies de transport que caracteritzen el transport intracel·lular. Concretament, la concentració de motors actius a l'interior de dominis especialitzats de la membrana podria ser doncs un punt important per tal entendre els mecanismes de regulació de la via de secreció de la cèl·lula. La segona estratègia consisteix en el control de la tensió de membrana. De fet, les cèl·lules controlen la tensió dels seus orgànuls per mecanismes que encara no es coneixen en detall. Així doncs, canvis globals en la tensió de membrana d'un orgànul permetrien controlar el transport provinent d'aquest orgànul, podent-lo fins i tot suprimir en cas de necessitat.

En el cas que els motors estiguin en condicions d'estirar tubs de membrana, és possible estudiar les propietats de creixement dels tubs i la distribució de motors al llarg del tub. L'estudi teòric que hem realitzat explica l'acumulació de motors a la punta dels tubs. Quan una força és aplicada a un motor molecular, la seva cinètica es veu afectada i, en particular, la seva velocitat disminueix. Com que la membrana és fluïda els motors que es mouen al llarg del tub no poden aplicar forces substancials per estirar-lo. En canvi, els motors que estan a la punta del tub apliquen forces substancials en la direcció normal de la membrana. Així doncs, els motors que estiren el tub a la punta es mouen més lentament que els motors que es mouen al llarg del tub. La velocitat del tub és la mateixa que la dels motors. Com a conseqüència, els motors que es mouen a llarg del tub s'acumulen a la punta del tub, explicant així l'acumulació observada experimentalment. Per altra banda, els motors situats a la punta del tub es desenganxen del microtúbul amb més freqüència degut a la força que sostenen i difonen enrere al llarg del tub. Aquests motors, que estan enganxats a la membrana però no al microtúbul, es poden tornar a enganxar al microtúbul i seguir el seu trajecte cap a la punta del tub. Es crea doncs una circulació de motors

en la proximitat de la punta del tub, on els motors estiren el tub una fracció petita de temps, es desenganxen del microtúbul, difonen cap enrere al llarg del tub, es tornen a enganxar al microtúbul i tornen a acostar-se a la punta del tub per contribuir un altre cop a la seva extracció. La dinàmica al llarg del tub definiex la seva distribució. Els nostres resultats teòrics prediuen un decreixement exponencial de la densitat de motors des de la punta del tub, amb una longitud característica de decreixement donada pels parametres cinètics dels motors i la mateixa velocitat del tub. Les observacions experimentals indiquen un decreixement exponencial de la densitat de motors des de la punta del tub, tal com hem predit teòricament. La comparació quantitativa de l'escala de longitud de decreixement de la densitat amb les dades experimentals ens ha permès estimar el temps mitjà necessari per tal que un motor desenganxat del microtúbul s'hi torni a enganxar. Així doncs, la comparació dels resultats teòrics i els experimentals permet la determinació d'un paràmetre molecular associat a la kinesina en una geometria similar a la del transport en cèl·lules.

L'anàlisi teòric de la distribució de motors al llarg del tub reprodueix i explica les observacions experimentals. Aquests resultats demostren que els motors moleculars s'acumulen dinàmicament per estirar tubs de membrana. Així doncs, no és en principi necessària cap altre proteïna que agregui els motors en grups per tal d'estirar els tubs. Com expliquem més avall, els resultats de les simulacions suggereixen que per tal de desenvolupar forces importants, aquesta agregació mediada per altres proteïnes és però convenient.

Un cop estudiat el procés d'extracció i creixement de tubs, ens hem interessat també en els règims dinàmics de creixement de tubs, en condicions on la tensió de la membrana creix durant el procés d'extracció del tub. Malgrat hem centrat el nostre estudi en tubs llargs, per als quals la variació de tensió de la vesícula no és negligible, els mateixos règims dinàmics caracteritzen el creixement de xarxes de tubs de membrana, com ara el reticle endoplasmàtic. Un cop el tub és extret pels motors la força necessària per estirar el tub creix amb la longitud del tub degut a l'increment de la tensió de la vesícula. Per tant, els motors estirant el tub senten cada cop més força. Aquesta situació dóna lloc a dos règims dinàmics. Existeix un règim estable en el qual el tub creix fins que es para a una certa longitud. Per altra banda, dependent de la mida de la vesícula i de la densitat de motors en la membrana, els tubs poden entrar en un règim oscil·latori, en el qual el tub mostra fases de creixement alternades amb ràpides retraccions. Aquestes oscil·lacions altament no-lineals són degudes a la dinàmica col·lectiva dels motors moleculars que estiren el tub. De fet, el caràcter no-lineal de les oscil·lacions prové de la combinació de la dinàmica col·lectiva dels motors amb la seva cinètica, la qual depèn de la força de manera molt no-lineal.

Les oscil·lacions predites teòricament en el nostre estudi han estat observades en els experiments descrits anteriorment. Concretament, les oscil·lacions observades presenten les mateixes característiques no-lineals que les predites. Malgrat aquesta concordància a nivell qualitatiu entre la teoria i els experiments, en aquest cas no va ser possible dur a terme un estudi quantitatiu. Estem en aquests moments extenent els nostres resultats teòrics per entendre millor la física d'aquestes oscil·lacions.

Malgrat es fa difícil identificar una certa funció biològica a les oscil·lacions de tubs, el seu origen és rellevant per diversos moviments cel·lulars. Existeixen

moltíssimes situacions en biologia cel·lular, com ara la contracció muscular, el moviment de flagels i cilis, i el moviment de cromosomes en la divisió cel·lular, on apareixen oscil·lacions molt similars. De fet, el punt en comú de tots aquests moviments és que estan generats per grups de motors moleculars que desenvolupen forces de manera col·lectiva. Per tant, la inestabilitat oscil·latòria descrita teòricament en el nostre estudi, basada en el comportament col·lectiu dels motors moleculars, pot ser, de fet, un fenòmen molt més general que aparegui en diversos processos de generació de força i moviment a l'escala cel·lular.

Un cop estudiat el procés d'extracció de tubs, el seu creixement i els seus règims dinàmics, hem dut a terme simulacions numèriques de l'extracció de tubs estirats per motors moleculars, per tal d'entendre com s'organitzen els motors moleculars per estirar col·lectivament un tub de membrana. Hi ha diversos resultats de les simulacions que poden ser comparats quantitativament a les dades experimentals. Aquesta comparació ens ha permès distingir entre diferents posibles esquemes d'organització de motors. Concretament, els nostres resultats indiquen que els motors han d'utilitzar simultàniament diversos protofilaments d'un mateix microtúbul per tal de poder generar les forces que requereix l'extracció d'un tub. L'anàlisi de les diverses organitzacions possibles dels motors que estiren un tub indica que els motors en contacte poden repartir-se la força que han de suportar. Les simulacions demostren que la dinàmica d'enganxament i desenganxament dels motors al microtúbul estableix un nombre molt petit de motors en contacte a la punta d'un tub de membrana. Degut a que el nombre de motors en contacte per protofilament és petit, la força que poden desenvolupar és també petita i, típicament, inferior a la força necessària per estirar un tub. Estimem que en les condicions experimentals mencionades anteriorment els motors utilitzen tres protofilaments simultàniament.

Aquests resultats estableixen límits importants a les forces que els motors moleculars poden crear de manera col·lectiva quan estiren membranes fluïdes, ja siguin tubs de membrana o vesícules. Malgrat les forces necessàries per transportar vesícules en l'interior de la cèl·lula no han estat encara mesurades, és molt probable que aquestes siguin molt superiors a les que pot desenvolupar un motor molecular únic, ja que aquestes vesícules han de moure's a través del citoesquelet de la cèl·lula. El creixement de tubs de membrana en l'interior de la cèl·lula es pot veure també afectat per diversos obstacles. Per tal de generar les forces suficients per transportar les vesícules o estirar els tubs de membrana, és doncs possible que existeixin proteïnes encarregades d'agregar els motors moleculars. En aquest cas, l'alt grau d'acoblament entre els motors permetria crear forces més grans.

A.3.2 Tràfic de motors moleculars

L'estudi de la distribució de motors al llarg del tub que hem descrit anteriorment no té en compte les interaccions entre els motors, ja que les observacions experimentals en les condicions anteriors suggerien una fase diluïda de motors al llarg del microtúbul. En cas que la concentració de motors sigui augmentada, l'aproximació de baixa densitat no és vàlida i les interaccions entre els motors juguen llavors un pa-

per important. Per tal de comprendre millor l'acumulació de motors en la proximitat de la punta del tub, hem dut a terme simulacions numèriques del creixement del tub.

En cas que la tensió de la vesícula no augmenti significativament durant el creixement del tub, els nostres resultats indiquen que si la densitat de motors en la vesícula és gran, una fase d'alta densitat de motors es desenvolupa progressivament en la proximitat de la punta del tub. Com que en l'escala de temps dels experiments sempre hi ha motors en la vesícula, existeix sempre un flux net de motors que avança des de la vesícula cap a la punta del tub. Aquesta situació implica que no existeix un estat estacionari pel sistema. Concretament, els motors que constantment arriben a la proximitat de la punta del tub es van acumulant i, malgrat que inicialment la fase d'alta densitat de motors ("traffic jam") és petita, aquesta envaeix progressivament el tub.

Hem realitzat també simulacions en el cas que la tensió de la vesícula no sigui constant, sinó que augmenti a causa del mateix creixement del tub. En aquest cas observem que el tub creix fins a una certa longitud i finalment es para. Com hem discutit anteriorment, els motors al llarg d'un sol protofilament no poden generar grans forces ja que la cinètica d'engaxament i desenganxament al microtúbul no permet crear paquets de motors molt grans que estirin conjuntament el tub. Per tant, la força que poden crear els motors no és molt gran i, malgrat ser suficient per estirar inicialment el tub, si la força augmenta, arriba un moment en el qual no poden estirar més. Quan el tub es para, hi ha un flux net de motors al llarg del tub que s'acumula a la seva punta i l'envaeix progressivament. Aquests resultats estan en concordància amb les observacions experimentals a nivell qualitatiu.

Per altra banda, s'observa experimentalment que la densitat de motors al llarg del tub presenta clares inhomogeneïtats. Aquestes observacions no es poden entendre en l'estudi analític que hem descrit anteriorment. Per aquesta raó, hem estudiat el tràfic de motors moleculars a gran escala, en presència d'interaccions entre els motors. De fet, les inhomogeneïtats de densitat en el tràfic de motors constitueixen un problema més general que el del tràfic de motors al llarg del tub.

El tràfic de motors a gran escala juga un paper important en moltes situacions biològiques, com el transport intracel·lular i intraflagelar o el transport al llarg dels axons. Diverses malalties neurodegeneratives han estat relacionades amb anomalies en el tràfic de motors al llarg d'axons. És clar que el transport en als axons és el que es pot veure més afectat per anomalies de tràfic ja que el material sintetitzat al cos cel·lular ha de ser transportat llargues distàncies, que poden ser de l'ordre de centímetres, a través dels axons fins arribar al terminal sinàptic. A més, el medi intracel·lular conté moltes proteïnes que poden suposar obstacles per al tràfic de motors al llarg de filaments. En aquestes condicions, les no-linealitats en el tràfic poden jugar un paper important. Hi ha també altres raons per estudiar el tràfic de motors. De fet, el tràfic en general, ja sigui de motors moleculars, de persones o de vehicles, constitueix un sistema físic allunyat de l'equilibri. Aquest tipus de sistemes són, per tant, molt adients per a l'estudi de transicions de fase de no-equilibri. Per tal d'entendre les inhomogeneïtats en el tràfic de motors, hem dut a terme simulacions numèriques on estudiem principalment l'efecte de les interaccions mútues dels motors en les inhomogeneïtats del camp de densitat.

Els nostres resultats indiquen que en presència de només interaccions de volum exclòs entre els motors, les inhomogeneïtats en el tràfic són petites i no es corresponen amb les observades experimentalment. De fet, aquestes inhomogeneïtats, anomenades ones cinemàtiques, han estat descrites en múltiples treballs referents al tràfic de vehicles i en altres sistemes on partícules auto-propulsades es mouen al llarg d'una estructura periòdica unidimensional. Concretament, el temps de vida i la mida de les inhomogeneïtats són molt més petits que els observats experimentalment. Hi ha diversos experiments que suggereixen una interacció entre motors moleculars més enllà de la simple interacció de volum exclòs. Per tal d'esclarir si la causa de les inhomogeneïtats són les possibles interaccions entre els motors, hem simulat el tràfic de motors en presència d'interaccions efectives, tant atractives com repulsives, entre els motors. El nostre estudi demostra que en presència d'interaccions repulsives, el camp de densitat és més homogeni que en el cas on només hi ha interaccions de volum exclòs entre els motors. Pel contrari, en presència d'interaccions atractives entre els motors, grans inhomogeneïtats de la densitat de motors apareixen espontàniament. La vida mitja i la mida d'aquesta inhomogeneïtats es corresponen amb les observades experimentalment. Les inhomogeneïtats no són estàtiques, sinó que poden moure's en ambdues direccions al llarg del microtúbul. Malgrat els motors moleculars només es mouen en una direcció, existeixen ones de densitat que es mouen tant en la direcció del moviment dels motors com en la contrària. Aquestes acumulacions locals de motors es coneixen com retencions ("traffic jams") en el tràfic de vehicles, on s'observen també les ones de densitat esmentades. Les prediccions teòriques pel què fa a les ones de densitat estan en concordància amb els experiments, on s'observen ones de densitat movent-se tant en la direcció del moviment dels motors com en l'oposada.

Així doncs, els nostres resultats suggereixen que existeixen interaccions atractives entre els motors moleculars i que aquestes són responsables de l'aparició de retencions de motors ("traffic jams") al llarg del microtúbul.

A.3.3 Comportament col·lectiu de motors moleculars estirant membranes fluïdes

Els resultats del nostre estudi demostren que els motors moleculars són capaços d'estirar col·lectivament tubs de membrana. El comportament col·lectiu de motors ha estat estudiat amb anterioritat, però tots els estudis estan basats en un acoblament rígid o elàstic entre els motors. Quan els motors treballen conjuntament per estirar una membrana fluida, aquest acoblament rígid és inexistent. En aquest cas, les interaccions entre els motors tenen un paper decisiu en el seu comportament col·lectiu. En vista dels resultats precedents, en el capítol 6 estudiem el procés de generació de força quan un grup de motors moleculars estiren una membrana fluïda com, per exemple, un tub de membrana. Els motors només poden aplicar forces significatives per estirar el tub a la seva punta ja que és l'únic lloc on els motors poden aplicar forces normals a la membrana. Suposant que el primer motor, aquell que està situat a la punta del tub, és l'únic que aplica forces a la membrana, hem estudiat com els motors que s'acumulen al seu darrere contribueixen a la generació de força. Els motors

moleculars es mouen per una seqüència de salts al llarg del microtúbul. Típicament, un motor molecular salta més freqüentment en una direcció que en l'altra i, per tant, en mitjana es mou en una direcció concreta. En presència d'una força aplicada sobre el motor, la freqüència de salts en la direcció del moviment és menor i la freqüència de salts en la direcció contrària al moviment augmenta. La generació col·lectiva de força és deguda a que els motors acumulats darrere el primer motor modifiquen algunes de les seves transicions estocàstiques i, en particular, eviten algunes de les seves transicions en la direcció contrària al moviment. Així doncs, malgrat és el primer motor el que suporta tota la força, els altres motors contribueixen a estirar el tub pricipalment evitant que el primer motor es mogui endarrere.

Hem realitzat un estudi analític i també hem dut a terme simulacions per tal de determinar la relació entre la velocitat mitjana del tub i la força aplicada al primer motor, per sistemes amb diferent nombre de motors. Els nostres resultats demostren que les interaccions entre motors modifiquen substancialment la corba de força-velocitat. Concretament, interaccions fortament atractives entre motors redueixen la velocitat per sota la d'un motor únic per forces petites, mentre que a forces grans el sistema amb major nombre de motors es mou més ràpid. Interaccions repulsives entre motors fan que el sistema sempre es mogui més rapid que un motor únic. Més important que la dependència de la corba de força-velocitat en les interacions és el fet que, per qualsevol tipus d'interacció entre els motors, la corba de força-velocitat és significativament diferent que la que s'obté si s'assumeix que els motors es reparteixen uniformement la força. El nostre estudi corregeix doncs la corba de força-velocitat que s'utilitza normalment, on es suposa el repartiment uniforme de la força entre els motors.

D'altra banda, els nostres resultats demostren que la corba de força-velocitat satura a una sola corba si el nombre de motors en el sistema és prou gran. Utilitzant els paràmetres de la kinesina convencional, trobem que la corba de força-velocitat satura quan el sistema conté dos motors. Això implica que independentment del nombre de motors que estiren la membrana, la corba de força-velocitat és sempre la mateixa i igual a la de dos motors. Les diferents interaccions entre motors només fan variar lleugerament el nombre de motors al qual es dóna la saturació de les corbes. Els nostres resultats suggereixen que com a conseqüència d'aquesta saturació, la força màxima que poden desenvolupar un nombre elevat de kinesines convencionals al llarg d'un protofilament estirant una membrana no és major que la força que poden fer simplement dos motors.

Aquesta anàlisi suggereix que és necessari que les kinesines utilitzin simultàniament diversos protofilaments d'un microtúbul per tal d'estirar un tub de membrana o transportar una vesícula. L'estudi posa també de manifest que per tal de generar forces molt més grans que la força de parada ("stall force") d'un sol motor molecular, és més eficient acoblar rígidament o elàsticament els motors. Així doncs, és possible que en algunes situacions referents al transport intracel·lular, les cèl·lules utilitzin proteïnes accessòries per agregar els motors i permetre la generació de forces més grans que possibilitin el transport en condicions adverses. D'altra banda, la comparació dels nostres resultats amb dades experimentals referents a la generació de força de motors individuals en presència d'altres motors, permetria discernir el tipus

d'interacció entre els motors. Finalment, la saturació de les corbes de força-velocitat fa que no sigui possible estimar el nombre de motors que estiren una membrana amb el coneixement de la força que sostenen i la seva velocitat, com ha estat fet en estudis de tràfic intracel·lular.

A.4 Moviment de cromosomes en la mitosi

Els organismes multicel·lulars, com ara nosaltres, necessiten una constant generació de cèl·lules per simplement sobreviure. La duplicació d'una cèl·lula eucariota és el resultat del procés de divisió nuclear (mitosi) i la posterior divisió del citoplasma. En la mitosi, les dues còpies del codi genètic s'estructuren formant els cromosomes, els quals han de ser repartits a parts iguals entre les dues cèl·lules filles que resulten del procés de divisió. Per tal de repartir de manera equitativa els cromosomes, aquests s'han de moure i separar de manera coordinada. De fet, el correcte posicionament i moviment dels cromosomes és essencial per a la divisió cel·lular. Un mal posicionament dels cromosomes dóna lloc a retards en la separació dels cromosomes que poden, fins i tot, portar a la mort cel·lular.

En la mitosi, els cromosomes segueixen una seqüència complexa de moviments coordinats. Just després de la degradació de la membrana nuclear, els cromosomes interaccionen amb els microtúbuls que formen el fus mitòtic, una estructura originada per l'autoorganització de microtúbuls i motors moleculars de diverses classes. Aquesta estructura permet la transmissió de les forces necessàries per moure els cromosomes. Generalment, un microtúbul provinent d'un dels pols del fus mitòtic contacta lateralment un dels dos cinetocors d'un cromosoma i aquest es mou ràpidament cap al pol d'on prové el microtúbul. Un cop més a prop del pol, alguns dels microtúbuls que emanen radialment del pol connecten amb el cinetocor i creen un feix de microtúbuls que connecta fortament el cromosoma al pol. Es diu llavors que el cromosoma està monoorientat ja que només està connectat a un dels dos pols del fus mitòtic. En cèl·lules animals, cada un dels cromosomes es mou cap al pol i després se n'allunya, de manera periòdica. Aquest moviment oscil·latori, el qual persisteix en les diferents fases de la mitosi (des de la prometafase fins a l'anafase A), és degut a les forces que actuen sobre el cromosoma. Així doncs, la seva descripció quantitativa pot ajudar a comprendre la relació entre els moviments a escala cel·lular i les forces a nivell molecular durant la divisió cel·lular.

Tots els models que descriuen el moviment oscil·latori dels cromosomes tenen com a punt en comú que el cinetocor controla, d'alguna manera, les fases de moviment del cromosoma. És a dir, aquests models proposen que el cinetocor és el responsable del moviment oscil·latori. Malgrat que aquesta és una hipòtesi plausible, es coneixen poques coses del cinetocor i no existeix encara una explicació per a aquest hipotètic mecanisme de control del moviment del cromosoma en el cinetocor. Alguns d'aquests estudis reprodueixen el moviment oscil·latori del cromosoma, però malgrat això, no expliquen aquest moviment ja que aquests models postulen la dependència espaial de les forces que actuen sobre el cromosoma. És important entendre que un model que postula la natura de les forces, sense evidències experimentals

per a tal suposició, no pot explicar l'origen del moviment encara que sigui capaç de reproduir-lo. L'objectiu de l'estudi que presentem en el capítol 8 és demostrar que el moviment dels cromosomes i el seu posicionament en la cèl·lula poden ser entesos a partir dels mateixos conceptes físics.

Hi ha dues forces que actuen sobre un cromosoma durant la divisió cel·lular. S'ha demostrat que el cinetocor aplica una força al cromosoma dirigida vers el pol del fus mitòtic al qual està connectat. Malgrat que l'origen molecular d'aquesta força no està encara ben establert, es creu que les contribucions principals a aquesta força provenen de les dineïnes citoplasmàtiques i de la depolimerització de microtúbuls. D'altra banda, hi ha diversos experiments que demostren l'existència d'una força que ejecta el cromosoma lluny del pol. L'origen molecular d'aquesta força ha estat identificat recentment. Les cromokinesines, un tipus de kinesines que estan associades als braços dels cromosomes, es mouen al llarg dels microtúbuls i generen la força d'ejecció que intenta allunyar el cromosoma del pol. Aquests motor moleculars generen forces de l'ordre dels picoNewtons. Com que s'ha mesurat que les forces necessàries per moure un cromosoma són de l'ordre de nanoNewtons, això implica que les cromokinesines treballen en grup per tal de moure el cromosoma. Recents observacions experimentals demostren el paper clau que juguen aquests motors en el moviment dels cromosomes, ja que una reducció dràstica del seu nombre dóna lloc a un apropament significatiu del cromosoma al pol del fus mitòtic i suprimeix les oscil·lacions.

El moviment del cromosoma resulta de la competició entre la força que ejecta el cromosoma lluny del pol i la força que aplica el cinetocor, la qual intenta apropar el cromosoma al pol. La força d'ejecció té un origen dinàmic ja que està generada de manera col·lectiva per les cromokinesines i, per tant, depèn fortament de la cinètica d'aquests motors. De manera genèrica, el comportament col·lectiu de motors dóna lloc a inestabilitats dinàmiques, però no té perquè donar lloc a oscil·lacions si la dinàmica del sistema no està acoblada a algun grau de llibertat espaial. La nostra descripció proposa que aquest acoblament és degut a la interacció de les cromokinesines amb els microtúbuls que configuren el fus mitòtic, ja que la configuració espaial dels microtúbuls en forma d'estrella constitueix un substrat en el què l'enganxament de motors depèn de la posició. Així doncs, l'enganxament de cromokinesines als microtúbuls del fus mitòtic permeten al cromosoma determinar la seva posició dins la cèl·lula. El nostre estudi demostra que l'acoblament entre la inestabilitat associada a la dinàmica col·lectiva dels motors i la morfologia del fus mitòtic dóna lloc a les oscil·lacions observades.

En una primera part centrem el nostre estudi en el moviment de cromosomes mono-orientats. L'anàlisi de l'estabilitat dinàmica de la posició del cromosoma demostra que aquest està caracteritzat per dos possibles estats dinàmics. O bé el cromosoma està fix en una certa posició espaial, o bé oscil·la entre dues posicions. Concretament, hem determinat la influència de diversos paràmetres, com ara el nombre total de cromokinesines, en l'estabilitat posicional del cromosoma. Trobem que existeix un nombre mínim de cromokinesines per sobre del qual el cromosoma presenta oscil·lacions altament no-lineals. La integració numèrica de la dinàmica del cromosoma, demostra que les oscil·lacions obtingudes són molt similars a les obser-

vades *in vivo*. La comparació de resultats obtinguts i les dades experimentals referents al moviment de cromosomes ens han permès estimar que aproximadament unes mil cromokinesines estan associades a un sol cromosoma. Apart de la influència del nombre total de cromokinesines, hem analitzat també la dependència del moviment dels cromosomes en la morfologia del fus mitòtic. Els nostres resultats concorden amb les dades experimentals al respecte, les quals indiquen que un augment de la densitat de microtúbuls indueix un allunyament del cromosoma respecte al pol del fus mitòtic.

Un cop realitzat l'estudi de cromosomes monoorientats, hem extès la descripció per tal d'entendre el moviment de cromosomes biorientats. Aquests cromosomes estan connectats a ambdós pols del fus mitòtic a través de dos feixos de microtúbuls que connecten cada un dels dos cinetocors d'un cromosoma a un pol diferent. En aquest cas, les forces dels cinetocors vers cada un dels pols en cancel·len entre elles, i les forces dominants responsables del moviment del cromosoma són aquelles que apliquen les cromokinesines. El fus mitòtic està composat per dos centres de nucleació de microtúbuls. Els microtúbuls es distribueixen de manera radial des de cada un dels centres de nucleació, els quals es corresponen amb els dos pols del fus mitòtic. A diferència d'un cromosoma monoorientat, el qual interacciona essencialment amb els microtúbuls d'un dels pols, les cromokinesines d'un cromosoma biorientat es poden enganxar a microtúbuls provinents dels dos pols. Com a conseqüència, existeixen dues forces oposades que ejecten el cromosoma biorientat de cada un dels pols. La competició entre aquestes dues forces dóna lloc al moviment del cromosoma. L'estudi de l'estabilitat dinàmica del cromosoma biorientat demostra que, de la mateixa manera que els cromosomes monoorietats, els biorientats poden o bé quedar-se en una posició espaial fixa, o bé oscil·lar entre dues posicions. La posició estable d'un cromosoma biorientat es troba a la posició mitjana entre els dos pols, degut a la simetria del fus mitòtic. Experimentalment, els cromosomes biorientats es localitzen al pla mitòtic, situat precisament al punt mig entre els dos pols.

La descripció del moviment dels cromosomes que hem introduït permet també analitzar com els cromosomes biorientats es mouen cap al pla mitòtic, en un procés conegut com "chromosome congression". L'origen d'aquest moviment ha estat explicat durant molt temps per un mecanisme on es suposa que la força que aplica cada un dels cinetocors creix linealment amb la distància del cromosoma al pol. El nostre estudi proposa que no és la força del cinetocor la que varia amb la distància del cromosoma al pol, sinó que és la força neta dirigida cap a cada un dels pols la que augmenta, degut a la disminució de la força d'ejecció com a conseqüència de la disminució de la concentració de microtúbuls a distàncies més grans del pol.

Així doncs, en el capítol 8 introduïm una descripció teòrica que permet comprendre el posicionament, el moviment i la congressió de cromosomes a partir de la mateixa base física. Demostrem que el moviment oscil·latori dels cromosomes és degut a l'acoblament de la inestabilitat dinàmica associada al comportament col·lectiu de les cromokinesines amb la cinètica d'enganxament de les cromokinesines als microtúbuls del fus mitòtic. Concretament, és aquesta mateixa cinètica d'enganxament de les cromokinesines al microtúbuls, la qual depèn de la concentració local de microtúbuls en el fus mitòtic, la que permet al cromosoma sen-

tir la seva posició dins la cèl·lula. Aquest estudi fa diverses prediccions que seria interessant comprovar experimentalment, com per exemple el nombre mínim de cromokinesines per sota del qual el cromosoma no oscil·la, o la variació de les característiques del moviment del cromosoma degudes a variacions controlades de la morfologia del fus mitòtic.

Juntament amb l'estudi sobre l'extracció de tubs de membrana presentat anteriorment, l'anàlisi del moviment de cromosomes posa de manifest l'origen dinàmic de les forces creades col·lectivament per grups de motors moleculars. Com que existeixen moltíssimes situacions en les que el moviment cel·lular és originat per grups de motors moleculars, creiem que les inestabilitats obtingudes en el nostre anàlisi poden permetre comprendre altres moviments cel·lulars.

A.5 Estabilitat del fus mitòtic

Diverses estructures en cèl·lules eucariotes provenen de l'autoorganització de filaments polars i proteïnes motores. Hi ha diversos estudis *in vitro* que demostren que barreges de microtúbuls i kinesines desenvolupen espontàniament estructures complexes. Aquests fenòmens d'autoorganització són essencials en la divisió de cèl·lules eucariotes.

En la mitosi, diferents proteïnes motores organitzen els microtúbuls en una estructura bipolar, el fus mitòtic, que permet transmetre les forces necessàries per moure els cromosomes. L'estabilitat del fus mitòtic és essencial per al procés de divisió cel·lular, ja que defectes en l'estructura poden impedir la repartició dels cromosomes en les cèl·lules filles. El fus mitòtic consisteix en dos conjunts de microtúbuls que es distrubueixen radialment des de cada un dels dos centres de nucleació de microtúbuls. Aquests dos conjunts de microtúbuls interaccionen mitjançant proteïnes motores. Dels diferents tipus de motors moleculars que es creu que estan involucrats en la divisió cel·lular, s'ha demostrat que un tipus concret de motors bipolars (Eg5 o Klp61F, de la familia BimC) juga un paper molt important en l'estabilitat del fus mitòtic. Concretament, si es disminueix la concentració d'aquests motors per sota un llindar, el fus mitòtic col·lapsa. A més, s'ha demostrat també que la seva inhibició total impedeix la formació del fus mitòtic. D'altra banda, altres estudis demostren la implicació d'aquests motors en la formació de feixos de microtúbuls i en la generació del característic flux de microtúbuls vers els pols del fus mitòtic. En vista de totes aquestes observacions experimentals, hem analitzat teòricament el paper que juguen aquests motors en l'estabilitat d'estructures similars al fus mitòtic. En el capítol 9 presentem una descripció de la generació de forces i estabilitat del fus mitòtic basada en el comportament col·lectiu dels motors bipolars.

Els motors bipolars són kinesines capaces de crear lligams entre diferents microtúbuls i moure's simultàniament i independentment sobre cada un d'ells. D'aquesta manera, fan lliscar aquells microtúbuls disposats en una configuració antiparal·lela l'un respecte l'altre. Com a resultat d'aquest lliscament relatiu dels microtúbuls, els motors generen una força en la direcció de simetria del feix, la qual separa els dos pols. Aquesta situació té lloc en la zona central del fus mitòtic en la metafase de la

mitosi. La força de compressió imposada externament és equilibrada per la força que generen de manera col·lectiva els motors que lliguen els microtúbuls antiparal·lels. Malgrat que les forces estan equilibrades internament en l'estructura, la dinàmica del sistema imposa restriccions importants a la seva estabilitat.

Concretament, estudiem l'estabilitat de configuracions antiparal·leles de microtúbuls sotmesos a forces longitudinals, en presència de motors bipolars que sostenen col·lectivament l'estructura creant estocàsticament lligams entre els microtúbuls. La nostra descripció acobla el tràfic de motors en els microtúbuls que constitueixen l'estructura amb la dinàmica en la zona central, on els motors bipolars fan lliscar els microtúbuls antiparal·lels i generen la força necessària per sostenir l'estructura.

Per tal de determinar en quines condicions el fus de microtúbuls és estable, fem una anàlisi d'estabilitat lineal. Els resultats del nostre estudi demostren que, malgrat que les forces sempre es poden equilibrar internament en l'estructura, els motors bipolars no sempre poden suportar-la. Quan els motors no poden suportar les forces, els lligams que creen entre microtúbuls antiparal·lels es trenquen i els fus de microtúbuls col·lapsa. L'anàlisi d'estabilitat prediu que el col·lapse del fus es produeix a una concentració finita de motors. És a dir que existeix un llindar en la concentració de motors bipolars per sota del qual l'estructura col·lapsa. Aquest col·lapse ha estat observat experimentalment a nivell qualitatiu per diversos grups i, experiments més recents, han demostrat que el col·lapse es dóna a una concentració finita de motors, en concordància amb els nostres resultats. L'origen físic del col·lapse de l'estructura es troba en la dinàmica col·lectiva dels motors bipolars que sostenen el fus. Per concentracions prou elevades de motors bipolars, n'hi ha molts en la zona central del fus que estan lligant microtúbuls antiparal·lels i que, per tant, contribueixen a la generació de força. Hem vist anteriorment que els motors moleculars es desenganxen dels microtúbuls amb més freqüència quan una força s'aplica sobre ells. Degut a que per concentracions grans de motors, n'hi ha molts que es reparteixen la força total que han de suportar, la força que sosté cada un d'ells és petita i la freqüència amb què aquests es desenganxen dels microtúbuls no augmenta significativament. Quan un motor bipolar que lliga dos microtúbuls antiparal·lels es desenganxa d'un d'ells, ja no és capaç de generar forces per sostenir l'estructura. Si la concentració de motors és petita, hi ha pocs motors que sostenen l'estructura i, per tant, la força que cada un d'ells ha de resistir és gran. Com a conseqüència, els motors es desenganxen dels microtúbuls amb més freqüència i, per concentracions de motors prou petites, el flux de motors que s'enganxen als microtúbuls i lliguen microtúbuls antiparal·lels no és prou gran per equilibrar el flux de motors que se'n desenganxen. Aquesta situació porta a un trencament total dels lligams entre microtúbuls antiparal·lels i, en absència de motors bipolars suportant la força imposada externament, l'estructura col·lapsa.

Aquesta anàlisi emfatitza el paper clau que juga el fet que la cinètica dels motors depengui de la força aplicada sobre ells, en l'autoorganització de motors i microtúbuls. En les estructures resultants d'aquests fenòmens d'autoorganització, els motors generen esforços interns en l'estructura que afecten la cinètica dels mateixos motors que creen els esforços. Els nostres resultats posen de manifest que la influència dels esforços interns en la cinètica dels motors pot imposar limits molt restrictius a l'estabilitat d'estructures autoorganitzades.

Un cop determinades les condicions que porten al col·lapse de l'estructura, hem estudiat quin és el nombre de motors bipolars que sosté les estructures estables. Utilitzant valors experimentals, el nostre estudi demostra que malgrat que dos microtúbuls en una configuració antiparal·lela poden ser estables, el temps de vida de l'estructura és petit respecte a la durada del procés de divisió cel·lular. D'altra banda, els feixos estables de microtúbuls antiparal·lels estan caracteritzats per un temps de vida molt major, degut al major nombre de motors bipolars que sostenen l'estructura. Els nostres resultats suggereixen que el fus mitòtic ha d'estar constituït per feixos de microtúbuls antiparal·lels enlloc d'estar format per moltes parelles de microtúbuls antiparal·lels. Experimentalment, s'observa que el fus mitòtic conté diversos feixos consituïts per un nombre considerable de microtúbuls antiparal·lels. Malgrat que en aquest estudi no expliquem la formació dels feixos, els nostres resultats expliquen una de les seves possibles funcions, la de donar major estabilitat al fus mitòtic.

Més enllà de l'estudi d'estabilitat, hem analitzat el moviment de microtúbuls vers els pols generat pel lliscament de microtúbuls antiparal·lels induït pels motors bipolars. Els nostres resultats indiquen que la velocitat de lliscament dels microtúbuls disminueix si la concentració de motors bipolars és reduïda. Aquesta dismunició ha estat observada experimentalment i està en acord semi-quantitatiu amb els nostres resultats. Per concentracions grans de motors bipolars, el lliscament de l'estructura està caracteritzat per la velocitat màxima dels motors. Això és degut a que per concentracions grans la força que cada un dels motors sosté és petita i la seva velocitat no es veu afectada significativament. En aquest cas, els motors semblen estàtics en l'estructura ja que la seva velocitat respecte ella és la mateixa que la velocitat de lliscament de l'estructura. Aquesta aparent immobilitat dels motors ha estat observada experimentalment. La nostra anàlisi prediu que una disminució de la concentració de motors permetria l'observació del seu moviment.

L'estudi presentat en el capítol 9 constitueix doncs una descripció simple que explica, a partir d'un únic marc conceptual, diverses observacions en la mitosi, com el col·lapse del fus mitòtic, el moviment de microtúbuls vers els pols, l'aparent immobilitat dels motors en el fus mitòtic i la funcionalitat dels feixos de microtúbuls antiparal·lels.

A.6 Conclusions

En aquest treball hem estudiat com els generadors de forces moleculars treballen conjuntament per generar les forces que donen lloc a diversos moviments cel·lulars. Malgrat que cada un dels casos estudiats és diferent, tots ells tenen com a punt en comú l'acció col·lectiva dels generadors elementals de força i, com a conseqüència, presenten similituds en la seva dinàmica. En particular, hem demostrat que en tots els casos hi ha inestabilitats dinàmiques similars, degudes al caràcter col·lectiu de la dinàmica dels generadors de força elementals. El moviment saltatòri del bacteri *Listeria*, les oscil·lacions de tubs de membrana, el moviment oscil·latori de cromosomes i, fins i tot, el llindar per a l'extracció de tubs de membrana i el llindar associat al col·lapse del fus mitòtic, tenen tots el mateix origen. Comportaments similars han es-

tat observats en altres sistemes caracteritzats per la resistència col·lectiva d'enllaços moleculars a forces aplicades. L'adhesió cel·lular n'és un exemple. En aquest cas existeix un llindar de força per sobre del qual l'adhesió es perd totalment i les cèl·lules perden el contacte. Altres sistemes físics caracteritzats per friccions no-lineals presenten inestabilitats similars. En els sistemes biològics però, les forces que afecten la cinètica dels generadors de força elementals són les que produeixen ells mateixos i, per tant, les inestabilitats són intrínsiques a la seva dinàmica. El nostre estudi suggereix doncs que alguns aspectes dels moviments cel·lulars es poden entendre en un únic marc conceptual.

References

Aderem, A. and Underhill, D. M. (1999). Mechanisms of phagocytosis in macrophages. *Annu Rev Immunol*, 17:593–623.

Alberts, B., Bray, D., Lewis, J., Raff, M., Roberts, K., and Watson, J. D. (2004). *Molecular Biology of the Cell, 3rd Edition*. Garland, New York.

Allan, V. and Vale, R. (1994). Movement of membrane tubules along microtubules in vitro: evidence for specialised sites of motor attachment. *J Cell Sci*, 107 (Pt 7):1885–97.

Antonio, C., Ferby, I., Wilhelm, H., Jones, M., Karsenti, E., Nebreda, A. R., and Vernos, I. (2000). Xkid, a chromokinesin required for chromosome alignment on the metaphase plate. *Cell*, 102(4):425–35.

Aranson, I. S. and Tsimring, L. S. (2005). Pattern formation of microtubules and motors: inelastic interaction of polar rods. *Phys Rev E Stat Nonlin Soft Matter Phys*, 71(5 Pt 1):050901.

Aridor, M. and Hannan, L. A. (2000). Traffic jam: a compendium of human diseases that affect intracellular transport processes. *Traffic*, 1(11):836–51.

Aridor, M. and Hannan, L. A. (2002). Traffic jams ii: an update of diseases of intracellular transport. *Traffic*, 3(11):781–90.

Astumian, R. D. (1997). Thermodynamics and kinetics of a brownian motor. *Science*, 276(5314):917–22.

Ault, J. G., DeMarco, A. J., Salmon, E. D., and Rieder, C. L. (1991). Studies on the ejection properties of asters: astral microtubule turnover influences the oscillatory behavior and positioning of mono-oriented chromosomes. *J Cell Sci*, 99 (Pt 4):701–10.

Bajer, A. S. (1982). Functional autonomy of monopolar spindle and evidence for oscillatory movement in mitosis. *J Cell Biol*, 93(1):33–48.

Bamburg, J. R., McGough, A., and Ono, S. (1999). Putting a new twist on actin: Adf/cofilins modulate actin dynamics. *Trends Cell Biol*, 9(9):364–70.

Batchelor, G. K. (2000). *An Introduction to Fluid Dynamics*. Cambridge University Press.

Bernheim-Groswasser, A., Wiesner, S., Golsteyn, R. M., Carlier, M. F., and Sykes, C. (2002). The dynamics of actin-based motility depend on surface parameters. *Nature*, 417(6886):308–11.

Block, S. M., Asbury, C. L., Shaevitz, J. W., and Lang, M. J. (2003). Probing the kinesin reaction cycle with a 2d optical force clamp. *Proc Natl Acad Sci U S A*, 100(5):2351–6.

Bonifacino, J. S. and Glick, B. S. (2004). The mechanisms of vesicle budding and fusion. *Cell*, 116(2):153–66.

Borghi, N., Rossier, O., and Brochard-Wyart, F. (2003). Hydrodynamic extrusion of tubes from giant vesicles. *Europhys Lett*, 64(6):837–843.

Borisy, G. G. and Svitkina, T. M. (2000). Actin machinery: pushing the envelope. *Curr Opin Cell Biol*, 12(1):104–12.

Boukellal, H. (2004). *Propulsion par l'actine: Génération de force*. PhD thesis, Université Paris VI.

Boukellal, H., Campas, O., Joanny, J. F., Prost, J., and Sykes, C. (2004). Soft listeria: actin-based propulsion of liquid drops. *Phys Rev E Stat Nonlin Soft Matter Phys*, 69(6 Pt 1):061906.

Bray, D. (1992). *Cell Movements*. Garland, New York.

Bretscher, M. S. (1973). Membrane structure: some general principles. *Science*, 181(100):622–9.

Brochard, F. and Lennon, J. F. (1975). Frequency spectrum of flicker phenomenon in erythrocytes. *J Phys*, 36(11):1035–1047.

Brochard-Wyart, F. and de Gennes, P. G. (2002). Adhesion induced by mobile binders: dynamics. *Proc Natl Acad Sci U S A*, 99(12):7854–9.

Brochard-Wyart, F. and de Gennes, P. G. (2003). Unbinding of adhesive vesicles. *C R Physique*, 4(2):281–287.

Brouhard, G. J. and Hunt, A. J. (2005). Microtubule movements on the arms of mitotic chromosomes: polar ejection forces quantified in vitro. *Proc Natl Acad Sci U S A*, 102(39):13903–8.

Brouzes, E. and Farge, E. (2004). Interplay of mechanical deformation and patterned gene expression in developing embryos. *Curr Opin Genet Dev*, 14(4):367–374.

Busoni, L., Dupont, A., Symonds, C., Prost, J., and Cappello, G. (2006). Short time investigation of the neurospora-kinesin step. *J Phys: Condens Matter*, 18:1–10.

Camalet, S. and Julicher, F. (2000). Generic aspects of axonemal beating. *N J Phys*, 2:1–23.

Cameron, L. A., Footer, M. J., van Oudenaarden, A., and Theriot, J. A. (1999). Motility of acta protein-coated microspheres driven by actin polymerization. *Proc Natl Acad Sci U S A*, 96(9):4908–13.

Cameron, L. A., Giardini, P. A., Soo, F. S., and Theriot, J. A. (2000). Secrets of actin-based motility revealed by a bacterial pathogen. *Nat Rev Mol Cell Biol*, 1(2):110–9.

Campas, O., Casademunt, J., and Pagonabarraga, I. (2006a). Dynamic stability of spindles controlled by molecular motor kinetics. Submitted for publication.

Campas, O., Kafri, Y., Zeldovich, K. B., Casademunt, J., and Joanny, J. F. (2006b). Collective dynamics of interacting molecular motors. Accepted for publication in Phys. Rev. Lett.

Campas, O., Leduc, C., Bassereau, P., Casademunt, J., Joanny, J. F., and Prost, J. (2006c). Organitzation and traffic of molecular motors pulling membrane tubes. Article in preparation.

Campas, O., Leduc, C., Bassereau, P., Joanny, J. F., and Prost, J. (2006d). Collective oscillations of processive molecular motors. Article in preparation.

Campas, O. and Sens, P. (2006). Chromosome oscillations in mitosis. Submitted for publication.

Canham, P. B. (1970). The minimum energy of bending as a possible explanation of the biconcave shape of the human red blood cell. *J Theor Biol*, 26(1):61–81.

Cappello, G., Badoual, M., Ott, A., Prost, J., and Busoni, L. (2003). Kinesin motion in the absence of external forces characterized by interference total internal reflection microscopy. *Phys Rev E Stat Nonlin Soft Matter Phys*, 68(2 Pt 1):021907.

Carlsson, A. E. (2001). Growth of branched actin networks against obstacles. *Biophys J*, 81(4):1907–23.

Carlsson, A. E. (2003). Growth velocities of branched actin networks. *Biophys J*, 84(5):2907–18.

Carter, N. J. and Cross, R. A. (2005). Mechanics of the kinesin step. *Nature*, 435(7040):308–12.

Cassimeris, L., Rieder, C. L., and Salmon, E. D. (1994). Microtubule assembly and kinetochore directional instability in vertebrate monopolar spindles: implications for the mechanism of chromosome congression. *J Cell Sci*, 107 (Pt 1):285–97.

Champion, J. A. and Mitragotri, S. (2006). Role of target geometry in phagocytosis. *Proc Natl Acad Sci U S A*, 103(13):4930–4.

Chapman, D. (1975). Phase transitions and fluidity characteristics of lipids and cell membranes. *Q Rev Biophys*, 8(2):185–235.

Chowdhury, D., Santen, L., and Schadschneider, A. (2000). Statistical physics of vehicular traffic and some related systems. *Phys Rep*, 329(4-6):199–329.

Cole, N. B. and Lippincott-Schwartz, J. (1995). Organization of organelles and membrane traffic by microtubules. *Curr Opin Cell Biol*, 7(1):55–64.

Cuvelier, D., Chiaruttini, N., Bassereau, P., and Nassoy, P. (2005a). Pulling long tubes from firmly adhered vesicles. *Europhys Lett*, 71(6):1015–1021.

Cuvelier, D., Derenyi, I., Bassereau, P., and Nassoy, P. (2005b). Coalescence of membrane tethers: experiments, theory, and applications. *Biophys J*, 88(4):2714–26.

Dabora, S. L. and Sheetz, M. P. (1988). The microtubule-dependent formation of a tubulovesicular network with characteristics of the er from cultured cell extracts. *Cell*, 54(1):27–35.

de Gennes, P. G. (1979). *Scaling Concepts in Polymer Physics*. Cornell University Press.

de Gennes, P. G., Puech, P. H., and Brochard-Wyart, F. (2003). Adhesion induced by mobile stickers: A list of scenarios. *Langmuir*, 19(17):7112–7119.

Derenyi, I., Julicher, F., and Prost, J. (2002). Formation and interaction of membrane tubes. *Phys Rev Lett*, 88(23):238101.

Derrida, B. (1998). An exactly soluble non-equilibrium system: The asymmetric simple exclusion process. *Phys Rep*, 301(1-3):65–83.

Devaux, P. F. and Morris, R. (2004). Transmembrane asymmetry and lateral domains in biological membranes. *Traffic*, 5(4):241–6.

DoCarmo, M. (1995). *Differential Geometry of Curves and Surfaces*. Prentice-Hall, N. Jersey.

Dogterom, M., Kerssemakers, J. W., Romet-Lemonne, G., and Janson, M. E. (2005). Force generation by dynamic microtubules. *Curr Opin Cell Biol*, 17(1):67–74.

Dogterom, M. and Yurke, B. (1997). Measurement of the force-velocity relation for growing microtubules. *Science*, 278(5339):856–60.

Doi, M. and Edwards, S. F. (1986). *The Theory of Polymer Dynamics*. Oxford University Press.

Dommersnes, P. G., Orwar, O., Brochard-Wyart, F., and Joanny, J. F. (2005). Marangoni transport in lipid nanotubes. *Europhys Lett*, 70(2):271–277.

Duke, T. and Leibler, S. (1996). Motor protein mechanics: a stochastic model with minimal mechanochemical coupling. *Biophys J*, 71(3):1235–47.

Evans, E. (2001). Probing the relation between force–lifetime–and chemistry in single molecular bonds. *Annu Rev Biophys Biomol Struct*, 30:105–28.

Evans, E. and Rawicz, W. (1990). Entropy-driven tension and bending elasticity in condensed-fluid membranes. *Physical Review Letters*, 64(17):2094–2097.

Evans, E. and Ritchie, K. (1997). Dynamic strength of molecular adhesion bonds. *Biophys J*, 72(4):1541–55.

Evans, M. R. (1996). Bose-einstein condensation in disordered exclusion models and relation to traffic flow. *Europhys Lett*, 36(1):13–18.

Farge, E. (2003). Mechanical induction of twist in the drosophila foregut/stomodeal primordium. *Curr Biol*, 13(16):1365–1377.

Farsad, K. and Camilli, P. D. (2003). Mechanisms of membrane deformation. *Curr Opin Cell Biol*, 15(4):372–81.

Fisher, M. E. and Kolomeisky, A. B. (1999). The force exerted by a molecular motor. *Proc Natl Acad Sci U S A*, 96(12):6597–602.

Fournier, J. B., Ajdari, A., and Peliti, L. (2001). Effective-area elasticity and tension of micromanipulated membranes. *Phys Rev Lett*, 86(21):4970–3.

Fournier, J. B., Lacoste, D., and Raphael, E. (2004). Fluctuation spectrum of fluid membranes coupled to an elastic meshwork: jump of the effective surface tension at the mesh size. *Phys Rev Lett*, 92(1):018102.

Fujiwara, I., Takahashi, S., Tadakuma, H., Funatsu, T., and Ishiwata, S. (2002). Microscopic analysis of polymerization dynamics with individual actin filaments. *Nat Cell Biol*, 4(9):666–73.

Funabiki, H. and Murray, A. W. (2000). The xenopus chromokinesin xkid is essential for metaphase chromosome alignment and must be degraded to allow anaphase chromosome movement. *Cell*, 102(4):411–24.

Gadde, S. and Heald, R. (2004). Mechanisms and molecules of the mitotic spindle. *Curr Biol*, 14(18):R797–805.

Gerbal, F., Chaikin, P., Rabin, Y., and Prost, J. (2000a). An elastic analysis of listeria monocytogenes propulsion. *Biophys J*, 79(5):2259–75.

Gerbal, F., Laurent, V., Ott, A., Carlier, M. F., Chaikin, P., and Prost, J. (2000b). Measurement of the elasticity of the actin tail of listeria monocytogenes. *Eur Biophys J*, 29(2):134–40.

Gerbal, F., Noireaux, V., Sykes, C., Julicher, F., Chaikin, P., Ott, A., Prost, J., Golsteyn, R. M., Friederich, E., Louvard, D., Laurent, V., and Carlier, M. F. (1999). On the 'listeria' propulsion mechanism. *Pramana - Journal of Physics*, 53(1):155–170.

Giardini, P. A., Fletcher, D. A., and Theriot, J. A. (2003). Compression forces generated by actin comet tails on lipid vesicles. *Proc Natl Acad Sci U S A*, 100(11):6493–8.

Gillespie, D. T. (1976). General method for numerically simulating stochastic time evolution of coupled chemical-reactions. *J Comp Phys*, 22(4):403–434.

Girard, P. (2004). *Membranes hors d'équilibre: échanges et transport actif*. PhD thesis, Université Paris VII.

Goldberg, M. B. (2001). Actin-based motility of intracellular microbial pathogens. *Microbiol Mol Biol Rev*, 65(4):595–626, table of contents.

Goshima, G. and Vale, R. D. (2003). The roles of microtubule-based motor proteins in mitosis: comprehensive rnai analysis in the drosophila s2 cell line. *J Cell Biol*, 162(6):1003–16.

Gradshteyn, I. S. and Ryzhik, I. M. (2000). *Table of Integrals, Series, and Products*. Academic Press, 6th edition.

Grill, S. W., Kruse, K., and Julicher, F. (2005). Theory of mitotic spindle oscillations. *Phys Rev Lett*, 94(10):108104.

Gruss, O. J., Wittmann, M., Yokoyama, H., Pepperkok, R., Kufer, T., Sillje, H., Karsenti, E., Mattaj, I. W., and Vernos, I. (2002). Chromosome-induced microtubule assembly mediated by tpx2 is required for spindle formation in hela cells. *Nat Cell Biol*, 4(11):871–9.

Guckenheimer, J. and Holmes, P. (1990). *Nonlinear Oscillations, Dynamical Systems, and Bifurcations of Vector Fields*, volume 42 of *Applied Mathematical Sciences*. Springer-Verlag.

Hackney, D. D. (1994). The rate-limiting step in microtubule-stimulated atp hydrolysis by dimeric kinesin head domains occurs while bound to the microtubule. *J Biol Chem*, 269(23):16508–11.

Hayden, J. H., Bowser, S. S., and Rieder, C. L. (1990). Kinetochores capture astral microtubules during chromosome attachment to the mitotic spindle: direct visualization in live newt lung cells. *J Cell Biol*, 111(3):1039–45.

Hays, T. S., Wise, D., and Salmon, E. D. (1982). Traction force on a kinetochore at metaphase acts as a linear function of kinetochore fiber length. *J Cell Biol*, 93(2):374–89.

Helbing, D. (2001). Traffic and related self-driven many-particle systems. *Rev Mod Phys*, 73(4):1067–1141.

Helfrich, W. (1973). Elastic properties of lipid bilayers: theory and possible experiments. *Z Naturforsch [C]*, 28(11):693–703.

Helfrich, W. (1985). Effect of thermal undulations on the rigidity of fluid membranes and interfaces. *J Phys*, 46(7):1263–1268.

Hirokawa, N. (1996). Organelle transport along microtubules - the role of kifs. *Trends Cell Biol*, 6(4):135–41.

Hirokawa, N. (1998). Kinesin and dynein superfamily proteins and the mechanism of organelle transport. *Science*, 279(5350):519–26.

Howard, J. (2001). *Mechanics of Motor Proteins and the Cytoskeleton*. Sinauer Press: Sunderland, Massachusetts.

Howard, J., Hudspeth, A. J., and Vale, R. D. (1989). Movement of microtubules by single kinesin molecules. *Nature*, 342(6246):154–8.

Hua, W., Chung, J., and Gelles, J. (2002). Distinguishing inchworm and hand-over-hand processive kinesin movement by neck rotation measurements. *Science*, 295(5556):844–8.

Huxley, A. F. and Simmons, R. M. (1971). Proposed mechanism of force generation in striated muscle. *Nature*, 233(5321):533–8.

Hyman, A. A. and Karsenti, E. (1996). Morphogenetic properties of microtubules and mitotic spindle assembly. *Cell*, 84(3):401–10.

Inoue, S. and Salmon, E. D. (1995). Force generation by microtubule assembly/disassembly in mitosis and related movements. *Mol Biol Cell*, 6(12):1619–40.

Israelachvili, J. (1992). *Intermolecular and Surface Forces*. Academic Press (London), 2nd edition.

Janson, M. E., de Dood, M. E., and Dogterom, M. (2003). Dynamic instability of microtubules is regulated by force. *J Cell Biol*, 161(6):1029–34.

Janson, M. E. and Dogterom, M. (2004). Scaling of microtubule force-velocity curves obtained at different tubulin concentrations. *Phys Rev Lett*, 92(24):248101.

Joglekar, A. P. and Hunt, A. J. (2002). A simple, mechanistic model for directional instability during mitotic chromosome movements. *Biophys J*, 83(1):42–58.

Jolimaitre, P., Roux, A., Blanpain, A., Leduc, C., Bassereau, P., and Bourel-Bonnet, L. (2005). Synthesis and preliminary physical applications of a rhodamin-biotin phosphatidylethanolamine, an easy attainable lipid double probe. *Chem Phys Lipids*, 133(2):215–23.

Julicher, F., Ajdari, A., and Prost, J. (1997). Modeling molecular motors. *Rev Mod Phys*, 69(4):1269–1281.

Julicher, F. and Prost, J. (1995). Cooperative molecular motors. *Physical Review Letters*, 75(13):2618–2621.

Julicher, F. and Prost, J. (1997). Spontaneous oscillations of collective molecular motors. *Phys. Rev. Lett.*, 78(23):4510–4513.

Kamien, R. D. (2002). The geometry of soft materials: a primer. *Rev Mod Phys*, 74(4):953–971.

Kapitein, L. C., Peterman, E. J., Kwok, B. H., Kim, J. H., Kapoor, T. M., and Schmidt, C. F. (2005). The bipolar mitotic kinesin eg5 moves on both microtubules that it crosslinks. *Nature*, 435(7038):114–8.

Kapoor, T. M. and Compton, D. A. (2002). Searching for the middle ground: mechanisms of chromosome alignment during mitosis. *J Cell Biol*, 157(4):551–6.

Kapoor, T. M., Mayer, T. U., Coughlin, M. L., and Mitchison, T. J. (2000). Probing spindle assembly mechanisms with monastrol, a small molecule inhibitor of the mitotic kinesin, eg5. *J Cell Biol*, 150(5):975–88.

Kapoor, T. M. and Mitchison, T. J. (2001). Eg5 is static in bipolar spindles relative to tubulin: evidence for a static spindle matrix. *J Cell Biol*, 154(6):1125–33.

Karsenti, E. and Vernos, I. (2001). The mitotic spindle: a self-made machine. *Science*, 294(5542):543–7.

Khodjakov, A., Gabashvili, I. S., and Rieder, C. L. (1999). "dumb" versus "smart" kinetochore models for chromosome congression during mitosis in vertebrate somatic cells. *Cell Motil Cytoskeleton*, 43(3):179–85.

Khodjakov, A. and Rieder, C. L. (1996). Kinetochores moving away from their associated pole do not exert a significant pushing force on the chromosome. *J Cell Biol*, 135(2):315–27.

Kiehart, D. P. and Franke, J. D. (2002). Actin dynamics: the arp2/3 complex branches out. *Curr Biol*, 12(16):R557–9.

Klumpp, S. and Lipowsky, R. (2005). Cooperative cargo transport by several molecular motors. *Proc Natl Acad Sci U S A*, 102(48):17284–9.

Kocks, C., Gouin, E., Tabouret, M., Berche, P., Ohayon, H., and Cossart, P. (1992). L. monocytogenes-induced actin assembly requires the acta gene product, a surface protein. *Cell*, 68(3):521–31.

Kocks, C., Hellio, R., Gounon, P., Ohayon, H., and Cossart, P. (1993). Polarized distribution of listeria monocytogenes surface protein acta at the site of directional actin assembly. *J Cell Sci*, 105 (Pt 3):699–710.

Koshland, D. E., Mitchison, T. J., and Kirschner, M. W. (1988). Polewards chromosome movement driven by microtubule depolymerization in vitro. *Nature*, 331(6156):499–504.

Koster, G., Cacciuto, A., Derenyi, I., Frenkel, D., and Dogterom, M. (2005). Force barriers for membrane tube formation. *Phys Rev Lett*, 94(6):068101.

Koster, G., VanDuijn, M., Hofs, B., and Dogterom, M. (2003). Membrane tube formation from giant vesicles by dynamic association of motor proteins. *Proc Natl Acad Sci U S A*, 100(26):15583–8.

Kramers, H. A. (1940). Brownian motion in a field of force and the diffusion model of chemical reactions. *Physica (Utrecht)*, 7:284–304.

Kruse, K., Joanny, J. F., Julicher, F., Prost, J., and Sekimoto, K. (2004). Asters, vortices, and rotating spirals in active gels of polar filaments. *Phys Rev Lett*, 92(7):078101.

Kruse, K. and Julicher, F. (2000). Actively contracting bundles of polar filaments. *Phys Rev Lett*, 85(8):1778–81.

Kwok, R. and Evans, E. (1981). Thermoelasticity of large lecithin bilayer vesicles. *Biophys J*, 35(3):637–52.

Landau, L. D. and Lifshitz, E. M. (1986). *Theory of Elasticity, 3rd Edition*, volume 7 of *Landau, L.D. Course of Theoretical Physics*. Butterworth-Heinemann.

Lane, J. D. and Allan, V. J. (1999). Microtubule-based endoplasmic reticulum motility in xenopus laevis: activation of membrane-associated kinesin during development. *Mol Biol Cell*, 10(6):1909–22.

Leduc, C. (2005). *Système biomimétique d'intermédiaires de transport tubulaires: Etude quantitative*. PhD thesis, Université Paris VII.

Leduc, C., Campas, O., Zeldovich, K. B., Roux, A., Jolimaitre, P., Bourel-Bonnet, L., Goud, B., Joanny, J. F., Bassereau, P., and Prost, J. (2004). Cooperative extraction of membrane nanotubes by molecular motors. *Proc Natl Acad Sci U S A*, 101(49):17096–101.

Lee, H. Y. and Kardar, M. (2001). Macroscopic equations for pattern formation in mixtures of microtubules and molecular motors. *Phys Rev E Stat Nonlin Soft Matter Phys*, 64(5 Pt 2):056113.

Leibler, S. and Huse, D. A. (1993). Porters versus rowers: a unified stochastic model of motor proteins. *J Cell Biol*, 121(6):1357–68.

Levesque, A. A. and Compton, D. A. (2001). The chromokinesin kid is necessary for chromosome arm orientation and oscillation, but not congression, on mitotic spindles. *J Cell Biol*, 154(6):1135–46.

Lighthill, M. and Whitham, G. (1955). On kinematic waves: Ii. a theory of traffic flow on long crowded roads. *Proc R Soc London A*, 229(1178):317–345.

Lipowsky, R. (2000). Universal aspects of the chemomechanical coupling for molecular motors. *Phys Rev Lett*, 85(20):4401–4.

Lipowsky, R., Klumpp, S., and Nieuwenhuizen, T. M. (2001). Random walks of cytoskeletal motors in open and closed compartments. *Phys Rev Lett*, 87(10):108101.

Lipowsky, R. and Sackmann, E., editors (1995). *Structure and Dynamics of Membranes: from Cells to Vesicles*, volume 1A. Elsevier sciences B.V.

Lippincott-Schwartz, J., Cole, N. B., Marotta, A., Conrad, P. A., and Bloom, G. S. (1995). Kinesin is the motor for microtubule-mediated golgi-to-er membrane traffic. *J Cell Biol*, 128(3):293–306.

Lippincott-Schwartz, J., Donaldson, J. G., Schweizer, A., Berger, E. G., Hauri, H. P., Yuan, L. C., and Klausner, R. D. (1990). Microtubule-dependent retrograde transport of proteins into the er in the presence of brefeldin a suggests an er recycling pathway. *Cell*, 60(5):821–36.

Littlefield, R. and Fowler, V. M. (2002). A minor actin catastrophe. *Nat Cell Biol*, 4(9):E209–11.

Liverpool, T. B. and Marchetti, M. C. (2003). Instabilities of isotropic solutions of active polar filaments. *Phys Rev Lett*, 90(13):138102.

Lodish, H., Berk, A., Zipursky, L., Matsudaira, P., Baltimore, D., and Darnell, J. (2000). *Molecular Cell Biology, 4th Edition*. W.H. Freeman and Co.

Logarinho, E., Bousbaa, H., Dias, J. M., Lopes, C., Amorim, I., Antunes-Martins, A., and Sunkel, C. E. (2004). Different spindle checkpoint proteins monitor microtubule attachment and tension at kinetochores in drosophila cells. *J Cell Sci*, 117(Pt 9):1757–71.

Mahadevan, L. and Matsudaira, P. (2000). Motility powered by supramolecular springs and ratchets. *Science*, 288(5463):95–100.

Mahadevan, L. and Mitchison, T. J. (2005). Cell biology: powerful curves. *Nature*, 435(7044):895–7.

Mallik, R., Carter, B. C., Lex, S. A., King, S. J., and Gross, S. P. (2004). Cytoplasmic dynein functions as a gear in response to load. *Nature*, 427(6975):649–52.

Marcy, Y., Prost, J., Carlier, M. F., and Sykes, C. (2004). Forces generated during actin-based propulsion: a direct measurement by micromanipulation. *Proc Natl Acad Sci U S A*, 101(16):5992–7.

Mastronarde, D. N., McDonald, K. L., Ding, R., and McIntosh, J. R. (1993). Interpolar spindle microtubules in ptk cells. *J Cell Biol*, 123(6 Pt 1):1475–89.

McGough, A., Pope, B., Chiu, W., and Weeds, A. (1997). Cofilin changes the twist of f-actin: implications for actin filament dynamics and cellular function. *J Cell Biol*, 138(4):771–81.

McNiven, M. A. (1998). Dynamin: a molecular motor with pinchase action. *Cell*, 94(2):151–4.

Mitchison, T. J. and Cramer, L. P. (1996). Actin-based cell motility and cell locomotion. *Cell*, 84(3):371–9.

Mitchison, T. J., Maddox, P., Groen, A., Cameron, L., Perlman, Z., Ohi, R., Desai, A., Salmon, E. D., and Kapoor, T. M. (2004). Bipolarization and poleward flux correlate during xenopus extract spindle assembly. *Mol Biol Cell*, 15(12):5603–15.

Mitchison, T. J. and Salmon, E. D. (2001). Mitosis: a history of division. *Nat Cell Biol*, 3(1):E17–21.

Miyamoto, D. T., Perlman, Z. E., Burbank, K. S., Groen, A. C., and Mitchison, T. J. (2004). The kinesin eg5 drives poleward microtubule flux in xenopus laevis egg extract spindles. *J Cell Biol*, 167(5):813–8.

Miyata, H., Nishiyama, S., Akashi, K., and K Kinosita, J. (1999). Protrusive growth from giant liposomes driven by actin polymerization. *Proc Natl Acad Sci U S A*, 96(5):2048–53.

Mogilner, A. and Oster, G. (1996). Cell motility driven by actin polymerization. *Biophys J*, 71(6):3030–45.

Mogilner, A. and Oster, G. (2003a). Force generation by actin polymerization ii: the elastic ratchet and tethered filaments. *Biophys J*, 84(3):1591–605.

Mogilner, A. and Oster, G. (2003b). Polymer motors: pushing out the front and pulling up the back. *Curr Biol*, 13(18):R721–33.

Morse, P. M. and Feshbach, H. (1953). *Methods of Theoretical Physics, Part I*. McGraw-Hill.

Mullins, R. D., Heuser, J. A., and Pollard, T. D. (1998). The interaction of arp2/3 complex with actin: nucleation, high affinity pointed end capping, and formation of branching networks of filaments. *Proc Natl Acad Sci U S A*, 95(11):6181–6.

Murase, M. (1992). *The Dynamics of Cellular Motility*. Nonlinear Science. Wiley, New York.

Murray, A. W. and Mitchison, T. J. (1994). Mitosis. kinetochores pass the iq test. *Curr Biol*, 4(1):38–41.

Muto, E., Sakai, H., and Kaseda, K. (2005). Long-range cooperative binding of kinesin to a microtubule in the presence of atp. *J Cell Biol*, 168(5):691–6.

Nagel, K. (1996). Particle hopping models and traffic flow theory. *Physical Review. E. Statistical Physics, Plasmas, Fluids, And Related Interdisciplinary Topics*, 53(5):4655–4672.

Nedelec, F. (2002). Computer simulations reveal motor properties generating stable antiparallel microtubule interactions. *J Cell Biol*, 158(6):1005–15.

Nedelec, F., Surrey, T., and Karsenti, E. (2003). Self-organisation and forces in the microtubule cytoskeleton. *Curr Opin Cell Biol*, 15(1):118–24.

Nedelec, F. J., Surrey, T., Maggs, A. C., and Leibler, S. (1997). Self-organization of microtubules and motors. *Nature*, 389(6648):305–8.

Nelson, D., Weinberg, S., and Piran, T., editors (2004). *Statistical Mechanics of Membranes and Surfaces*. World Scientific Publishing, 2nd edition.

Nicklas, R. B. (1983). Measurements of the force produced by the mitotic spindle in anaphase. *J Cell Biol*, 97(2):542–8.

Nicklas, R. B. (1997). How cells get the right chromosomes. *Science*, 275(5300):632–7.

Nicklas, R. B., Campbell, M. S., Ward, S. C., and Gorbsky, G. J. (1998). Tension-sensitive kinetochore phosphorylation in vitro. *J Cell Sci*, 111 (Pt 21):3189–96.

Nishinari, K., Okada, Y., Schadschneider, A., and Chowdhury, D. (2005). Intracellular transport of single-headed molecular motors kif1a. *Phys Rev Lett*, 95(11):118101.

Nishiyama, M., Higuchi, H., and Yanagida, T. (2002). Chemomechanical coupling of the forward and backward steps of single kinesin molecules. *Nat Cell Biol*, 4(10):790–7.

Noireaux, V., Golsteyn, R. M., Friederich, E., Prost, J., Antony, C., Louvard, D., and Sykes, C. (2000). Growing an actin gel on spherical surfaces. *Biophys J*, 78(3):1643–54.

Olbrich, K., Rawicz, W., Needham, D., and Evans, E. (2000). Water permeability and mechanical strength of polyunsaturated lipid bilayers. *Biophys J*, 79(1):321–7.

Ostergren, G. (1951). The mechanism of co-orientation in bivalents and multivalents. *Hereditas*, 37:85–156.

Pantaloni, D., Clainche, C. L., and Carlier, M. F. (2001). Mechanism of actin-based motility. *Science*, 292(5521):1502–6.

Parmeggiani, A., Franosch, T., and Frey, E. (2003). Phase coexistence in driven one-dimensional transport. *Phys Rev Lett*, 90(8):086601.

Peskin, C. S., Odell, G. M., and Oster, G. F. (1993). Cellular motions and thermal fluctuations: the brownian ratchet. *Biophys J*, 65(1):316–24.

Pfeffer, S. R. (1999). Transport-vesicle targeting: tethers before snares. *Nat Cell Biol*, 1(1):E17–22.

Pinsky, B. A. and Biggins, S. (2005). The spindle checkpoint: tension versus attachment. *Trends Cell Biol*, 15(9):486–93.

Polishchuk, E. V., Pentima, A. D., Luini, A., and Polishchuk, R. S. (2003). Mechanism of constitutive export from the golgi: bulk flow via the formation, protru-

sion, and en bloc cleavage of large trans-golgi network tubular domains. *Mol Biol Cell*, 14(11):4470–85.

Pollard, T. D., Blanchoin, L., and Mullins, R. D. (2000). Molecular mechanisms controlling actin filament dynamics in nonmuscle cells. *Annu Rev Biophys Biomol Struct*, 29:545–76.

Pollard, T. D. and Borisy, G. G. (2003). Cellular motility driven by assembly and disassembly of actin filaments. *Cell*, 112(4):453–65.

Powers, T. R., Huber, G., and Goldstein, R. E. (2002). Fluid-membrane tethers: minimal surfaces and elastic boundary layers. *Phys Rev E Stat Nonlin Soft Matter Phys*, 65(4 Pt 1):041901.

Press, W. H., Flannery, B. P., Teukolsky, S. A., and Vetterling, W. T. (2002). *Numerical Recipes in C : The Art of Scientific Computing, 2nd Edition*. Cambridge University Press.

Prost, J. (2001). The physics of listeria propulsion. In *Physics of Biomolecules and Cells*, Les Houches Lecture Notes, pages 215–236. Springer-Verlag.

Rambourg, A., Clermont, Y., and Hermo, L. (1979). Three-dimensional architecture of the golgi apparatus in sertoli cells of the rat. *Am J Anat*, 154(4):455–76.

Rawicz, W., Olbrich, K. C., McIntosh, T., Needham, D., and Evans, E. (2000). Effect of chain length and unsaturation on elasticity of lipid bilayers. *Biophys J*, 79(1):328–39.

Ray, S., Meyhofer, E., Milligan, R. A., and Howard, J. (1993). Kinesin follows the microtubule's protofilament axis. *J Cell Biol*, 121(5):1083–93.

Rieder, C. L. (1990). Formation of the astral mitotic spindle: ultrastructural basis for the centrosome-kinetochore interaction. *Electron Microsc Rev*, 3(2):269–300.

Rieder, C. L. and Alexander, S. P. (1990). Kinetochores are transported poleward along a single astral microtubule during chromosome attachment to the spindle in newt lung cells. *J Cell Biol*, 110(1):81–95.

Rieder, C. L., Davison, E. A., Jensen, L. C., Cassimeris, L., and Salmon, E. D. (1986). Oscillatory movements of monooriented chromosomes and their position relative to the spindle pole result from the ejection properties of the aster and half-spindle. *J Cell Biol*, 103(2):581–91.

Rieder, C. L. and Khodjakov, A. (2003). Mitosis through the microscope: advances in seeing inside live dividing cells. *Science*, 300(5616):91–6.

Rieder, C. L. and Salmon, E. D. (1994). Motile kinetochores and polar ejection forces dictate chromosome position on the vertebrate mitotic spindle. *J Cell Biol*, 124(3):223–33.

Rieder, C. L. and Salmon, E. D. (1998). The vertebrate cell kinetochore and its roles during mitosis. *Trends Cell Biol*, 8(8):310–8.

Roos, W., Campas, O., Bassereau, P., and Cappello, G. (2006). Interaction dependent attachment/detachment kinetics of kinesin motors. Article in preparation.

Rossier, O., Cuvelier, D., Borghi, N., Puech, P. H., Derenyi, I., Buguin, A., Nassoy, P., and Brochard-Wyart, F. (2003). Giant vesicles under flows: Extrusion and retraction of tubes. *Langmuir*, 19(3):575–584.

Roux, A., Cappello, G., Cartaud, J., Prost, J., Goud, B., and Bassereau, P. (2002). A minimal system allowing tubulation with molecular motors pulling on giant liposomes. *Proc Natl Acad Sci U S A*, 99(8):5394–9.

Sackmann, E. (1990). Molecular and global structure and dynamics of membranes and lipid bilayers. *Can J Phys*, 68(9):999–1012.

Safran, S. A. (1999). Curvature elasticity of thin films. *Adv Phys*, 48(4):395–448.

Safran, S. A. (2003). *Statistical Thermodynamics of Surfaces, Interfaces, and Membranes*. Westview Press.

Sandre, O., Moreaux, L., and Brochard-Wyart, F. (1999). Dynamics of transient pores in stretched vesicles. *Proc Natl Acad Sci U S A*, 96(19):10591–6.

Schiff, P. B. and Horwitz, S. B. (1980). Taxol stabilizes microtubules in mouse fibroblast cells. *Proc Natl Acad Sci U S A*, 77(3):1561–5.

Schluter, K., Jockusch, B. M., and Rothkegel, M. (1997). Profilins as regulators of actin dynamics. *Biochim Biophys Acta*, 1359(2):97–109.

Schmittmann, B. and Zia, R. K. P. (1995). Statistical mechanics of driven diffusive systems. In Domb, C. and Lebowitz, J. L., editors, *Phase Transitions and Critical Phenomena*, volume 17. Academic (New York).

Schnitzer, M. J. and Block, S. M. (1997). Kinesin hydrolyses one atp per 8-nm step. *Nature*, 388(6640):386–90.

Schnitzer, M. J., Visscher, K., and Block, S. M. (2000). Force production by single kinesin motors. *Nat Cell Biol*, 2(10):718–23.

Scholey, J. M., Brust-Mascher, I., and Mogilner, A. (2003). Cell division. *Nature*, 422(6933):746–52.

Schwartz, I. M., Ehrenberg, M., Bindschadler, M., and McGrath, J. L. (2004). The role of substrate curvature in actin-based pushing forces. *Curr Biol*, 14(12):1094–8.

Sciaky, N., Presley, J., Smith, C., Zaal, K. J., Cole, N., Moreira, J. E., Terasaki, M., Siggia, E., and Lippincott-Schwartz, J. (1997). Golgi tubule traffic and the effects of brefeldin a visualized in living cells. *J Cell Biol*, 139(5):1137–55.

Sekimoto, K., Prost, J., Julicher, F., Boukellal, H., and Bernheim-Grosswasser, A. (2004). Role of tensile stress in actin gels and a symmetry-breaking instability. *Eur Phys J E Soft Matter*, 13(3):247–59.

Sens, P. and Turner, M. S. (2006). Budded membrane microdomains as tension regulators. *Phys Rev E Stat Nonlin Soft Matter Phys*, 73(3 Pt 1):031918.

Sharp, D. J., McDonald, K. L., Brown, H. M., Matthies, H. J., Walczak, C., Vale, R. D., Mitchison, T. J., and Scholey, J. M. (1999). The bipolar kinesin, klp61f, cross-links microtubules within interpolar microtubule bundles of drosophila embryonic mitotic spindles. *J Cell Biol*, 144(1):125–38.

Sharp, D. J., Rogers, G. C., and Scholey, J. M. (2000a). Cytoplasmic dynein is required for poleward chromosome movement during mitosis in drosophila embryos. *Nat Cell Biol*, 2(12):922–30.

Sharp, D. J., Rogers, G. C., and Scholey, J. M. (2000b). Microtubule motors in mitosis. *Nature*, 407(6800):41–7.

Skibbens, R. V., Rieder, C. L., and Salmon, E. D. (1995). Kinetochore motility after severing between sister centromeres using laser microsurgery: evidence

that kinetochore directional instability and position is regulated by tension. *J Cell Sci*, 108 (Pt 7):2537–48.

Skibbens, R. V. and Salmon, E. D. (1997). Micromanipulation of chromosomes in mitotic vertebrate tissue cells: tension controls the state of kinetochore movement. *Exp Cell Res*, 235(2):314–24.

Skibbens, R. V., Skeen, V. P., and Salmon, E. D. (1993). Directional instability of kinetochore motility during chromosome congression and segregation in mitotic newt lung cells: a push-pull mechanism. *J Cell Biol*, 122(4):859–75.

Small, J. V., Stradal, T., Vignal, E., and Rottner, K. (2002). The lamellipodium: where motility begins. *Trends Cell Biol*, 12(3):112–20.

Smith, G. A., Portnoy, D. A., and Theriot, J. A. (1995). Asymmetric distribution of the listeria monocytogenes acta protein is required and sufficient to direct actin-based motility. *Mol Microbiol*, 17(5):945–51.

Snider, J., Lin, F., Zahedi, N., Rodionov, V., Yu, C. C., and Gross, S. P. (2004). Intracellular actin-based transport: how far you go depends on how often you switch. *Proc Natl Acad Sci U S A*, 101(36):13204–9.

Solari, C. A., Ganguly, S., Kessler, J. O., Michod, R. E., and Goldstein, R. E. (2006). Multicellularity and the functional interdependence of motility and molecular transport. *Proc Natl Acad Sci U S A*, 103(5):1353–8.

Spohn, H. (1991). *Large Scale Dynamics of Interacting Particles*. Springer (New York).

Stossel, T. P. (1993). On the crawling of animal cells. *Science*, 260(5111):1086–94.

Surrey, T., Nedelec, F., Leibler, S., and Karsenti, E. (2001). Physical properties determining self-organization of motors and microtubules. *Science*, 292(5519):1167–71.

Svitkina, T. M. and Borisy, G. G. (1999). Arp2/3 complex and actin depolymerizing factor/cofilin in dendritic organization and treadmilling of actin filament array in lamellipodia. *J Cell Biol*, 145(5):1009–26.

Svoboda, K., Schmidt, C. F., Schnapp, B. J., and Block, S. M. (1993). Direct observation of kinesin stepping by optical trapping interferometry. *Nature*, 365(6448):721–7.

Taunton, J., Rowning, B. A., Coughlin, M. L., Wu, M., Moon, R. T., Mitchison, T. J., and Larabell, C. A. (2000). Actin-dependent propulsion of endosomes and lysosomes by recruitment of n-wasp. *J Cell Biol*, 148(3):519–30.

Terasaki, M., Chen, L. B., and Fujiwara, K. (1986). Microtubules and the endoplasmic reticulum are highly interdependent structures. *J Cell Biol*, 103(4):1557–68.

Thorn, K. S., Ubersax, J. A., and Vale, R. D. (2000). Engineering the processive run length of the kinesin motor. *J Cell Biol*, 151(5):1093–100.

Tilney, L. G. and Portnoy, D. A. (1989). Actin filaments and the growth, movement, and spread of the intracellular bacterial parasite, listeria monocytogenes. *J Cell Biol*, 109(4 Pt 1):1597–608.

Tokai, N., Fujimoto-Nishiyama, A., Toyoshima, Y., Yonemura, S., Tsukita, S., Inoue, J., and Yamamota, T. (1996). Kid, a novel kinesin-like dna binding protein, is localized to chromosomes and the mitotic spindle. *Embo J*, 15(3):457–67.

Trichet, L., Campas, O., Sykes, C., and Plastino, J. (2006). Vasp governs actin dynamics by modulating filament anchoring. Submitted for publication.

Upadhyaya, A., Chabot, J. R., Andreeva, A., Samadani, A., and van Oudenaarden, A. (2003). Probing polymerization forces by using actin-propelled lipid vesicles. *Proc Natl Acad Sci U S A*, 100(8):4521–6.

Upadhyaya, A. and Sheetz, M. P. (2004). Tension in tubulovesicular networks of golgi and endoplasmic reticulum membranes. *Biophys J*, 86(5):2923–8.

Upadhyaya, A. and van Oudenaarden, A. (2003). Biomimetic systems for studying actin-based motility. *Curr Biol*, 13(18):R734–44.

Urbakh, M., Klafter, J., Gourdon, D., and Israelachvili, J. (2004). The nonlinear nature of friction. *Nature*, 430(6999):525–8.

Vale, R. D. (2003). The molecular motor toolbox for intracellular transport. *Cell*, 112(4):467–80.

Vale, R. D., Funatsu, T., Pierce, D. W., Romberg, L., Harada, Y., and Yanagida, T. (1996). Direct observation of single kinesin molecules moving along microtubules. *Nature*, 380(6573):451–3.

Vale, R. D. and Milligan, R. A. (2000). The way things move: looking under the hood of molecular motor proteins. *Science*, 288(5463):88–95.

Vale, R. D., Soll, D. R., and Gibbons, I. R. (1989). One-dimensional diffusion of microtubules bound to flagellar dynein. *Cell*, 59(5):915–25.

Valentine, M. T., Fordyce, P. M., Krzysiak, T. C., Gilbert, S. P., and Block, S. M. (2006). Individual dimers of the mitotic kinesin motor eg5 step processively and support substantial loads in vitro. *Nat Cell Biol*, 8(5):470–6.

van der Gucht, J., Paluch, E., Plastino, J., and Sykes, C. (2005). Stress release drives symmetry breaking for actin-based movement. *Proc Natl Acad Sci U S A*, 102(22):7847–52.

van Kampen, N. G. (2004). *Stochastic Processes in Physics and Chemistry*. North Holland, Amsterdam.

van Oudenaarden, A. and Theriot, J. A. (1999). Cooperative symmetry-breaking by actin polymerization in a model for cell motility. *Nat Cell Biol*, 1(8):493–9.

Vedrenne, C. and Hauri, H. P. (2006). Morphogenesis of the endoplasmic reticulum: beyond active membrane expansion. *Traffic*, 7(6):639–46.

Veigel, C., Molloy, J. E., Schmitz, S., and Kendrick-Jones, J. (2003). Load-dependent kinetics of force production by smooth muscle myosin measured with optical tweezers. *Nat Cell Biol*, 5(11):980–6.

Veigel, C., Schmitz, S., Wang, F., and Sellers, J. R. (2005). Load-dependent kinetics of myosin-v can explain its high processivity. *Nat Cell Biol*, 7(9):861–9.

Verkhovsky, A. B., Svitkina, T. M., and Borisy, G. G. (1999). Self-polarization and directional motility of cytoplasm. *Curr Biol*, 9(1):11–20.

Vilfan, A. and Duke, T. (2003). Instabilities in the transient response of muscle. *Biophys J*, 85(2):818–27.

Vilfan, A., Frey, E., and Schwabl, F. (1998). Elastically coupled molecular motors. *Eur Phys J B*, 3(4):535–546.

Vilfan, A., Frey, E., Schwabl, F., Thormahlen, M., Song, Y. H., and Mandelkow, E. (2001). Dynamics and cooperativity of microtubule decoration by the motor protein kinesin. *J Mol Biol*, 312(5):1011–26.

Visscher, K., Schnitzer, M. J., and Block, S. M. (1999). Single kinesin molecules studied with a molecular force clamp. *Nature*, 400(6740):184–9.

Waterman-Storer, C. M. and Salmon, E. D. (1998). Endoplasmic reticulum membrane tubules are distributed by microtubules in living cells using three distinct mechanisms. *Curr Biol*, 8(14):798–806.

Waters, J. C., Skibbens, R. V., and Salmon, E. D. (1996). Oscillating mitotic newt lung cell kinetochores are, on average, under tension and rarely push. *J Cell Sci*, 109 (Pt 12):2823–31.

Weaver, A. M., Young, M. E., Lee, W. L., and Cooper, J. A. (2003). Integration of signals to the arp2/3 complex. *Curr Opin Cell Biol*, 15(1):23–30.

Welch, M. D., DePace, A. H., Verma, S., Iwamatsu, A., and Mitchison, T. J. (1997). The human arp2/3 complex is composed of evolutionarily conserved subunits and is localized to cellular regions of dynamic actin filament assembly. *J Cell Biol*, 138(2):375–84.

Welch, M. D., Rosenblatt, J., Skoble, J., Portnoy, D. A., and Mitchison, T. J. (1998). Interaction of human arp2/3 complex and the listeria monocytogenes acta protein in actin filament nucleation. *Science*, 281(5373):105–8.

Welte, M. A. (2004). Bidirectional transport along microtubules. *Curr Biol*, 14(13):R525–37.

White, J., Johannes, L., Mallard, F., Girod, A., Grill, S., Reinsch, S., Keller, P., Tzschaschel, B., Echard, A., Goud, B., and Stelzer, E. H. (1999). Rab6 coordinates a novel golgi to er retrograde transport pathway in live cells. *J Cell Biol*, 147(4):743–60.

Widom, B., Bhimalapuram, P., and Koga, K. (2003). The hydrophobic effect. *Phys Chem Chem Phys*, 5:3085–3093.

Wiesner, S., Helfer, E., Didry, D., Ducouret, G., Lafuma, F., Carlier, M. F., and Pantaloni, D. (2003). A biomimetic motility assay provides insight into the mechanism of actin-based motility. *J Cell Biol*, 160(3):387–98.

Winey, M., Mamay, C. L., O'Toole, E. T., Mastronarde, D. N., T H Giddings, J., McDonald, K. L., and McIntosh, J. R. (1995). Three-dimensional ultrastructural analysis of the saccharomyces cerevisiae mitotic spindle. *J Cell Biol*, 129(6):1601–15.

Wittmann, T., Hyman, A., and Desai, A. (2001). The spindle: a dynamic assembly of microtubules and motors. *Nat Cell Biol*, 3(1):E28–34.

Yajima, J., Edamatsu, M., Watai-Nishii, J., Tokai-Nishizumi, N., Yamamoto, T., and Toyoshima, Y. Y. (2003). The human chromokinesin kid is a plus end-directed microtubule-based motor. *Embo J*, 22(5):1067–74.

Yarar, D., To, W., Abo, A., and Welch, M. D. (1999). The wiskott-aldrich syndrome protein directs actin-based motility by stimulating actin nucleation with the arp2/3 complex. *Curr Biol*, 9(10):555–8.

Yildiz, A., Tomishige, M., Vale, R. D., and Selvin, P. R. (2004). Kinesin walks hand-over-hand. *Science*, 303(5658):676–8.